Gauge theory for relaxor ferroelectrics

Yousra Nahas

Ecole Centrale Paris

Doctoral Thesis

Gauge theory for relaxor ferroelectrics

Author:
Yousra Nahas

Supervisor:
Igor Kornev

Committee members:
Wolfgang Kleemann
Jirka Hlinka
Alexander Tagantsev
Laurent Bellaiche
Sergey Vakhrushev
Brahim Dkhil

A thesis submitted in fulfillment of the requirements for the degree of Doctor of Philosophy

Laboratoire Structures, Proprietes et Modelisation des Solides (SPMS), CNRS UMR 8580

July 2013

Acknowledgements

I here wish to express my deeply-felt gratitude to Igor Kornev, my Ph.D. advisor, for his guidance during these years. It has been both a challenge and a pleasure to work on giving shape to his inspiring intuition that has had a substantial influence on me, and on the course of the research. I gratefully acknowledge the members of my Ph.D. committee for their time, encouragement, and valuable feedback on a preliminary version of this thesis. I also want to express my thanks to my office mate Sergei Prokhorenko, not only for introducing me to Mathematica, but also for his pertinent remarks and the patience he had listening to me whenever I was thrilled by an idea or disappointed by an impasse. I would also like to thank Ali Al Zein, Pierre-Eymeric Janolin, Brahim Dkhil, Catherine Lhopital, Pascale Salvini and Christine Vinee-Jacquin for their presence whenever it was needed.

Contents

Acknowledgements iii

List of Figures ix

Introduction 1

1 General background 3
- 1.1 Theory of ferroelectrics . . . 4
  - 1.1.1 General background . . . 4
  - 1.1.2 Landau-Ginzburg-Devonshire phenomenological theory . . . 6
  - 1.1.3 Soft-mode microscopical theory . . . 9
  - 1.1.4 First-principles theory . . . 10
- 1.2 Relaxors vs Ferroelectrics . . . 12
- 1.3 Theoretical approaches to Relaxors . . . 15
  - 1.3.1 Compositional fluctuations and glassy like approaches to relaxors . . . 18
    - 1.3.1.1 Spin glasses : an overview . . . 18
    - 1.3.1.2 Compositional fluctuation model . . . 23
    - 1.3.1.3 Superparaelectric model . . . 24
    - 1.3.1.4 Dipole glass models . . . 25
    - 1.3.1.5 From local structure to global properties . . . 30
  - 1.3.2 Random Fields in Relaxors . . . 34
    - 1.3.2.1 Random Field Ising Model : An overview . . . 35
    - 1.3.2.2 Random fields in relaxors . . . 37
    - 1.3.2.3 First-principles-based effective Hamiltonian approach for random fields . . . 38
  - 1.3.3 Spherical Random bond-Random Field model . . . 42
    - 1.3.3.1 Uncoupled Pseudospin Model . . . 43
    - 1.3.3.2 Coupled spherical pseudospin-phonon model . . . 48
- 1.4 Case of study : PLZT . . . 52
  - 1.4.1 PLZT x/65/35 . . . 56
  - 1.4.2 PLZT x/40/60 . . . 60

2 Gauge approach for relaxors 63
- 2.1 A few landmarks on gauge theories . . . 63
  - 2.1.1 Introduction: Local symmetry and Gauge fields . . . 63
  - 2.1.2 Continuum gauge theories . . . 66
    - 2.1.2.1 From a symmetry principle to a Lagrangian . . . 67

2.1.3 Lattice gauge theories . . . 70
2.1.3.1 Geometrical approach . . . 71
2.1.3.2 Sites, links, plaquettes . . . 71
2.1.3.3 Lattice formulation . . . 72
2.1.4 Gauge invariance and frustration in spin glasses . . . 77
2.1.4.1 Gauge transformation . . . 78
2.1.4.2 Gauge invariant frustration . . . 79
2.1.4.3 Continuum gauge glasses models . . . 85
2.1.5 Gauge theory of defects . . . 86
2.1.5.1 Gauge theoretical approaches . . . 87
2.1.5.2 Geometrical approaches . . . 89
2.2 Methodology . . . 91
2.2.1 Postulate of a gauge theoretical approach for relaxors . . . 91
2.2.2 Density functional theory . . . 93
2.2.3 Effective Hamiltonian for ferroelectrics . . . 93
2.2.3.1 General framework . . . 94
2.2.3.2 Construction of the effective Hamiltonian . . . 95
2.2.3.3 Generalization of H_{eff} to mixed compounds . . . 98
2.2.3.4 Physical properties . . . 100
2.2.4 Gauge modified effective Hamiltonian for relaxors . . . 102
2.2.4.1 Gauge-invariant short-range interaction . . . 103
2.2.4.2 Quenched and dynamic contributions to disorder . . . 106
2.2.4.3 Monte-Carlo simulations . . . 110

3 Numerical results 115
3.1 Macroscopic observables . . . 115
3.1.1 Polarization and specific heat . . . 116
3.1.2 Effects of quenched disorder on the dipoles pattern . . . 121
3.1.3 Dielectric response and departure from Curie-Weiss behavior . . . 122
3.1.4 Correlation length . . . 128
3.1.5 Phase Sequence . . . 133
3.1.6 Glassy-like signature and effects of local electric fields . . . 137
3.2 Clustering of the local modes . . . 145
3.3 Under Pressure . . . 151
3.3.1 Strengthened disorder . . . 151
3.3.2 Temperature-Pressure phase diagram . . . 152
3.3.3 Pressure-induced diffuseness . . . 153
3.3.4 Correlation length reduction . . . 154
3.4 Topological defects . . . 156
3.4.1 Finding hedgehogs . . . 156
3.4.2 Dipoles pattern and hedgehogs network . . . 158
3.4.3 Density of hedgehogs . . . 158
3.4.4 Mobility of hedgehogs ⋯ . . . 160
3.4.5 ⋯ in a free background . . . 163
3.4.6 From an hydrodynamic approach ⋯ . . . 163
3.4.7 ⋯ to Vogel-Fulcher's kinetics law . . . 165
3.4.8 Polarization and deformation . . . 165
3.4.9 Binding-unbinding mechanism . . . 166

3.4.10 The underlying gauge 170

Conclusion **173**

A Parallel transport **175**

B Density functional theory **179**

Bibliography **185**

List of Figures

1.1 Schematic view of the cubic prototype perovskite-type structure with the formula $A^{2+}B^{4+}O^{2-}$. The space group is $Pm\bar{3}m$ with a lattice constant $a \sim 4$ Å. 3

1.2 Hysteresis dependence of the polarization of a typical ferroelectric crystal on electric field, P_S is the spontaneous polarization, P_r the remanent polarization and E_c is the coercive field (figure after [37]). 4

1.3 Second order phase transition. (a) Free energy as a function of the polarization at $T > T_0$, $T = T_0$, and $T < T_0$; (b) Spontaneous polarization as a function of temperature; (c) The susceptibility and its inverse. (After Chandra *et al.* [50]) 8

1.4 First order phase transition. a) Free energy as a function of the polarization at $T > T_c$, $T = T_c$, and $T = T_0 < T_c$; (b) Spontaneous polarization as a function of temperature; (c) Susceptibility χ. (After Chandra *et al.* [50]) 9

1.5 Contrast between the properties of normal ferroelectrics and relaxors ferroelectrics (After Samara [4]) 14

1.6 Rhombohedral distortion and ionic displacements along the $\langle 111 \rangle$ direction in PMN at 5 K. (After Mathan *et al.* [7]) 16

1.7 Zero-field cooled ((b),(d)) and field-cooled ((a),(c)) static susceptibilities of spin glass CuMn for 1.08% Mn and 2.02% Mn, demonstrating preparation-dependence and implying metastability. After zero-field cooling ($H < 0.05$ Oe), initial susceptibilities (b) and (d) were taken for increasing temperature in a field of $H = 5.9$ Oe. The susceptibilities (a) and (c) were obtained in the field $H = 5.9$ Oe, which was applied above T_f before cooling the samples.(After Nagata *et al.* [126]) 19

1.8 Temperature dependence of the real part of the magnetic susceptibility of spin glass CuMn (0.94% Mn). Inset is an expanded view revealing the rounding ad the frequency dispersion at and below the peak. (After Mulder *et al.* [125]) . 20

1.9 (a) Simple free energy: In a ferromagnet the free energy as a function of the state of the system has a simple structure (b) Multivalley structure: The free energy of the spin glass state is considered to have many minima and the barriers between them are expected to grow indefinitely as the system size increases. Within a limited time scale, the physical properties of the system are determined by one of the valleys. After a an extremely long time, the observed behavior would reflect the properties of all the valleys (After Nishimori [88]). 21

1.10 Schematic temperature dependencies of the refractive index n, the unit cell volume V, and the reciprocal dielectric permittivity $1/\varepsilon'$ in the canonical relaxor (After Bokov *et al.* [2]) 26

1.11 (a) Schematic representation of the deviation of ε' from the hypothetical Curie and Curie-Weiss behaviors calculated from the values of C and θ obtained by extrapolation from temperatures above that of the onset of local polarization. (b) The inverse susceptibility as function of temperature. The dashed line is the Curie-Weiss behavior determined from high temperature and the inset shows the temperature dependence of the local order parameter q obtained using Eq.(1.22). (After Viehland *et al.* [72]) 28
1.12 The non-Arrhenius character of the relaxational response of PMN. The solid line is a V-F equation fit to the data. (After Viehland *et al.* [73]) 28
1.13 Average size of polar nanoregions in the PMN crystal (determined from diffuse neutron scattering) as function of temperature. The vertical dashed line corresponds to T_f. (After Xu *et al.* [96]) 29
1.14 Measure of the dependency of the dispersion ΔT_{disp} on the fraction x of the ferroelectric end members in (1-x)PSW-xPT, (1-x)PSW-xPZ, (1-x)PMN-xPT, (1-x)PMN-xPZ and (1-x)PMN-xPSN solid solutions. ΔT_{disp} exhibits a smooth monotonic trend as the fraction x of the ferroelectric end members increases, making it suitable to serve as an order parameter for the compositional phase transitions between the relaxor and ferroelectric phases. (After Grinberg *et al.* [134]) 31
1.15 ΔT_{disp} evolution with pressure in PLZT from the experimental results of Samara [104]. ΔT_{disp} increases with increasing pressure. Since off-center displacements are smaller at reduced volumes of perovskites [137], ΔT_{disp} is increased by lower off-centering displacements. (After Grinberg *et al.* [134]) . 33
1.16 Dependence of ΔT_{disp} on $\langle V^2 \rangle$ in PMN-PSN solid solution, revealing a strong resemblance to the behavior of of the order-parameter in a second-order phase transition. (After Grinberg *et al.* [134]) 34
1.17 Comparison of the ΔT_{disp} results of the Landau theory fit with experimental ΔT_{disp}. Data points are close to the $y = x$ line, indicating that the Landau theory of the relaxor-to-ferroelectric transition encapsulated by Eq.1.28 and 1.29 quantitatively captures the trend of the experimental ΔT_{disp} data, and attesting that local effects govern the magnitude of the dispersion in Pb-based relaxor ferroelectrics. (After Grinberg *et al.* [134]) 34
1.18 Droplet of overturned spins in a supposed ferromagnetic (up) ground state. A quenched random field acts at each site of the system; the field points up on the blue sites and down on the green sites. The configuration with the overturned droplet, or domain, can have a lower energy than that consisting of all-pointing up spins. This can happen because the droplet occurs in a region in which the random fields points predominantly down. Imry and Ma estimated the probability of occurrence of such droplets and concluded that the ferromagnetic state is unstable with respect to the formation of large droplets in fewer than 2 dimensions. (Adapted from Fisher *et al.* [120]) 36
1.19 Linear birefringence measured subsequently as a function of temperature on zero-field cooling (ZFC), field heating with E = 1.2kV/cm, E < E_{cr} (FH), field cooling (FC) and zero-field heating (ZFH), illustrating the nonergodic behaviour of PMN crystal. (After Kleemann et al. [123]) 38
1.20 Projection of the Pb-site local fields (in arbitrary units) on a (110) plane through the simulation box of $Pb(Sc_{1/2}Nb_{1/2})O_3$. Chemically ordered regions have relatively small homogeneous fields whereas chemically disordered regions have larger, more varied disordered local fields. (After Burton *et al.* [146]) . . 40

1.21 Snapshot of local mode polarizations of PSN at $T = 600$ K ($\approx T_c$). Highly correlated regions are chemically ordered whereas the disordered matrix is chemically disordered. (After Burton *et al.* [146]) 40
1.22 Simulated PSN polarization as a function of temperature at hydrostatic pressure in the range $0 < P < 22$ GPa. The first-order character of the transition, signaled by the jumps, is accentuated as the pressure increases. (After Burton *et al.* [148]) 41
1.23 Cumulative histogram of P_x values for chemically ordered regions at different temperature for PSN under 18 GPa. The three curves correspond to paraelectric (320 K), relaxor (120 K), and ferroelectric (80 K) states. (After Burton *et al.* [148]) 41
1.24 Predicted pressure vs temperature phase diagram for PSN, indicating the ferroelectric to relaxor transition and the estimated Burns temperature (After Burton *et al.* [148]). 42
1.25 Experimental temperature vs pressure phase diagram for the PSN crystal at 10^4 Hz. The $T_{\mathrm{FE}}(P)$ phase boundary terminates at a finite temperature and pressure, as depicted by the star. Such termination represent a critical point which, from a thermodynamic point of view, would be somewhat akin to the vapor-liquid critical point. (After Samara *et al.* [154]). 43
1.26 Temperature dependence of the Edwards-Anderson order parameter q_{EA} of the reorientable part of the inhomogeneous frequency distribution in PMN ($q_{\mathrm{EA}} \propto M_2$). The inset shows the Gaussian shape of the probability distribution of local polarization. (After Blinc *et al.* [99]) 44
1.27 Generalized temperature-coupling parameter J_0 phase diagram of the spherical random bond-random field model of a relaxor in zero field. (After Pirc *et al.* [98]) 46
1.28 Temperature dependence of the quasistatic non linear susceptibility $a_3 = \chi_3/\chi_1^4$ in PMN for $E = 0$; $a_3(T)$ is found to increase sharply on lowering the temperature between 320 and 220 K. This is incompatible with the case of a random-field frustrated ferroelectric, but quantitatively agrees with the SR-BRF model's predictions (solid line is obtained using Eq.(1.44)). The dashed line represents the temperature dependence of a_3 evaluated for $E/J = 0.01$. Note that with increasing field strength the peak in $a_3(T)$ disappears, *i.e.*, for a large enough field a crossover from a glass phase to ferroelectric one occurs. (After Blinc *et al.* [99]) 47
1.29 Schematic electric field-temperature (E-T) phase diagram. For $E < E_c$ and $J < J_0$, the dipolar freezing temperature $(J^2 + \Delta)^{1/2}/k$ is independent of E and a vertical phase boundary is found in the E-T phase diagram between the ergodic and non-ergodic relaxor phases, indicating the braking of ergodicity associated to the divergence of the longest relaxation time.(After Kutnjak *et al.* [102]) 48

1.30 *(a)*: Scaled third-order nonlinear response a_3 in the spherical-glass (SG) phase ($J_0 = 0$) as a function of temperature, plotted for various values of the random-field strength Δ. Top to bottom: $\Delta/J^2 = 0, 0.001, 0.01, 0.1$. If $\Delta = 0$, corresponding to a pure SG, a_3 diverges at the freezing temperature J/k. For $\Delta \neq 0$ the denominator in Eq.(1.44) never vanishes, the divergence is suppressed. For $\Delta/J^2 \ll 1$, a_3 shows a sharp peak around J/k. This peak broadens at $\Delta/J^2 \geq 0.1$ and ultimately disappears for larger Δ/J^2. *(b)*: Temperature and field dependence of the nonlinear response $a_3(E)$ in the SG phase ($J_0 = 0$) and for fixed value of $\Delta/J^2 = 0.01$. Top to bottom $E/J = 0, 0.01, 0.1, 0.2, 0.5$. With increasing field strength the peak in a_3 gradually disappears. (This effect is similar to that occurring when the value of Δ is increased) *(c)*: Temperature and field dependence of the nonlinear response in the FE in random fields phase ($J = 0$)and for fixed $\Delta/J_0^2 = 0.01$. Top to bottom $E/J_0 = 0, 0.01, 0.1, 0.2, 0.5$.$a_3$ remains finite as $T \to T_c$, but makes a jump at T_c in accordance with mean-field theory. In contrast to the SG case, a_3 in a random-field frustrated ferroelectric does not show any anomalous peak.(After Pirc *et al.* [98]) 49

1.31 Temperature-pressure phase diagram of the relaxor ferroelectric PLZT 6/65/35. The solid and dashed lines are evaluated from the static and dynamic coupled SRBRF-phonon models respectively, whereas the solid triangles and solid circles are experimental points obtained by Samara [104]. The horizontal line is determined by $J_0^*(P_c)$ and separates the FE phase from the nonergodic relaxor phase where the longest relaxation time diverges. The vertical dotted line corresponds to the freezing temperature T_f, where the static nonlinear permittivity has a peak. (After Blinc *et al.* [103]) 51

1.32 Schematic temperature dependence of the dielectric permittivity and spontaneous polarisation, after Hirota *et al.* [3]: (a) relaxors with a diffuse relaxor-to-ferroelectric phase transition. T_C is below $T_m(f)$ and spontaneous polarisation occurs already above T_C. (b) canonical relaxors. At the Burns temperature T_d, polar regions nucleate and after growing with decreasing temperature, they freeze to a non-ergodic state at T_f. Polarisation appears only under an external electric field. 52

1.33 Room-temperature phase diagram for the PLZT solution. The relaxor range is indicated by dashed lines (After Haertling *et al.* [155]). 53

1.34 Phase diagram of PLZT system showing constant La concentration levels (After Haertling *et al.* [155]). 54

1.35 Curie point lowering with incresing La content (After Haertling *et al.* [155]). . 55

1.36 Dielectric constant as a function of temperature (After Haertling *et al.* [155]). 55

1.37 Dielectric constant as a function of temperature (After Viehland *et al.* [158]). 56

1.38 Index of refraction versus temperature $n(T)$ for different La concentration x/65/35 as measured at 6328 Å. The high temperature part can be approximated by a straight line, and the value of T_d, temperature at which the deviation from the straight line occurs, are about the same for the investigated compositions $\sim$ 623 K (After Burns *et al.* [82]). 57

1.39 *Left panel*: Temperature and frequency dependences of the dielectric constant and the dissipation for PLZT 6/65/35 at 1 bar (0 kbar). *Right panel*: Temperature and frequency dependences of the dielectric constant and the dissipation for PLZT 6/65/35 at 15 kbar. The inset shows the increase in the frequency dispersion in T_m with pressure (After Samara [104]). 58

1.40 Temperature-Pressure phase diagram of PLZT 6/65/35 (After Samara [104]). 59

1.41 The dielectric response of PLZT x/40/60 for x = 8, 12 and 15 % La, showing the composition-induced crossover from normal ferroelectric to relaxor behavior. (After Dai *et al.* [156]). 60
1.42 Dielectric response of PLZT 12/40/60 showing the pressure induced FE-R crossover (After Samara [4]). 61
1.43 *Left panel*: Temperature dependence of the reciprocal of $\varepsilon'(T)$ of PLZT 12/40/60 measured at 10^5 Hz and different pressures. The location of the structural phase transition is denoted by T_C for the 1-bar response. *Right panel*: Variation of the correaltion radius (in arbitrary units) for polarization fluctuations with temperature for PLZT 12/40/60 (After Samara [104]). 62

2.1 An internal symmetry space is attached to each point x in space. In the case of the U(1) local symmetry group, the internal symmetry space consists of all possible values of the phase of ϕ, and can be represented by the unit circle, points of which are the phase value. A particular field configuration $\phi(x)$ means a choice of one point on each circle attached to each point in space. For instance, in Figures (a) and (b) the phase values taken by ϕ at points x and $x + \delta x$ are indicated by dots on the unit circle. There is a rule to take a point $\phi(x)$ and parallel transport it to an infinitesimally neighboring point $\phi(x + \delta x)$. The gauge connection exactly specifies how a certain point $\phi(x)$ is mapped into another point $\phi(x + \delta x)$. The gauge connection is illustrated by the arrow between Figures (a) and (b). Local symmetry thus turns the phase into a local variable. The invariance under local transformations, i.e. the freedom to choose any value or convention for the phase (*i.e.*, any point on the circle), is ensured by a compensating change in the connection. Thus, if one phase is rotated, such as Figure (c) with respect to Figure (a), the rotated point, $\phi'(x)$, should still map the same neighboring point $\phi(x + \delta x)$, which demands a change in the connection, as represented by a new arrow between Figures (c) and (d) (after Moore [178]). 64
2.2 A link of the lattice. The links connects the sites x and $x + a\hat{\mu}$. 72
2.3 A plaquette of a lattice. The plaquette boundary is made of four links. 72
2.4 Illustration of a 2-dimensional lattice compactified to a torus by periodic boundary conditions. 73
2.5 Parallel transport: consider an ordinary vector in the plane, expressed in polar coordinates. Consider the unit basis vectors $\mathbf{e}_r$ and $\mathbf{e}_\theta$ at the point P. Parallel transport of $\mathbf{e}_r$ to the point P' (i.e. the transport keeping $\mathbf{e}_r$ parallel to what it was) yields the vector labeled $g\mathbf{e}_r$, different from the unit radial vector $\mathbf{e}'_r$ at point P'. 74
2.6 *Left*: Link $U_{x,\mu}$ from site x in direction μ. *Right*: Link $U^{-1}_{x,\mu}$ in the reverse direction, from site $x + a\hat{\mu}$ in direction $-\mu$. 75
2.7 A contour in the form of an oriented boundary of a plaquette p. 75
2.8 Location of the degrees of freedom of the spin-glass system. The dots represent the spin (site) variables S, and the crosses represent the gauge (link) variables J (after Fradkin *et al.* [204]). 78
2.9 Gauge transformation on the central site. Dark circles are spins pointing up and white circles are spins pointing down. All bonds stemming from the central site have been made negative; the gauge-modified configuration yields the same energy, with the central spin flipped (after Fradkin *et al.* [204]). . . 79

2.10 Illustration of the concept of *frustration*, one of the key ingredients of a spin glass system. Dark circles represent spins pointing up. " + " denotes the ferromagnetic interaction, where parallel spins have the lowest energy, and " − " denotes the antiferromagnetic interaction, where the lowest energy is for anti-parallel spins. If there is an odd number of " − " interactions or bonds around the square, no spin configuration will simultaneously minimize each contribution to the energy. The configuration shown minimizes the energy of the upper and lower bonds, as well as the right hand bond, leaving the left hand bond in a high-energy state, the plaquette is frustrated, $\Phi = 1$ (after Fradkin *et al.* [204]). 79

2.11 Frustration on a sphere. The parallel transport of a vector on a sphere is defined by minimizing the energy locally as one moves around a path. When the path crosses itself forming a loop, there will in general be a change in the direction of the vector, and for small loops this change will be proportional to the area enclosed. The frustration represented by this change is described by the curvature tensor $\mathcal{R}$ of the sphere (after Sethna [203]). 81

2.12 *Left:* In the two-dimensional case, the elementary curved unit is one plaquette. It is thus possible to isolate a single frustrated plaquette at the expense of a dual string of flipped antiferromagnetic bonds starting from the frustration center to the boundary of the system. In the upper figure, the isolated frustrated plaquette is signaled by a cross, the antiferromagnetic bonds are shown in bold and the dual string crossing non-frustrated plaquettes is indicated by a dashed line. A ground state configuration is obtained by pairing the frustrated plaquettes, with minimal total length of the strings (going through adjacent non-frustrated plaquette centers), as shown is the lower figure. *Right:* In the three-dimensional case, a frustrated plaquette cannot be isolated. This follows from the conservation law of curvature, which is the strict analogue of the conservation of magnetic flux in electromagnetism [20]. The elementary unit is thus a *loop* of frustrated plaquettes, as shown in the upper figure. A ground state configuration involves loops of minimal area, enclosing non-frustrated plaquettes as shown in the lower figure. The spin direction across this area changes discontinuously, *i.e.*, one has disclinations. These disclinations induced by frustration have non-trivial topological properties and have been associated to the gauge fields in the continuous version of gauge theory for glasses as formulated by [21, 197, 198]. 82

2.13 Illustration of the degeneracy introduced by frustration. Dark circles are spins pointing up and white circles are spins pointing down. Represented is the 8-fold degenerate ground state of a frustrated plaquette composed of an odd (here one) number of antiferromagnetic bonds on its perimeter, i.e., $\Phi = -1$. Competing interactions render impossible the accommodation of all bonds. There exist a bond at which the lowest state is not achieved, such a bond is frustrated and indicated by the wavy line. This simple investigation shows that competing interactions raise the ground state energy and the ground state degeneracy. 83

2.14 Multivaluedness of displacement field: In the presence of a dislocation, the displacement field is intrinsically non-unique. The figure shows the ambiguity in the assignment of the displacement $u_i(\mathbf{x})$ to the nearest equilibrium position. When removing a layer of atoms, S, the result is a dislocation line along the boundary of the layer. Across the layer, the positions $u_i(\mathbf{x})$ jump by a lattice spacing. The same dislocation line could have been constructed by removing a different layer of atoms, S', just as long it has the same boundary line. Physically there is no difference. There is only a difference in the discriptions which amounts to a difference in the assignment of the equilibrium positions from where to count the displacement field $u_i(\mathbf{x})$ (After Kleinert [19]). 87

2.15 *Left* Dislocation of a hollow ring. The ring is cut along the radial lines AA′ and BB′, the wedge AA′BB′ is removed, and AA′ is joined to BB′. The same dislocation could be made by cutting along CC′ and DD′. *Right* The dislocated ring. The neighbouring points Q_1 and Q_2 lie on opposite sides of the cut (after Nabarro [211]) 88

2.16 Crystalline defects may be generated via so called Volterra process, when layers or sections of matter are cut from a crystal with a subsequent smooth rejoining of the cutting surfaces. A crystal can have two different types of topological defects, which are line-like defects in the 3-dimensional space. A first type of topological defects are translational defects called dislocations: a single-atom layer is removed from the crystal and the remaining atoms relax to equilibrium under the elastic forces. A second type of defects are of the rotation type and called disclinations. They arise by removing an entire wedge from the crystal and re-gluing the free surfaces. Geometrically, the former transformation introduces torsion, the latter curvature (After Kleinert [19]). . 89

2.17 Relation between physical and geometrical notions in the geometric theory of defects (after Katanaev [217]). 90

2.18 Point defect: a vacancy appears when a ball is cut out from the medium, and the boundary sphere is shrunk to a point (after Katanaev [217]). 91

2.19 Vector field distributions on the plane x^1,x^2 for linear disclinations parallel to the x^3 axis. The length of the Frank vector $|\Theta|$ is equal to the total angle of rotation (multiple of 2π) of the field as it goes around the disclination. In the left panel $|\Theta| = 2\pi$, whereas in the right panel $|\Theta| = 4\pi$ (after Katanaev [217]). 91

2.20 Perovskite cubic structure ABO_3, where A and B atoms are respectively located at the corners and in the center of the cube. The octahedra connect O atoms. 94

2.21 Independent intersite interactions corresponding to the parameters j_1, j_2 (first neighbor), j_3, j_4, j_5 (second neighbor), and j_6, j_7 (third neighbor). (After Zhong *et al.* [226]). 97

2.22 Phase diagram of $PbZr_{1-x}T_xO_3$ near the MPB, as predicted by a first-principles-derived scheme that incorporates ferroelectric and antiferrodistortive degrees of freedom. In addition to recovering five of the well-known expected phases (namely, the paraelectric $Pm\bar{3}m$, FE rhombohedral $R3m$, FE tetragonal $P4mm$, FE monoclinic Cm, and the rhombohedral $R3c$ phases), accounting for both FE and AFD motions leads to the prediction of a sixth phase, a monoclinic Cc ground state at intermediate Ti compositions, thereby resolving controversies about its nature. Moreover, a seventh phase $I4cm$ emerges as a discovery for the largest displayed Ti compositions. (After Kornev *et al.* [244]). 101

2.23 Properties of PZT (open dots), and PSN (filled dots), as a function of T/T_m. Panel (a) shows one third of the trace of the dielectric susceptibility tensor directly obtained from MC simulations. Dots in panel (b) show the supercell averaged mean component of the local modes. The arrow in panel (b) emphasizes the highest temperature at which the polarization begins to develop in PSN (After Iniguez *et al.* [48]). 101
2.24 Schematic illustration of the global directional SO(2) symmetry of the first nearest neighbors short-range interaction. Local modes vectors attached to the vertices are omitted. Cylinders, each of which axes coincide with either the x, y or z direction, represent rotations by angles θ_1, θ_2 and θ_3 respectively (three different colors). These rotation angles affect all points in the lattice equivalently, *i.e.*, they are independent of the lattice point i. E^{short} is thus invariant under global directional SO(2) rotations acting in the internal space of the dipole moments $\mathbf{u}_i$ in the plane perpendicular to the linking direction $\hat{\mathbf{R}}_{ij}$. 103
2.25 Schematic illustration of the local directional SO(2) symmetry of the first nearest neighbors short-range interaction. Local modes vectors attached to the vertices are omitted. From each lattice site i stem three cylinders, each of which axes coincide with either the x, y or z direction. These cylinders represent space-dependent rotations (as many colors as there are rotations) by angles $\theta_1(i)$, $\theta_2(i)$ and $\theta_3(i)$ respectively, and are associated with the compensating gauge fields that have been introduced so as to guarantee the invariance of E^{short} under local directional SO(2) rotations acting in the internal space of the dipole moments $\mathbf{u}_i$ in the plane perpendicular to the linking direction $\hat{\mathbf{R}}_{ij}$. 104
2.26 First-principles derived coefficients in the case of PZT with 60% of Zr and 40% of Ti [233, 244]. 106
2.27 Schematic view of two unit cells (cubes) centered around La^{3+} (a) and Pb^{2+} (d). Solid lines indicate quenched links, whereas dotted lines signal relaxing ones. The boundaries of each cube consists of six (b) curved (frustrated) or (e) flat (unfrustrated) plaquettes. Panels (c) and (f) show the parallel transport of a vector around a curved and flat plaquette, respectively. 107
2.28 Schematic view of the random La^{3+}-disorder in the supercell. La^{3+}-containing unit cells are the elementary blue cubes whose edges are associated to quenched links. 108
2.29 The plaquette energy $E_\square$ as a function of βk, with k the gauge coupling parameter and β the inverse temperature, on a 12^3 cubic lattice with cold start configuration (*i.e.* all links are initially set to unit matrices). The temperature is kept fixed at high values in the course of this simulation. Right and left insets show snapshots of plaquettes $\mathbf{U}_\square$ that deviate from unity for high and low values of βk, respectively. 109
2.30 Schematic sketch of a Markov chain in the space of all configurations. The boundary delimits the space of all configurations. The dots represent configurations visited by a Markov chain and are connected with straight lines to indicate that they are visited subsequently. The Markov chain starts in the upper left corner and then evolves towards the center, where the density of dots is larger. This corresponds to a region where the Boltzmann factor $\exp[-\beta H(\mathbf{X})]$ is large, and thus with large probability (After C. Gattringer *et al.* [189]). 112

3.1 Temperature evolutions of the specific heat (filled symbols) and the scaled polarization (open symbols) in $PZ_{60}T_{40}$ system. Dotted vertical line corresponds to T_C. 117
3.2 Temperature evolutions of the specific heat (filled symbols) and the scaled polarization (open symbols) in $PL_5Z_{60}T_{40}$ system. The inset shows the distribution of the quenched (lanthanum containing) unit cells inside the supercell. Dotted vertical line corresponds to T_C. 117
3.3 Temperature evolutions of the specific heat (filled symbols) and the scaled polarization (open symbols) in $PL_{10}Z_{60}T_{40}$ system. The inset shows the distribution of the quenched (lanthanum containing) unit cells inside the supercell. Dotted vertical line corresponds to T_C. 118
3.4 Temperature evolutions of the specific heat (filled symbols) and the scaled polarization (open symbols) in $PL_{15}Z_{60}T_{40}$ system. The inset shows the distribution of the quenched (lanthanum containing) unit cells inside the supercell. Dotted vertical line corresponds to T_C. 118
3.5 Temperature evolutions of the specific heat (filled symbols) and the scaled polarization (open symbols) in $PL_{20}Z_{60}T_{40}$ system. The inset shows the distribution of the quenched (lanthanum containing) unit cells inside the supercell. Dotted vertical line corresponds to T_C. 119
3.6 Temperature evolution of $|\langle \mathbf{u} \rangle|$ for $PZ_{60}T_{40}$ and $PL_xZ_{60}T_{40}$ with $x = 5\%, 10\%, 15\%$ and 20%. The inset shows the variation of the transition temperature T_C with different concentration of lanthanum. Filled symbols refer to the experimental results of Ref. [155], whereas empty symbols correspond to the results of our simulations, dashed lines are guide to the eye. 119
3.7 Integral curves of the local modes ($\propto$ the dipole moments) within a given (x, y) plane of the supercell at $T = 34$ K for $PZ_{60}T_{40}$, $PL_5Z_{60}T_{40}$, $PL_{10}Z_{60}T_{40}$, $PL_{15}Z_{60}T_{40}$ and $PL_{20}Z_{60}T_{40}$ systems. The integral curves are obtained from the local Cartesian components $(\langle u_x \rangle, \langle u_y \rangle)$ averaged over sweeps. 120
3.8 Schematic view of two unit cubes. Left cube has edges corresponding to quenched links (solid lines) and will be referred to as quenched cube (lanthanum containing) QC. Right cube has edges associated with relaxing link variables (dotted lines) and will be reffered to as non-quenched cube (lead containing) $nonQC$. Each of QC and $nonQC$ have relaxing local modes attached to their nodes. 122
3.9 Temperature evolution of the mean angular deviation between the local modes u_i and the ground-state spontaneous polarization $\mathbf{P}_s$ for PZT, PL_5ZT, $PL_{10}ZT$, $PL_{15}ZT$ and $PL_{20}ZT$ systems. Open symbols denote the deviation as experienced by local modes attached to non-quenched cubes $nonQC$, whereas filled symbols denote the deviation of the local modes when attached to quench cubes QC. Dotted vertical lines correspond to T_C. Insets show the distribution of the quenched cubes (lanthanum containing unit cells) inside the supercell. 123
3.10 Integral curves of the local modes ($\propto$ the dipole moments) within a given (x, y) plane of the supercell at $T = 34$ K for $PL_5Z_{60}T_{40}$, $PL_{10}Z_{60}T_{40}$, $PL_{15}Z_{60}T_{40}$ and $PL_{20}Z_{60}T_{40}$ systems. The integral curves are obtained from the local Cartesian components $(\langle u_x \rangle, \langle u_y \rangle)$ averaged over sweeps. Straight lined squares refer to in plane quenched cubes and dotted ones stand for those contained in the upper and lower parallel planes. 124

3.11 Temperature evolution of the inverse dielectric susceptibility and the specific heat for $PZ_{60}T_{40}$. $T_C = 652$ K corresponds to the maximum of the specific heat and the reduced temperature refers to T/T_C. The inverse dielectric susceptibility at $T > T_C$ can be well approximated to a Curie-Weiss form $\chi^{-1} = C\,(T/\Theta - 1)^{\gamma}$ with $\gamma \simeq 1$ and $\Theta \simeq T_C$. 125
3.12 Inverse susceptibility of $PZ_{60}T_{40}$ with varying box size $L = 12, 14, 16, 18$. Table indicates the parameters of the fitted values of the inverse susceptibility to the Curie-Weiss law $\chi^{-1} = C(T - T_0)$. 126
3.13 Temperature evolution of the inverse dielectric susceptibility and the specific heat for $PL_5Z_{60}T_{40}$. $T_C \simeq 408$ K corresponding to the maximum of the specific heat and $T_m \simeq 442$ K corresponding to that of the dielectric susceptibility, are indicated by vertical dashed lines. The reduced temperature refers to T/T_m. The onset of deviation from the Curie-Weiss law at $T_d \simeq 754$ K is indicated by a vertical dashed line. 126
3.14 Temperature evolution of the inverse dielectric susceptibility and the specific heat for $PL_{10}Z_{60}T_{40}$. $T_C \simeq 292$ K corresponding to the maximum of the specific heat and $T_m \simeq 326$ K corresponding to that of the dielectric susceptibility, are indicated by vertical dashed lines. The reduced temperature refers to T/T_m. The onset of deviation from the Curie-Weiss law at $T_d \simeq 455$ K is indicated by a vertical dashed line. 127
3.15 Temperature evolution of the inverse dielectric susceptibility and the specific heat for $PL_{15}Z_{60}T_{40}$. $T_C \simeq 156$ K corresponding to the maximum of the specific heat and $T_m \simeq 176$ K corresponding to that of the dielectric susceptibility, are indicated by vertical dashed lines. The reduced temperature refers to T/T_m. The onset of deviation from the Curie-Weiss law at $T_d \simeq 469$ K is indicated by a vertical dashed line. 127
3.16 Temperature evolution of the correlation length of the gauge field $\xi_{g.f.}$ for $PL_5Z_{60}T_{40}$, $PL_{10}Z_{60}T_{40}$, $PL_{15}Z_{60}T_{40}$ and $PL_{20}Z_{60}T_{40}$ systems. 128
3.17 Temperature evolution of the correlation length of the the local modes $\xi_{l.m.}$ for $PZ_{60}T_{40}$, $PL_5Z_{60}T_{40}$, $PL_{10}Z_{60}T_{40}$, $PL_{15}Z_{60}T_{40}$ and $PL_{20}Z_{60}T_{40}$ systems. Dotted vertical lines refer to the temperatures at which the correlation lengths peak. 131
3.18 Temperature evolution of the correlention length of $PZ_{60}T_{40}$ (cross symbols). Solid line corresponds to the result of the fit yielding $\nu(PZ_{60}T_{40}) = 0.664$ and red squares correspond to the Harris threshold critical exponent $\nu(H) = 0.667$. Dashed line corresponds to the mean field expectations $\nu(\text{mean field}) = 0.5$. . 132
3.19 Cartesian components ($\langle u_x \rangle$, $\langle u_y \rangle$ and $\langle u_z \rangle$) of $\langle \mathbf{u} \rangle$ in $PZ_{60}T_{40}$ as a function of rescaled temperature [155]. T_C corresponds to the maximum of the specific heat and is signaled by a vertical dotted line. Left side inset shows that all the Cartesian components are zero within the error bars in the close vicinity of T_C. Right side insets correspond to the temperature evolution of the lattice axes and the lattice angles. 134
3.20 Cartesian components ($\langle u_x \rangle$, $\langle u_y \rangle$ and $\langle u_z \rangle$) of $\langle \mathbf{u} \rangle$ in $PL_5Z_{60}T_{40}$ as a function of rescaled temperature [155]. T_C corresponds to the maximum of the specific heat and is signaled by a vertical dotted line. Left side inset shows that two of the Cartesian components are zero within the error bars near T_C. Right side insets correspond to the temperature evolution of the lattice axes and the lattice angles, and indicate a transition from a high temperature cubic phase to a low temperature monoclinic (M_A) ferroelectric phase. 134

3.21 Cartesian components ($\langle u_x \rangle$, $\langle u_y \rangle$ and $\langle u_z \rangle$) of $\langle \mathbf{u} \rangle$ in $PL_{10}Z_{60}T_{40}$ as a function of rescaled temperature [155]. T_C corresponds to the maximum of the specific heat and is signaled by a vertical dotted line. Left side inset shows that two of the Cartesian components are zero within the error bars near T_C. Right side insets correspond to the temperature evolution of the lattice axes and the lattice angles, and indicate a transition from a high temperature cubic phase to a low temperature monoclinic (M_A) (close to triclinic) ferroelectric phase. 135

3.22 Cartesian components ($\langle u_x \rangle$, $\langle u_y \rangle$ and $\langle u_z \rangle$) of $\langle \mathbf{u} \rangle$ in $PL_{15}Z_{60}T_{40}$ as a function of rescaled temperature [155]. T_C corresponds to the maximum of the specific heat and is signaled by a vertical dotted line. Left side inset shows that two of the Cartesian components are zero within the error bars near T_C. Right side insets correspond to the temperature evolution of the lattice axes and the lattice angles, and indicate a transition from a high temperature cubic phase to a low temperature monoclinic (M_B) (close to triclinic) ferroelectric phase. 135

3.23 Cartesian components ($\langle u_x \rangle$, $\langle u_y \rangle$ and $\langle u_z \rangle$) of $\langle \mathbf{u} \rangle$ in $PL_{20}Z_{60}T_{40}$ as a function of rescaled temperature [155]. T_C corresponds to the maximum of the specific heat and is signaled by a vertical dotted line. Left side inset shows that two of the Cartesian components are zero within the error bars near T_C. Right side insets correspond to the temperature evolution of the lattice axes and the lattice angles, and indicate a transition from a high temperature cubic phase to a low temperature triclinic phase. 136

3.24 Probability histograms for the averaged over sweeps unit cell local mode components of $PL_5Z_{60}T_{40}$ in the tetragonal phase (T= 461K) in the close vicinity of the transition. 136

3.25 Schematic representation of the influence of the lanthanum substitution on the low temperature structural properties of $PL_xZ_{60}T_{40}$ for increasing lanthanum content $x = 0, 5, 10, 15\%$. 137

3.26 Temperature evolutions of the Edwards-Anderson parameter q_{EA} and squared polarization $\langle \mathbf{u} \rangle^2$, for PZT, PL_5ZT, $PL_{10}ZT$, $PL_{15}ZT$ and $PL_{20}ZT$ systems. Dotted vertical lines correspond to T_C (*i.e.*, the temperature at which the specific heat peaks). 139

3.27 Temperature evolution of the mean angular deviation between the local modes u_i and the local electric fields E_i, for PZT, PL_5ZT, $PL_{10}ZT$, $PL_{15}ZT$ and $PL_{20}ZT$ systems.Insets show snapshots of the local modes (in blue) and fields (in light purple) configurations for PL_5ZT and $PL_{15}ZT$ at $T = 34$ K in (x, y) plane. 140

3.28 Temperature evolution of the mean magnitude of the local electric fields (upper panel) and of their standard deviation (lower panel) for $PZ_{60}T_{40}$ and $PL_xZ_{60}T_{40}$ with $x = 5\%, 10\%, 15\%$ and 20%. Dotted vertical lines refer to T_C, obtained from the maximum of the specific heat. 142

3.29 Temperature evolution of the mean angular deviation between the local modes u_i and the local fields E_i^{RF}, for $PL_{10}ZT$, $PL_{15}ZT$ and $PL_{20}ZT$ systems. 143

3.30 Integral curves within a (x, y) plane associated with the local modes (LM) and with the derived $E_{i\alpha}^{\mathrm{RF}}$ local field (LF) for $PL_{10}ZT$. The upper and lower panels show the configurations for T= 34K and T= 1358K, respectively. At low temperatures, encircled regions illustrate the bending effect of the LF on the LM. 144

3.31 Icosahedron and its associated planar graph representation. The icosahedron is a regular polygon of twelve nodes and twenty triangular faces. Its spherical projection defines a regular tiling of the circumscribing sphere, therefore splitting the maximal solid angle into twenty equal parts. The numbers appearing in the planar graph representation of the icosehdraon correspond to a labeling of the faces. 145

3.32 Theta-Phi diagram of the considered regular triangulation. Each region of the diagram represents the theta-phi extension of the solid angle associated to the face. The blue dots correspond to the eight equivalent rhombohedral ground-state directions. In the chosen labeling, one can see that the $[1, 1, 1]$ direction for example is assigned to the fifth face. 146

3.33 $PZ_{60}T_{40}$: Temperature evolution of the number of clusters (N_{Cl}), their average volume (V_{Cl}^{av}) and their total volume (V_{Cl}^{tot}) per face. The y axis refers to the face label, the x axis denotes temperature. Let's first put our attention on the high-temperature region. *(i)* High temperatures are characterized by small values of N_{Cl}, V_{Cl}^{av} and V_{Cl}^{tot} for all faces. Thus spatial correlations are very weak, and all directions are equivalent. This is merely indicative of full disorder. *(ii)* While approaching T_C (indicated by a vertical line) from above, one observes signatures of critical fluctuations, such as emergence of preferred orientations (some directions are no longer represented while large spatial clusters corresponding to certain equivalent rhombohedral orientations appear) and scale invariance (indicated by the fact that differently populated directions acquire equal number of clusters). *(iii)* Below T_C, up to $\sim$ 440K, one observes the condensation of only several clusters oriented in $[1, -1, 1]$ and $[1, -1, -1]$ directions (faces 4, 14 and 16). Whereas the single cluster corresponding to $[1, -1, 1]$ (major phase) direction stands out in terms of large volume, the clusters with $[1, -1, -1]$ (minor phase) orientation are numerous and, in contrast, relatively much smaller in volume. This latter observation shows that below T_C the percolation of $[1, -1, 1]$ clusters has been achieved, however the volume corresponding to the major phase is not simply connected. This situation is not persistent since a further decrease of the temperature drives this minor phase to gradually shrink, ultimately disappearing at 440K. *(iv)* At temperatures below $\sim$ 440K the ground state is achieved. It is important to mention that what could appear as a switching of direction is, in fact, only an artifact of Metropolis Monte-Carlo method. 147

3.34 $PL_5Z_{60}T_{40}$: Temperature evolution of the number of clusters (N_{Cl}), their average volume (V_{Cl}^{av}) and their total volume (V_{Cl}^{tot}) per face. The y axis refers to the face label, the x axis denotes temperature.*(i)* Qualitatively, the high temperature region features the same full-disorder characteristics as those featured by the pure system $PZ_{60}T_{40}$. *(ii)* However, on approaching T_C fom above, a slight difference emerges in comparison with $PZ_{60}T_{40}$. The proloferation of clusters is enhanced, as attested by the increase of both the N_{Cl} and V_{Cl}^{tot}, while V_{Cl}^{av} stays the same for the two systems. This indicates the emergence of a somewhat shy, short-range correlated order above T_C *(iii)* Just below T_C, the main difference between $PL_5Z_{60}T_{40}$ and $PZ_{60}T_{40}$ concerns the dispersion of the major phase around its rhombohedral direction. Indeed, while the ground state corresponds to $[1, 1, -1]$ direction (contained in face 8), V_{Cl}^{av} of faces 7, 15 and 18 stays comparable to that of face 8 on a wide temperature range, thereby indicating a dispersion around the ground state direction.*(iv)* At low temperatures, the aforementioned dispersion subsists, explaining the drop in magnitude of $PL_5Z_{60}T_{40}$ relatively to $PZ_{60}T_{40}$. 148

3.35 $PL_{10}Z_{60}T_{40}$: Temperature evolution of the number of clusters (N_{Cl}), their average volume (V_{Cl}^{av}) and their total volume (V_{Cl}^{tot}) per face. The y axis refers to the face label, the x axis denotes temperature. *(i)* The high temperature range exhibits full-disorder characteristics. *(ii)* Above T_C and up to ∼500 K, one observes that for faces labeled by 1, 2 and 3, both N_{Cl} and V_{Cl}^{tot} gradually increase, while V_{Cl}^{av} stays the same. This trend seems of the same nature as that described for $PL_5Z_{60}T_{40}$, yet monotonical and more pronounced. *(iii)* Below T_C, faces 1, 13 and 20 experience a weak depopulation of their clusters, as attested by the decay of V_{Cl}^{tot}. This trend is similar to that described for $PL_5Z_{60}T_{40}$, but weaker. *(iv)* The ground state is thus populated by clusters belonging to faces dispersed around two rhombohedral directions (a main one, $[-1,-1,1]$ associated with face 3, and $[-1,1,1]$ associated with face 1), making the average symmetry monoclinic (section 3.1.5). 149

3.36 $PL_{15}Z_{60}T_{40}$: Temperature evolution of the number of clusters (N_{Cl}), their average volume (V_{Cl}^{av}) and their total volume (V_{Cl}^{tot}) per face. The y axis refers to the face label, the x axis denotes temperature. *(i)* The high temperature range exhibits full-disorder characteristics. *(ii)* Above T_C, faces 6, 14 and 16 exhibit a monotonical increase of V_{Cl}^{tot} and of V_{Cl}^{av}. The fact that V_{Cl}^{av} also increases in the case of $PL_{15}Z_{60}T_{40}$ is an indication of a more developed local order. *(iii)* Below T_C, large volumes of differently ordered regions make the ground state direction mixed between different directions, mainly composed of the directions $[1,-1,-1]$ (faces 6, 7, 14 and 16) and $-[1,-1,-1]$ (faces 10, 20), making the average symmetry monoclinc on the verge of being triclinic (section 3.1.5). 149

3.37 $PL_{20}Z_{60}T_{40}$: Temperature evolution of the number of clusters (N_{Cl}), their average volume (V_{Cl}^{av}) and their total volume (V_{Cl}^{tot}) per face. The y axis refers to the face label, the x axis denotes temperature. *(i)* In this case, disorder extends over a wide temperature range. *(ii)* The ground state is strongly mixed, resulting in a triclinic average symmetry (section 3.1.5). 150

3.38 Biggest clusters of local modes for $PZ_{60}T_{40}$ system, just above T_C, and for $PL_5Z_{60}T_{40}$, $PL_{10}Z_{60}T_{40}$, $PL_{15}Z_{60}T_{40}$ and $PL_{20}Z_{60}T_{40}$ systems, for temperatures just above their T_m. 150

3.39 Influence of pressure on the temperature evolution of $|\langle \mathbf{u} \rangle|$ in $PL_5Z_{60}T_{40}$ systems. Plot of the polarization as a function of T for various pressures in the range $0 \leq P \leq 100$ kbar. 151

3.40 Integral curves of the local dipole moments within a given (x, y) plane for $PL_5Z_{60}T_{40}$ at $T = 34K$ under 1 bar, 10 kbar, 30 kbar and 40 kbar for the same realization of random disorder. 152

3.41 Evolution with temperature of the specific heat (left) and the inverse dielectric response (right) for $PL_5Z_{60}T_{40}$ under 1 bar, 10 kbar, 20 kbar, 30 kbar and 50 kbar. The temperature at which the specific heat peaks is used for the determination of T_C while that at which the dielectric response peaks corresponds to T_m. 153

3.42 Temperature-Pressure phase diagram for $PL_5Z_{60}T_{40}$. Dotted lines delimit the relaxor region and their slopes are exctracted from linear fits of the T_C and T_m data, $dT_C/dP = -4.85$ K/kbar and $dT_m/dP = -4.66$ K/kbar respectively. 153

3.43 Plots of $\mathrm{Ln}(\chi^{-1} - \chi_m^{-1})$ versus $\mathrm{Ln}\,(T/T_m - 1)$ in the paraelectric regions for $PL_5Z_{60}T_{40}$ under 1 bar and 30 kbar. Linearly fitting the data yields $\gamma \simeq 1$ in both cases for high enough temperatures. As the temperature is lowered slopes increase, $\gamma \simeq 1.66$ and $\gamma \simeq 2.31$ for 1 bar and 30 kbar respectively. . . 154

3.44 Variation of the correlation length for local modes $\xi_{l.m.}$ (left panel) and gauge field $\xi_{g.f.}$ (right panel) fluctuations for $PL_5Z_{60}T_{40}$ showing the influence of pressure. (Both $\xi_{l.m.}$ and $\xi_{g.f.}$ are computed according to the method provided in section 3.1.4). 155
3.45 Temperature evolution of the density of pairs of hedgehogs n_p for PL_5ZT under increasing pressure. 155
3.46 Schematic view of the ordered clusters pattern within a plane. Jaggerred perimeters cross at contact points, depicted by red points and representing hedgehogs. 156
3.47 Schematic view of dipoles configurations showing ideal hedgehogs of charges $Q = +1$ (source-like) and $Q = -1$ (sink-like). 157
3.48 Integral curves associated to the local modes vector fields within a (x, y) plane and projection onto the plane of topological defects (represented by points) for PL_5ZT, $PL_{10}ZT$, $PL_{15}ZT$ and $PL_{20}ZT$. Results correspond to $T \geqslant T_m$, specifically, $T = 441$K, $T = 340$K, $T = 203$K and $T = 170$K for 5%, 10%, 15% and 20%, respectively. 159
3.49 Temperature evolution of the density of pairs of hedgehogs $\langle n_p \rangle$ (averaged over MC sweeps) for PZT, PL_5ZT, $PL_{10}ZT$, $PL_{15}ZT$ and $PL_{20}ZT$ (left figure). The horizontal dashed line indicates the site percolation threshold p_c for pairs for Rubik neighborhood. Right figure shows the temperature dependence of the derivative $\mathrm{d}\langle n_p \rangle / \mathrm{d}T$ of the density of pairs. Dotted vertical lines in both left and right figures correspond to the temperature at which the derivative peaks. 160
3.50 Plot of the logarithm of the defect pair density versus the inverse temperature for $PZ_{60}T_{40}$, $PL_5Z_{60}T_{40}$, $PL_{10}Z_{60}T_{40}$, $PL_{15}Z_{60}T_{40}$ and $PL_{20}Z_{60}T_{40}$. Dotted lines are linear fits to the data for $T < T_C$. The right figure collects the extracted slopes of the fit, yielding the evolution of the activation energy (arb. units) with the percentage of quenched disorder. 160
3.51 Supercell snapshots of $PL_5Z_{60}T_{40}$, as obtained for three consecutive MC sweeps at $T = 407K$. Dark blue cubes are associated to the topologically defective unit cells whose variable location in the supercell over the sweeps is indicative of a dynamical nature. 161
3.52 Supercell snapshots of $PL_5Z_{60}T_{40}$, as obtained for six consecutive MC sweeps at $T = 271K$. Pale cubes are associated to the quenched (*i.e.* lanthanum containing) unit cells and thus display a fixed spatial distribution in the supercell over the sweeps. Red cubes correspond to quenched unit cells which are also topologically defective while dark blue cubes are associated to topologically defective unit cells whose location is different from that of the quenched unit cells. Topological defects are hence hopping dynamical entities, whose location in the supercell is not necessarily in correspondence with that of the quenched cells. 161
3.53 Evolution with temperature of the fraction $N_{QC_{Q\neq 0}}/N_{QC}$ of quenched cubes QC carrying a non-zero topological charge $Q \neq 0$, for PL_5ZT, $PL_{10}ZT$, $PL_{15}ZT$ and $PL_{20}ZT$. 162
3.54 Temperature evolution of the free volume $d_{f.v}$ (left figure) and of its fractal dimension (right figure) for the pure system PZT and different PL_xZT systems. 164
3.55 Evolution with temperature of the density of topological defects $\langle n \rangle$. Solid lines correspond to the $\langle n \rangle = a + \langle n_0 \rangle \exp[-b/(T - T_0)]$ fits, where T_0 are signaled by dotted vertical lines 164
3.56 Evolution with temperature of the average volume of zero-charged unit cells (Q=0) and of topologically defective cells (with Q=1 and Q=-1) for $PL_{10}ZT$. 166

3.57 Temperature evolution of the number of clusters (left panels) and their average volume (right panels) for $PZ_{60}T_{40}$ and $PL_5Z_{60}T_{40}$ systems. Curves associated to $|Q| = 1$ correspond to the clustering procedure performed on the hedgehogs population regardless of the sign of the charge they carry, while curves associated to $Q = 1$ and $Q = -1$ correspond to the charge-specific clustering carried out on each of the subpopualtions of hedgehogs independently, *i.e.*, on that of the positively charged hedgehogs and on that of the antihedgehogs, respectively. 167

3.58 Temperature evolution of the number of clusters (left panels) and their average volume (right panels) for $PL_{10}Z_{60}T_{40}$, $PL_{15}Z_{60}T_{40}$ and $PL_{20}Z_{60}T_{40}$ systems. Curves associated to $|Q| = 1$ correspond to the clustering procedure performed on the hedgehogs population regardless of the sign of the charge they carry, while curves associated to $Q = 1$ and $Q = -1$ correspond to the charge-specific clustering carried out on each of the subpopualtions of hedgehogs independently, *i.e.*, on that of the positively charged hedgehogs and on that of the antihedgehogs, respectively. The inset of the figure depicting the number of clusters for $PL_{10}Z_{60}T_{40}$ shows that clusters corresponding to $\{|Q| = 1\}$-clustering procedure increase in number in the $0 < T < 200$ K temperature range. 168

3.59 Temperature evolution of the average charge of $\{|Q| = 1\}$-obtained clusters for $PL_5Z_{60}T_{40}$, $PL_{10}Z_{60}T_{40}$, $PL_{15}Z_{60}T_{40}$ and $PL_{20}Z_{60}T_{40}$ systems. 169

3.60 Two-dimensional schematic representation of the unbinding mechanism of hedgehog/antihedgehog pairs with increasing temperature. While at low temperatures, pairs of oppositely charged defects are bound yielding a phase akin to a gas of (hedgehog/antihedgehog) dipoles, the higher temperature phase constitutes a plasma of unbound hedgehogs. 170

3.61 Temperature evolution of the density of pairs of hedgehogs n_p in $PL_{15}ZT$ for k=0.01 and k=0.05. Lower panels depict the integral curves of the order parameter field within a (x, y) plane for T=17 K. Squares indicate the spatial distribution of the quenched cells. 171

A.1 Rotation of the internal space direction of a moving test particle. The internal angles change from $\theta(x)$ to $\theta(x+\mathrm{d}x)$ as the test charge moves from x to $x+\mathrm{d}x$ (after Moriyasu, [15]). 176

Introduction

Relaxor ferroelectrics constitute a class of disordered crystals possessing peculiar structure and properties. They were discovered more than 50 years ago among the complex oxides with perovskite structure, and so far, in spite of numerous investigations, the microscopic origin of the peculiar behavior of relaxor ferroelectrics remains unsettled.

In these materials, the disorder and frustration stemming from spatial heterogeneities are an integral part of their characteristics. Several theoretical formulations have been conducted in the attempt of elucidating the origin of the relaxor behavior, mainly either involving phenomenological approaches or resorting to statistical spin models. However, the understanding remains scattered and a unifying approach is still lacking. The experimental picture that has emerged from local structural probing yet clearly indicates the necessity of distinguishing the short-range effects from the long-range ones. At short range and at relatively low temperatures the local symmetry is polar and the atomic shifts from their ideal cubic symmetry positions are correlated. At long range however, the global symmetry is cubic due to the statistical atomic disorder that results in a spatially varying polarization, yielding zero net global polarization. In this respect, these materials have a structure that locally deviates from the average global one, giving rise to remarkable dielectric, electrostrictive, and electrooptic properties, making them of both a technological and fundamental interest.

It is the purpose of this work to account for the relevance of the local scale and of the short-range interactions to the properties of relaxors by proposing a microscopical model based on *local symmetry*, within the lattice gauge theoretical framework. This postulate is mainly motivated by the manifest lack of generalized rigidity, *i.e.*, by the inability of correlations to fully develop so as to achieve homogeneous order. In another words, the competition between ordering and disordering interactions has to be assessed on a local scale rather than on a global one, since the mere consideration of the global scale may conceal the underlying local effects from which the global properties originate. Essentially, our approach revolves around the postulate of a local gauge symmetry and stands as a generalization of the first-principles-derived effective Hamiltonian so as to incorporate gauge fields taking values in a Lie group, in addition to ferroelectric and elastic degrees of freedom. It is then applied to a specific relaxor, namely, disordered $(Pb_{1-3/2x}La_x)(Zr_yTi_{1-y})O_3$ (PLZT) solid solutions.

The work is organized as follows.

* Chapter 1 constitutes an overview of relaxor ferroelectrics. Since the parent compounds of ABO_3 perovskite relaxors are prototypical ferroelectrics, it is worthwhile starting the chapter by a brief review of the phenomoneological, soft-mode and first-principles theories of ferroelectrics. This will be followed by a discussion of the properties of relaxor ferroelectrics and the contrast between these properties and those of normal ferroelectrics. We then give a detailed presentation of both the accumulated and current knowledge about relaxors. Finally, a section is devoted to PLZT family of relaxors, as these compounds will later serve as a case of study in the assessment of our model.

* Chapter 2 is concerned with providing the conceptual foundations and framework for a gauge theory for relaxors, and is subdivided into two main parts. The first part introduces the common concepts and methods underlying various related gauge approaches, emphasizing their lattice formulation and they reliability in describing defects and disorder-induced frustration. The second part is methodological and provides a detailed description of the implementation of local symmetry and related gauge concepts to the case of relaxor ferroelectrics.

* Chapter 3 collects the main results that were obtained from Monte Carlo simulations and also presents an attempt to characterize the underlying role of topological defects in the relaxor behavior.

Finally, concluding remarks and future directions are gathered in the conclusion.

Chapter 1

General background

The most studied and most technologically [32–34] important relaxor ferroelectrics are mixed ABO_3 perovskite oxides (Fig.1.1).

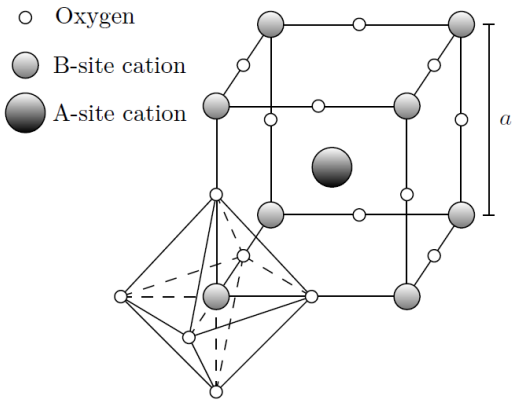

Fig. 1.1: Schematic view of the cubic prototype perovskite-type structure with the formula $A^{2+}B^{4+}O^{2-}$. The space group is $Pm\bar{3}m$ with a lattice constant $a \sim 4\,\text{Å}$.

Since the parent compounds of ABO_3 perovskite relaxors are prototypical ferroelectrics (FE), it is worthwhile reviewing the phenomenological, soft-mode and first-principles theories of ferroelectrics. This will be addressed in section 1.1. In order to appreciate the properties of relaxor ferroelectrics, some of their properties are contrasted with those of normal ferroelectrics in section1.2. Section 1.3 surveys both the accumulated and current knowledge about relaxors, and is subdivided into three parts, referring to the three main categories of models. The subdivision is indicative and aims only into highlighting the conceptual analogies invoked to understand the relaxor behavior. Whereas the first category has made wide use of the random exchange mechanism, the second one envisioned disorder as a source of random fields, and the third one has combined both, in a random-bond random-field model. Finally, section 1.4 reviews the main features of the PLZT family of relaxors, as these compounds will later serve as a case of study to assess our model.

1.1 Theory of ferroelectrics

1.1.1 General background

From a crystallographic point of view, crystals are classified into seven systems according to their geometry: triclinic, monoclinic, orthorhombic, tetragonal, trigonal, hexagonal, and cubic. These systems can be subdivided into 32 possible crystal classes, or point groups, according to their symmetry with respect to a point. 11 of them are centrosymmetric and thus cannot exhibit polar properties. The remaining 21 lack a center of symmetry, and thus can possess one or more polar axes. All but one exhibit piezoelectricity, the property that the application of mechanical stress induces polarization, and conversely, the application of an electric field produces mechanical deformation. Of these 20 piezoelectric classes, 10 have a unique polar axis and thus are spontaneously polarized, *i.e.*, polarized in the absence of an electric field. Crystals belonging to these 10 classes are called pyroelectric, as they display a temperature dependent polarization. Ferroelectric crystals belong to the pyroelectric family[1], but have the particularity of exhibiting the additional property of reversibility under applied electric field of the spontaneous polarization's direction as shown by the hysteresis loop in Fig.1.2 [4, 36].

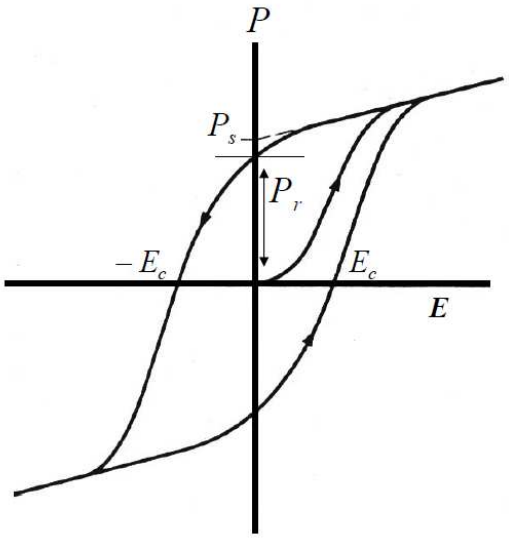

Fig. 1.2: Hysteresis dependence of the polarization of a typical ferroelectric crystal on electric field, P_S is the spontaneous polarization, P_r the remanent polarization and E_c is the coercive field (figure after [37]).

In the linear approximation, a dielectric sample placed in an external electric field **E** acquires a macroscopic polarization that is proportional to the strength of the applied field:

$$P_i = \varepsilon_0 \chi_{ik} E_k \tag{1.1}$$

[1]Ferroelectricity is accompanied by the appearance of new components in the pyroelectric tensor [35].

where χ_{ik} is the tensor of the dielectric susceptibility of the material and where $\varepsilon_0 = 8.854 \times 10^{-12}\left[F.m^{-1}\right]$ is the dielectric permittivity of the vacuum. If the dielectric is isotropic and uniform, χ is a scalar and Eq.(1.1) is reduced to:

$$\mathbf{P} = \varepsilon_0 \chi \mathbf{E} \tag{1.2}$$

The electric flux density, or electric displacement, $\mathbf{D}$ is defined as [2]

$$\mathbf{D} = \varepsilon_0 \mathbf{E} + \mathbf{P} = \varepsilon \mathbf{E} \tag{1.3}$$

where $\varepsilon = \varepsilon_0(1+\chi)$ is the dielectric response of the medium. When the dielectric is subjected to a time dependent electric field, $\mathbf{D}$ and $\mathbf{P}$ do not follow instantaneously, but rather over a period of time due to inertial and dissipation effects. A relaxation time τ is thus needed to reach equilibrium values. Therefore, if $\mathbf{E} = \mathbf{E}_0 \exp(i\omega t)$, then $\mathbf{D} = \mathbf{D}_0 \exp(i\omega t - \delta)$, where ω is the frequency of the applied field and δ the loss angle. In the presence of dielectric losses and relaxation effects, ε is a complex quantity $\varepsilon = \varepsilon' + i\varepsilon''$, where the real part, ε', is called the dielectric response and the imaginary part, ε'', is the so-called loss. Both are related, at any given frequency, by the Kramers-Kronig dispersions relation, and define the loss angle $\tan\delta = \varepsilon''/\varepsilon'$ [4, 36].

Although ferroelectric crystals are a widely varied group, they exhibit general characteristic properties among which [4]:

- ◇ The hysteresis loop disappears at a certain temperature, the Curie point T_C, above which the crystal behaves as a normal dielectric.
- ◇ Above T_C a ferroelectric crystal loses its intrinsic polarization and transforms to a phase of higher symmetry. This higher temperature phase is usually nonpolar, or paraelectric.
- ◇ The polar crystal structure of a ferroelectric can be derived from the high temperature paraelectric structure by a slight distortion of the crystal lattice. This is the main reason behind the success of the phenomenological theory of ferroelectricity which assumes that the same free energy function is applicable for both the ferroelectric and paraelectric phases.
- ◇ Ferroelectrics generally have a ε (or χ) larger than in normal dielectrics, which rises to a peak value at T_C.
- ◇ Above T_C, ε of a ferroelectric (measured along the polar axis) usually obeys the Curie-Weiss law $\varepsilon = C/(T - T_0)$, where C and T_C, are the Curie-Weiss constant and Curie-Weiss temperature, respectively, and where T_0 coincides with T_C in the case of a second order transition.

[2] For anisotropic dielectrics, χ as well as ε are tensors and Eq.(1.3) must be written as $D_i = \sum_{j=1}^{3} \varepsilon_{ij} E_j$, $i = 1, 2, 3$.

1.1.2 Landau-Ginzburg-Devonshire phenomenological theory

Based solely on symmetry considerations, Landau theory can provide a reliable description of a system's equilibrium behavior near a phase transition. This phenomenological approach[3] relates measurable quantities to one another using a minimum set of input parameters that can be determined either by comparison to experiment or from first-principles approaches. Because it assumes spatial averaging of all local fluctuations, this theory is particularly well-suited to systems with long-range interactions such as ferroelectrics [49, 50].

The fundamental idea of the Landau approach is that the free energy can be represented as a series expansion of the order parameter in the vicinity of the transition. Although it is suspicious that singular behavior associated with a transition can emerge from such a regular expansion, this assumption is to a certain extent justified because the value of the order parameter that minimizes the free energy is itself a singular function of the expansion coefficients which are temperature-dependent. However, the power-law form of the free-energy may not be valid very close to the transition. Furthermore Landau theory is based on the presumption that local fluctuations in the order parameter are small, whereas in the immediate vicinity of the transition, critical fluctuations occur. Given those limitations, Levanyuk and Ginzburg [51, 52] developed a criterion to assess the validity of Landau theory. Qualitatively [50] their criterion suggests that Landau Theory works well [4] when the coordination number is high, condition that can be achieved either by large dimensionality or by long-range interactions (such as dipole-dipole interactions).

The first step in the development of a thermodynamic theory is the identification of the relevant degrees of freedom of the problem under consideration. Three independent variables have to be chosen among the conjugate pairs temperature-entropy, stress-strain, and electric field-electric displacement (or polarization). Different combinations yield different thermodynamic potentials related by the proper Legendre transformations between the independent variables [49]. The next step is the choice of a prototype state. For perovskite oxides this state usually corresponds to a non-polar phase. Then, a polynomial expansion of the thermodynamic potential as a function of the independent variables is done and is assumed to remain valid before and after the phase transition. Coupling terms between the independent variables are also considered [5]. Finally, the thermodynamic potential is minimized to find the equilibrium thermodynamic states, and specific thermodynamic functions

[3] Let us note that the Landau theory of phase transitions is a mean self-consistent theory.

[4] *i.e.* the critical exponents are mean-field-like

[5] The major difference between Landau theory treatments of ferroelectricity and ferromagnetism arises from the strong coupling between the polarization and the lattice, feature which is usually insignificant in the magnetic case. Ferroelectric dipoles are generated by the displacement of atoms, and thus on a local scale there is strong spatial anisotropy. In general the development of a macroscopic polarization in a ferroelectric will be accompanied by a macroscopic strain, and thus ferroelectricity and ferroelasticity are closely related phenomena. Elastic degrees of freedom thus must be represented in a Landau theory for most ferroelectrics.

are subsequently computed by differentiating it accordingly. The effect of the temperature arises from a temperature dependence of some parameters assumed *a priori*.

Let us exemplify the approach considering polarization and strains as independent degrees of freedom. The expression for the thermodynamic potential around the unpolarized cubic crystal takes the following form, as first suggested by Ginzburg [53–55] and further developed by Devonshire [56, 57]:

$$\begin{aligned} F(T,\eta,P) &= \frac{1}{2}C_{11}(\eta_{11}^2+\eta_{22}^2+\eta_{33}^2)+C_{12}(\eta_{22}\eta_{33}+\eta_{33}\eta_{11}+\eta_{11}\eta_{22}) \\ &+ \frac{1}{2}C_{44}(\eta_{12}^2+\eta_{23}^2+\eta_{31}^2)+a_1(P_1^2+P_2^2+P_3^2) \\ &+ a_{11}(P_1^4+P_2^4+P_3^4)+a_{12}(P_1^2P_2^2+P_1^2P_3^2+P_2^2P_3^2) \\ &+ a_{111}(P_1^6+P_2^6+P_3^6)+g_{11}(\eta_{11}P_1^2+\eta_{22}P_2^2+\eta_{33}P_3^2) \\ &+ g_{12}\left[\eta_{11}(P_2^2+P_3^2)+\eta_{22}(P_1^2+P_3^2)+\eta_{33}(P_1^2+P_2^2)\right] \\ &+ g_{44}(\eta_{23}P_2P_3+\eta_{31}P_3P_1+\eta_{12}P_1P_2) \end{aligned} \tag{1.4}$$

where C_{11}, C_{12}, and C_{44} stand for the elastic stiffness of the material, and the subindices refer to the Cartesian directions. The expansion has been cut at 6th order in P for simplicity, and it does not contain odd terms in polarization since the prototype state is centrosymmetric. The last three terms in the expansion couple the strain and the polarization[6].

For simplicity, let us ignore the strain fields and suppose that the polarization is directed along one of the Cartesian directions. Under these conditions, the expression for the thermodynamic potential reduces to

$$F(T,\eta,P) = a_1P^2 + a_{11}P^4 + a_{111}P^6 \tag{1.5}$$

The signs and magnitudes of the coefficients determine the nature of the transition and the behavior of the dielectric properties in the immediate vicinity of T_c. As previously mentioned, the coefficients of the expansion should be temperature dependent. However, for practical purposes, it usually sufficient to consider the quadratic coefficient as T-dependent, of the form $a_1 = a(T - T_0)$, with a a positive constant and where the temperature T_0 signals the sign change of a_1. a_{111} is fixed to positive constant values.

$$F(T,\eta,P) = a(T-T_0)P^2 + a_{11}P^4 + a_{111}P^6 \tag{1.6}$$

Depending on the sign of a_{11} two cases are to be considered:

- ▷ If $a_{11} > 0$, then a second order phase transition occurs at $T = T_0$: For $T > T_0$ the quadratic term is positive and the thermodynamic functional is a single well with its

[6] As it will appear clearly later, this expression shows strong similitude with the effective Hamiltonian that also corresponds to an expansion in terms of polarization and strain with appropriate coupling terms.

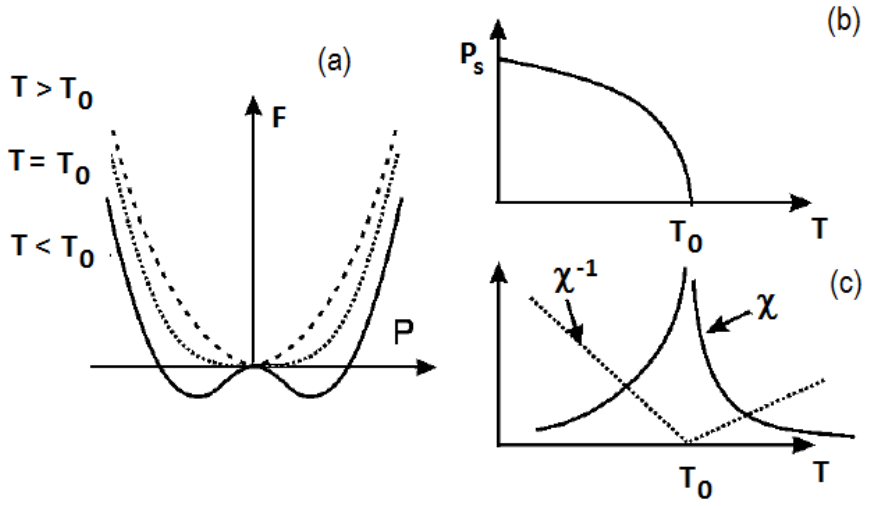

Fig. 1.3: Second order phase transition. (a) Free energy as a function of the polarization at $T > T_0$, $T = T_0$, and $T < T_0$; (b) Spontaneous polarization as a function of temperature; (c) The susceptibility and its inverse. (After Chandra *et al.* [50])

minimum corresponding to the non-polar $P = 0$ phase. For $T < T_0$ the quadratic coefficient is negative, and the thermodynamic potential displays the typical double well shape. There are two minima for $P \neq 0$. In this case the change in temperature of P is continuous and T_0 corresponds to the Curie point T_c (Fig.1.3).

▷ If $a_{11} < 0$, even if $T > T_0$ (such that the quadratic coefficient is positive) the free energy may have a subsidiary minimum at non-zero P. As T is reduced, this minimum will drop in energy below that of the unpolarized state, and thus will correspond to the thermodynamically favored configuration. The temperature at which this happens is, by definition, the Curie temperature T_c which however in this case exceeds T_0. At any temperature between T_c and T_0 the unpolarized phase exists as a local minimum of the free energy. The most important feature of this phase transition is that the order parameter jumps discontinuously to zero at T_c. This type of phase transition is usually called a first-order or discontinuous transition (Fig.1.4).

Landau theory offers a simple and coherent framework to classify and describe structural phase transitions at a phenomenological level. For this reason it was widely used in the past to study ferroelectric systems and still remain a valuable approach. We emphasize that Landau theory is strictly a macroscopic approach and thus it cannot describe any microscopic physics (e.g. atomic displacements etc.) associated with the phase transition.

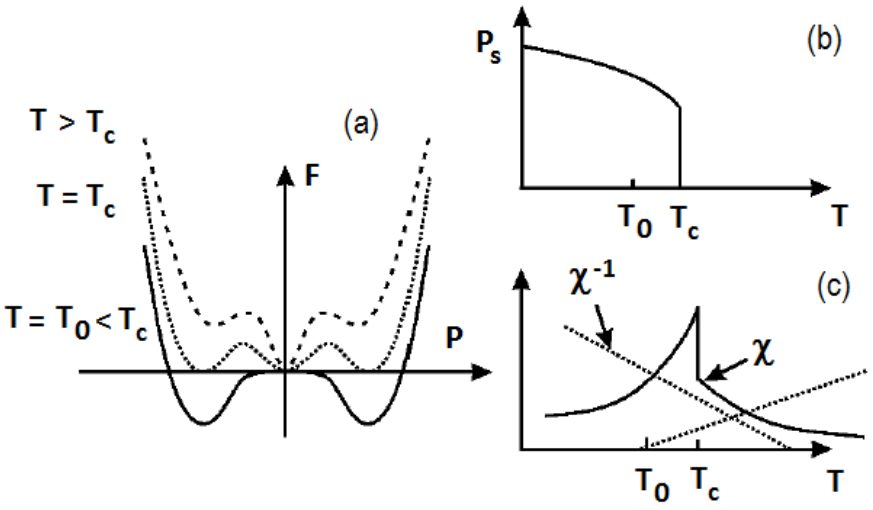

Fig. 1.4: First order phase transition. a) Free energy as a function of the polarization at $T > T_c$, $T = T_c$, and $T = T_0 < T_c$; (b) Spontaneous polarization as a function of temperature; (c) Susceptibility χ. (After Chandra *et al.* [50])

1.1.3 Soft-mode microscopical theory

One of the most significant theoretical development in ferroelectricity was reported by Cochran [58, 59], within a dynamical phenomenological description of the ferroelectric transition. He realized that the theory describing the instability should be cast within the framework of lattice dynamics, considering one of the lattice mode as the basic variable. The notion of soft-mode was introduced and provided the link whereby the static phenomenology of Landau-Ginzburg-Devonshire could be interconnected with atomistic descriptions through the elementary excitations, phonons, of the crystal lattice.

From a lattice dynamics point of view, the condition for stability implies that the crystal is stable with respect to three distinct types of deformations: long wavelength homogeneous deformations or displacements (zone-center acoustic modes, $\mathbf{k} = 0$ at the Γ point in the Brillouin zone), long wavelength inhomogeneous deformations associated with an opposite motion between positive and negative ions (zone-center transverse optical mode), and short wavelength deformations (zone-boundary optical modes of vibrations, at points such as X or R). Hence, the general condition of lattice stability is that all normal modes of vibration have real finite frequencies. The limit of stability against a particular mode of vibration is approached as the corresponding frequency approaches zero.

The soft-mode theory has been successful in understanding many displacive ferroelectrics, especially ABO_3 perovskites. On approaching T_c, the restoring forces to the original equilibrium positions in the high-symmetry phase are weakened, ultimately vanishing and resulting in a new set of equilibrium positions associated to a distorted crystalline structure, whose symmetry is dictated by the symmetry of the mode driving the instability. The decrease

and ultimate vanishing of the soft-mode frequency as the transition is approached, is caused by cancellation between competing forces, namely, short-range covalent repulsions that favor centrosymmetric structure, and long-range dipole-dipole interactions that stabilize long-range order. This cancellation can be induced by changes in composition, temperature, or other external fields. In particular, the application of pressure can significantly influence the balance between competing forces and thereby strongly influence, or induce, soft-mode behavior [93]. In perovskites, it is the softening of the transverse optical zone-center mode that drives the ferroelectric instability $\omega_{TO}(T \to T_c) \to 0$. The spontaneous displacements associated to the soft phonon can be regarded as the order parameter of the transition, since they are directly related to the the spontaneous polarization.

Experimentally, the square of the soft-mode frequency is found to vary linearly with temperature:

$$\omega_{TO}^2 = K(T - T_c) \tag{1.7}$$

where K is a positive constant and T_c is the second order transition temperature. According to the Lyddane-Sachs-Teller relation which connects the macroscopic dielectric constants to the microscopic optical phonon frequencies,

$$\frac{\varepsilon_s(T)}{\varepsilon_\infty} = \frac{\omega_{LO}^2}{\omega_{TO}^2(T)}. \tag{1.8}$$

Here ε_s and ε_∞ are the static and the high frequency dielectric constants, and ω_{LO} and ω_{TO} are the frequencies of the longitudinal and transverse optical phonon modes, respectively. It is generally found that the frequency of the higher optical mode ω_{LO} exhibit no considerable variation with temperature. The decrease in the soft-mode frequency as the temperature approaches T_c, will thus cause a dramatic increase of ε_s, ultimately resulting in the dielectric anomaly ascribed to the soft-mode condensation. Combining Eqs. (1.7) and (1.8) yields the observed Curie-Weiss temperature dependence of the static dielectric constant, namely

$$\varepsilon_s = C/(T - T_c) \tag{1.9}$$

1.1.4 First-principles theory

Although Landau and soft-mode theories have been very successful in the analysis and interpretation of FE properties and in identifying the mechanism for the FE transition in soft-mode systems, the atomic-level origin of ferroelectricity, particularly in the ABO_3 perovskites, remained unclear. The remaining questions pertained to the underlying cause of the ferroelectric instability, and to the vastly different FE behavior in seemingly similar compounds.

In 1990, Boyer *et al.* [44] anticipated that first-principles theory could lead to a deeper understanding of FE properties. The reason to use first-principles methods is that (i) one is not reliant on parametrized theories or (ii) on fitting possible inaccurate experiments, (iii) one has access to the underlying potential surfaces, (iv) can clearly see the origin of observed behavior, and (v) they can be applied to hypothetical or not yet synthesized materials, or (vi) for temperature, pressure or compositions for which data are not available [45]. First-principles methods refer to the exclusive use of parameters obtained from the fundamental interactions among electrons and nuclei rather then constrained by experimental data.

Among the advances made have been the understanding of the role of covalency and hybridization in driving ferroelectricity in perovskites. Carrying first-principles calculations based on the density functional theory (DFT) within the local density approximation, Cohen *et al.* [46, 137] elucidated the difference between $BaTiO_3$ [7] and $PbTiO_3$ [8]. Performing lattice dynamics and electronic structure calculations for the two materials, the calculated potential as a function of soft-mode distortion for the two crystals featured much deeper well for $PbTiO_3$ than for $BaTiO_3$, when accounting for the tetragonal strain. Thus the tetragonal strain stabilizes the tetragonal phase in $PbTiO_3$ but not in $BaTiO_3$, where the rhombohedral phase remains more stable.

Analysis of the charge densities and densities of states further showed that the ferroelectric instability is due to hybridization between the oxygen $2p$ states and the titanium $3d$ states. If this hybridization is inhibited, the FE instability is suppressed and the cubic phase is stable. Additionally, in $BaTiO_3$ the Ba is ionic and spherical, whereas the Pb in $PbTiO_3$ is highly nonspherical in the FE phase, and its polarization helps stabilize the tetragonal ground state.

More generally, the above calculations [45] have shown that (i) all Coulomb lattices are unstable with respect to off-center ferroelectric ionic displacements, and (ii) the short-range repulsive forces tend to stabilize the lattice against such displacements. In particular, in the perovskites the hybridization of oxygen $2p$ states and the d states of the transition-metal ion reduces the short range repulsions thus allowing off-center displacements.

These recent theoretical developments made possible the microscopic and first-principles modeling of ferroelectrics. DFT was successfully applied to various ABO_3 compounds. However, it has also its limitations. The most important one is the limited number of atoms that can be handled considering explicitly the electronic degrees of freedom (few hundreds atoms for basic ground-state calculations). This imposes serious restrictions to the applicability of pure DFT calculations for the study of complex ferroelectrics. Second, ferroelectrics exhibit structural phase transitions and their properties strongly evolve with temperature. Meaningful predictions and direct comparison with the experiment requires therefore to estimate the

[7] $BaTiO_3$ exhibits on cooling a sequence of three FE phase transitions, cubic to tetragonal to orthorhombic to rhombohedral.

[8] $PbTiO_3$ exhibits a single cubic-to-tetragonal FE transition.

properties at finite temperature, unaffordable within DFT, mainly because random thermal vibrations cannot be described properly with too small simulation box.

The advent of an effective Hamiltonian approach allowed to overcome these limitations and treat finite temperature effects [12, 149]. In this approach the soft mode is considered as the driving force for the phase transitions. The Hamiltonian is constructed from a Taylor expansion of the energy around the paraelectric phase in terms of the soft mode ionic degree of freedom and the strains (and can be generalized to mixed crystals by including compositional degrees of freedom to account for the alloy nature of the compounds). All parameters that appear in the expansion are determined from DFT total energy. The total energy based on this Hamiltonian is then used in Monte Carlo simulations enabling the study of the structural phase transitions of ferroelectrics [149, 150] and the temperature dependence of their dielectric, piezoelectric and optical properties.

Since the local polarization is directly related to the local mode, the effective Hamiltonian can be viewed has an expansion of the energy in terms of local polarization and strains (also including their coupling). In this regard, its form strongly resembles that of the Landau-Ginzburg-Devonshire theory with polarization and strain as primary and secondary order parameters. This provides a connection between the first-principles approach and phenomenological models [49]. However, it is worthwhile emphasizing that the effective Hamiltonian approach remains a microscopic theory in which the polarization can fluctuate locally. It is also a truly first-principles approach with parameters directly fitted on DFT simulations and not adjusted to reproduce the experiment.

Now the challenge is to address problems in more complex mixed perovskites, that are structurally and/or chemically heterogeneous with possibly frequency dependent properties, such as relaxors [47, 48].

1.2 Relaxors vs Ferroelectrics

Compositional disorder, *i.e.*, the disorder in the arrangement of different ions on the crystallographically equivalent sites, is the common feature of relaxors [2]. The relaxor behavior was first observed in the perovskites with disorder of non-isovalent ions, including the stoichiometric complex perovskite compounds, e.g. $Pb(Mg_{1/3}Nb_{2/3})O_3$ (PMN) [63] or $Pb(Sc_{1/2}Ta_{1/2})O_3$ (PST) [83] (in which Mg^{2+}, Sc^{3+},Ta^{5+} and Nb^{5+} ions are fully or partially disordered in the B-sublattice of the perovskite ABO_3 structure) and non-stoichiometric solid solutions, e.g. $Pb_{1-x}La_x(Zr_{1-y}Ti_y)_{1-x/4}O_3$ (PLZT) [74, 157] where the substitution of La^{3+} for Pb^{2+} ions necessarily leads to vacancies on the A-sites. Recently an increasing amount of reported data has shown that many homovalent solid solutions, e.g. $Ba(Ti_{1-x}Zr_x)O_3$ (BTZ) [75, 76] and $Ba(Ti_{1-x}Sn_x)O_3$ (BTS) [77] can also exhibit relaxor behavior. Other examples of relaxor

ferroelectrics are complex perovskites $Pb(Zn_{1/3}Nb_{2/3})O_3$ (PZN) $Pb(Mg_{1/3}Ta_{2/3})O_3$ (PMT), $Pb(Sc_{1/2}Nb_{1/2})O_3$ (PSN) and the solid solutions $(1-x)Pb(Mg_{1/3}Nb_{2/3})O_3 - xPbTiO_3$ (PMN-PT) and $(1-x)Pb(Zn_{1/3}Nb_{2/3})O_3 - xPbTiO_3$ (PZN-PT) [2].

The diversity in interpretations of the relaxor properties is due to the fact that so far, a general microscopic model capable of describing the generic behavior of all relaxors is still lacking. One difficulty in unifying the descriptions is related to the fact that in the case of some compounds like PST [83] and PLZT [4], in contrast to the canonical PMN for example, in addition to the relaxor behavior, a relaxor-to-ferroelectric transition occurs at low temperatures.

The general qualitative understanding, beyond points of disagreement among authors, could be summarized in the following [4]. Chemical substitution and accompanying lattice defects can introduce dipolar entities in mixed ABO_3 perovskites. At very high temperatures, thermal fluctuations are large and there are no well-defined dipole moments. Upon cooling, the presence of these dipolar entities manifests itself at a temperature T_d (the so-called Burns or dipolar temperature), higher than the temperature at which the dielectric response peaks T_m. At and below T_d each dipolar entity induces polarization (or dipoles) in its vicinity within a correlation length, forming polar regions whose extent is determined by the polarizability of the medium. With decreasing temperature, the size of these regions increases, ultimately either percolating the whole sample and yielding a cooperative FE phase transition at T_C, or exhibiting a dynamic slowing down of their fluctuations at $T < T_m$, leading to an isotropic relaxor state with random orientation of the polar regions.

Despite the wide variety of the relaxor group, it is possible to gather some common points. In the perspective of appreciating and understanding their properties, it is useful to contrast some of their characteristic features with those of normal ferroelectrics [4] :

- ◇ The P-E hysteresis loop (Fig.1.5(a)) is the signature of an FE in the low temperature FE phase. The large remanent polarization, P_R, is a manifestation of the cooperative nature of the FE phenomenon. A relaxor, on the other hand, exhibits a so-called slim-loop as shown on the right-hand side. For sufficiently high electric fields, the polar regions of the relaxor can be oriented with the field leading to large polarization; however, on removing the field most of these re-acquire their random orientations resulting in a small P_R.

- ◇ The saturation and remanent polarizations of a ferroelectric decrease with increasing temperature and vanish at the FE transition temperature (T_c). The vanishing of P at T_c is continuous for a second-order phase transition (Fig.1.5(b)) and discontinuous for a first-order transition. No polar domains exist above T_c. By contrast, the field-induced polarization of a relaxor decreases smoothly through the dynamic dielectric maximum

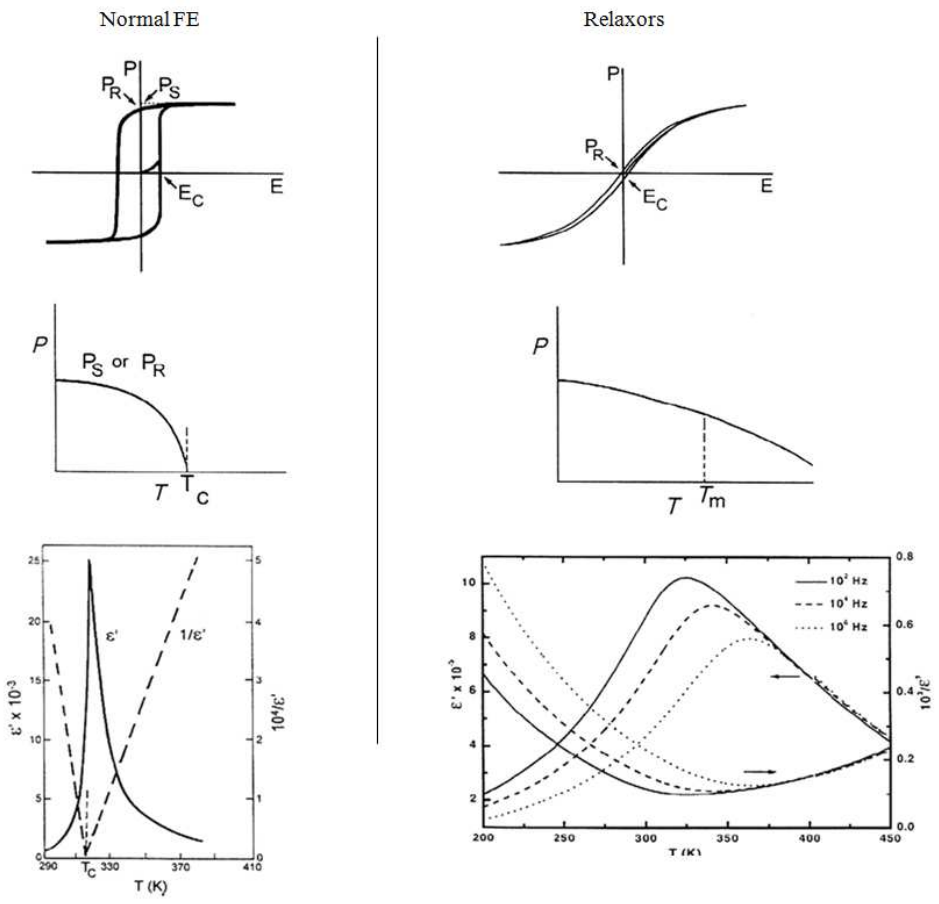

Fig. 1.5: Contrast between the properties of normal ferroelectrics and relaxors ferroelectrics (After Samara [4])

temperature, T_m, and retains finite values to rather high temperatures due to the fact that the polar regions persist to well above T_m.

◇ The static dielectric susceptibility, or dielectric constant ε', of an FE exhibits a sharp, narrow peak at T_c (Fig.1.5(c)). For a single crystal, the peak is very sharp and the width at half max is ∼10-20 K. For a mixed oxide FE, *e.g.*, a PZT, the peak is somewhat rounded due to compositional fluctuations, and the width at half max is typically ∼20-40 K. The FE response is frequency independent in the audio frequency range. By contrast, a relaxor exhibits a very broad $\varepsilon'(T)$ peak, and strong frequency dispersion in the peak temperature, T_m, and in the magnitude of ε' below T_m.

◇ The temperature dependence of ε' of an FE obeys a Curie-Weiss law, $\varepsilon' = C/(T - T_0)$, above T_c as shown by the linear $1/\varepsilon'$ versus T response in Fig.1.5(c). By contrast $\varepsilon'(T)$ of a relaxor exhibits strong deviation from this law for temperatures well above T_m. It is only at very high temperatures that a linear $1/\varepsilon'$ versus T response is recovered.

◇ The FE transition can be thermodynamically first or second order and involves a macroscopic symmetry change at T_c. By contrast, there is no structural phase transition across T_m in a relaxor.

1.3 Theoretical approaches to Relaxors

In many solid materials, where intrinsic quenched randomness exists in form of defects, impurities or as a general structural property, the disorder stemming from spatial heterogeneities is an integral part of their characteristics. In certain circumstances, even a weak disorder can have a crucial effect on their critical behavior, by altering the stability of the low-temperature ordered phase, and inducing non-trivial properties governed by rare regions. As it will be later pointed out, one of the essential requirements for the occurrence of the relaxor behavior in ferroelectric perovskites, is *lattice disorder*. In order to describe disordered systems and to explore their thermodynamic behavior, simple spin systems are frequently invoked. The model Hamiltonian

$$H = -\sum_{\langle ij \rangle} J_{ij} S_i S_j - \sum_i h_i S_i \tag{1.10}$$

accounts for random interactions (or random bonds RBs), J_{ij}, between nearest neighbor spins S_i and S_j, and for quenched random fields (RFs), h_i acting on the spins S_i. While the RBs are at the origin of spin glass behavior, RFs may give rise to disordered domain states provided that the order parameter has continuous symmetry [5]. In the two next subsections, we examine the different models that have been resorted to in order to explain the relaxor behavior and that conceptually belong to either one (RBs models) or the other (RFs models) of the categories. In the third subsection, we review the spherical random bond random field model (SRBRF model), which combined both sources of disorder. The second ingredient for the relaxor behavior seems to be the existence of *polar areas*, at temperature higher than T_m, that are either referred to as polar nanoregions (PNR), when regarded as the result of local phase transitions embedded in a cubic matrix within the RBs models, or as polar nanodomains separated by domain walls in random-field models [2].

As it will be later seen, although the existence of polar regions seems doubtless to many, the mechanisms of their formation, and thus their nature itself, are not conclusively understood. The picture that has emerged from numerous investigations, using local structural probes, clearly indicates the necessity of distinguishing the short-range effects from the long-range ones. At short range and at low temperatures the local symmetry is polar and the atomic shifts [7–9] from their ideal cubic symmetry positions are correlated. At long range however, the global symmetry is cubic due to the statistical atomic disorder that results in a spatially variable polarization, yielding zero net global polarization. Thus, the crystal does not behave as a polar homogeneous crystal, because the coherence length of the polar zones is spatially limited, nor does it behave as a perfectly cubic crystal, because of the strong deviations from the cubic symmetry; in this sense, it is neither polar nor cubic.

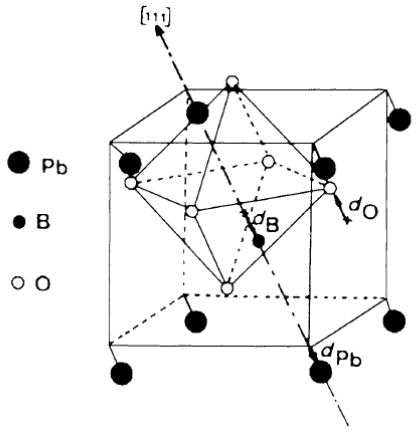

Fig. 1.6: Rhombohedral distortion and ionic displacements along the ⟨111⟩ direction in PMN at 5 K. (After Mathan *et al.* [7])

This picture meets the experimental observations. For example, de Mathan *et al.* studied the low temperature phase of PMN at 5 K [7]. The widenings observed at the basis of some X-ray and neutron diffraction lines were interpreted as scattering induced by atomic shift correlations, leading to a locally polar structure, characterized by antiparallel shifts of the cations against oxygen atoms inducing a dipolar moment (Fig.1.6). The local symmetry was assumed to be rhombohedral, with atomic shifts along the ⟨111⟩ rhombohedral axis. The correlation length of the polar regions was found to increase as the temperature is lowered, reaching a value of 10 nm at 5 K. Additionally, a rough estimate suggested that the polar nanoregions occupy only 20% of the volume of the crystal (polar phase amount), clearly indicating the coexistence of two phases at 5 K.

As stated above, the presence of two local phases has led to two main theoretical approaches *i)* one approach has been to consider polar nano-regions as resulting from local phase transitions, so that the system is regarded as consisting of nanosized polar regions embedded into a cubic matrix. The relaxor behavior is attributed to a dipolar glass state with randomly interacting polar regions in presence of random fields. *ii)* in the second approach the charge disorder is considered to be at the origin of the occurrence of polar nanoregions and the relaxor behavior is attributed to a ferroelectric state broken up into polar nanodomains under the constraint of those quenched random fields. In the two cases the crystal is not of a single-nature [9].

As it will be further developed, it has been considered that randomly polarized nanoregions, that are the precursors of the polar clusters, start to form at the so-called Burns temperature T_d, *i.e.*, the temperature at which mean-field fit deviates from experimental points. A matter of dispute is still the physical significance of this temperature. Recently, Bobnar *et al.* reported high-temperature dielectric investigations of PMN, revealing that the dielectric

[9] These two situations can hardly be distinguished experimentally by structural examinations because the thickness of domain walls (*i.e.* the interdomain regions where polarization is not well defined) is comparable with the size of nanodomains and thus can not be neglected [7].

dispersion that appears around 600K might be due to the Maxwell-Wagner-type contributions of interface layers between sample and contacts [60]. Even more recently, Hlinka [61] questioned the necessity of the convenient but speculative concept of polar nanoregions. Specifically, he demonstrated the possibility of analyzing the experimental signatures of the so-called PNRs in a alternative way, namely by referring to a matrix-free scenario involving ferroelectric nanodomains.

Moreover, many of the existing models interpret the dielectric relaxation as stemming from the thermally activated reorientation of dipole moments of polar nanoregions, which are considered as interacting (directly or via the surrounding matrix) entities constituting a glassy system. However, another type of contribution from the polar regions to the dielectric permittivity has been formulated in terms of vibration of their boundaries within the *breathing model* proposed by Glazounov and Tagantsev [79] . The idea of the model lies in the use of the theory of randomly pinned interface, earlier developed for magnetic materials, and can be formulated as follows. The relaxor is considered as an ensemble of polar regions, elongated along the direction of the local spontaneous polarization $\mathbf{P}_S$, the boundaries of which are initially pinned by the spatial fluctuations of internal random electric fields induced by the charge disorder. In this picture, the interface of a polar region is effectively free on a characteristic length scale L_c, smaller than the size of the polar region and determined by both the distribution of the pinning centers (*i.e.* the internal random local fields) and the elastic properties of the interface. The application of an external field $\mathbf{E}$ will exert pressure $\mathbf{E}.\mathbf{P}_S$ on the interphase boundary, leading to its bending and a modification $\Delta\mathbf{p_E}$ of the dipole moment associated to the polar region : $\Delta\mathbf{p_E} \propto \mathbf{P}_S L_c^2(\mathbf{E}.\mathbf{P}_S)$. The contribution from the polar region to the dielectric permittivity is proportional to $\Delta\mathbf{p_E}.\mathbf{E}/\varepsilon_0 E^2$. Therefore, the polarization response of the system is believed to occur as a consequence of the motion of the boundaries of the polar regions under applied ac field, without any change in the orientation of $\mathbf{P}_S$.

Before addressing the dipole-glass class of models in detail, lets us briefly consider the following atomistic model, developed by Egami and aiming at getting atomistic insight to the relaxor behavior. Based on pulsed neutron atomic pair-density function (PDF) analysis of PMN, Egami observed that the prerequired atomic disorder for the onset of relaxor behavior mainly affects the Pb polarization, making its direction random, resulting in a non-collinear structure. In this picture, in PMN, the Pb ions cannot form covalent bonds with O ions which are bonded to Nb. On the other hand, Mg ions create purely ionic bonds and do not prevent the Pb-O bonding. As a result, the direction towards Mg is an easy direction for Pb displacement. Egami addressed the atomistic mechanisms within the so-called random anisotropy model [11], described by the following Hamiltonian $H = H_{dip} + H_{aniso}$

$$H_{dip} = -\sum_{ij} J_{ij}\mathbf{P}_i\mathbf{P}_j \qquad , \qquad H_{aniso} = \sum_i \sum_{lm} D_l^m O_l^m(\mathbf{P}_i) \tag{1.11}$$

where $\mathbf{P}_i$ is the local polarization caused by the displacement of the i-th Pb ion, J_{ij} describes the interaction between local polarization mediated by oxygen and B-site ions, D_l^m describes the anisotropy energy to rotate the Pb polarization, and O_l^m are the operators equivalent of the spherical harmonics. Since Mg is randomly distributed around Pb, the preferred direction of displacement of Pb varies from site to site. It is the anisotropy term that accounts for the directional dependence of the energy of Pb displacements in the compositionally disordered crystal. Consequently, the random anisotropy model analyzes the relaxor behavior within the idea of competing ordering (H_{dip}, favoring collinear structure) and disordering (H_{aniso}, favoring random non collinear structure) interactions, and leads to the concept of critical level of disorder associated to a threshold value of the D/J ratio between regular and relaxor ferroelectric behaviors. Although this model was established to account for the relaxor properties, the appearance of polar regions was not derived.

1.3.1 Compositional fluctuations and glassy like approaches to relaxors

The early model by Smolensky *et al.* [62, 64, 65] attributed the *diffuse phase transition* in mixed perovskites to compositional heterogeneity in the materials and thereby to the existence of wide distributions in transition, or Curie, temperatures. It it in this context that first appeared the notion of polar regions. Cross then extended this first approach and proposed a *superparaelectric* model for relaxors in analogy with the superparamagnetic state [1]. Central to this proposal is the hypothesis that the polar nanodomains that exist above T_m, are in dynamic disorder undergoing random reorientation of their polarization along one of the eight $\langle 111 \rangle$ equivalent directions in the cubic paraelectric phase of ABO_3 perovskites. In support of this model, Viehland *et al.* [127] have given evidence for the dipolar glass-like character of PMN. Specifically, they showed that the polarization fluctuations have a freezing temperature analogous to that of spin glasses and that the correlations among polar regions control the kinetics of the fluctuations as well as the freezing process. Subsequently, these correlations were held responsible for the large deviation of the dielectric response from Curie-Weiss behavior above T_m.

Because there are similarities between spin glasses and dielectric dipolar glasses, and because of the wealth of available knowledge on the former, it is useful to start this section by summarizing briefly some of the characteristics of spin glasses.

1.3.1.1 Spin glasses : an overview

Spin glasses are disordered magnetic alloys, widely regarded as paradigmatic complex systems. As an emergent state from the random magnetic system, the spin glass state differs from other statistical systems in several ways. In particular the competitive interactions give

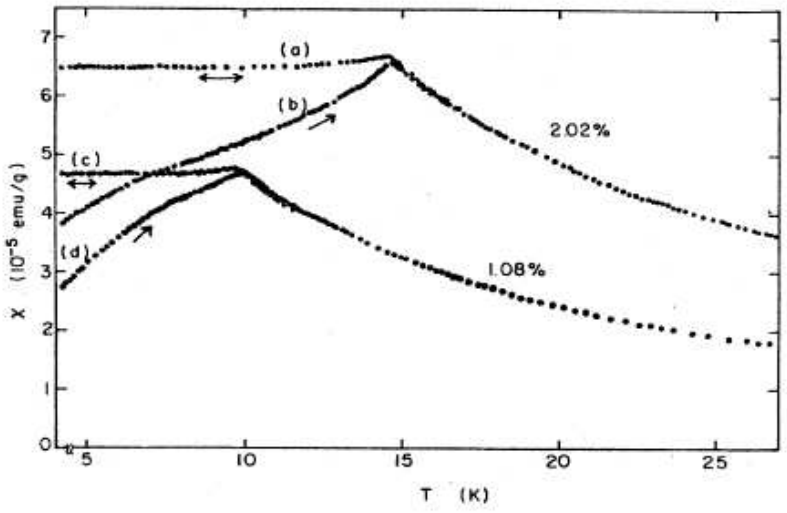

Fig. 1.7: Zero-field cooled ((b),(d)) and field-cooled ((a),(c)) static susceptibilities of spin glass CuMn for 1.08% Mn and 2.02% Mn, demonstrating preparation-dependence and implying metastability. After zero-field cooling ($H < 0.05$ Oe), initial susceptibilities (b) and (d) were taken for increasing temperature in a field of $H = 5.9$ Oe. The susceptibilities (a) and (c) were obtained in the field $H = 5.9$ Oe, which was applied above T_f before cooling the samples.(After Nagata *et al.* [126])

rise to non-trivial degeneracies of the ground states. The simplest definition of spin glass is that of a spin system whose low temperature state appears as a disordered one. In order to produce such a state, two requirements are necessary: the Hamiltonian must contain *randomness*, and there must be *frustration*. Randomness means that the Hamiltonian depends on some random parameters, such as the couplings among the elementary degrees of freedom, whose probability distribution is supposed to be known. These random couplings are collectively denoted as spatially *quenched* disorder, physically meaning that the dynamics of the impurities in the disordered system is by many orders of magnitude slower than the dynamics of the spin degrees of freedom. Therefore, the disorder does not thermalize, it can be considered as fixed. Frustration refers to the presence of competing interactions which can not be simultaneously satisfied, such that the Hamiltonian can not be reduced to a sum of many terms, all of which can be minimized by a single ground state configuration, but rather gives rise to low-lying metastable configurations, as shown by zero-field and field cooled susceptibilities measures (Fig.1.7). Upon cooling in the absence of an applied field, the magnetic moments do not achieve neither ferromagnetic nor antiferromagnetic long-range order, rather, they exhibit a freezing temperature, T_f, below which the moments are randomly frozen over macroscopic times. T_f is manifested by a relatively sharp but rounded peak in the frequency-dependent susceptibility $\chi(\omega, T)$, as shown for example in Fig.1.8. This is a universal feature of a spin glass, among history-dependence, observation-time dependence, *etc.* In this short overview, we present some of their characteristic features [4, 85]:

- ◇ A broad spectrum of relaxation times just above T_f, with the spatial extent of the

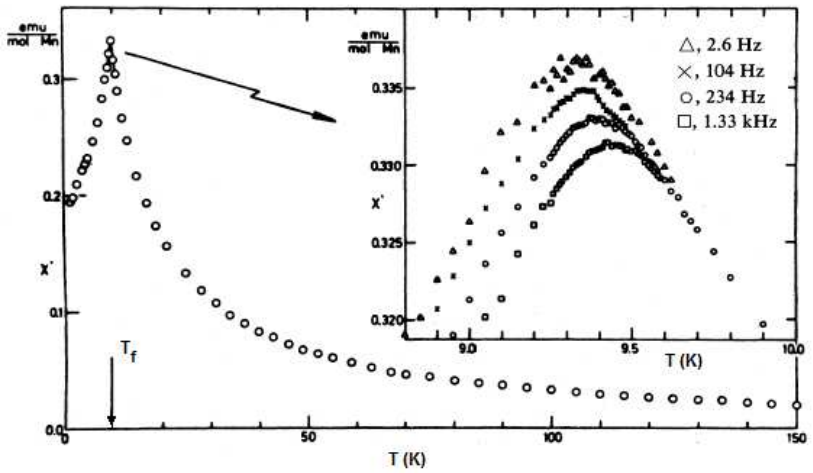

Fig. 1.8: Temperature dependence of the real part of the magnetic susceptibility of spin glass CuMn (0.94% Mn). Inset is an expanded view revealing the rounding ad the frequency dispersion at and below the peak. (After Mulder *et al.* [125])

spin correlations (*i.e.*, the correlation length, r_c) increasing as $T \to T_f$ from above, indicating that collective behavior of the spins is coming into play. Thus on a local scale strong magnetic correlations develop far above the freezing temperature. It is these collective effects that presumably give rise to the long relaxation times. For a system of Ising spins, the spin-spin correlation function for spins i and j averaged over time, τ, is $\langle S_i S_j \rangle$. Its sign for a spin glass is random, and thus there is no net magnetization. However, the quantity $\langle S_i S_j \rangle^2$ is not random but decays exponentially to zero as the separation between spins $|r_i - r_j|$ becomes comparable to r_c, *i.e.*,

$$\langle S_i S_j \rangle^2 \propto \exp\left[-|r_i - r_j|/r_c\right] \tag{1.12}$$

◇ At sufficiently high temperature, $\chi(T)$ follows a Curie-Weiss law. However, deviations from this law set in and grow at temperatures much higher than T_f as $T \to T_f$ from above. These deviations are attributed to spin-spin correlations.

◇ Cooling in the presence of an applied magnetic field (field cooling) the spins tend to align with the field, leading to magnetic hysteresis and remanence below T_f. At sufficiently high fields, the spin-glass state is destroyed.

◇ A prototype model for the description of cooperative phenomena in disordered magnets was formulated by Edwards and Anderson [81], who considered that the *site randomness* of the spin-carrying atoms is less relevant to the properties of spin glasses compared to the randomness in interactions or *bond randomness*. The Hamiltonian of the random bond Ising model (RBIM) in the absence of an external field is then expressed as

$$H_{\mathrm{EA}} = -\sum_{(i,j)} J_{ij} S_i S_j \tag{1.13}$$

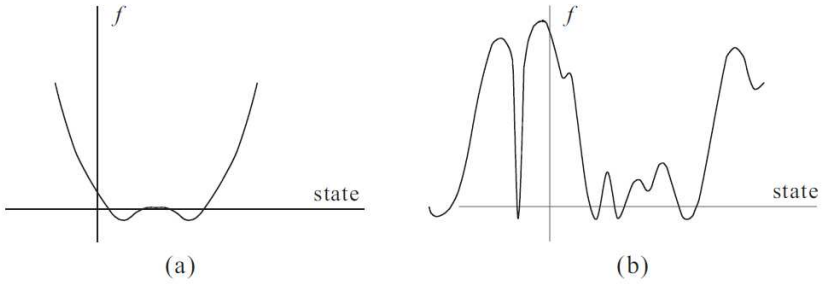

Fig. 1.9: (a) Simple free energy: In a ferromagnet the free energy as a function of the state of the system has a simple structure (b) Multivalley structure: The free energy of the spin glass state is considered to have many minima and the barriers between them are expected to grow indefinitely as the system size increases. Within a limited time scale, the physical properties of the system are determined by one of the valleys. After a an extremely long time, the observed behavior would reflect the properties of all the valleys (After Nishimori [88]).

The spin variables are assumed to be of the Ising type $S_i = \pm 1$, placed on a regular $\mathbb{Z}^d$ lattice, where d is the spatial dimension. Each interaction J_{ij} between a neighboring spin pair (ij) is considered to be distributed independently according to a probability distribution $P(J_{ij})$. As typical examples of the distribution of exchange bonds, one often uses

- ▷ *Gaussian model*: $P(J_{ij}) = (2\pi J^2)^{-1/2} \exp\left[-J_{ij}^2/2J^2\right]$, with zero mean and J^2 variance.
- ▷ $\pm J$ *model* or *frustration model* : $P(J_{ij}) = p\,\delta(J_{ij} - J) + (1-p)\,\delta(J_{ij} + J)$, where J_{ij} is either $J(> 0)$ (with probability p) or $-J$ (with probability $1-p$).

◇ There exist in spin glasses a large number of thermodynamic states with the same macroscopic properties, but with different microscopic configurations, separated by large energy barriers in phase space. The free energy landscape is then expected to exhibit many minima (Fig.1.9).

◇ A long-standing question for spin glasses is whether or not the $\chi(T)$ peak at T_f represents a true equilibrium phase transition. For a phase transition, both τ and r_c should diverge at T_f, otherwise both quantities become large and finite. To assess the spin ordering in a single valley, it is necessary to take the thermodynamic limit to separate the valley from the others by increasing the barriers indefinitely so as to ignore transitions between valleys and observe the long-time behavior of the system in one valley. Under these conditions, the Edwards-Anderson order parameter for one valley $q_{\rm EA}$ is defined as follows:

$$q_{\rm EA} = \lim_{t\to\infty} \lim_{N\to\infty} \left[\langle S_i(t_0) S_i(t_0+t)\rangle\right] \tag{1.14}$$

where $\langle . \rangle$ denotes statistical mechanics average over thermal fluctuations and $[.]$ denotes the configurational average over the random interactions. $q_{\rm EA}$[10] measures the similarity (overlap) of a spin state at site i at $t_0 + t$ to its initial state at t_0[11].

◇ The multivalley structure in phase space leads to a breakdown of ergodicity. Whereas symmetry considerations relate every thermodynamic state to another one of the same free energy with spins inverted (note that this symmetry can be broken in any nonzero field conjugated to the order parameter), mean-field theory [12] predicts additional states, unrelated by symmetry, with virtually the same free energy. This phenomenon corresponds to "ergodicity breaking." and is associated to accidental degeneracy, which in turn occurs because of randomness and frustration in the system.

◇ There is evidence that ferromagnetic clusters are the building blocks out of which the spin-glass state is formed. This points to some degree of correlations and distinguishes the spin-glass state from the superparamagnetic state where the magnetic particles are dilute (or free) and non-interacting.

◇ Measurements of the frequency and temperature dependencies of the real and imaginary parts of the susceptibility reveal a broad spectrum of relaxation times even well above T_f. The temperature dependence of the maximum relaxation time, τ_{max}, is generally found to be non-Arrhenius, *i.e.*. not compatible with simple thermally activated hopping over barriers: rather $\tau_{max}(T)$ can be well fit by the Vogel-Fulcher equation $\tau_{max} = \tau_0 \exp\left[E/k_B(T - T_0)\right]$ where T_0 is a characteristic temperature.

As we have seen above, spin glass behavior results if disorder is introduced into magnets with competing interactions. Thus it is immediately plausible to expect that similar behavior may occur for other ordering phenomena, if there is competition between various interactions in presence of disorder. Candidates for such behavior are systems associated with structural transitions as they occur in ferroelectrics or antiferroelectrics. In this case, the local ordering is due to electric dipoles, and hence one is talking about "dipolar glasses" [121, 124]. From a theoretical point of view, the spin representing a magnetic moment turns into a "pseudospin" representing the electric moment; dielectric rather than magnetic susceptibilities need to be considered, while otherwise the situation is similar to that for magnetic spin glasses.

[10] One can rewrite this quantity using the square of the local magnetization $m_i^a = \langle S_i \rangle_a$, where a labels the restriction of the system to a specific valley a, and the probability $P_a = e^{-\beta F_a}/Z$ that the system is located in a valley a. $q_{\rm EA} = \left[\sum_a P_a (m_i^a)^2\right] = \left[\sum_a P_a \frac{1}{N} \sum_i (m_i^a)^2\right]$. In this second equality, it is assumed that the averaged square magnetization does not depend on the location

[11] In addition to $q_{\rm EA}$ that probes the single valley ordering, it is possible to define $\overline{q}_{\rm EA}$ that represents the average over all valleys corresponding in the long-time observation. It can be expressed explicitly as $\overline{q}_{\rm EA} = \left[(\sum_a P_a m_i^a)^2\right] = \frac{1}{N}\left[\sum_{ab} P_a P_b \sum_i m_i^a m_i^b\right]$ which can be rewritten using $m_i = \sum_a P_a m_i^a$ as $\overline{q}_{\rm EA} = \left[\langle S_i \rangle^2\right]$, that accounts for the average overlaps between valleys for time scales longer than transition times between valleys [88].

[12] The mean field theory of spin glasses was developed in Sherrington-Kirpatrick model [89], the infinite-range version of the Edwards-Anderson model.

1.3.1.2 Compositional fluctuation model

In this early phenomenological model developed by Smolenskii, Kirillov and Isupov [62, 64, 65], the *diffuse* nature of the *phase transition* in perovskites was attributed to the disordered distribution of hetero-valent cations over equivalent cristallographic sites. Due to the dependence of the Curie temperature on the concentration of the components, the resulting spatial micro-inhomogeneities consequently lead to a statistical distribution of local ferroelectric transition temperatures $T_{C,loc}$, causing the broad temperature dependence of dielectric properties and the diffuseness of the transition. In this model, the relaxor ferroelectric is considered as an ensemble of randomly oriented non-interacting polar regions in paraelectric environment, whose number increase upon cooling. Thus PNRs correspond to regions with enhanced local T_C. It was suggested that the total number of polar regions contributing to the dielectric response in the vicinity of the permittivity peak is given by a Gaussian distribution characterized by a mean value corresponding to the temperature of permittivity maximum T_m, and by a standard deviation δ, also regarded as the diffuseness coefficient. Assuming that the phase transition of the polar regions is of the first order, the following expression for ε' was obtained:

$$\varepsilon'(T) = \varepsilon'_m \exp -\frac{(T - T_m)^2}{2\delta^2} \tag{1.15}$$

Taking the limit of high diffuseness $\delta \gg T - T_m$ and expanding Eq.(1.15) into a truncated power series, the following expression, known as the square Curie-Weiss law, was then derived:

$$\frac{\varepsilon'_m}{\varepsilon'} = 1 + \frac{(T - T_m)^2}{2\delta_m^2} \tag{1.16}$$

Deviation to the quadratic dependence (Eq.(1.16)) incited many authors [67–70] to search for a new formula describing the diffuse phase transition. In order to characterize the dielectric diffuseness an empirical power law was proposed:

$$\frac{\varepsilon'_m}{\varepsilon'} = 1 + \frac{(T - T_m)^\gamma}{2\delta_\gamma^2}, \quad (1 \leqslant \gamma \leqslant 2) \tag{1.17}$$

The limiting values $\gamma = 1$ and $\gamma = 2$ reduce the expression, in the first case to the Curie-Weiss law valid in the case of a normal ferroelectric (and in the case of relaxors [71, 72] for temperatures above the characteristic Burns T_d), and in the second case to the quadratic dependence corresponding to Eq.(1.16). The exponent γ, determining the degree of the diffuseness of the phase transition, is usually obtained from the slope of the $\log - \log$ plot of $(1/\varepsilon' - 1/\varepsilon'_m)$ versus $(T - T_m)$.

By introducing the notion of polar regions, this model has initiated the conceptual foundation for subsequent models. However, this static model fails in describing the dispersive nature of

the transition. Moreover, the effect of pressure in tuning the relaxor behavior in ferroelectrics compounds of fixed compositions can not be recovered.

Following the idea of Smolenskii *et al.*, Nambu *et al.* proposed a mean field theory of the diffuse phase transition [66]. In this phenomenological model, the existence of clusters is postulated *a priori* and the diffuseness is ascribed to the gradual condensation of local polarizations in these clusters. Specifically, the free energy is expanded in terms of a uniform polarization P, and a local polarization P_i, yielding

$$\begin{aligned} F &= \frac{1}{2}N\alpha_1 P^2 + \frac{1}{4}N\alpha_{11}P^4 + \frac{1}{6}N\alpha_{111}P^6 \\ &+ \frac{1}{2}\gamma P^2 \sum_{i=1}^{N} P_i^2 + \frac{1}{2}\sum_{\langle ij\rangle} a_{ij}P_iP_j + \frac{1}{4}a_{11}\sum_{i=1}^{N} P_i^4 \end{aligned} \tag{1.18}$$

where $\alpha_i = (T - T_0)/\epsilon_0 C$, N is the total number of lattice sites, α_{11} and α_{111} are constants ($\alpha_{11} < 0$). From symmetry considerations, the coupling term between the two polarizations is of the form $\gamma P^2 P_i^2$. The interaction a_{ij} between local polarization is assumed to be of the form $a_{ij} = (T - J_{ij})/\epsilon_0 c'$ where J_{ij} is a random variable with zero mean value. All the parameters were determined so as to fit to the measured dielectric susceptibility. Using this free energy, numerical calculations were carried out for PMN and ordered PST ($Pb(Sc_{1/2}Ta_{1/2})O_3$), yielding $\varepsilon'(T)$ behaviors in close agreement with experimental observations.

1.3.1.3 Superparaelectric model

An extension of the *compositional fluctuation model* was made by Cross [1] who, in the spirit of superparamagnetism [78], proposed the *superparaelectric model*. This model ackowledge the existence of polarized regions within the relaxor ferroelectrics similarly to the single-domain spin clusters in the super-paramagnetics, and consequently regard them as non-interacting dynamical entities, flipping between alternative orientational states under thermal activation. The multiwell stucture of the potential is ascribed to the compositional fluctuation that locally breaks the global symmetry and creates favorable directions. In this case of dynamic polar regions each of which contributes independently to the dielectric response in a Debye-like fashion, the relaxation time τ follows the Arrhenius law:

$$\tau = \tau_0 \exp(E_b/k_B T) \tag{1.19}$$

where E_b is the volume dependent energy barrier between orientational states. Given the nanometric scale of the polarized regions and under sufficient thermal fluctuation, the polarization can overcome the energy barrier, leading to the frequency dependence of the dielectric response. The *superparaelectric model* emphasizes the dynamic behavior of the polarized

regions, which enables reasonable explanation to aging, electrostriction and the nonlinear behavior of the thermoelastic and optical properties. However, as reported by Isupov [80], whereas superparamagnetic particules are embedded in a non magnetic host, thereby justifying the concept of *paraelectric gas*, in relaxor ferroelectrics, polar regions are surrounded by polarizable para-electric (rather than dielectric) regions. Moreover, although the frequency dependence reflects a slowdown in the dynamics at low temperatures, Debye relaxation is insufficient in reproducing the frequency dependence of T_m. It is this shortcoming, together with the inability of the assumption of independent cluster in predicting the appearance of long-range order with the change of the composition or due to an applied external field, that have motivated the consideration of interactions among polar regions.

1.3.1.4 Dipole glass models

At high temperature, relaxors exhibit a non-polar paraelectric phase, which is in many aspects similar to the paraelectric phase of normal ferroelectrics. Upon cooling they transform into the ergodic relaxor state in which polar regions of nanometer scale with randomly distributed directions of dipole moments appear. This transformation which occurs at the Burns temperature, T_d, can not be considered a structural phase transition because it is not accompanied by any change of crystal structure on the macroscopic or mesoscopic scale. Nevertheless, the polar nanoregions affect the behavior of the crystal drastically, giving rise to unique physical properties. For this reason the state of crystal at $T < T_d$ is often considered as a new phase different from the paraelectric one. At temperatures close to T_d the polar nanoregions are mobile and their behavior is ergodic [2]. Upon cooling, their dynamics slows down and at a low enough temperature, T_f[13](typically hundreds degrees below T_d), the polar nanoregions in the canonical relaxors become frozen into a nonergodic state, while the average symmetry of the crystal still remains cubic. Similar kind of nonergodicity is characteristic of a dipole glass (or spin glass) phase [2]. It is precisely the identification of the two characteristic temperatures, *i)* the Burns temperature[14] , T_d (greater than T_m), below which the condensation of local polarization occurs, marking an onset of deviation from a simple extrapolation of higher temperature properties, and *ii)* the freezing temperature, T_f, below which thermal energy is insufficient for reorientational activation, heralding the onset of non-ergodic behavior, that led to a *glassy* interpretation of the relaxor behavior.

Evidence for the existence of polarized regions above T_m Since the average value of the dipole polarization $\mathbf{P}_d$ reduces to zero under thermal fluctuation, it is $\mathbf{P}_d^2$−dependent

[13]Let's note that T_m of relaxors corresponds to T_f of spin glasses, while T_f of relaxors corresponds to T_0 of spin glasses.

[14]The Burns temperature is not a usual phase transition temperature, rather, it can be associated [5] to the onset of a Griffiths phase [153], *i.e.*, a phase in disordered systems where nonanalytic behavior above the critical point is ascribed to rare spatial regions that are in a different thermodynamic phase (ferro) from the bulk system (para).

properties, such as the quadratic electro-optic effect and electrostiction, that were best expected to reveal the existence of polarized regions. Measurement of the temperature dependence of the refractive index $n(T)$ by Burns and Dacol [82], led to the observations that relaxors, unlike normal ferroelectrics, exhibit a deviation to linear behavior occurring at a temperature higher than T_C, the so-called Burns temperature T_d associated to the onset of randomly polarized regions. Moreover, the absence of anomaly in $n(T)$ near T_m reflects the absence of a phase transition at T_m (Fig.1.10). Assuming that the polarized regions develop randomly along one of the eight $\langle 111 \rangle$ directions in the cubic paraelectric phase of ABO_3 perovskites, the long wavelength of the light averages n over the crystal, so that the deviation can be quantitatively described by :

$$\Delta n = \frac{\Delta n_{\parallel} + \Delta n_{\perp}}{3} = -\frac{n_0^3}{2}\left[\frac{g_{33} + 2g_{13}}{3}\right]\mathbf{P}_d^2 \tag{1.20}$$

where $\Delta n_{\parallel}$ and $\Delta n_{\perp}$ are the changes in the parallel and perpendicular components of n, n_0 is the index in the absence of polarization, and the g_{ij} are the quadratic electrooptic coefficients.

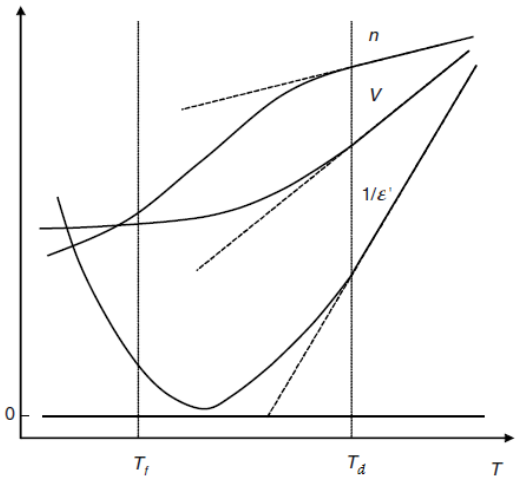

Fig. 1.10: Schematic temperature dependencies of the refractive index n, the unit cell volume V, and the reciprocal dielectric permittivity $1/\varepsilon'$ in the canonical relaxor (After Bokov *et al.* [2])

Another evidence for the onset of polarized regions above T_m is reflected in the measured thermal expansion [1]. In contrast to the normal linear dependence of the length of a sample with respect to temperature as given by $l_T = l_0\,[1 + \alpha(T - T_0^*)]$, where l_T is the length at temperature T, l_0 is the reference length at the reference temperature $T_0^\star$, and α is the linear coefficient of thermal expansion, or equivalently by $x = \Delta l/l_0 = \alpha(T - T_0^*)$ where x is the thermal strain, an anomalous deviation to linearity, occurring at T_d is reported in relaxors. This deviation can be explained in terms of electrostriction, and it can be shown [1, 4] using the Landau expansion of the free energy in terms of stress and polarization, that for a cubic

perovskite the axial thermal strain x_{11} is given by:

$$x_{11} = \alpha(T - T_0^*) + (Q_{11} + 2Q_{12})\mathbf{P}_d^2 \tag{1.21}$$

where Q_{11} and Q_{12} are electrostrictive coefficients. Consequently, a deviation from linearity is also measured in the lattice parameter (Fig.1.10) [84].

Evidence for the existence of polarized regions in relaxors well above T_m has also been deduced from the temperature dependence of the susceptibility (Fig.1.10). As noted earlier, deviations to the Curie-Weiss behavior were modeled using the compositional heterogeneity model predicting a power-law (Eq.(1.17)) relationship, where γ was approximately equal to 2 [64, 87]. Although this expression gives a reasonable fit of the data for some relaxors, it has been generally observed [73] that no single value of γ is found that uniquely describes the $1/\varepsilon'$ dependence of relaxors. Rather, different γ's can be found for given relaxors, depending on the width of the temperature range analyzed above T_m and on the measurement frequency. In spin glasses, the Curie-Weiss law is obeyed at temperatures much greater than T_f ($T > 5T_f$), but at lower temperatures strong deviations occur [85, 86]. Sherrington and Kirpatrick [89] developed an infinite range model for a spin glass which related the temperature dependence of the magnetic susceptibility χ below T_f to the onset of a local (spin glass) order parameter q in the following way:

$$\chi = \frac{C\,[1 - q(T)]}{T - \theta\,[1 - q(T)]} \tag{1.22}$$

Whereas the ideal (non-interacting) superparamagnetic is known to exhibit Curie-Weiss behavior, in spin glasses, the deviation to it is ascribed to the development of strong magnetic correlations on the local scale when approaching T_f and the onset of local spin glass order below T_f. Similarly, Viehland *et al.* [72] proposed that the deviation to Curie-Weiss in PMN and other relaxors, arises due to short-range correlations among polar regions, and that these correlations at high temperature are the precursor to a freezing of the polarization fluctuations into a glassy state at lower temperatures. Invoking Eq.(1.22), and considering that the local order parameter due to to correlation between neighboring polar regions of polarization P_i and P_j is $q = \langle P_i P_j \rangle^{1/2}$, Viehland *et al.* phenomenologically modeled the susceptibility data of PMN using the values of C and θ determined from high temperatures, and calculated the temperature dependence of q (Fig.1.11). In this picture, at T_d, local ferroelectric transitions start to occur, leading to the condensation of the polar nano-regions. In the temperature interval between 400 and 600 K, the disordering effect of temperature is large enough to prevent most polar regions from coupling, *i.e.* $\langle P_i P_j \rangle^{1/2} = 0$. As the temperature decreases, correlations develop as the volume fraction of polar regions increases and the thermal disordering effect decreases, ultimately leading to a freezing of the polarization fluctuation.

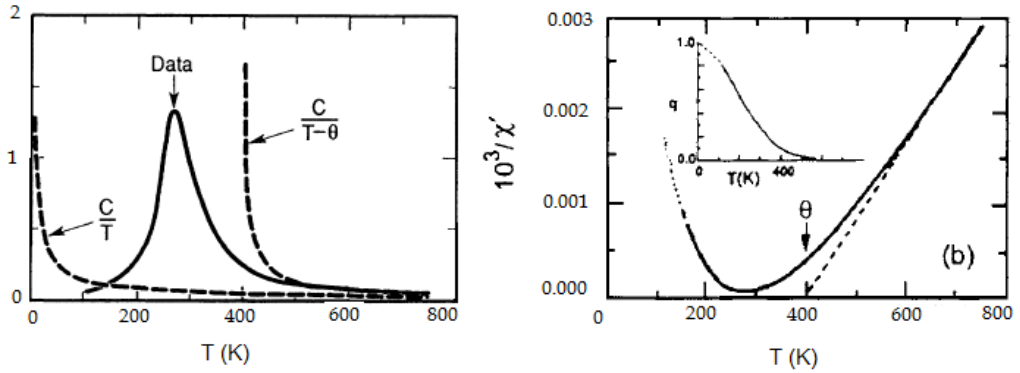

Fig. 1.11: (a) Schematic representation of the deviation of ε' from the hypothetical Curie and Curie-Weiss behaviors calculated from the values of C and θ obtained by extrapolation from temperatures above that of the onset of local polarization. (b) The inverse susceptibility as function of temperature. The dashed line is the Curie-Weiss behavior determined from high temperature and the inset shows the temperature dependence of the local order parameter q obtained using Eq.(1.22). (After Viehland *et al.* [72])

Dynamics of the dipolar slowing down and freezing process In many aspects, relaxors exhibit non-ergodic behavior similar to that of the spin (or dipole) glasses. On cooling, a slowing down of the relaxation of their orientational degrees of freedom, ultimately results in a frozen-in polar state that lacks long-range orientational order. As noted earlier, the

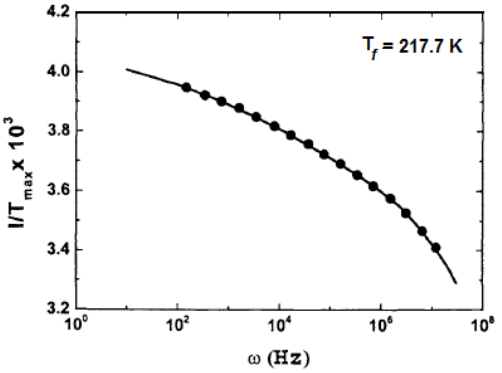

Fig. 1.12: The non-Arrhenius character of the relaxational response of PMN. The solid line is a V-F equation fit to the data. (After Viehland *et al.* [73])

non-Arrhenius character (Eq.(1.19)) of the relaxors response [73, 92, 93] underlines a fundamental difference between relaxors and superparaelectrics (Fig.1.12). Whereas in the latter, the thermal localization process stems from an independent behavior, in relaxors the glassy dipole freezing emerges from a cooperative one. This departure from Arrhenius behavior can be described in the form of the empirical Vogel-Fulcher (V-F) equation [107, 108]:

$$\tau^{-1} = \omega_0 \exp\left[-E_b/k_B(T_m - T_f)\right] \tag{1.23}$$

where ω_0 is the attempt frequency related to the cut-off frequency of the distribution of relaxation times, E_b is the energy barrier between equivalent dipole directions and T_f is the

freezing temperature (*i.e.* where all relaxations times diverge) which can be viewed as the static dipolar freezing temperature for the relaxation process.

Validity of the Vogel-Fulsher Equation Although the V-F equation is often considered to be a sign of freezing in the system, no microscopic prescription for it has clearly emerged. Moreover, it is not unanimously accepted and other equations have been proposed. For example, it was shown in by Cheng *et al.* [94], that the temperature dependence of the relaxation time τ should be replaced by a super exponential function given by:

$$\tau = \frac{1}{\omega_0} \exp\left[(E_b/k_B T_m)^p\right] \tag{1.24}$$

where $p\,(>1)$ is a constant that characterizes the degree of dielectric relaxation.

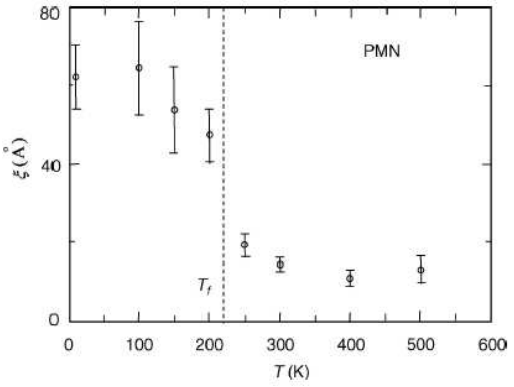

Fig. 1.13: Average size of polar nanoregions in the PMN crystal (determined from diffuse neutron scattering) as function of temperature. The vertical dashed line corresponds to T_f. (After Xu *et al.* [96])

Furthermore, the V-F relation can be directly derived from different assumptions and alternative mechanisms. For instance, based on experiments performed by neutron scattering [95, 96] indicating that the average size of polar nanoregions increases with decreasing temperature (Fig.1.13), and saturates below T_f, Pirc *et al.* suggested the possibility of a percolation-type transition into a frozen relaxor state [97]. The proposed mesoscopic mechanism for the V-F relaxation process is based on the qualitative picture of a network of polar nanoregions embedded in a highly polarizable medium. Each polar nanoregion polarizes the medium within a space region bounded by the correlation radius r_c. As the temperature is lowered, r_c is expected to increase; ultimately, freezing will occur due to the growth of both the size of the polar regions and the correlations among them. The basic idea is that thermodynamic stability of the polarization density with a power-law distribution $P(r) \sim r^{-3}$ implies a temperature dependence of the correlation radius $r_c \sim T^{-1/3}$. Thus the mean volume v of the polar regions increases until the percolation limit is reached. Using the mean field theory of continuum percolation, they showed that $v \sim (1 - T_f/T)^{-1}$, and since the reorientational activation energy is proportional to v, the V-F relation follows immediately. According to

this model, the two physical pictures, namely that of cluster growth and of the freezing of the local modes, are essentially two parts emerging from the same considerations.

Tagantsev [109] showed that the V-F relation can be obtained in the framework of a simple phenomenological model, all the parameters of which manifest analytical and gradual temperature and frequency dependencies. Within this model, the dielectric response is considered as a sum of relaxators having an exponentially wide and smooth spectrum of relaxation times. Following this approach, the V-F relation can be obtained as a direct consequence of gradual broadening of the spectrum with decreasing temperature. In doing so, it was demonstrated that the V-F behavior for the maximum of the dielectric permittivity can be observed in systems that manifest a regular temperature dependence of the spectrum at any temperature, i.e. without any assumption of freezing in the system.

To conclude this section, at early stages, local phase transitions models owing to chemical heterogeneity, and cluster-glassiness owing to dipolar disorder and frustrated interaction, allowed a number of achievements to be made based on a extension of spin-glass results to relaxors. However, the underlying abstraction from the very nature of the dipoles in the cluster-glassiness interpretation grid has proven to be insufficient, and accounting for the real nature of dipoles has become necessary [80].

1.3.1.5 From local structure to global properties

Since the works of Burns and Dacol [82], the dielectric and structural properties of relaxors have been ascribed to the appearance of polar nanoregions within the cubic matrix at the Burns temperature T_d, and their ensuing growth as the temperature is lowered. The formation of these polar nonregions have been attributed to the presence of nanoscale compositional inhomogeneities. Such inhomogeneities would lead to strong random electric fields and a smearing out of the ferroelectric phase transition. However, the structure and dynamics of the polar nanoregions on a atomistic level is not fully understood and reports on relaxor behavior in perovskites with long range B-cation ordering call into question the polar nanoregions based models [132]. While it is known that heterovalency on the B-site is necessary for relaxor behavior in some lead-based relaxors, quantitative relations between local structure and relaxor dispersion are still lacking. With this in mind, Grinberg *et al.* suggested that a local-structure-based approach could result in a deepened understanding of the relaxor behavior.

Leveraging the availability of local structural information from density functional theory studies (within the local density approximation [128–130] for the exchange and correlations between electrons) and molecular dynamics simulations (performed with the bond valence model for the atomistic potential [131]), Grinberg *et al.* examined the connections between composition, local structure and dynamics in lead-based relaxor ferroelectrics, showing that

the interactions behind the relaxor behavior are of short range type and are controlled by the variations in the local chemical bounding in perovskites.

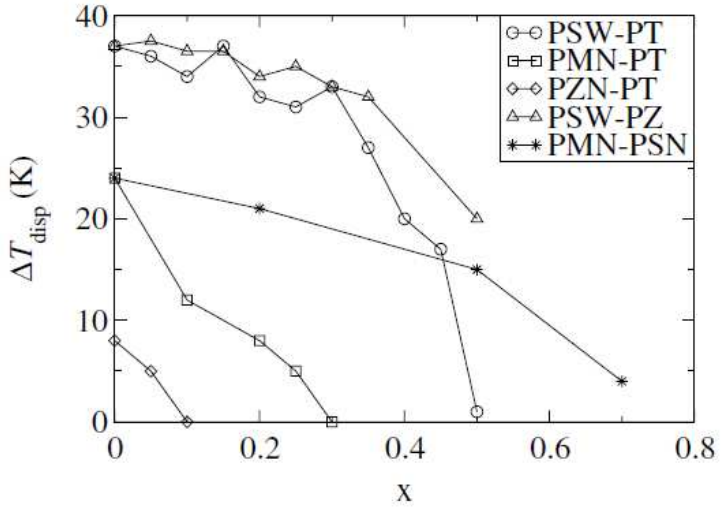

Fig. 1.14: Measure of the dependency of the dispersion ΔT_{disp} on the fraction x of the ferroelectric end members in (1-x)PSW-xPT, (1-x)PSW-xPZ, (1-x)PMN-xPT, (1-x)PMN-xPZ and (1-x)PMN-xPSN solid solutions. ΔT_{disp} exhibits a smooth monotonic trend as the fraction x of the ferroelectric end members increases, making it suitable to serve as an order parameter for the compositional phase transitions between the relaxor and ferroelectric phases. (After Grinberg *et al.* [134])

In order to assess the effect of the compositional variation on the extent of the relaxor behavior, the parameter ΔT_{disp} was introduced to evaluate the strength of the dielectric dispersion:

$$\Delta T_{\text{disp}} = T_{\epsilon,\max}(10^2\text{Hz}) - T_{\epsilon,\max}(10^6\text{Hz}) \tag{1.25}$$

where $T_{\epsilon,\max}(10^2\text{Hz})$ and $T_{\epsilon,\max}(10^6\text{Hz})$ are the temperatures at which the dielectric constant ϵ is maximal for $\omega = 100$ Hz and $\omega = 1$ MHz respectively. The magnitude of ΔT_{disp} is related to the Vogel-Fulcher [97] activation barrier U_a:

$$\omega = \omega_0 e^{-U_a/k_B(T_{\epsilon,\max} - T_f)} \tag{1.26}$$

where ω is the frequency of applied field, ω_0 is an attempt frequency and T_f is the freezing temperature at which the relaxation frequency vanishes. ΔT_{disp} is thus equal to zero for normal ferroelectrics. Furthermore, in solid solutions mixing relaxors with normal ferroelectrics, ΔT_{disp} exhibits a smooth monotonic trend from high values (on the relaxor side of the phase diagram) to zero (on the ferroelectric side), making it suitable to serve as an order parameter for compositional phase transitions between relaxor and ferroelectric phases (Fig.1.14).

To understand the origin of the large dispersion in such solid solutions, the correlations between the experimentally observed ΔT_{disp} values and crystal chemical parameters, such as the

ionic valence and the *ionic displacement*, are then investigated. The choice of these local parameters is achieved by the inspection of previous works which indicate *(i)* that compositional phase transitions in lead-based solid solutions are driven by changes in the local potential energy surface of the Pb cations [130, 136], *(ii)* that Pb off-centering, which give rise to ferroelectricty in $PbTiO_3$ (and related $Pb(B)O_3$ materials), is due to the energetically favorable formation of short $Pb-O$ bonds of Pb with a subset of its oxygen neighbors [137], *(iii)* that B-site disorder[15] in $Pb(B,B')O_3$ solid solutions produces overbonded and underbonded oxygen atoms depending on the valence of their B-cation neighbors [138–140], leading to a preferential displacement of Pb towards underbonded oxygens[16] thereby inducing variations in the local potential energy surface[17].

As a measure of these variations, the second moment of the valence of the two B-cation nearest neighbors of each oxygen atom $\langle V^2 \rangle$ was chosen as a local structural parameter. It is defined as:

$$\langle V^2 \rangle = \frac{1}{N_O} \sum_i (V_{i,1}^B + V_{i,2}^B - 2\overline{V^B})^2 \tag{1.27}$$

where $V_{i,1}^B$ and $V_{i,2}^B$ are the valences of the two nearest B-cation neighbors of the i-th O atom. The first moment of the oxygen atom B-cation neighbor valence $\overline{V^B}$ is equal to four in all Pb-based perovskites. The other crystal chemical parameter of relevance is the average off-center displacement D_{avg}^B of the B-cations. This choice stems from the observation by the means of DFT calculations [129, 130], of a correlation between a low average B-cation displacement D_{avg}^B and a large ΔT_{disp}. The relevance of ionic displacement can also be inferred from the effect of pressure on the relaxor behavior. The application of pressure shortens interatomic distances and decreases off-centering displacements [137] *i.e.* it lowers D_{avg}^B. This leads to an alteration of interatomic interactions that in turn affects the balance between long range Coulomb forces (which favor the ferroelectric state) and short-range repulsions (which favour the nonpolar cubic structure). The decay of the correlation radius results in a enhanced relaxor behavior and in a increased frequency dispersion [104], *i.e.* a higher ΔT_{disp} (Fig.1.15). The $\langle V^2 \rangle$ values and the average values of B-cation displacements D_{avg}^B were obtained by DFT calculations using the local density approximation.

[15] Setter and Cross studied that the role of B-site cation disorder in diffuse phase transition behavior of perovskite ferroelectrics [138]. In particular, they showed that ordered cationic arrangements on the B-site of $Pb(Sc_{0.5}Ta_{0.5})O_3$ give rise to a normal first-order ferroelectric phase transition (long annealing), whereas B-site disorder leads to a diffuse phase transition with broad Curie range and strong low-frequency dielectric dispersion (rapid quenching).

[16] Burton *et al.* compared first-principles calculations for $Ba(B,B')O_3$ and $Pb(B,B')O_3$ perovskites in order to elucidate why the latter disorder at lower temperatures than their Ba counterparts. This tendency was attributed to an enhanced Pb-O hybridization between Pb *6s* and O *2p* states of underbonded oxygens, yielding more competitive short-range interactions.

[17] Grinberg *et al.* connect these B-disorder induced variations in the local potential energy surface, to that of the value of h in random field spin models, which is known to hinder ferroelectricty and bring about the relaxor phase [91, 141].

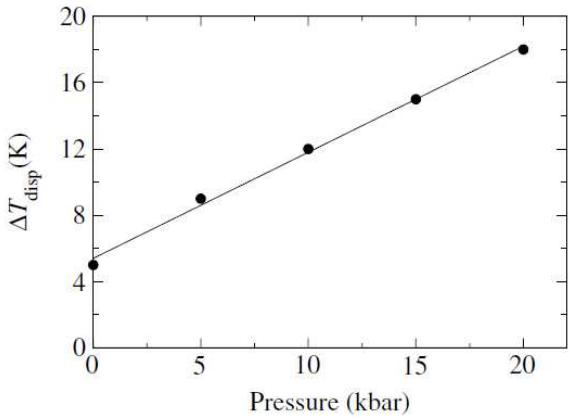

Fig. 1.15: ΔT_{disp} evolution with pressure in PLZT from the experimental results of Samara [104]. ΔT_{disp} increases with increasing pressure. Since off-center displacements are smaller at reduced volumes of perovskites [137], ΔT_{disp} is increased by lower off-centering displacements. (After Grinberg *et al.* [134])

The dependence of ΔT_{disp} on $\langle V^2 \rangle$ being found similar to that of the order parameter on temperature in standard Landau theory of a second order phase transition (Fig.1.16), the authors combined the two local criteria in a Landau theory equation [132] for describing ferroelectric-to-relaxor compositional phase transition, with ΔT_{disp} as the order parameter

$$G = G_0 - \frac{1}{2}A(\langle V^2 \rangle, D^B_{\text{avg}})(\Delta T_{\text{disp}})^2 + \frac{1}{4}(\Delta T_{\text{disp}})^4 \tag{1.28}$$

$$A(\langle V^2 \rangle, D^B_{\text{avg}}) = a_0 + a_v \langle V^2 \rangle + a_d e^{-\kappa D^B_{\text{avg}}} \tag{1.29}$$

where G is the free energy of the relaxor phase, G_0 is the energy of the parent ferroelectric phase, and the Landau coefficient A is function of $\langle V^2 \rangle$ and D^B_{avg} (a_0,a_v,a_d and κ are constants). The exponential dependence of $A(\langle V^2 \rangle, D^B_{\text{avg}})$ on D^B_{avg} (Eq.1.29) is chosen for its providing the best fit to experimental ΔT_{disp} data[18]. The values of the coefficients in Eq.1.28 were obtained by the use of experimental ΔT_{disp} values for different compositions for which full long-range B-cation ordering enables precise $\langle V^2 \rangle$ evaluation. The good agreement between the fit and the experimental values (Fig.1.17) validates the Landau theory of ferroelectric-to-relaxor compositional phase transition and supports the idea that the interactions that give rise to the characteristic dispersion of relaxors are of short range type and that they are governed by the variations in the local chemical bonding in perovskites.

To further assess the model and investigate in greater depth the connections between composition, local structure and dynamics in lead-based relaxor ferroelectrics, the authors performed molecular dynamics study of the dielectric response in GHz frequencies [133]. The obtained results show that some essential features of the dielectric response in relaxors can be driven

[18]The exponential dependence of $A(\langle V^2 \rangle, D^B_{\text{avg}})$ on D^B_{avg} derives its justification from the exponential variation of the bonding overlap with interatomic distances [132].

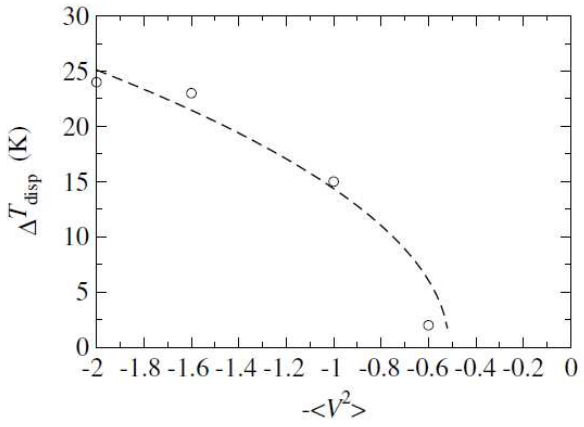

Fig. 1.16: Dependence of ΔT_{disp} on $\langle V^2 \rangle$ in PMN-PSN solid solution, revealing a strong resemblance to the behavior of of the order-parameter in a second-order phase transition. (After Grinberg *et al.* [134])

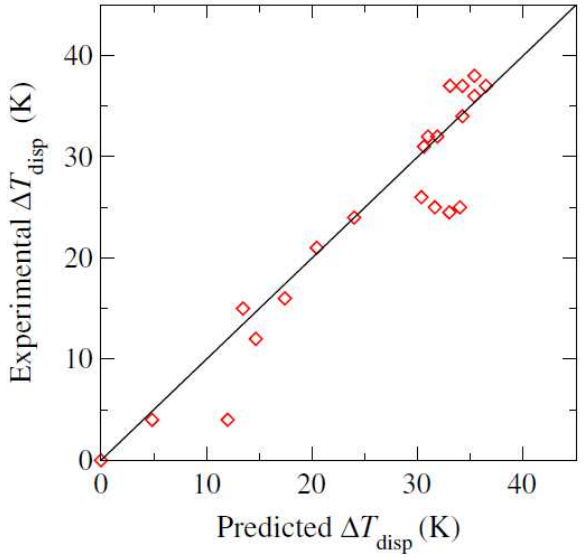

Fig. 1.17: Comparison of the ΔT_{disp} results of the Landau theory fit with experimental ΔT_{disp}. Data points are close to the $y = x$ line, indicating that the Landau theory of the relaxor-to-ferroelectric transition encapsulated by Eq.1.28 and 1.29 quantitatively captures the trend of the experimental ΔT_{disp} data, and attesting that local effects govern the magnitude of the dispersion in Pb-based relaxor ferroelectrics. (After Grinberg *et al.* [134])

by local phenomena without the requirement of PNRs [129, 133, 134], thereby supporting the idea according to which PNRs represent a useful but largely speculative concept [135].

1.3.2 Random Fields in Relaxors

The second canonical class of disordered systems relies on the random fields theory. Since in relaxors, inherent charge disorder due to the random distribution of heterovalent cations on the B-site of the perovskites naturally leads to quenched random fields, it wasn't long

before Westphal *et al.* and others asserted that random fields (RF) were in fact at the origin of the observed slowing down of the dynamics of relaxors and their eventual freezing into a domain state on a nanometric length scale. Before considering random fields models in detail, it is worthwhile to briefly review the canonical random field Ising model (RFIM) since it captures the competing mechanisms for order and disorder. The local spin couplings favor ferromagnetic ordering, whereas variations in the random fields favor disorder.

1.3.2.1 Random Field Ising Model : An overview

The Ising model in a random field is a prominent example of a lattice spin model with quenched disorder, representative of a large number of impure materials. The RFIM model is defined on a lattice in the following way:

$$H = -J \sum_{\langle ij \rangle} S_i S_j - \sum_i h_i S_i \tag{1.30}$$

The spins variables can only point up or down, so that the order parameter falls in the *discrete symmetry* framework. This models describes the competition between random ordering fields and long range order. The probability distribution for the disorder average is typically a Gaussian or a bimodal one, where the latter one is given by $h_i = \pm h$ with equal probability and h being some constant value of the field. The following assumptions about h_i are generally made:

$$\overline{h}_i = 0 \quad , \quad \overline{h_i h_j} = h^2 \delta_{ij} \quad , \quad h \ll J \tag{1.31}$$

The RFIM was first discussed in 1975 by Imry and Ma [116] and is currently under strong theoretical and experimental investigation. The important question that was first addressed is whether or not there a tendency due to disorder to suppress the ordering in lower dimensions, and hence to shift the lower critical dimension d_l, above which long range order occurs, to higher values. The situation of interest is $h \ll J$, since it is clear that in the opposite case the system will be disordered. Regarding this question, the two main conflicting arguments were Imry and Ma domain argument [116] and the dimensional reduction argument proposed by Parisi [118].

(i) *Imry and Ma domain argument*[19] In one of the earliest studies of the random field Ising model, Imry and Ma [116] argued that quenched random fields in a system may cause a uniform ferromagnetic state to break into domains, *i.e.* , that the ferromagnetically ordered state becomes unstable with respect to the formation of ill oriented domains in all dimensions $d \leq 2$, so that $d_l = 2$. The intuitive argument that was given goes is the

[19] Imry and Ma actually extended Peierls proof [119] of the existence of a phase transition in the two-dimensional Ising model to the situation with symmetry breaking randomness in RFIM.

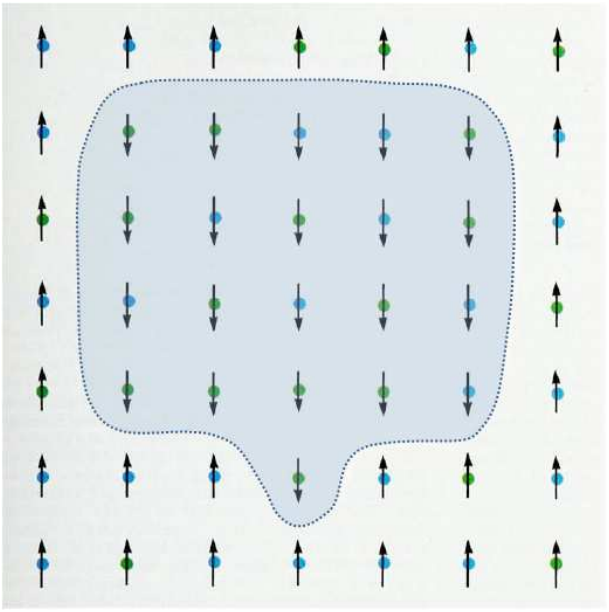

Fig. 1.18: Droplet of overturned spins in a supposed ferromagnetic (up) ground state. A quenched random field acts at each site of the system; the field points up on the blue sites and down on the green sites. The configuration with the overturned droplet, or domain, can have a lower energy than that consisting of all-pointing up spins. This can happen because the droplet occurs in a region in which the random fields points predominantly down. Imry and Ma estimated the probability of occurrence of such droplets and concluded that the ferromagnetic state is unstable with respect to the formation of large droplets in fewer than 2 dimensions. (Adapted from Fisher *et al.* [120])

following (Fig.1.18): In a region of linear dimension L, the energy cost for reversing the spins in this region is proportional to the domain wall area, hence this energy scales as JL^{d-1}. However, the associated bulk energy gain due to the interaction with the random fields scales as $-hL^{d/2}$. Obviously, for $h \ll J$, *i.e.*, there will be a characteristic length over which the bulk energy gain will overcome the cost of the surface energy. In other words, even for arbitrary week random fields, domains will spontaneously form and field fluctuations should prevent any long-range order in $d \leq 2$, yielding $d_l = 2$ (rather than $d_l = 1$ for pure Ising model).

(ii) *Dimensional reduction* Other arguments were subsequently put forward for $d_l = 3$ rather than $d_l = 2$. Among these is the correspondence between a random system in d dimensions and its pure counterpart in $d - 2$ dimensions. This corresponds to the so-called dimensional reduction and was first suggested in the context of the perturbation theoretical formulation of the critical behavior of the Ising model in a quenched random magnetic field [118]. In particular, since the lower critical dimension of the ordinary pure Ising model is $d_l = 1$, this should imply that the 3-dimensional random field Ising model has no phase transition, *i.e.* $d_l = 3$ in the random version.

The debate was finally resolved by two papers in mathematical physics proving *ferromagnetic ordering in* 3 *or more dimensions* at low temperature [114], and absence of ferromagnetic ordering in 2 dimensions at any temperature [115], thereby confirming the domain argument and infirming the dimensional reduction. The breakdown of the perturbation theory is mainly due to a large number of local minima in the energy landscape[20].

The domain argument of Imry and Ma can be generalized to the case where the order parameter is of *continuous symmetry*. The random-field instability of the ordered state of continuous symmetry sets in at $d_l = 4$. So that in $d < 4$, the ordered state is unstable against an arbitrarily weak random field, *i.e.*, a field much weaker than the interactions that favor the ordered state. Instead of a long-range ordered state, it becomes energetically favorable for such a system to break up on cooling into sufficiently large domains to form a so-called low-temperature domain state. The size of the domains is determined by a balance between the domain wall energy and the statistics of the random field. We now turn to the random fields models as they were formulated for describing the relaxor behavior.

1.3.2.2 Random fields in relaxors

Shortly after the work of Imry and Ma [116] on the effect of forzen-in random fields in ferromagnets, Halperin and Varma [117] advanced the possibility that similar ideas could be extended to understand the effect of atomic disorder in ferroelectric perovskites. In particular, they showed that atomic impurities couple linearly to the ferroelectric order parameter, in a equivalent manner to the random fields in ferromagnets, leading to the smearing of the transition. Although disregarded for a while, this idea resurfaced after that it had been realized that the random-bond concept was insufficient in accounting for all of the observed effects featured by relaxors.

Westphal, Kleemann and Glinchuk [122] applied the results of the theoretical work by Imry and Ma to relaxors. They considered that the applicability was legitimate for PMN for instance, despite its (only) eight-fold dipolar degeneracy. In this view, the quasi-continuous symmetry of the order parameter was held responsible for a disordered ground state on macroscopical scales, consisting of low-symmetry nanodomains separated by domain walls. The disordered substitution of the heterovalent ions inherent to the compositionally disordered structure, provides the source for quenched random electric fields. Moreover, the lattice strains associated with these substituents also couple to the polarization setting up additional random fields or enhancing their presence. The authors have argued that random fields are responsible for the observed strong slowing down of the dynamics of PMN, and for

[20]This failure often arises from the difficulty encountered when applying formal perturbative methods to random systems, where the procedures of averaging over randomness typically neglect the effects of statistically unlikely regions of the random system; such regions can make essential contributions to physical quantities.

its eventual freezing into a domain state. Within this framework, the frequency dispersion of the dielectric response is explained via a complex domain-wall motion.

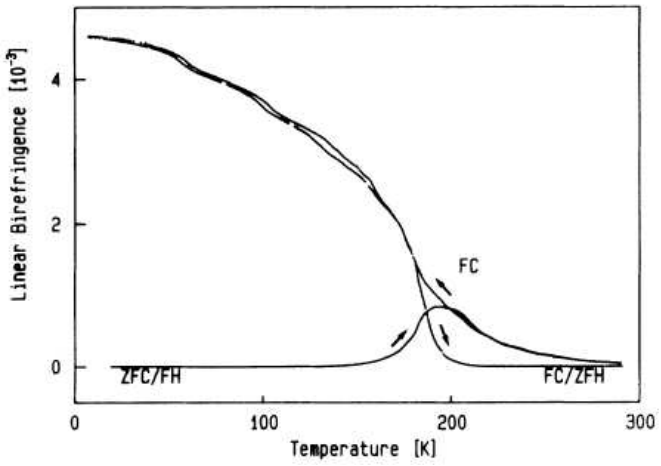

Fig. 1.19: Linear birefringence measured subsequently as a function of temperature on zero-field cooling (ZFC), field heating with E = 1.2kV/cm, E < E_{cr} (FH), field cooling (FC) and zero-field heating (ZFH), illustrating the nonergodic behaviour of PMN crystal. (After Kleemann et al. [123])

One of the salient features of this model is its ability to explain the observed non-ergodic behavior (Fig.1.19) in terms different of those referring to the glass concept. For instance, the Kohlrausch-Williams-Watts-type and the Curie-von Schweidler-type relaxations of birefringence that were found in the temperature intervals of $180 < T < 210$K and $210 < T < 230$K, respectively, were successfully explained by domain wall displacements, rather then by the reorientation of dipoles. Furthermore, this model could explain some features of relaxors, unknown to the spin and dipole glasses, such as the Barkhausen jumps during poling process [2].

1.3.2.3 First-principles-based effective Hamiltonian approach for random fields

Substitutional charge disorder on the B-site of $Pb(B,B')O_3$ perovskites such as PMN, PSN and PST, gives rise to quenched electric random fields $\vec{h_i}$, which are believed to be at the origin of the behavior of relaxor ferroelectrics [122, 143]. Another contribution to local random fields can stem from structural cation vacancies such as Pb vacancies[21]. A work by Chu *et al.* [142] studying the role of lead vacancies in impeding the spontaneous relaxor-to-ferroelectric phase transition in incipient relaxor ferroelectrics such as PSN and PST, supports the interrelation between random fields and the relaxor behavior. In the same stream, the vanishing of the relaxor-to-ferroelectric transition induced by the application of hydrostatic pressure [104] at a critical point, can be understood by assessing the relative strength of the interactions that

[21] Most likely Pb-O divacancies [144]

favor ferroelectricity and that are pressure-sensitive on the one hand, and the practically[22] pressure-independent spatial average strength of quenched local fields $\langle|\vec{h_i}|\rangle$, which disrupt long range ordering and favor the relaxor state on the other hand. Thus, both pressure-induced and polar-defects-induced vanishing of the relaxor-to-ferroelectric phase transition in incipient RFE emphasize the role of random fields in contributing to the relaxor behavior.

Polar nanoregions whose existence is supported by neutron scattering [145], are believed to originate from the coupling between the random fields $\vec{h_i}$ and the ferroelectric degrees of freedom [146]. Within the paradigmatic view of polar nanoregions embedded in a non polar matrix and deemed to be at the origin of the relaxor behavior below T_d, Burton *et al.* developed molecular dynamics simulations of a first-principles effective Hamiltonian model, where random local field terms were combined with an effective Hamiltonian for a normal FE, in order to elucidate the correlations between chemical and polar short range orders, [146–148].

The effective Hamiltonian H_{eff} is obtained from a Taylor expansion of the total energy around a high-symmetry perovskite reference structure in terms of a chosen set of relevant degrees of freedom:

$$H_{\text{eff}} = H(\{\vec{\xi_i}\}) + H(e_{\alpha\beta}) + H(\{\vec{\xi_i}\}, e_{\alpha\beta}) + H(\{\vec{\xi_i}\}, \sigma_l, \mathsf{v}_{\text{Pb-O}}, \cdots) \tag{1.32}$$

where $\{\vec{\xi_i}\}$ represent local polar distortion variables, or local vibrational modes, centered on Pb sites, $\{e_{\alpha\beta}\}$ the homogeneous strain variables and $H(\{\vec{\xi_i}\}, e_{\alpha\beta})$ a coupling term between polar and strain variables. The first four terms give a valid H_{eff} for modeling normal FE perovskites without local fields [12, 149, 150]. The term $H(\{\vec{\xi_i}\}, \sigma_l, \mathsf{v}_{\text{Pb-O}}, \cdots)$ is a random local field term [151], proportional to $\sum_i \vec{h_i} \,.\, \vec{\xi_i}$, in which $\vec{h_i}$ is the local electric field at Pb site i arising from the screened electric fields of the quenched distribution of B-site cations, σ_l, or from any other polar-defect contribution such as $\mathsf{v}_{\text{Pb-O}}$ that stands for Pb-O divacancy pairs.

Molecular dynamics simulations were performed in a 40^3 unit-cell simulation boxes. Accessible time scales of the order of 0.1 ns imply that only frequencies greater then approximately 10 Ghz are accessible, therefore preventing the access to the GHz-Hz frequency range in which the dielectric dispersion is measured. A given chemical configuration of $Sc^{3+} - Nb^{5+}$ ordering on next-neighboring A-sites generates a random field configuration that can be regarded as quenched since diffusive order-disorder mechanisms are negligible in the temperature range of interest for the relaxor properties ($T \lesssim 400$ K in PSN). The quenched chemical configurations, and therefore random fields $\vec{h_i}$ configurations, consist of 20 chemically ordered regions (so-called COR) in a matrix composed of 80 chemically disordered regions (so-called CDR). Both types of regions are of spherical shapes and enclose around 800 Pb sites. Fig.1.20

[22] In reality, the local electric fields vary as the inverse of square of the lattice constant. However, the increase at 20 GPa is estimated to be less then 5% in PSN [148].

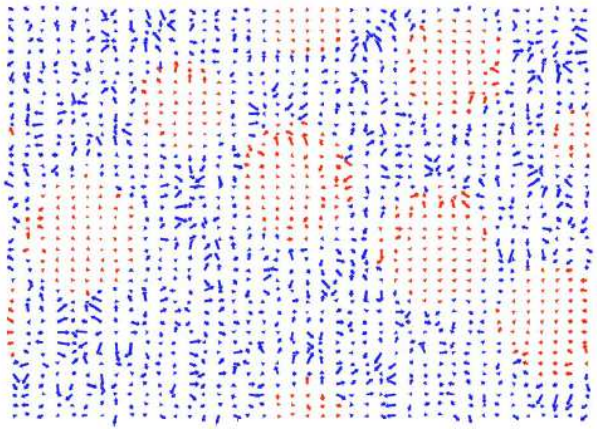

Fig. 1.20: Projection of the Pb-site local fields (in arbitrary units) on a (110) plane through the simulation box of $Pb(Sc_{1/2}Nb_{1/2})O_3$. Chemically ordered regions have relatively small homogeneous fields whereas chemically disordered regions have larger, more varied disordered local fields. (After Burton *et al.* [146])

illustrates a (110) cross-section through the simulation box, in which arrows represent projected $\vec{h_i}$, that are larger and more disordered in the disordered matrix than in the built-in chemically ordered regions. As a consequence, the weak but homogeneous local fields config-

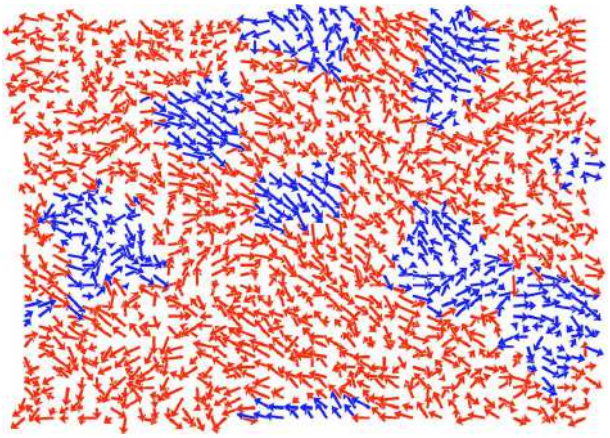

Fig. 1.21: Snapshot of local mode polarizations of PSN at $T = 600$ K ($\approx T_c$). Highly correlated regions are chemically ordered whereas the disordered matrix is chemically disordered. (After Burton *et al.* [146])

urations at the CORs gives rise to preferential local polar ordering (Fig. 1.21). Comparing the cluster-cluster correlations ξ_{ij} (Eq.(1.33)) as functions of intercluster separation between COR-COR, CDR-CDR and COR-CDR,

$$\xi_{ij} = \langle \vec{S_i}(t).\vec{S_j}(t) \rangle - \langle \vec{S_i}(t) \rangle \langle \vec{S_j}(t) \rangle \ , \quad \vec{S_i} : \ \text{cluster moment} \tag{1.33}$$

the authors find the following hierarchy $\xi_{\mathrm{CDR-CDR}} < \xi_{\mathrm{COR-CDR}} < \xi_{\mathrm{COR-COR}}$, from which they infer the identification of PNRs to the built-in CORs.

In addition to some obvious redundancy among the assumptions and inferences of the model, the extrinsic implementation of what would be identified as PNRs makes the procedure

somewhat factitious. It is interesting to report Kleemann's view on the matter:

> "*In our opinion, the authors' conclusion that the "lengthscale of PNRs is the same as for chemical short range order" is disappointing, since it just manifests that the correlation length in the CDR part of the model is limited by the size of the simulation box. Hence, we are left with a PNR structure of a heterogeneous system - a plausible but probably trivial result.*" [152]

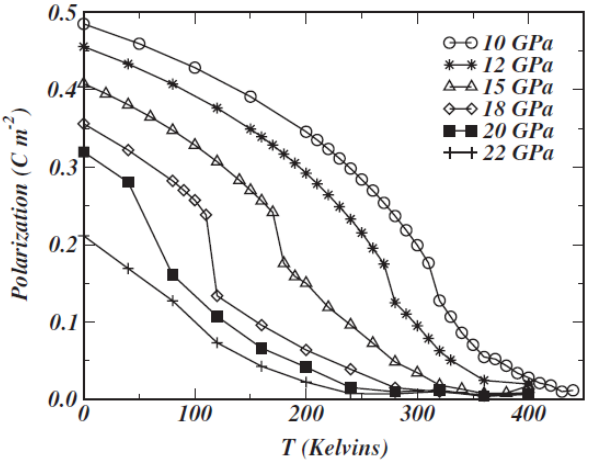

Fig. 1.22: Simulated PSN polarization as a function of temperature at hydrostatic pressure in the range $0 < P < 22$ GPa. The first-order character of the transition, signaled by the jumps, is accentuated as the pressure increases. (After Burton *et al.* [148])

Adding the standard pressure-volume $+PV$ term to the effective Hamiltonian, the authors studied the effect of hydrostatic pressure on PSN [148]. Fig.1.22 shows PSN bulk polarization as a function of T at various pressures. According to the authors, a first-order phase transition occur at the polarization jump, the character of which increases with P as the transition temperature approaches zero. The Burns temperature is associated to the temperature at

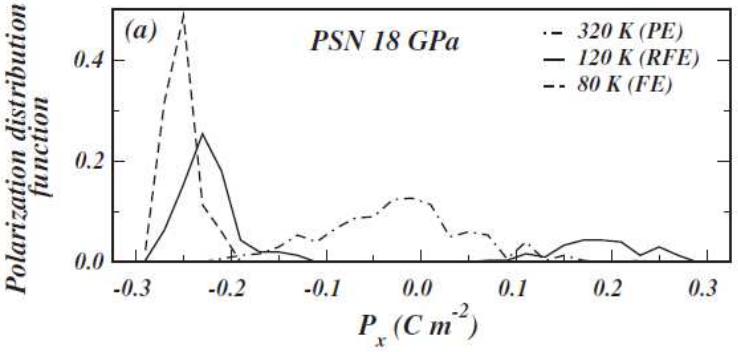

Fig. 1.23: Cumulative histogram of P_x values for chemically ordered regions at different temperature for PSN under 18 GPa. The three curves correspond to paraelectric (320 K), relaxor (120 K), and ferroelectric (80 K) states. (After Burton *et al.* [148])

which the COR become polar. This is illustrated in Fig.1.23 where plots of the cumulative histogram of the x component of the polarization P_x of the CORs in PSN under 18 GPa

are shown at three qualitatively different temperatures. Above 320 K, the distribution is unimodal centered at zero, this is representative of the paraelectric state. At 120 K, in the pre-transition region, the distribution is bimodal with two unequal peaks centered at non-zero opposite values. At this temperature, the system is in its relaxor state. The asymmetry in the peaks is ascribed to finite-size effects, since the relaxor state belong to the paralectric phase and should exhibit zero bulk polarization. Below the first-order phase transition (80 K), the symmetry is broken and the distribution is unimodal centered at non zero value; the system is in its ferroelectric phase.

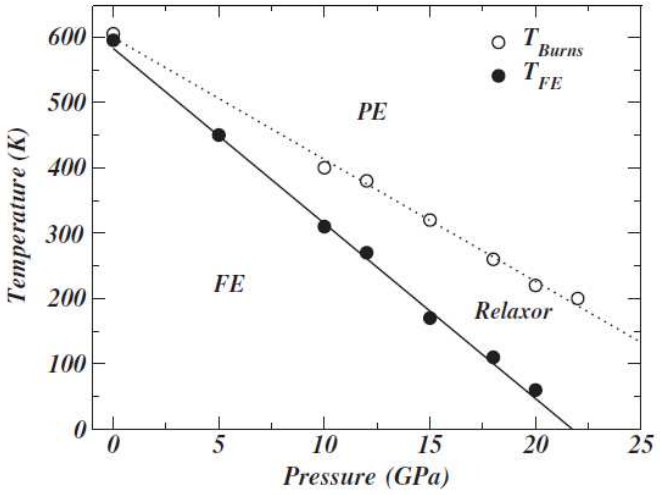

Fig. 1.24: Predicted pressure vs temperature phase diagram for PSN, indicating the ferroelectric to relaxor transition and the estimated Burns temperature (After Burton *et al.* [148]).

The predicted pressure vs temperature phase diagram is shown in Fig.1.24. The FE transition temperature was estimated from Fig.1.22 and the Burns temperature from the temperature at which the distributions of COR polarization components changed from unimodal to bimodal (Fig.1.23). Although qualitatively consistent with experiment, the predicted pressure vs temperature phase diagram exhibit no termination of the FE/RFE transition line at an isolated critical point as measured in Ref. [154]. Moreover, when comparing the slopes of the FE/RFE lines in the predicted (Fig.1.24) and experimental (Fig.1.25) phase diagrams, one finds a large discrepancy: $dT_{\mathrm{FE}}/dP \sim$ -27 K GPa^{-1} in the simulated line whereas $dT_{\mathrm{FE}}/dP \sim$ -100 K GPa^{-1} in the experimental one.

1.3.3 Spherical Random bond-Random Field model

In spite of intensive investigations, the nature of the diffuse phase transition in relaxors has remained the subject of some controversy. As noted earlier, the basic open question is whether the relaxor state in PMN and related systems in zero field is either *(i)* a ferroelectric state broken up into nanodomains under the constraint of quenched random electric fields,

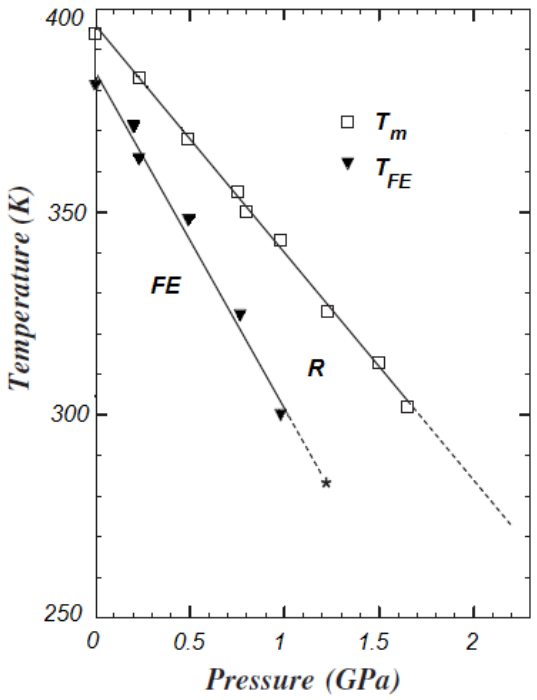

Fig. 1.25: Experimental temperature vs pressure phase diagram for the PSN crystal at 10^4 Hz. The $T_{\mathrm{FE}}(P)$ phase boundary terminates at a finite temperature and pressure, as depicted by the star. Such termination represent a critical point which, from a thermodynamic point of view, would be somewhat akin to the vapor-liquid critical point. (After Samara *et al.* [154]).

or *(ii)* a dipolar glass state with randomly interacting polar microregions in the presence of random fields. To assess the relevance of these two classes of models, Blinc *et al.* reported the temperature dependence of the Edwards-Anderson order parameter q_{EA} and the local polarization distribution function $W(\vec{p})$ in a PMN single crystal via two-dimensionnal ^{39}Nb NMR [99]. The obtained results were then described by a newly proposed spherical random bond-random field (SRBRF) model of relaxor ferroelectrics.

1.3.3.1 Uncoupled Pseudospin Model

The picture adopted in this model is that of reorientable interacting polar clusters, each consisting of n dipolar unit cells of dipole moment $\vec{m}$. The dipole moment of the ith cluster is thus $\vec{M}_i = n_i\vec{m}_i$. A dimensionless order parameter field is then introduced:

$$\vec{S}_i = (\vec{M}_i/n_i)\left[(m_i^2)_{av}/3\right]^{-1/2} \tag{1.34}$$

where $(m_i^2)_{av} = (1/N)\sum_i m_i^2$ with N the total number of reorientable clusters. The Edwards-Anderson order parameter for a crystal with average cubic symmetry (PMN in zero field) is

defined as:

$$q_{\mathrm{EA}} = \frac{1}{N}\sum_{i}^{N}\langle S_i\rangle^2 = \left[\langle S_i\rangle^2\right]_{av} \tag{1.35}$$

The average probability distribution of local polarization $\vec{p}_i \equiv \langle\vec{S}_i\rangle$ is defined as:

$$W(\vec{p}) = \frac{1}{N}\sum_{i}\delta(\vec{p}-\vec{p}_i) \tag{1.36}$$

where the first moment of $W(\vec{p})$ is the total polarization $\vec{P}$, which for a relaxor in the glass phase is zero in the absence of an external electric field, while the second moment is q_{EA}.

The measured ^{93}Nb NMR spectrum consists of two lines, one of which is relatively broad and temperature independent, attributed to pinned nanodomains, the second being relatively narrow and temperature dependent, attributed to reorientable clusters. The temperature dependence of the second moment M_2 of the inhomogeneous frequency distribution corresponding to the narrow line is shown in Fig. 1.26. It is seen that the Edwards-Anderson order parameter q_{EA}, which is proportional to M_2, is nonzero in the whole investigated temperature range between 400 and 30 K. It is rather small and weakly T-dependent above 300 K. Below 260 K it increases nearly linearly with decreasing temperature down to 100 K.

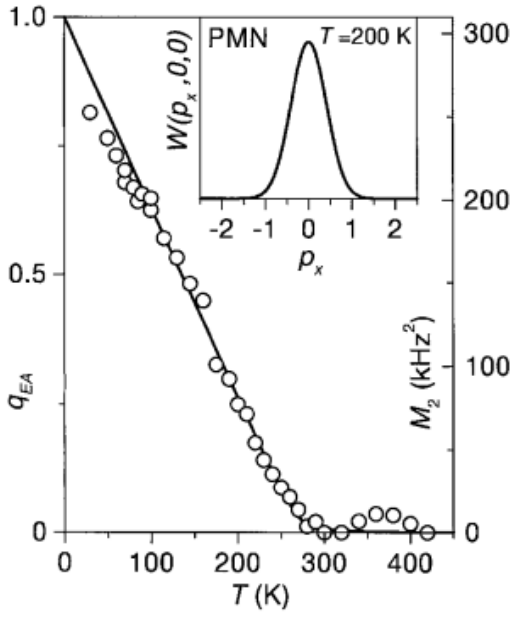

Fig. 1.26: Temperature dependence of the Edwards-Anderson order parameter q_{EA} of the reorientable part of the inhomogeneous frequency distribution in PMN ($q_{\mathrm{EA}} \propto M_2$). The inset shows the Gaussian shape of the probability distribution of local polarization. (After Blinc *et al.* [99])

Blinc *et al.* also noted that the local polarization distribution function $W(\vec{p})$ in PMN is Gaussian in shape (inset in Fig.1.26), whereas it is double-peaked in dipolar glasses below the freezing temperature T_f. According to Blinc *et al.*, this is incompatible with the assumption

of a fixed-length order parameter field typically made in (Ising-type) dipolar glasses. Rather, in a relaxor the order parameter field is described as a continuous vector field of variable length, which is associated with the dipole moment of reorientable polar clusters, and is subject to a global spherical constraint on the square of the total polarization. Within this picture, a relaxor thus corresponds to a new type of dipolar glass, namely, the spherical vector glass (SG).

Blinc *et al.* described the above features in terms of a new semimicroscopic model for relaxor ferroelectrics, based on randomly competing interactions between reorientable polar clusters of different sizes in the presence of random fields. The dimensionless order parameter $\vec{S}_i$ has a large number of equilibrium orientations lying on a spherical shell of radius $|\vec{S}_i|$ which scales with the cluster size n_i in the ith cluster ($i = 1 \cdots N$, the total number of clusters). Going over the continuous limit, it is assumed [98] that each component $S_{i\,\mu}$, where $\mu = x, y, z$, varies continuously in the range $-\infty < S_{i\,\mu} < +\infty$, and that the set of all the fields is subject to the spherical constraint given by the following closure relation:

$$\sum_{i}^{N} \vec{S}_i^{\,2} = 3N \tag{1.37}$$

The model Hamiltonian of a system of interacting polar clusters is then formally written as:

$$\mathcal{H}_S = -\frac{1}{2}\sum_{ij} J_{ij}\vec{S}_i.\vec{S}_j - \sum_i \vec{h}_i.\vec{S}_i - g\sum_i \vec{E}_i.\vec{S}_i \tag{1.38}$$

Here J_{ij} are random frustrated interactions, or bonds. These random bonds are infinitely ranged[23] with a Gaussian probability distribution characterized by the following mean value and variance:

$$[J_{ij}]^c_{av} = J_0/N \qquad , \qquad \left[(J_{ij})^2\right]^c_{av} = J^2/N \tag{1.39}$$

In Eq.(1.38), the random local electric fields $\vec{h}_i$ similarly obey an independent Gaussian distribution such that:

$$[h_{i\mu}]^c_{av} = 0 \qquad , \qquad [h_{i\mu}h_{j\nu}]^c_{av} = \Delta\delta_{ij}\delta_{\mu\nu} \tag{1.40}$$

The last term in Eq.(1.38) describes the influence of an external field $\vec{E}$, where g is an effective dipole moment corrected by the appropriate local field factor. Two order parameters characterize the model, the polarization,

$$P_\mu = \frac{1}{N}\sum_{i}^{N}\langle S_{i\mu}\rangle \tag{1.41}$$

[23] This assumption is supported by the long range nature of intercluster interactions mediated by the acoustic and optic phonons.

and the dipolar glass order parameter, written here in its Cartesian components,

$$q_\mu = \frac{1}{N}\sum_i^N \langle S_{i\mu}\rangle^2 \tag{1.42}$$

For a pseudocubic or isotropic system, both order parameters are independent of μ. After applying the replica method to the average free energy derived from Eq.(1.38), the usual saddle point condition leads to coupled equations for the order parameters and two sets of solutions, that in the case of zero external field can be expressed as: (i) For $J_0 < (J^2+\Delta)^{1/2}$, a spherical glass (SG) state $q \neq 0$ is obtained without long range order $P = 0$ below a dynamic glass transition temperature J/k, (ii) for $J_0 > (J^2+\Delta)^{1/2}$ on the other hand, an inhomogeneous ferroelectric phase (FE) is obtained, with $P \neq 0$ and $q \neq 0$ below a transition temperature given by J_0/k. (The generalized temperature-coupling parameter J_0 phase diagram is shown in Fig.1.27). In this latter case of FE phase, the Edwards-Anderson

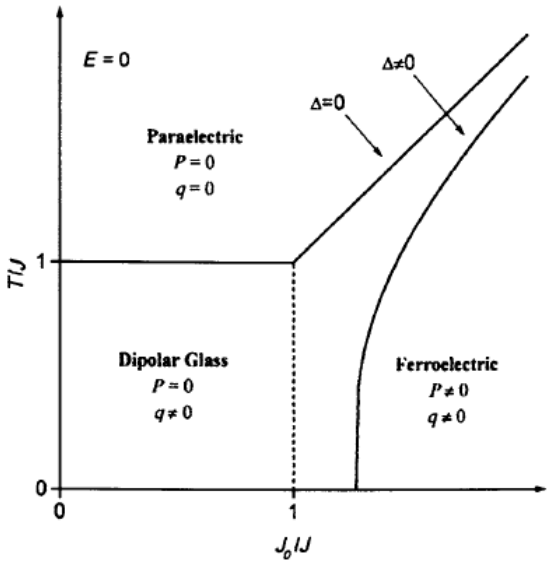

Fig. 1.27: Generalized temperature-coupling parameter J_0 phase diagram of the spherical random bond-random field model of a relaxor in zero field. (After Pirc *et al.* [98])

order parameter is given by $q_{\rm EA} = 1 - T/J_0$ and the spontaneous polarization by:

$$P^2 = \left[1 - \left(\frac{J}{J_0}\right)^2\right]\left[1 - \left(\frac{T}{J_0}\right)\right] - \frac{\Delta}{J^2} \tag{1.43}$$

The SRBRF model for relaxor behavior applied to PMN gives good agreement between model predictions and experiment. In Fig.1.26, the open circles representing the evolution with temperature of the second moment of $W(\vec{p})$ are from data, and the solid line is the theoretical fit. Whereas the local polarization distribution function $W(\vec{p})$ discriminates between dipolar and spherical glassy behavior, the third-order dielectric nonlinearity $a_3 = \chi_3/\chi_1^4$ [100], where χ_3 is the third order susceptibility, discriminates between a glassy state and a ferroelectric

state broken up into nanodomains due to the presence of random fields. In the case of no long range order, the SRBRF glass model yields the following expression for a_3[24]

$$a_3 = \frac{T}{(1-q^2)\left[1-\beta^2 J^2(1-q)(1-3q-2\Delta/J^2)\right]} \tag{1.44}$$

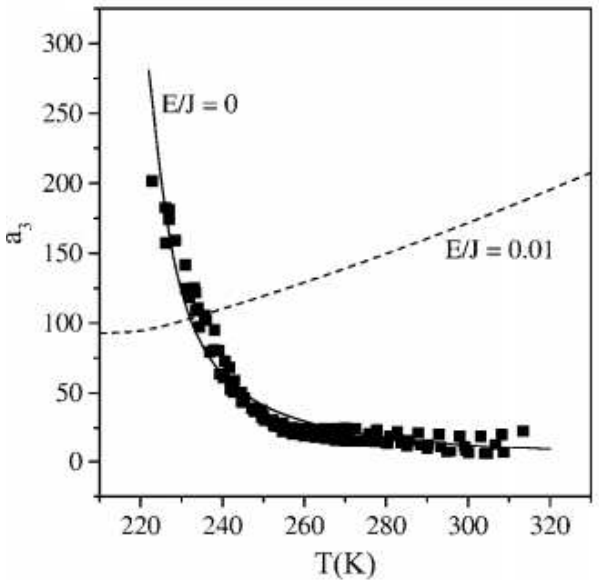

Fig. 1.28: Temperature dependence of the quasistatic non linear susceptibility $a_3 = \chi_3/\chi_1^4$ in PMN for $E = 0$; $a_3(T)$ is found to increase sharply on lowering the temperature between 320 and 220 K. This is incompatible with the case of a random-field frustrated ferroelectric, but quantitatively agrees with the SRBRF model's predictions (solid line is obtained using Eq.(1.44)). The dashed line represents the temperature dependence of a_3 evaluated for $E/J = 0.01$. Note that with increasing field strength the peak in $a_3(T)$ disappears, *i.e.*, for a large enough field a crossover from a glass phase to ferroelectric one occurs. (After Blinc *et al.* [99])

For a random-field frustrated ferroelectric $J_0 \gg J$ without random bonds ($J = 0$), *i.e.* the Westphal *et al.* model, a_3 is found to be a monotonically increasing function of temperature. On the other hand, for a random-bond glass $J_0 \ll J$ without random fields ($\Delta = 0$), *i.e.* the dipolar-glass model, a_3 diverges at a freezing temperature J/k, according to $a_3 \sim |T - T_f|^{-1}$. In the presence of weak random fields, *i.e.*, for $\Delta/J^2 \ll 1$, a_3 does not diverge, but shows a sharp peak near $T \approx J/k$ (Fig.1.30(a)). This last behavior was found in PMN [101] and PLZT [102], supporting the assumption that these systems can be described as a special

[24] In a system with average cubic symmetry, the phenomenological relation between polarization P_μ and electric field E_μ ($\mu = 1, 2, 3$) can be written as a power series $P_1 = \chi_1 E_1 - \chi_{122} E_1(E_2^2 + E_3^2) - \chi_{111} E_1^3 + \cdots$, or inversely, $E_1 = a_1 P_1 + a_{122} P_1(P_2^2 + P_3^2) + a_{111} P_1^3 + \cdots$. Comparing these two relations thus yields : $a_1 = \chi_1$, $a_{122} = \chi_{122}/\chi_1^4$, $a_{111} = \chi_{111}/\chi_1^4$, where χ_1 is the linear susceptibility, and χ_{122}, χ_{111} the third order non-linear susceptibilities. For a field $\vec{E}$ in the [111] direction and $P_1 = P_2 = P_3$, the following simplifications are obtained: $P = \chi_1 E - \chi_3 E^3 + \cdots$ and $E = a_1 P + a_3 P^3 + \cdots$ where $\chi_3 = 2\chi_{122} + \chi_{111}$ and $a_3 = \chi_3/\chi_1^4$. Even though one of the unique features of relaxors is their positive dynamic dielectric non-linearity, it won't be addressed in the third chapter due to the required time-consuming calculations.

kind of dipolar glasses, namely, the spherical glasses. Good agreement was found between calculated $a_3(T)$ from susceptibility data and calculations based on Eq.(1.44) (Fig.1.28).

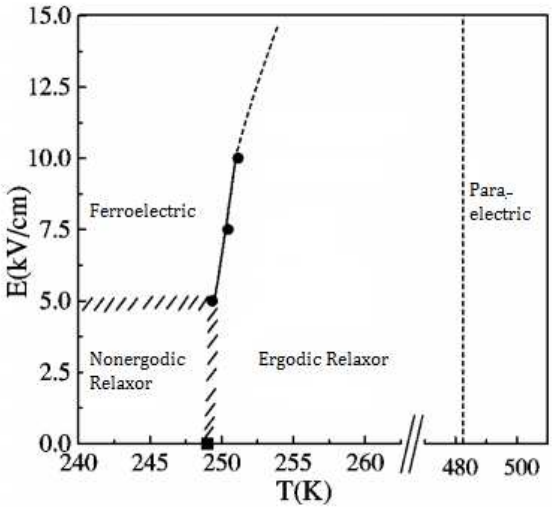

Fig. 1.29: Schematic electric field-temperature (E-T) phase diagram. For $E < E_c$ and $J < J_0$, the dipolar freezing temperature $(J^2 + \Delta)^{1/2}/k$ is independent of E and a vertical phase boundary is found in the E-T phase diagram between the ergodic and non-ergodic relaxor phases, indicating the braking of ergodicity associated to the divergence of the longest relaxation time.(After Kutnjak *et al.* [102])

In the presence of an external field E, the crossover from a glassy phase to a ferroelectric one (Fig.1.29) can occur since J_0 is expected to be field dependent, $J_0(E) = J_0(E = 0) + \alpha E^2$. This dependence can be explained by the field induced polarization-strain coupling. Thus, a critical field E_c may exist such that for $E > E_c$, $J_0(E) > (J^2 + \Delta)^{1/2}$. In this case the a_3 peak vanishes as it is found experimentally and in agreement with the SRBRF model (Fig.1.30(b)).

However, it is worthwhile noting that although the SRBRF can accurately reproduce [91] the aforementioned crossovers from paraelectric to glassy state (upon cooling in zero electric field) and from a glassy state to an inhomogeneous random-field-modulated ferroelectric state (in the presence of an external field exceeding the critical value E_c), since it is based on the reorientable polar cluster picture, it doesn't account for the underlying perovskite structure (directional anisotropy) of the system.

1.3.3.2 Coupled spherical pseudospin-phonon model

Motivated by recent investigations demonstrating the pressure induced crossover from ferroelectric to relaxor behavior [104, 105], occurring in PLZT for example, Blinc *et al.* [103], extended the SRBRF model so as to account for the coupling to the lattice. The physical explanation for this crossover is to be found in the pressure dependence of the soft-mode frequency ω_s, or equivalently, the pressure dependence of the polarizability of the host lattice ε',

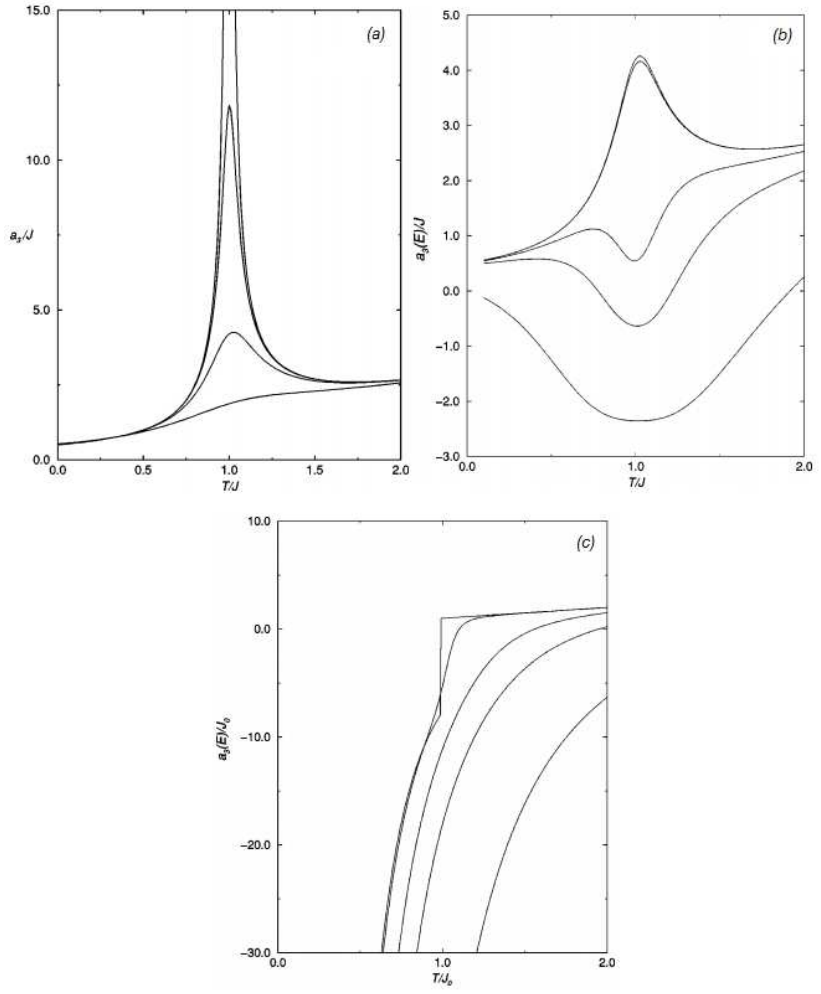

Fig. 1.30: *(a)*: Scaled third-order nonlinear response a_3 in the spherical-glass (SG) phase ($J_0 = 0$) as a function of temperature, plotted for various values of the random-field strength Δ. Top to bottom: $\Delta/J^2 = 0$, 0.001, 0.01, 0.1. If $\Delta = 0$, corresponding to a pure SG, a_3 diverges at the freezing temperature J/k. For $\Delta \neq 0$ the denominator in Eq.(1.44) never vanishes, the divergence is suppressed. For $\Delta/J^2 \ll 1$, a_3 shows a sharp peak around J/k. This peak broadens at $\Delta/J^2 \geq 0.1$ and ultimately disappears for larger Δ/J^2. *(b)*: Temperature and field dependence of the nonlinear response $a_3(E)$ in the SG phase ($J_0 = 0$) and for fixed value of $\Delta/J^2 = 0.01$. Top to bottom $E/J = 0$, 0.01, 0.1, 0.2, 0.5. With increasing field strength the peak in a_3 gradually disappears. (This effect is similar to that occurring when the value of Δ is increased) *(c)*: Temperature and field dependence of the nonlinear response in the FE in random fields phase ($J = 0$)and for fixed $\Delta/J_0^2 = 0.01$. Top to bottom $E/J_0 = 0$, 0.01, 0.1, 0.2, 0.5.a_3 remains finite as $T \to T_c$, but makes a jump at T_c in accordance with mean-field theory. In contrast to the SG case, a_3 in a random-field frustrated ferroelectric does not show any anomalous peak.(After Pirc *et al.* [98])

since both quantities are related by the relation $\omega_s^2(T)\varepsilon'(T)$ =constant. Since $r_c \propto 1/\omega_s$, the increase of ω_s with pressure causes a decrease in the correlation length r_c, upsetting the balance between long and short range forces.

Since the nanoregions are dispersed in a deformable lattice, Blinc *et al.* added the lattice

(phonon) contribution $\mathcal{H}_L$ and the pseudospin-polar phonon coulping term $\mathcal{H}_{SL}$ to the Hamiltonian given by Eq.(1.38). The total Hamiltonian of the coupled SRBRF-phonon system is formally written as:

$$\mathcal{H} = \mathcal{H}_S + \mathcal{H}_L + \mathcal{H}_{SL} \tag{1.45}$$

where

$$\mathcal{H}_L = \frac{1}{2}\sum_{\vec{k}p}\left[\omega^2_{\vec{k}p} Q_{\vec{k}p} Q_{-\vec{k}p} + P_{\vec{k}p} P_{-\vec{k}p}\right] \quad \text{and} \quad \mathcal{H}_{SL} = \sum_{\vec{k}p} Q_{-\vec{k}p}\vec{\gamma}_{\vec{k}p}.\vec{S}_{\vec{k}} \tag{1.46}$$

in which $Q_{\vec{k}p}$ and $P_{\vec{k}p}$ are respectively the normal coordinates and momenta of polar optic phonons with branch index p, wave vector $\vec{k}$ and frequency $\omega_{\vec{k}p}$. $\vec{\gamma}_{\vec{k}p}$ is the coupling constant, and $\vec{S}_{\vec{k}} = N^{-1/2}\sum_i \vec{S}_i \exp(i\vec{k}.\vec{R}_i)$ is the Fourier transform of the order parameter field. The main result is that the lattice coupling modifies the uncoupled interaction parameters J_0 and J to J_0^* and J^*, as follows:

$$J_0^* = J_0 + \sum_p \frac{|\vec{\gamma}_{0p}|^2}{\omega^2_{0p}} - \frac{1}{N}\sum_{\vec{k}p}\frac{|\vec{\gamma}_{\vec{k}p}|^2}{\omega^2_{\vec{k}p}} \tag{1.47}$$

and

$$(J^*)^2 = J^2 + \frac{1}{N}\sum_{\vec{k}}\left[\sum_p \frac{|\vec{\gamma}_{\vec{k}p}|^2}{\omega^2_{\vec{k}p}}\right]^2 - \left[\frac{1}{N}\sum_{\vec{k}p}\frac{|\vec{\gamma}_{\vec{k}p}|^2}{\omega^2_{\vec{k}p}}\right]^2 \tag{1.48}$$

where ω_0 is the $\vec{k} = 0$ optic phonon frequency. Blinc *et al.* then introduced the pressure dependencies of J_0^* and J^* via that of $\omega_{\vec{k}p} = \omega_{\vec{k}p}(P)$. Since the main contribution is given by the $\vec{k} = 0$ term in Eq.(1.47), and since in perovskites ω^2_{0p} linearly increases with pressure [106], the decrease in pressure of $J_0^*(P)$ is expressed as follows:

$$J_0^*(P) = J_0^*(0) - \alpha_1 P + \cdots \tag{1.49}$$

In contrast to J_0^*, the phonon contribution to $(J^*)^2$ is determined by the fluctuation of the averages over the optic-phonon branches. Because these branches are relatively flat, their weak dispersion leads to a weaker pressure dependence of $J^*(P)$ in comparison to that of $J_0^*(P)$. As in the case of the uncoupled SRBRF model, two limiting cases are reported. *(i)*: For $J_0^* < ((J^*)^2 + \Delta)^{1/2}$, a long range order can not exist and the system is in a spherical-glass phase (SG) with non-zero order parameter $q(T)$. For $\Delta = 0$, a transition from a high temperature PE phase to a SG phase occurs at J^*/k. For $\Delta \neq 0$ and $\Delta \ll (J^*)^2$ on the other hand, the sharp transition vanishes giving way to a mximum in the nonlinear susceptibility at $T_f \approx ((J^*)^2 + \Delta)^{1/2}$. *(ii)*: For $J_0^* > ((J^*)^2 + \Delta)^{1/2}$, long range order is possible and a phase transition to an inhomogeneous FE state occurs below a critical

temperature $T_c = (J_0^*/k)[1 - \Delta/((J_0^*)^2 - (J^*)^2)]$.

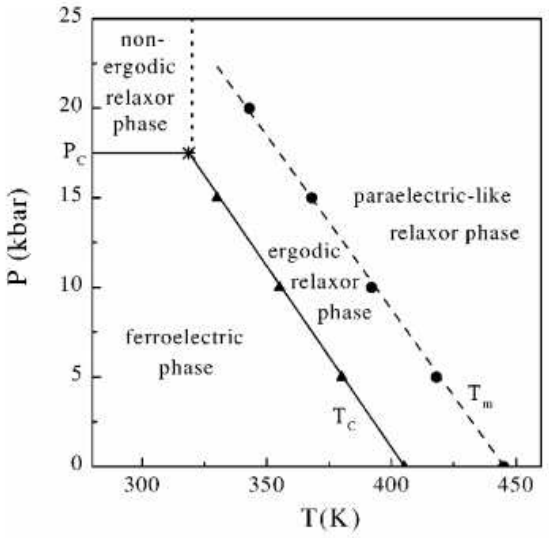

Fig. 1.31: Temperature-pressure phase diagram of the relaxor ferroelectric PLZT 6/65/35. The solid and dashed lines are evaluated from the static and dynamic coupled SRBRF-phonon models respectively, whereas the solid triangles and solid circles are experimental points obtained by Samara [104]. The horizontal line is determined by $J_0^*(P_c)$ and separates the FE phase from the nonergodic relaxor phase where the longest relaxation time diverges. The vertical dotted line corresponds to the freezing temperature T_f, where the static nonlinear permittivity has a peak. (After Blinc *et al.* [103])

Since J_0^* depends on pressure P, T_c is also a function of P. Thus the relative stability of the different phases is strongly affected by the application of an hydrostatic pressure. The model suggest that a critical pressure, P_c, given by $J_0^*(P_c) = ((J^*)^2 + \Delta)^{1/2}$, exists for which the FE order becomes unstable at any temperature, *i.e.* a ferroelectric-to-relaxor crossover occurs. The calculated pressure dependence of T_c in the range $0 < P < P_c$ is shown as a solid line representing the phase boundary $T_c(P)$ separating the ferroelectric from the ergodic relaxor phase in Fig.1.31. This line terminates at a critical point defined by P_c and the associated T_c.

It is interesting to note that Samara himself assessed the results of the coupled spherical pseudospin-phonon model contrasting its predictions with the experimental data he had gathered :

> "*It is significant that the model reproduces very well the qualitative features of the experimental data, including the vanishing of the $T_c(P)$ phase boundary at a critical point. The quantitative agreement is also very good, but perhaps a bit fortuitous given the approximations in the model and in estimating the model parameters and their dependences on pressure.*" [4]

1.4 Case of study : PLZT

Solid solutions of lead zirconate $PbZrO_3$ and lead titanate $PbTiO_3$, *i.e.*, $PbZr_{1-y}Ti_yO_3$ or PZT, represent a technologically important family of ferroelectrics and antiferroelectrics whose properties and phase transitions have been studied extensively [36]. At high temperatures these materials have the cubic perovskite ABO_3 structure, and on cooling they undergo FE and antiferroelectric (AFE) transitions to lower symmetry phases. Because the isovalent Zr^{4+} and Ti^{4+} are randomly distributed over the B lattice sites, local compositional fluctuations and strain inhomogeneities lead to some broadening of the transitions compared to the pure end members; however, there are generally no polar relaxational effects (*i.e.*, frequency dispersion) in the audio frequency range, and PZT exhibit normal, long-range FE and AFE order; the substitution of Ti^{4+} for Zr^{4+}, or vice versa, does not lead to the randomly oriented dipolar entities needed to induce relaxor behavior [4].

For practical purposes, aliovalent cations are substituted in PZT at both the A and B cationic sites. For example, La^{3+} is substituted for Pb^{2+} on the A sites to form a well-known family of ceramics referred to as PLZT that have unusual dielectric and electro-optic properties [155].

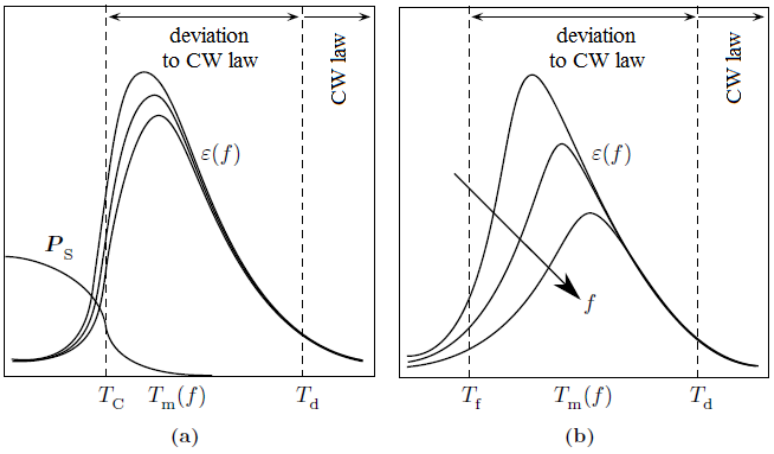

Fig. 1.32: Schematic temperature dependence of the dielectric permittivity and spontaneous polarisation, after Hirota *et al.* [3]: (a) relaxors with a diffuse relaxor-to-ferroelectric phase transition. T_C is below $T_m(f)$ and spontaneous polarisation occurs already above T_C. (b) canonical relaxors. At the Burns temperature T_d, polar regions nucleate and after growing with decreasing temperature, they freeze to a non-ergodic state at T_f. Polarisation appears only under an external electric field.

Relaxor behavior has been observed in several PLZT compositions. These materials have the chemical formula $(Pb_{1-3x/2}La_x)(Zr_{1-y}Ti_y)O_3$, where the substitution of La^{3+} for Pb^{2+} introduces one A-site-vacancy for every two La^{3+} ions, thus preserving charge neutrality. The role of La^{3+} in the development of the relaxational character is to break the translational symmetry of the polarization, either by heterogeneities in the composition or the electric field

associated with the defect structure. The net effect is that the polar behavior is localized on a scale where relaxational processes can contribute to the dielectric response [158]. Lanthanum substitution thus represents a type of disorder that can significantly modify the properties of these materials. One manifestation of this disorder is the condensation of local dipolar nanodomains leading to local, randomly oriented polarization at a temperature much higher than the ferroelectric transition temperature T_C [82]. These polar nanodomains increase in size with decreasing temperature and, for relatively low La concentration, ultimately result in the formation of macroscopic ferroelectric domains with long-range FE order. For higher La concentrations, the disorder hinders the onset of long-range order, and the polar nanodomains condense below the freezing temperature T_f of the polarization fluctuations [158] into a glasslike, or relaxor, state with no macroscopic phase (symmetry) change [4]. Thus depending on the La content, the system either exhibits a non-ergodic behaviour below a freezing temperature T_f (as in canonical relaxors such as PMN, PMT and PLZT with large x) or experiences a spontaneous structural phase transition into the FE phase (PLZT with small x) [2]. These two different paths of temperature evolution are shown schematically in Fig.1.32.

Fig.1.33 shows the room temperature phase diagram for the PLZT solution. Several features are noticeable: *i*) small variations in La content produce rather large changes in areas of phase stability, *ii*) increasing La content extends the antiferroelectric phase (AFE) over the ferroelectric (FE) phase, and *iii*) increasing La content favors the tetragonal ferroelectic phase over the rhombohedral one [155].

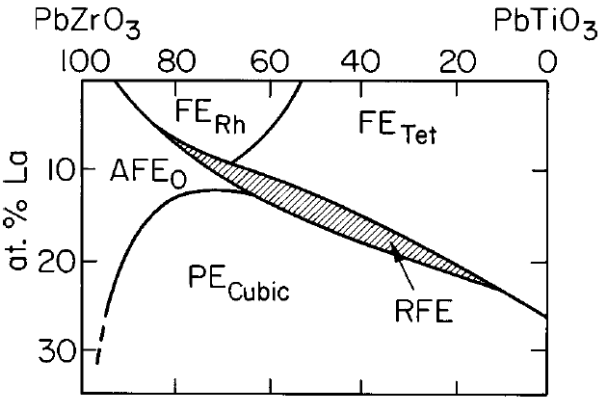

Fig. 1.33: Room-temperature phase diagram for the PLZT solution. The relaxor range is indicated by dashed lines (After Haertling *et al.* [155]).

The phase diagram as a function of temperature for various levels of La (Fig.1.34) illustrates the systematic change in Curie points for the complete system as the La content is increased. The extension of the AFE phase at the expense of the FE phase is evident, as well as the extension of the transition region to higher temperatures for varying Zr/Ti ratios [155]. Detailed studies have mainly been carried on two La-substituted PZT families:

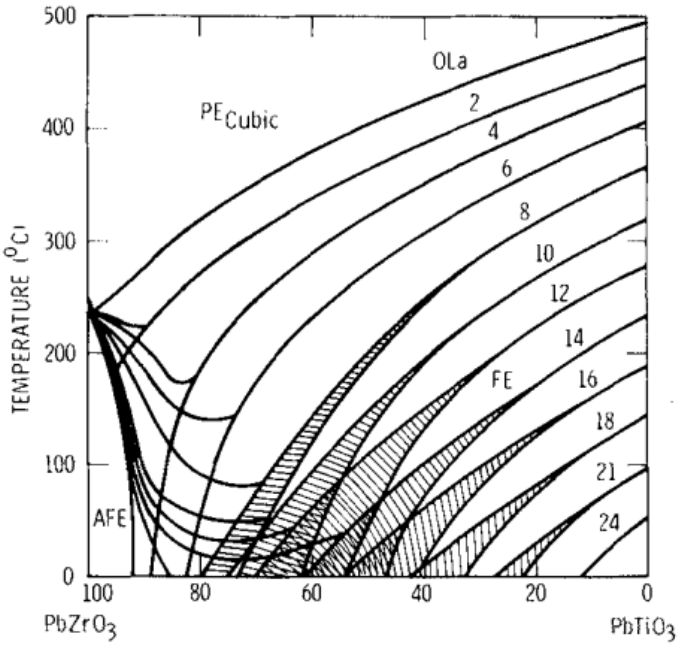

Fig. 1.34: Phase diagram of PLZT system showing constant La concentration levels (After Haertling *et al.* [155]).

- ◇ The $(Pb_{1-3x/2}La_x)Zr_{0.65}Ti_{0.35}O_3$ family denoted by PLZT $x/65/35$, where x is the mol % La. For these systems, relaxor behavior in the dielectric response becomes experimentally discernible for $x > 4\%$ [72, 156, 157] and much of the literature has dealt with compositions $4 < x < 14$ (Fig.1.33).
- ◇ The $PbZr_{0.40}Ti_{0.60}O_3$ family denoted by PLZT $x/40/60$ for which relaxor response becomes discernible for $x \geq 12$ % La [156] (Fig.1.33).

These two families represent regions of the PZT phase diagram that exhibit different crystal structures and properties. PZT 65/35 is representative of compositions on the Zr-rich side of the diagram. Here the cubic PE phase transforms on cooling into the high-temperature rhombohedral phase, the transformation accompanied by relatively little lattice strain. PZT 40/60, on the other hand, is representative of Ti-rich composition. Here the PE-FE transition is to a tetragonal FE phase, which involves relatively large lattice strain [4].

Fig.1.35 illustrates the Curie point lowering for increasing La concentration in the two series of compositions; the effect is essentially linear [155].

Relative dielectric constant as a function of temperature for compositions with 65/35 and 40/60 Zr/Ti ratios is shown in Fig.1.36. The peaks in the dielectric constant are reduced in height and in temperature as the La content is increased. For the series with 65/35 Zr/Ti ratios, a fairly consistent and gradual reduction in the Curie point occurs up to La concentrations of 4 at.% or less. Higher concentrations of La reduce the height of the dielectric constant peak, making it more diffuse, without significantly changing the temperature of the

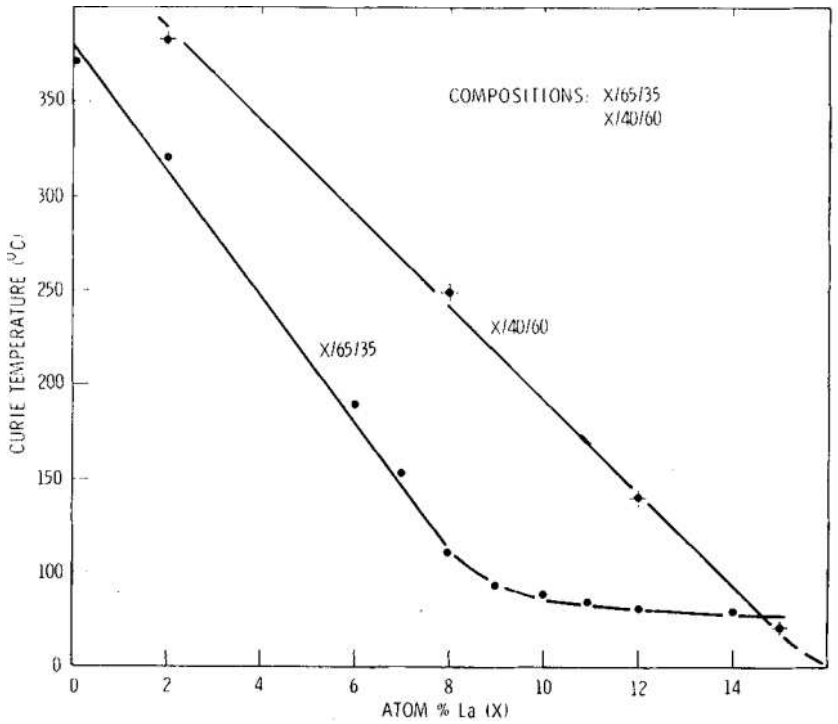

Fig. 1.35: Curie point lowering with incresing La content (After Haertling *et al.* [155]).

peak. This change in behavior between 8 and 9 at.% La may indicate that mixed FE/cubic phases are present on a microscopic or macroscopic scale [155].

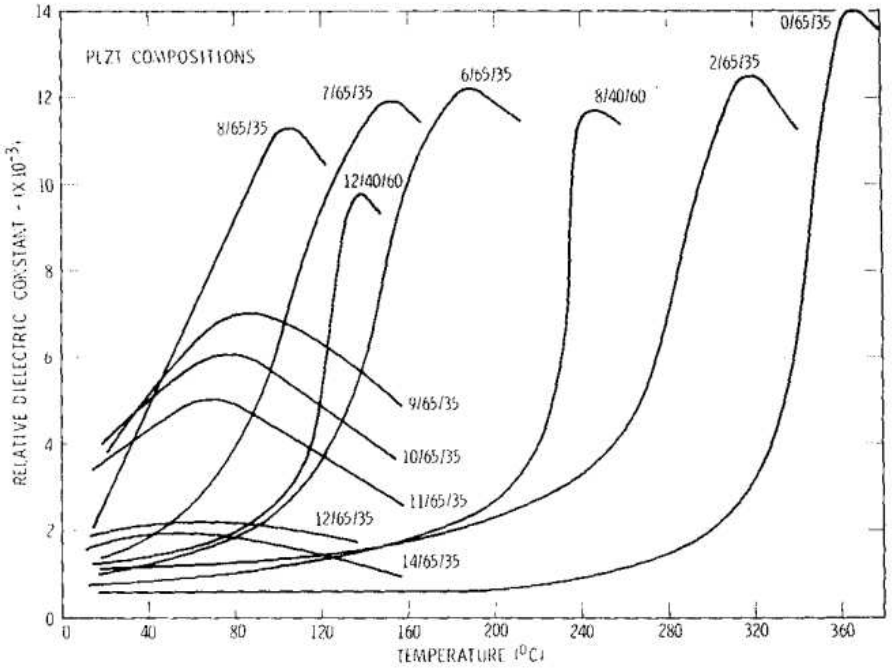

Fig. 1.36: Dielectric constant as a function of temperature (After Haertling *et al.* [155]).

1.4.1 PLZT x/65/35

On the basis of dielectric and internal friction measurements with and without bias on different compositions in the PLZT x/65/35 family, Viehland *et al.* [158] proposed the phase diagram shown in Fig.1.37. It shows that the relaxational character of the response becomes noticeable between 4 and 5 % La, as illustrated by the vertical dashed line in the diagram.

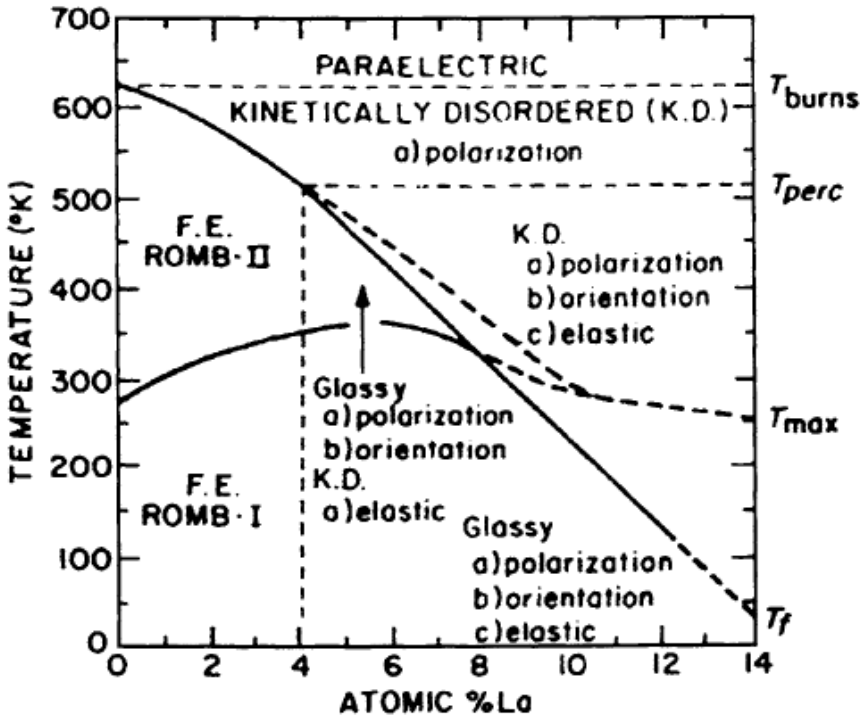

Fig. 1.37: Dielectric constant as a function of temperature (After Viehland *et al.* [158]).

The Burns temperature, T_d, which denotes the temperature at which dipolar clusters first begin to nucleate, is shown by the dashed horizontal line at 623 K. This is effectively the FE Curie temperature of the La-free composition, *i.e.*, PZT 65/35, and it is essentially independent of La content [82] (see Fig.1.38). Viehland *et al.* suggest a lower temperature percolation limit may be reached when the host matrix can start to deform in response to the polarization fluctuations; consequently, the orientation of the electrostrictive strain may begin to fluctuate. An isothermal dashed line at $\sim$ 510 K labeled T_{perc} is shown on the diagram. Although there is some evidence for this boundary, [158] its existence is not established [4]. The T_m (at 10^2 Hz) versus La content boundary is shown by a heavy dashed line, and the Vogel-Fulcher freezing temperature T_f, is denoted by a solid line. This freezing temperature is shown to approach 0 K near 14 % La, close to the composition at which the local structure is believed to be cubic. Two rhombohedral FE phases are shown. These are the well-known rhombohedral phases found in Zr-rich PZT compositions. On cooling these PZT compositions, as well as PLZT compositions with low La content, from the high-temperature cubic PE phase, the material first transforms to the FE rhombohedral phase II

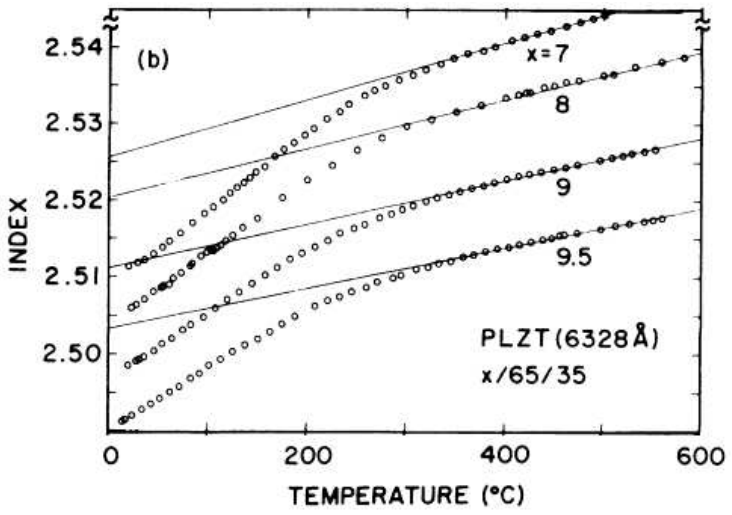

Fig. 1.38: Index of refraction versus temperature $n(T)$ for different La concentration x/65/35 as measured at 6328 Å. The high temperature part can be approximated by a straight line, and the value of T_d, temperature at which the deviation from the straight line occurs, are about the same for the investigated compositions $\sim$ 623 K (After Burns *et al.* [82]).

(space group $R3m$) which in turn transforms to the FE rhombohedral phase I (space group $R3c$) on further cooling. This transformation is driven by the softening of a zone boundary phonon at the R point of the ABO_3 Brillouin zone [4] and results in a doubling of the unit cell in phase I. In Fig.1.37 this rhombohedral-rhombohedral phase boundary is seen touching the T_f boundary at 8 % La and the T_m boundary at 10 % La. The region between T_d and T_{perc}, is shown to have fluctuations of only the polarization, whereas between T_{perc} and T_f, there are fluctuations in polarization, local electrostrictive strain fields, and the tilt of the oxygen octahedra. The region defined by the T_f phase line and the rhombohedral-rhombohedral phase boundary for $x > 4\%$ La, is shown to have fluctuations in the tilting of the oxygen octahedra, but the polarization and the electrostrictive strain are frozen. Finally, the region defined by the T_f phase line and the rhombohedral-rhombohedral phase boundary between 4 and 8 % La is shown to have all the fluctuations, polarization, strain, and tilt, frozen [4, 158].

The physics of the relaxor behavior and the spontaneous relaxor to FE (R-to-FE) transition is not well understood. Whereas the usual manner of studying these properties has been to vary the composition and degree of disorder in order to induce relaxor behavior, Samara [104] has suggested the use of hydrostatic pressure as a probing tool of the underlying physics. He considered that, in contrast to composition variation that introduce complications such as added randomness, compositional fluctuations, lattice defects, and changed interatomic forces leading to vagueness in interpretation, hydostratic pressure stands a cleaner variable, in the sense that the application of pressure to a sample of fixed composition only varies the interatomic interactions and balance between long and short range interactions.

The left panel of Fig.1.39 shows the temperature evolution of the dielectric constant and the

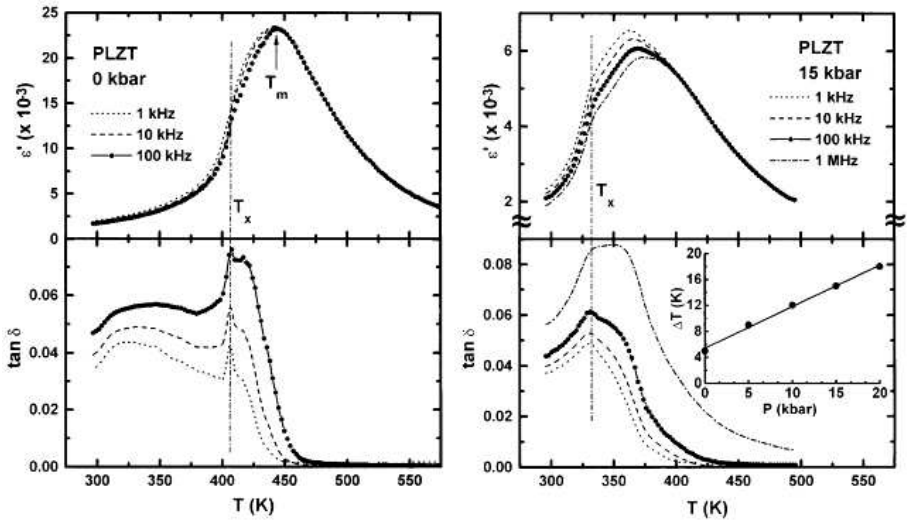

Fig. 1.39: *Left panel*: Temperature and frequency dependences of the dielectric constant and the dissipation for PLZT 6/65/35 at 1 bar (0 kbar). *Right panel*: Temperature and frequency dependences of the dielectric constant and the dissipation for PLZT 6/65/35 at 15 kbar. The inset shows the increase in the frequency dispersion in T_m with pressure (After Samara [104]).

dissipation for PLZT 6/65/35 at 1 bar (0 kbar) at different frequencies. Starting in the PE phase, the dielectric constant increases with decreasing temperature in a Curie-like manner and exhibits a maximum at the expected PE-FE transition temperature, here denoted by T_m. The dielectric constant is frequency independent in the PE phase, and its magnitude at T_m is also essentially independent of frequency. T_m exhibits weak dispersion having a value of 442 K at 10^2 Hz and increasing to 447 K at 10^6 Hz with most of this increase occurring above 10^4 Hz. On further cooling below T_m, there is some dispersion in the magnitude of the dielectric constant, primarily above 10^4 Hz. This dispersion becomes considerably smaller below a spontaneous R-to-FE transition denoted by T_x and manifested by a sharper drop in the dielectric constant and a sharp frequency-independent peak in the dissipation response.

Pressure causes large decreases in the amplitude of the dielectric constant anomaly at T_m and in the transition temperatures and induces full relaxor character for the PE-R transition by 5 kbar, in essence a FE-to-R crossover. The right panel of Fig.1.39 shows that at 15 kbar, T_x remains frequency independent, but there is increased dispersion in the dielectric constant at $T \leq T_x$ compared with the response at lower pressures. Taking the difference, ΔT, in T_m between 10^6 and 10^2 Hz as a measure of the dispersion in T_m, the inset shows the change in ΔT with pressure.

Fig.1.40 shows the shifts in T_m and T_x with pressure measured at 10^5 Hz. Within experimental uncertainty, T_m and T_x have the same slope, namely, $\mathrm{d}T_{m,x}/\mathrm{d}P = -5.2 \pm 0.2$ K /kbar, a value comparable to that for many perovskite ferroelectrics. Note that Fig.1.40 shows the pressure dependence of T_m at one frequency, T_m is, of course, frequency dependent, but its pressure derivative is only weakly dependent on frequency [4]. Moreover, the R-FE phase

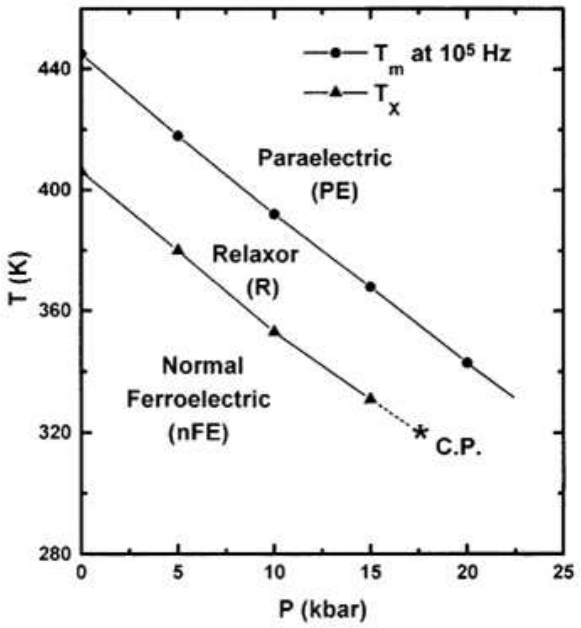

Fig. 1.40: Temperature-Pressure phase diagram of PLZT 6/65/35 (After Samara [104]).

boundary terminates in a critical point (CP), a point that should thermodynamically be equivalent to the liquid-gas critical point in fluids. For a solid, a CP can exist only if the two phases separated by the phase boundary have the same internal symmetry. In PLZT, the R phase, as determined by X rays, is macroscopically cubic, whereas the FE phase is rhombohedral. Thus the likely explanation is that whereas the macroscopic symmetry of the R phase is cubic, at the polar nanodomain level the symmetry is rhombohedral making a CP possible [4, 104].

The physics underlying this pressure induced FE-to-R crossover can be understood in terms of soft mode theory. The decrease of ω_s with decreasing T in the PE phase causes the polarizability of the lattice, and thereby the correlation length (or radius r_c) for polar fluctuations, which is inversely related to ω_s, to increase rapidly as $T \rightarrow T_C$. Because ω_s is determined by a delicate balance between long range and short range interactions, it is very strongly pressure (or volume V) dependent. A measure of this dependence is the soft mode Grüneisen parameter $\gamma = -(\partial \ln \omega_s / \partial \ln V)_T = 1/2(\partial \ln \varepsilon / \partial \ln V)_T$. γ is thus the ratio of the fractional change in ω_s to the fractional change in volume. For odinary dielctrics γ for TO phonons is of the order of 1-2 and very weakly temperature dependent. However, for soft TO mode systems, such as PLZT x/65/35 and PLZT x/40/60, γ is very large and strongly temperature dependent, approaching values of several hundred near T_C [104].

1.4.2 PLZT x/40/60

The dielectric studies performed on PLZT x/40/60 cover the range $0 < x < 21$ % La [156]. Fig.1.41 shows the dielectric response as function of temperature in zero field for three compositions of La. The PLZT 8/40/60 response is characteristic of that of a FE ceramic. There is essentially no frequency dispersion in T_C or in ε' and the rounding of the $\varepsilon'(T)$ peak is due to compositional heterogeneities. The 15/40/60 composition, on the other hand, exhibits classic relaxor response. The intermediate composition 12/40/60 displays the following features. On ZFC the sample first enters a relaxor state with strong dispersion and then undergoes a spontaneous R-to-FE transition at T_x with weak dispersion. The transition is reversible on ZFH but exhibits a large thermal hysteresis signifying its first-order character [156]. This transition in the absence of bias also occurs in PLZT 6/65/35 under zero bias and in PMN and other relaxors under bias [4].

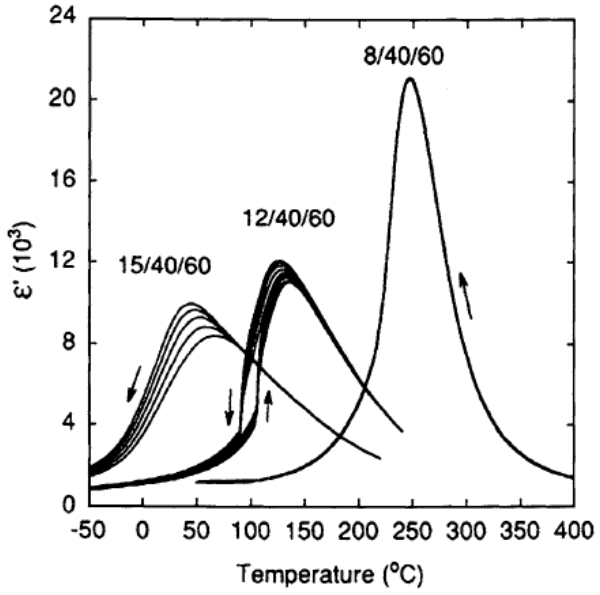

Fig. 1.41: The dielectric response of PLZT x/40/60 for x = 8, 12 and 15 % La, showing the composition-induced crossover from normal ferroelectric to relaxor behavior. (After Dai *et al.* [156]).

There is a remarkable similarity between the results in Fig.1.41 and those in Fig.1.39 for PLZT 6/65/35. In Fig.1.41 the FE-to-R crossover is induced by changing La content at 1 bar. Near the crossover concentration a spontaneous, first-order FE-R transition occurs. The transition vanishes for higher x. In Fig.1.39, on the other hand, the FE-to-R crossover is induced by hydrostatic pressure for a fixed La composition. At intermediate pressures a spontaneous, first-order FE-R transition occurs. This transition vanishes at higher pressures. This analogy between increasing La content and increasing pressure is significant for the mechanisms of the FE-to-R crossover in the FE ABO_3 oxides.

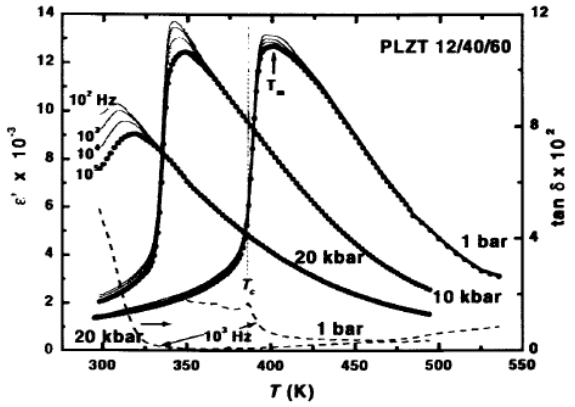

Fig. 1.42: Dielectric response of PLZT 12/40/60 showing the pressure induced FE-R crossover (After Samara [4]).

Pressure studies have been performed on PLZT 12/40/60 [104]. This composition was chosen because it is near that at which the FE-R crossover occurs at 1 bar, making it possible to observe the pressure-induced crossover at a readily accessible hydrostatic pressure (Fig.1.42). As for PLZT 6/65/35 described earlier, among the most interesting pressure effects on PLZT 12/40/60 are the following: *i*) a FE-to-R crossover and stabilization of the R phase, *ii*) continuous evolution of the energetics and dynamics of the relaxation process, and *iii*) the suppression of the spontaneous FE-R transition with indications that it might vanish at a pressure somewhat higher than the 20 kbar achieved in the study [4]. The dielectric response in Fig.1.42 shows the pressure-induced FE-to-R crossover. Only ZFH results are shown. At 1 bar the response is characteristic of a normal FE with a first-order FE-PE phase transition. The finite width of the transition at T_C, and the rounding of the $\varepsilon'(T)$ peak normally are features of ceramic samples, but in the present case the rounding also points to the early onset of some relaxor character. Pressure strengthens the relaxor character at a pressure higher than 10 kbar, and at 20 kbar and higher pressures, the sample exhibits classic relaxor character [104].

Left panel of Fig.1.43 shows the deviation from Curie-Weiss ($1/\varepsilon'(T) \sim (T - T_C)$) behavior above T_m in the PE phase. The onset of the deviation occurs at T_d temperature at which polar regions form and grow [4, 82]. The right panel of Fig.1.43 illustrates the strong influence of pressure on the r_c. The results were deduced from the pressure and temperature dependencies of the dielectric response, thus the absolute value of r_c cannot be accessed, but only relative changes in this quantity. The 1-bar results show the large increase in r_c with decreasing temperature, a remarkable feature of the soft mode response of the system. The decrease of r_c with pressure is nonlinear and explains the FE-to-R crossover [4, 104].

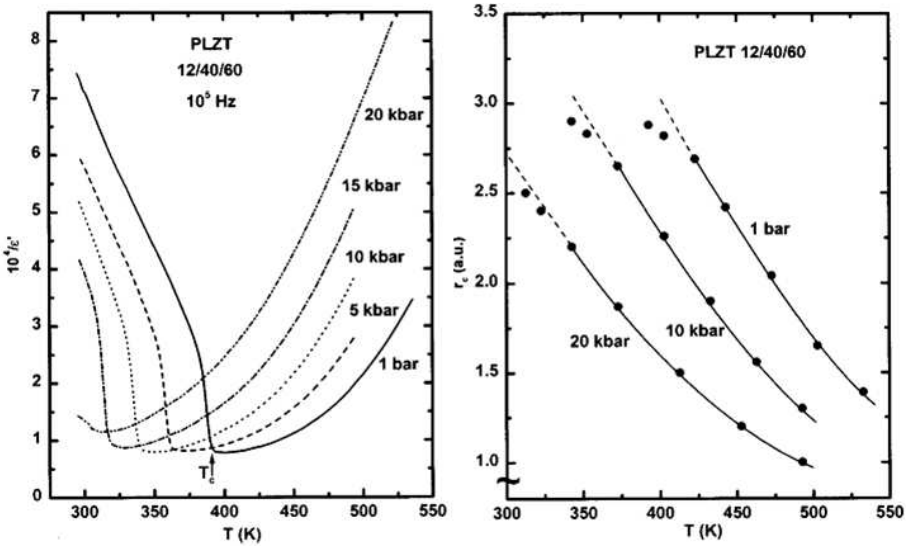

Fig. 1.43: *Left panel*: Temperature dependence of the reciprocal of $\varepsilon'(T)$ of PLZT 12/40/60 measured at 10^5 Hz and different pressures. The location of the structural phase transition is denoted by T_C for the 1-bar response. *Right panel*: Variation of the correaltion radius (in arbitrary units) for polarization fluctuations with temperature for PLZT 12/40/60 (After Samara [104]).

Chapter 2

Gauge approach for relaxors

This chapter is concerned with providing the conceptual foundations and framework for a gauge theory for relaxors, and is subdivided into two main parts. The first part serves the purpose of introducing the common concepts and methods underlying various related gauge approaches. The second part leverages on the first one and proceeds to applying and implementing the concepts related to gauge theories to the case of relaxor ferroelectrics.

2.1 A few landmarks on gauge theories

2.1.1 Introduction: Local symmetry and Gauge fields

Modern theories of fundamental interactions are gauge theories [179]. Roughly speaking, these field theories promote global symmetries to local ones and as will be seen further, express a central hypothesis of physics, namely that there is a flexibility in the local representation of nonlocal aspects of interactions. This flexibility denotes nothing but the robustness of a physical phenomenon, which should be the same independently of any choice of convention. In order for a theory to be a field theory, the dynamical degrees of freedom taking values in some internal space at each point $\phi(x)$ need to be coupled through nonlocal terms (of the form $\phi(x)\phi(x+\delta x)$), without which each point would have dynamic independent of its neighbors, and any symmetry, global $\phi(x) \mapsto e^{\alpha}\phi(x)$ or local $\phi(x) \mapsto e^{\alpha(x)}\phi(x)$, operating in the internal space would yield trivial consequences. These internal symmetries can be thought of as a change in the internal space basis [180]. Whereas the nonlocality of interactions is immune to global internal symmetry affecting all points in an equivalent manner, thus corresponding to a global redefinition of basis, the consideration of local symmetry on another hand, allowing independent choices of basis at each point, requires the introduction of a compensating external field, the gauge field, needed to compensate out the contributions of the inhomogeneous conventions at different points. Since two internal space variables residing at

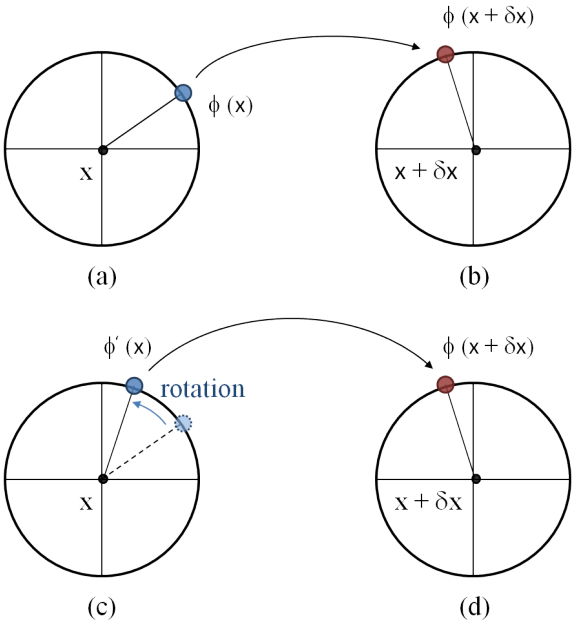

Fig. 2.1: An internal symmetry space is attached to each point x in space. In the case of the U(1) local symmetry group, the internal symmetry space consists of all possible values of the phase of ϕ, and can be represented by the unit circle, points of which are the phase value. A particular field configuration $\phi(x)$ means a choice of one point on each circle attached to each point in space. For instance, in Figures (a) and (b) the phase values taken by ϕ at points x and $x + \delta x$ are indicated by dots on the unit circle. There is a rule to take a point $\phi(x)$ and parallel transport it to an infinitesimally neighboring point $\phi(x + \delta x)$. The gauge connection exactly specifies how a certain point $\phi(x)$ is mapped into another point $\phi(x + \delta x)$. The gauge connection is illustrated by the arrow between Figures (a) and (b). Local symmetry thus turns the phase into a local variable. The invariance under local transformations, i.e. the freedom to choose any value or convention for the phase (*i.e.*, any point on the circle), is ensured by a compensating change in the connection. Thus, if one phase is rotated, such as Figure (c) with respect to Figure (a), the rotated point, $\phi'(x)$, should still map the same neighboring point $\phi(x + \delta x)$, which demands a change in the connection, as represented by a new arrow between Figures (c) and (d) (after Moore [178]).

two different locations can not be compared in their natural bases, the gauge field acquires an intrinsic geometrical role enabling the comparison by means of parallel transportation, a generalization of the construction of the covariant derivative (Fig. 2.1). Measurable quantities are independent of the choice of basis for the field variable, therefore they must be gauge invariant and in their most general form, gauge theories consist of a matter-field ϕ coupled to a gauge field A which mediates interactions[15].

The principle of gauge invariance is strongly associated with general relativity as it was derived as an extension of the general covariance under continuous reparametrizations of space-time. It was first introduced by Weyl [159] in field theory, in an attempt to describe gravitation and electromagnetism within a unifying geometrical framework. In particular, considering scale of length a local property of the metric, he proposed a so-called purely infinitesimal geometry, which stands as a generalization of Riemannian geometry. He required

a twofold invariance, supplementing the general covariance with *gauge* scale invariance. Scale invariance refers to invariance under a scale change of the metric tensor and is encoded by the substitution $g_{\mu\nu}(x) \to \lambda(x) g_{\mu\nu}(x)$, where the conformal[1] factor $\lambda(x)$ is an arbitrary, positive smooth function of position. Although this theory is generally deemed to have failed in its original form, it nevertheless defined the anchoring points for later success in the context of field theory. In particular, London [160] proposed a quantum mechanical interpretation of Weyl's proposal, by noticing its equivalency to the invariance of the wave equation, provided that $\lambda(x)$ was made imaginary. Weyl himself reinterpreted his original theory[161], this latter time emphasizing the role of gauge invariance as a constructive principle from which electromagnetism can be derived [162–164]. The gauge principle was later extended beyond the scope of quantum electrodynamics (QED of Abelian gauge group U(1)) to non-Abelian symmetries (Yang-Mills theories) and gauge theories have been proposed as fundamental theories of the so-called weak and strong interactions, with non-Abelian gauge group SU(2) and SU(3), respectively. The latter is quantum chromodynamics (QCD) which describes the strong interactions between the quarks (the constituents of hadronic matter) which are mediated by gluons [163, 164].

The concept of a gauge field in general has been extensively discussed in condensed matter physics, especially, in relation with modeling different types of topological defects, phase transitions, and properties of glasses. As pointed out in the previous chapter, in spite of numerous experimental investigations and theoretical formulations, the microscopic origin of the relaxor behavior remains a matter of fruitful debate. In many solid materials, where intrinsic quenched randomness exists in form of defects, impurities or as a general structural property, the disorder stemming from spatial heterogeneities is an integral part of their characteristics. Indeed, and since the discovery of relaxors [165], recurrent emphasis have been made on the role of disorder in inducing complex nanostructure [2, 5, 99, 152, 166–169], altering the stability of the low-temperature phase and driving their characteristic behavior. It is generally accepted that intrinsic inhomogeneity and hierarchical organization of relaxors strongly affect translational and rotational symmetries at a local scale, whereas global symmetries hardly change[170]. Therefore, the relaxor state is robust to local environment variations. As we shall later explicit, the non-trivial interplay between local and global scales can be captured within the framework of the *local gauge symmetry* [15, 16], which is known to provide a solid basis for describing defects and their interactions[17].

For the sake of sustaining the intuition of a gauge model for relaxors and establishing connections with related successful gauge descriptions, we will briefly review the occurrence of gauge symmetries in physics and geometry, such in:

[1] A conformal map is a function which preserves angles.

- ◇ scalar electrodynamics, where gauge theory finds its root and where the local phase symmetry gives rise to the electromagnetic interaction [171]. This part focuses on continuum gauge theories, as a preliminary step in dealing with the lattice case.

- ◇ lattice gauge theories, originally developed by Wegner [14] for the study of phase transitions without a local order parameter[2], and later used by [186] in their modern form, as a non perturbative regularization of a gauge theory, in connection with the problem of quark confinement in quantum chromodynamics (QCD). The lattice formulation revives the geometrical implications of gauge theories, for which it provides a natural framework. Indeed, remembering that the geometric role of the gauge potential is to specify the rotation of the reference frame in some internal symmetry space as one moves between nearby points in space, the continuum of points is replaced by the sites of a lattice, and the elementary displacements become those between neighboring sites, i.e., along the links of the lattice itself [16].

- ◇ spin-glasses (RBs models), where local gauge symmetry leads to the concept of gauge-invariant frustration, which in turn leads to a substantial analysis of disorder, in that it topologically discriminates between two types of disorder, namely, the so-called serious, or relevant disorder in contrast with the deceptive, trivial one [20, 190, 201, 204].

- ◇ gauge theoretical formulation of the defect theory in an elastic continuum[17], where nonintegrable deformations are incorporated by demanding invariance of the elastic Lagrangian under the local action of the Euclidean group SO(3)▷ T(3)[3] . Within this picture, dislocations arise from the inhomogeneous action of the group of translations, T(3), while the disclinations owe their origin to the action of the rotation group, SO(3).

This section does not pretend to be a review of the topic, and aims only at introducing some coherence among various related ideas, as they form the conceptual ground on which our approach stands.

2.1.2 Continuum gauge theories

Global symmetries (*e.g.* space groups) are not the most general form of invariance. The invariance principle would be stronger if it was possible to extend global symmetries to local, so-called gauge symmetries, where the transformation parameter would be dependent on spacetime. Symmetry transformations which are spacetime dependent are called local gauge transformations. Local gauge symmetry imposes constraints on the action, determining the

[2] A local order parameter, *e.g.* magnetization M, is obtained by averaging the local variables m_i over the volume.

[3] The Euclidean group is the set of all distance-preserving transformations of the Euclidean space. It is isomorphic to a semidirect product of the T(3) group (which describes translations) and the group SO(3) of orthogonal 3×3 matrices (which describes rotations).

interaction. In order to exemplify how local symmetry dictates the form of the interaction, it is instructive to examine the gauge invariance in electromagnetism, where local symmetry finds its root.

2.1.2.1 From a symmetry principle to a Lagrangian

Let us begin for simplicity with a complex scalar field $\phi(x)$. Let $\mathcal{L}\{\phi, \partial\phi\}$ be its Lagrangian density, which is a functional of the fields $\{\phi\}$ and their derivatives $\{\partial\phi\}$. A fundamental quantity common to any quantum field theory is the action, given by the time integral of the Lagrangian L, which is in turn given by the space integral of the Lagrangian density $\mathcal{L}$

$$S = \int_{-\infty}^{+\infty} L\mathrm{d}t = \int \mathrm{d}^4x \mathcal{L}\{\phi, \partial\phi\} \tag{2.1}$$

The equations of motion are derived by means of Hamilton's principle of stationary action:

$$\delta \int_{t_1}^{t_2} L\mathrm{d}t = 0 \tag{2.2}$$

Equation (2.2) implies that the Lagrange density must obey Euler's equations

$$\frac{\delta\mathcal{L}}{\delta\phi} = \partial_\mu \frac{\delta\mathcal{L}}{\delta(\partial_\mu\phi)} \tag{2.3}$$

As an example let us construct a field theory which is invariant under local phase transformations. Our starting point is the Lagrange density of a non-interacting complex scalar field given by:

$$\mathcal{L}\{\phi, \partial\phi\} = \frac{1}{2}\left[(\partial^\mu\phi^\star)(\partial_\mu\phi) - m^2\phi^\star\phi\right] \tag{2.4}$$

where m is the mass of the spinless particles associated to the quanta of the field. The Euler equation of motion for the field ϕ is the Klein-Gordon equation[4], which describes the quantum wave mechanics of spinless particles of mass m.

$$(\partial_\mu\partial^\mu + m^2)\phi \equiv (\Box + m^2)\phi = 0 \tag{2.5}$$

Global U(1) symmetry In order to assess the implications of symmetries of the Lagrangian, let us first see the case of a global U(1) symmetry. Consider the transformations

[4]In component form, the Klein-Gordon equation is expressed as $(\frac{\partial^2}{\partial t^2} - \nabla^2 + m^2)\phi = 0$ which, for $m = 0$, reduces to the standard wave equation. Performing the usual identifications $i\frac{\partial}{\partial t} \to E$ and $-i\nabla \to \mathbf{p}$, the Klein-Gordon equation follows from the relativistic kinematic conservation requirement $E^2 - \mathbf{p}^2 = m^2$.

of the fields ϕ under:

$$\phi(x) \mapsto e^{-iq\theta}\phi(x) \qquad \phi^\star(x) \mapsto e^{+iq\theta}\phi^\star(x) \tag{2.6}$$

where q is to be associated with the charge of the ϕ field and θ parameterizes the transformations. Since θ is independent of x, the Lagrangian density equation (2.5) is invariant under this set of rigid, or global, internal transformations, which form the group of unitary transformations U(1)[5]. In this case the U(1) symmetry expresses a redefinition of the phase factor convention for the ϕ field. The invariance under rigid transformations is ascribed to a degeneracy of certain degrees of freedom. Since the phase of the field ϕ is not an observable quantity, adding a constant θ to it merely redefines the phase convention, without affecting the predictions made by the theory. However, there is a priori no reason to require a transformation equivalently affecting all points in space, and a "rigid" transformation of the form $\phi(x) \mapsto e^{i\theta}\phi(x)$ is certainly not the most general. The question then arises as to how one can extend the global symmetry to a local one [6].

Local U(1) symmetry and interaction law To that end, one is thus led to consider theories which are invariant under symmetry operations performed *locally*, by allowing θ to vary over space, becoming $\theta(x)$. The extension of the invariance principle from global to local means that the Lagrangian (2.4), which was conserved under the global transformation (2.6), should also be invariant under the local transformation[7]:

$$\phi(x) \mapsto \phi(x)e^{-iq\theta(x)} \tag{2.7}$$

By insisting on the freedom to change fields by an arbitrary group transformation at each space-time point separately, it turns out that one needs a quantity that can carry information regarding these transformations from one space-time point to another. This quantity is the gauge field, whose existence can be regarded as a prime consequence of choosing a framework based on local gauge invariance. Explicitly, whereas the local aspect of the transformation does not alter the mass term which only involves fields taken at the same point in spacetime,

$$m^2\phi^\star(x)\phi(x) \mapsto m^2\phi^\star(x)\phi(x)\,, \tag{2.8}$$

[5]The family of transformations $U(\alpha) \equiv e^{i\alpha}$, where α may assume any real value, constitutes the unitary Abelian group, called U(1). Unitary groups satisfy the condition $U^\dagger = U^{-1}$ and Abelian groups have the property of commutativity under group multiplication $U(\alpha_1)U(\alpha_2) = U(\alpha_2)U(\alpha_1)$. One can think of the group U(1) as the unit circle, with the multiplication rule on its points given by addition of angles. Let us note in passing that SO(2) is Abelian and isomorphic to U(1).

[6]Note that in this example we are dealing with internal symmetries, since they do not involve any change in the space coordinate of the fields.

[7]From a geometric point of view, defining the phase of $\phi(x)$ locally is equivalent to defining a local frame with respect to which the phase of the field is measured. The gauge group thus defines an internal space, and local invariance is then the statement that the physical properties of the system must be independent of the particular choice of frame [15].

terms involving the gradients $\partial_\mu\phi$ of the ϕ fields on the other hand, are not invariant since under (2.7) their transformation yields:

$$\partial_\mu\phi \mapsto [\partial_\mu\phi(x) - iq\partial_\mu\theta(x).\phi(x)]\, e^{-iq\theta(x)} \tag{2.9}$$

Clearly, $\partial_\mu\phi$ does not have the same transformation rule as ϕ itself. For these terms the local character of the transformation is crucial, gradients which intrinsically compare fields at different points in spacetime will be subject to transformations at neighboring spacetime points. To compensate this lack of invariance, one can resort to the introduction of a compensating gauge field A_μ (which is later to be identified with the electromagnetic potential), whose variation will compensate for the supplemental $\partial_\mu\theta(x)$ terms in (2.9), that are induced by the transformations at neighboring spacetime points and proportional to the derivative of the transformation parameter. The usual procedure, referred to as minimal gauge coupling, consists in the replacement of the gradient operator ∂_μ in the Lagrangian density with a so-called covariant derivative D_μ :

$$\mathrm{D}_\mu \equiv \partial_\mu - iqA_\mu(x) \tag{2.10}$$

where A_μ is still to be defined by its transformation properties. The prescription of a covariant[8] transformation of D_μ operating on the field ϕ, *i.e.*, the requirement that this new quantity exhibits the same transformation law as that of equation (2.7) in order to ensure local invariance yields:

$$\mathrm{D}_\mu\phi(x) \mapsto e^{-iq\theta(x)}\mathrm{D}_\mu\phi(x) \tag{2.11}$$

which in turn requires the following local gauge transformation rule for the newly introduced gauge field A_μ

$$A_\mu(x) \mapsto \partial_\mu\theta(x) + A_\mu(x) \tag{2.12}$$

Therefore the modified Lagrangian takes the form $\frac{1}{2}\left[(\mathrm{D}_\mu\phi)^\star(\mathrm{D}^\mu\phi) - m^2\phi^\star\phi\right]$, and remains invariant under the local gauge transformation given by equations (2.11) and (2.12). One should also account for the pure gauge field contribution by including terms in the Lagrangian density which couple A_μ only to itself. One quantity involving only the A_μ is the antisymmetrical field strength second rank tensor

$$F^{\mu\nu} = \partial^\mu A^\nu - \partial^\nu A^\mu \tag{2.13}$$

[8]The term covariant refers to covariance with respect to the introduction of the local transformation of equation (2.7), and not to covariant-contravariant indices.

which is invariant[9] under the gauge transformation in equations (2.11) and (2.12). Consequently, the complete expression for the gauge invariant Lagrangian density is:

$$\mathcal{L}_{\text{local}} = \frac{1}{2}\left[(\mathrm{D}_\mu\phi)^\star(\mathrm{D}^\mu\phi) - m^2\phi^\star\phi\right] - \frac{1}{4}F_{\mu\nu}F^{\mu\nu} \tag{2.14}$$

where the last term is recognizable as that of pure electromagnetism $-\frac{1}{4}F_{\mu\nu}F^{\mu\nu} = \frac{1}{2}(\mathbf{E}^2 - \mathbf{B}^2)$. Thus $\mathcal{L}_{\text{local}}$ is the standard form of the Lagrange density of scalar electrodynamics, and equations (2.11) and (2.12) are the canonical gauge transformation of electrodynamics. The sole requirement of local gauge invariance on the free Lagrangian (2.4) leads to the formulation of scalar electrodynamics, a field theory that couples the $\phi(x)$ field to the gauge field A_μ which is nothing but the vector potential of electromagnetism. The original Lagrangian is also modified by an additional self-energetical contribution from the compensating gauge fields.

To conclude, let us stress that the prescription of a local symmetry affecting $\phi(x)$ by an arbitrary group transformation at each point separately, leads to the necessary introduction of a quantity that can carry information regarding these transformations from one point to another. This quantity is the gauge field, or connection, whose existence can be viewed as a prime consequence of choosing a framework based on local gauge invariance [15].

2.1.3 Lattice gauge theories

In 1971, Wegner studied a class of Ising models [14], where the global $Z(2)$ symmetry of the Hamiltonian was promoted to a local one. Although the models did not possess a local order parameter, they did exhibit a phase transition[10]. In constructing the models, Wegner introduced a number of concepts which turned out to play a fundamental role in the lattice formulation of gauge field theories[11], suwh as the concept of a nonlocal gauge invariant order parameter[12].

[9] The gauge invariance of $F^{\mu\nu}$ does not hold when the current analysis is extended to gauge groups other than U(1), rather it is a coincidence related to the fact that U(1) transformations are Abelian. The generalization of U(1) to non-Abelian groups as SU(N) or SO(3) is straightforward, the main modification arises in the definition of the field strength (Eq.(2.13)) that becomes $F^{\mu\nu} = \partial^\mu A^\nu - \partial^\nu A^\mu + [A^\mu, A^\nu]$.

[10] Among familar examples of models whose possible phases cannot be characterized by an order parameter is the XY-model, where du to Mermin-Wagner's theorem [183], the continuous O(2) symmetry cannot be spontaneously broken. In this case, it is the (non-local in nature) correlation function that encodes the phase change. Whereas in the disordered phase, it decays exponentially, below T_{KT}, the temperature at which the Kosterlitz-Thouless transition (KT) [184] takes place, it decays as a power law. Let us recall that this transition is of a topological nature, since it is associated to an unbinding of pairs of point defects carrying opposite topological charges for $T > T_{\text{KT}}$.

[11] Let us note that lattice gauge theories are not entirely discrete constructions, as they involve continuous ingredients; gauge groups are Lie groups and involve internal symmetries (they do not relate to the lattice symmetries) [185].

[12] This follows from Elitzur's theorem[172], which rigorously demonstrates that a local symmetry cannot be spontaneously broken, and hence, gauge non-invariant observables vanish. This means that the equilibrium state of the theory is gauge invariant at all temperatures. There can certainly be phase transitions in the theory, but one needs to resort to different arguments than spontaneous symmetry breaking to explain them. For example, in the confinement transition of gauge field theories topological properties of the theory are expected to play an important role [173–177].

2.1.3.1 Geometrical approach

Before addressing the lattice implementation of a gauge theory, it is worthwhile pointing out some of its geometrical implications. We here only briefly sketch some general ideas of the geometrical picture, as it can provide a unifying ground for discussing different gauge theories. The concepts of gauge fields and covariant derivatives can be translated into the language of differential geometry, based on differential forms. In general, the gauge field A_μ has a mathematical interpretation as a Lie-valued connection (1-form)[13]. It is used to construct covariant derivatives acting on fields and it generates parallel transport of the geometric objects under gauge transformations (Fig. 2.1).

The field tensor $F^{\mu\nu}$ is a 2-form given by the commutator of two covariant derivatives $[D^\mu, D^\nu]$. It is an element of the Lie algebra associated to the gauge group. As the tensor $F^{\mu\nu}$ measures the lack of commutativity, its effect is analogous to that of curvature[14] [15].

2.1.3.2 Sites, links, plaquettes

The first step in constructing a discretized version of gauge theory is to approximate the continuous spaceby a discrete set of points, that is, a *lattice*. The lattice is then defined as a set of points of the d-dimensional Euclidean space with the coordinates:

$$x_\mu = n_\mu a \tag{2.15}$$

where a is the lattice spacing and where the components of the vector

$$n_\mu = (n_1, n_2, \cdots, n_d) \tag{2.16}$$

are integer numbers. The points are called the lattice *sites*, or nodes. The next concept relates to the *links* of the lattice. A link is a line which connects two neighboring sites, and is usually denoted by the letter l. It is characterized by the coordinate x of its starting point and its direction $\mu = 1, \cdots, d$

$$l = \{x, \mu\} \tag{2.17}$$

The link l connects sites with the coordinates x and $x + a\hat{\mu}$, where $\hat{\mu}$ is a unit vector along the μ-direction (Fig. 2.2).

[13] The geometrical picture enables a strong parallelism between gauge theory and general relativity. The latter can be interpreted as a gauge theory, where gauge invariance is the invariance under diffeomorphisms (local smooth changes of coordinates) in the space-time manifold, and where gauge transformation corresponds to a change of local frame. The role of the gauge fields is played by the Christoffel symbols defining the connection which generates parallel transport [180].

[14] One encounters the same situation when considering translations on a curved surface, which do not commute for finite curvature.

Fig. 2.2: A link of the lattice. The links connects the sites x and $x + a\hat{\mu}$.

The elementary square enclosed by four links is called a *plaquette*. A plaquette p is specified by the coordinate x of a site and by the two directions μ and ν along which it is built.

$$p = \{x; \mu, \nu\} \tag{2.18}$$

The set of four links which bound the plaquette p is denoted by ∂p (Fig. 2.3), or else by the square symbol $\square$. Usually, in order to reduce artificial surface effects (finite-size effects),

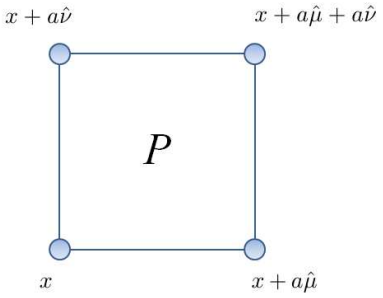

Fig. 2.3: A plaquette of a lattice. The plaquette boundary is made of four links.

one changes the topology of the lattice by imposing periodic boundary conditions in every direction μ, thus compactifying the d-dimensional hyper-cubic lattice to a d-dimensional hyper-torus (Fig. 2.4). The number of sites, links and plaquettes for a symmetric (spatial sizes $L_1 = L_2 = \cdots = L_d = L$) hyper-cubic lattice with periodic boundaries conditions are

$$N_s = L^d, \qquad N_l = dL^d, \qquad N_p = \frac{d(d-1)}{2} L^d, \tag{2.19}$$

respectively [179].

2.1.3.3 Lattice formulation

Consider a theory which involves a matter field $\phi(x)$, endowed with a local internal symmetry group G. In the following, we will consider the case of a group G of $n \times n$ orthogonal matrices with determinant 1. In its lattice formulation[15, 179], matter field is assigned to the lattice sites. A continuous field is thus approximated by its value at the lattice sites

$$\phi(x) \Longrightarrow \phi_x. \tag{2.20}$$

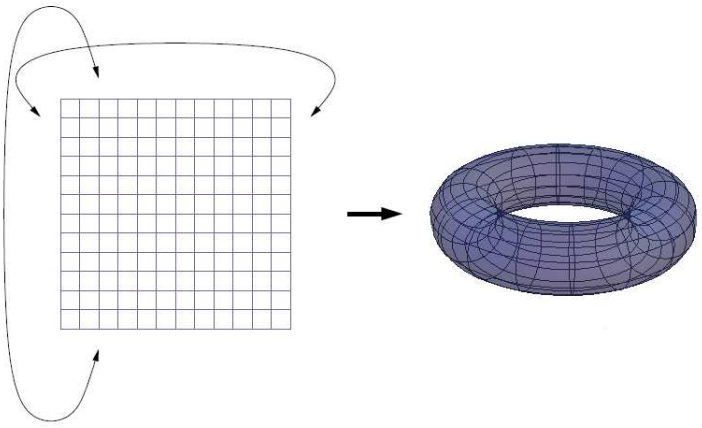

Fig. 2.4: Illustration of a 2-dimensional lattice compactified to a torus by periodic boundary conditions.

A transformation by an independent element $g \in G$ at each site yields

$$\phi_x \mapsto \phi'_x = g_x \phi_x. \tag{2.21}$$

If it is a symmetry, then one should observe the invariance of the theory under such transformations. As it is for the continuum case, gradient terms of the form $(\phi_x - \phi_y)^2$ spoil the invariance. Indeed,

$$\phi_x \phi_y \mapsto \phi_x \left(g_x^{-1} g_y\right) \phi_y \neq \phi_x \phi_y. \tag{2.22}$$

Parallel transporters A term of the form $(\phi_x - \phi_y)^2$, which only measures the change in the components from point to point, would have been suitable if the basis, or frame, didn't change. The problem is essentially that under a local gauge transformation, the meaning of comparing two vectors at different points in these terms is lost.

Since two internal vectors residing at two different locations can not be compared in their natural bases (or local frames), one needs a definition of what would physically equivalent internal vectors mean at different points. This is achieved by the parallel transport, which specifies the rotation of the frame in some intrinsic internal symmetry space upon transport between neighboring points. One could refer to Fig. 2.5 for an simple illustrative example and to the Appendix A for a formal derivation of the relation between gauge fields, connection and parallel transport [15]. The essential point of gauge theories is that by allowing local symmetry, parallel transport acquires the status of a new degree of freedom. Therefore, for each point on the lattice and each possible direction for parallel transport, there is a new dynamical variable, element of the symmetry group G. Building a theory with a local symmetry is thus achieved at the expense of introducing many new degrees of freedom, the gauge fields [188].

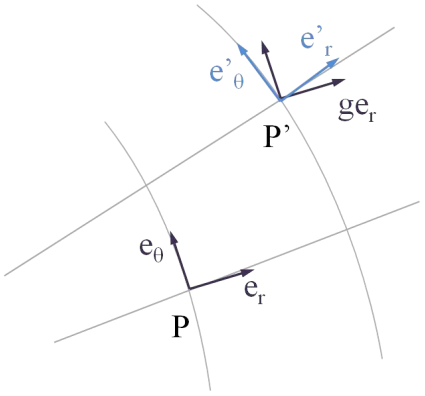

Fig. 2.5: Parallel transport: consider an ordinary vector in the plane, expressed in polar coordinates. Consider the unit basis vectors $\mathbf{e}_r$ and $\mathbf{e}_\theta$ at the point P. Parallel transport of $\mathbf{e}_r$ to the point P' (i.e. the transport keeping $\mathbf{e}_r$ parallel to what it was) yields the vector labeled $g\mathbf{e}_r$, different from the unit radial vector $\mathbf{e}'_r$ at point P'.

Since the gauge field $A_\mu(x)$ has the geometrical role of a connection (Section 2.1.3.1, Section A), a natural manner to encode the gauge variables in a discrete setting is by considering parallel transporters. To parallel as closely as possible the steps in the continuum formulation, we observe that, since $\phi_x\phi_y \mapsto \phi_x \left(g_x^{-1} g_y\right) \phi_y$, one must include a factor depending on the gauge potential which compensates the gauge variation [16, 179, 188]. This factor, known as the Schwinger line integral[15] [181], is given by:

$$U(x,y) = e^{\int_x^y dz^\mu A_\mu(z)} \tag{2.23}$$

where the integral is carried out along a path connecting x and y. We note that $U(x,y)$ is element of the gauge group G, and under a gauge transformation (Eq.(2.12)) it transforms as:

$$U(x,y) \mapsto g_x U(x,y) g_y^{-1}. \tag{2.24}$$

Taking $y = x + a\hat{\mu}$, the gauge variables acquire the meaning of elementary parallel transporters between neighboring lattice points and are thus assigned to the *links* of the lattice,

$$A_\mu(x) \Longrightarrow U_{x,\mu}. \tag{2.25}$$

where $U_{x,\mu} \approx e^{aA_\mu(x)}$ [179, 188]. Link variables, which are elements (*i.e.*, matrices) of the gauge group, thus obey the following transformation rule:

$$U_{x,\mu} \mapsto U'_{x,\mu} = g_x U_{x,\mu} g^{-1}_{x+a\hat{\mu}}. \tag{2.26}$$

[15] Also referred to as the operator of parallel transport, the phase factor or the Wilson line.

From the above considerations, we conclude that $\phi_x\phi_{x+a\hat{\mu}}$ must be modified as follows:

$$\phi_x\phi_{x+a\hat{\mu}} \Longrightarrow \phi_x U_{x,\mu}\phi_{x+a\hat{\mu}}, \tag{2.27}$$

The implementation of the parallel transport between neighboring points guarantees the sought invariance under gauge transformation. Indeed, simultaneous transformations operating on sites (Eq.(2.21)) and on links (Eq.(2.26)) leave the inner gauge product $\phi_x U_{x,\mu}\phi_{x+a\hat{\mu}}$ unaltered:

$$\phi'_x U'_{x,\mu}\phi'_{x+a\hat{\mu}} = \left(\phi_x g_x^{-1}\right)\left(g_x U_{x,\mu} g^{-1}_{x+a\hat{\mu}}\right)\left(g_{x+a\hat{\mu}}\phi_{x+a\hat{\mu}}\right) = \phi_x U_{x,\mu}\phi_{x+a\hat{\mu}} \tag{2.28}$$

Finally, let us not that the same link connecting x and $x + a\hat{\mu}$ can be regarded as a forward one, $\{x;\mu\}$, or as a backward one, $\{x + a\hat{\mu};-\mu\}$. They are related through $U_{x+a\hat{\mu},-\mu} = U^{-1}_{x,\mu}$ in the case of an orthogonal gauge group, since the backward link is simply the reversed forward one (Fig. 2.6).

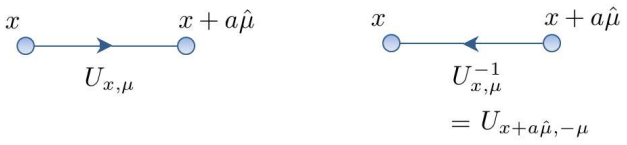

Fig. 2.6: *Left*: Link $U_{x,\mu}$ from site x in direction μ. *Right*: Link $U^{-1}_{x,\mu}$ in the reverse direction, from site $x + a\hat{\mu}$ in direction $-\mu$.

Wilson action To complete the lattice construction, one must include the lattice analog of the second term of equation (2.14), i.e., a gauge invariant term functional of the link variables only (see footnote 12). Such functionals are easily constructed by taking the product of link variables around closed loops. The simplest choice of a closed contour involves the product

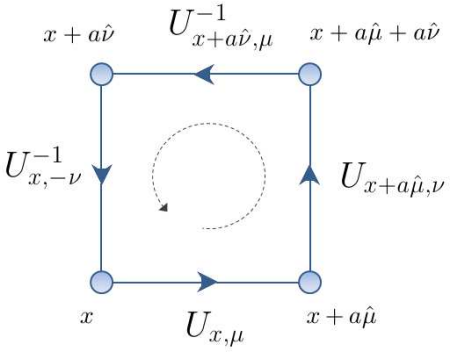

Fig. 2.7: A contour in the form of an oriented boundary of a plaquette p.

of contiguous link variables around an elementary plaquette p (Fig. 2.7)

$$U_{\partial p} = U_{x,\mu}U_{x+a\hat{\mu},\mu}U^{-1}_{x+a\hat{\nu},\mu}U^{-1}_{x,\nu}, \tag{2.29}$$

where $U_{\partial p}$ denotes the plaquette variable (also denoted by $U_{\square}$). Under the lattice gauge transformation (Eq.(2.26)), $U_{\partial p}$ transforms as:

$$U_{\partial p} \mapsto U'_{\partial p} = g_x U_{\partial p} g_x^{-1} \tag{2.30}$$

Therefore, its trace is gauge invariant. Indeed, by virtue of the cyclicity of the trace, one has

$$\mathrm{tr}(U'_{\partial p}) = \mathrm{tr}(g_x U_{\partial p} g_x^{-1}) = \mathrm{tr}(g_x^{-1} g_x U_{\partial p}) = \mathrm{tr}(U_{\partial p}). \tag{2.31}$$

The invariance of the trace under the gauge transformation is used in constructing the so-called Wilson action[14, 186] of a lattice gauge theory:

$$E_G = k \sum_p \left(1 - \frac{1}{n} \mathrm{Re}\,\mathrm{tr}(U_{\partial p})\right) \tag{2.32}$$

where k is the lattice gauge self-coupling parameter, and where n refers to the dimension of the representation of the gauge group G. The integration measure for the gauge variables over the local symmetry group must be invariant under gauge transformations, it is thus performed over the Haar measure[16] which is an invariant group measure [179, 187, 189].

Before ending this section, let us note that the pure gauge term could have been introduce equivalently from geometrical considerations. One way is to mimic the continuum construction, in which the second term in Eq.(2.14) involves $F_{\mu\nu}$, which is related to the lack of commutativity of the covariant derivatives,

$$[D_\mu D_\nu] = [\partial_\mu + A_\mu, \partial_\nu + A_\nu] = \partial_\mu A_\nu - \partial_\nu A_\mu + [A_\mu, A_\nu] = F_{\mu\nu} \tag{2.33}$$

Since in the discrete setting, the gauge variables (links) are used to parallel transport the matter field between neighboring sites, one can formulate a discrete analog of the covariant derivative, the covariant finite difference [16]:

$$\Delta_\mu \phi_x = U_{x,\mu} \phi_{x+a\hat{\mu}} - \phi_x, \tag{2.34}$$

where $U_{x,\mu}$ has served the purpose of transporting the matter field from site $x + a\hat{\mu}$ to site x. Computing $[\Delta_\mu, \Delta_\nu]$ leads to the lattice analog of $F_{\mu\nu}$ and enables recovering the previous result (Eq.(2.32))[187]. The second way is to recall that $F_{\mu\nu}$ is a curvature 2-form. A very natural way to define curvature is to measure the change in some arbitrary orientation due

[16] The partition function of a pure lattice gauge theory (*i.e.* without matter field) is defined by $Z = \int \mathcal{D}[U]\, e^{-E_G[U]}$, where E_G denotes the gauge field action (Eq.(2.32)). As for any integral, the result of a path integral should be invariant under a change of variables, in particular under the gauge transformation (Eq.(2.26)). This requirement reads $\mathcal{D}[U] = \mathcal{D}[U']$. Using the fact that the integration measure for the link variables is the product measure $\int \mathcal{D}[U] = \int \prod_{x,\mu} \mathrm{d}U_{x,\mu}$, the condition $\mathrm{d}U_{x,\mu} = \mathrm{d}U'_{x,\mu} = \mathrm{d}(g_x U_{x,\mu} g^{-1}_{x+a\hat{\mu}})$ for the integration over the individual link variables is derived. Since g_x and $g_{x+a\hat{\mu}}$ can be chosen independently, the measure $\mathrm{d}U$ for a group element must be invariant under left and right multiplication by another arbitrary group element $V \in G$, $\mathrm{d}U = \mathrm{d}(VU) = \mathrm{d}(UV)$, which is a defining property of the Haar measure[179, 189].

to parallel transportation around a closed path, and this is exactly what the Wilson action measures. In this sense, the $1 - \frac{1}{n}\mathrm{tr}\,(U_{\partial p})$ term appearing in equation (2.32) can be seen as a measure of deviation from flatness. Indeed, in the case of trivial identity link matrices, the traced plaquette variable amounts to n, yielding vanishing energy term.

2.1.4 Gauge invariance and frustration in spin glasses

In order to provide some conceptual foundation for a gauge model for relaxor ferroelectrics, we now turn to the gauge description of frustrated systems. Gauge glasses [23, 200], that is, gauge theories with quenched random couplings stand as geometrical extensions of the spin-glass models, emphasizing the relevance of local symmetries in describing the disorder-induced frustration.

For a given realization of all the couplings or bonds, the Hamiltonian of a spin-glass model is clearly not invariant under neither translational nor rotational symmetries. However, some sort of subtler symmetry remains: since the probability distribution of the bonds corresponding to a certain realization of disorder is unchanged by lattice translation, *i.e.* the corresponding couplings are independently chosen from the same distribution, one can recover a certain notion of symmetry for a disordered system, that is, a statistical symmetry [196]. In this sense, although the randomness of glasses leads to a lack of generic rotational or translational symmetry, one can nevertheless regard them as globally homogeneous such that each of the constitutive points is equally suitable as a reference point as any other, despite different local surroundings[17]. The free energy of a glass is thus invariant under transforming the local surroundings of an atom into those of another (mainly by performing local rotation of the attached frame) provided that the connection with the remaining system is adjusted in a covariant way. The local rotation is then a gauge transformation and the glass homogeneity can be written in terms of a gauge invariance parametrized by the rotation group. By virtue of statistical global invariance, one can convert the translational probing of global homogeneity into a local modification of environment under gauge transformation [194].

To be more explicit, let us consider the symmetry of the Edwards-Anderson model [81] of an Ising spin system in an arbitrary configuration of bonds, to show that a simple transformation of variables using the local symmetry leads to non-trivial conclusions. The Hamiltonian of this model is expressed in the following manner:

$$H_{\mathrm{EA}} = -\sum_{(i,\,j)} J_{ij} S_i S_j \tag{2.35}$$

The spin variables are assumed to be of the Ising type $\sigma_i = \pm 1$, placed on the sites of a regular $\mathbb{Z}^d$ lattice. The sum over (ij) is in this case limited to nearest neighbors, so that

[17] According to Rivier and Duffy [194], it is this kind of symmetry one is facing while being lost in a random forest. Every tree is then as good as another to be the reference point.

the variables J_{ij} specify the distribution of the bonds and reside at the links ij joining the sites of the lattice (Fig. 2.8). Each of the J_{ij} is considered to be distributed independently according to a probability distribution $P(J_{ij})$. In the $\pm J$ *model*, the distribution $P(J_{ij})$ of exchange bonds takes the form:

$$P(J_{ij}) = p\,\delta(J_{ij} - J) + (1-p)\,\delta(J_{ij} + J) \tag{2.36}$$

where J_{ij} is either $J(>0)$ (with probability p) or $-J$ (with probability $1-p$). In this model, disorder is thus expressed in terms of a competition between random ferromagnetic and antiferromagnetic interactions.

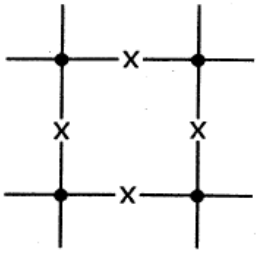

Fig. 2.8: Location of the degrees of freedom of the spin-glass system. The dots represent the spin (site) variables S, and the crosses represent the gauge (link) variables J (after Fradkin *et al.* [204]).

2.1.4.1 Gauge transformation

A gauge transformation of the system (2.35) at site i is defined as the following change of variables [20]:

$$\begin{cases} S_i \mapsto & -S_i \\ J_{ij} \mapsto & -J_{ij} \text{ (for all } j \text{ adjacent to } i) \end{cases} \tag{2.37}$$

The most important feature of the transformation (2.37) is its locality (see Fig. 2.9 for an illustration). The transformation is performed independently at all sites. A more general expression of this transformation is possible [23]:

$$\begin{cases} S_i \mapsto & T_i S_i \\ J_{ij} \mapsto & T_i J_{ij} T_j \end{cases} \tag{2.38}$$

where T is some suitable transformation, $T \in \{+1, -1\}$ in this case[18]. The above transformation leaves the Hamiltonian invariant and does not change the partition function, *i.e.*,

[18] For instance if the transformation (2.37) is performed only at site i, then $T_i = -1$ ($T_i = +1$ otherwise) and $T_j = +1$ for all $j \neq i$, so that (2.38) reduces to (2.37).

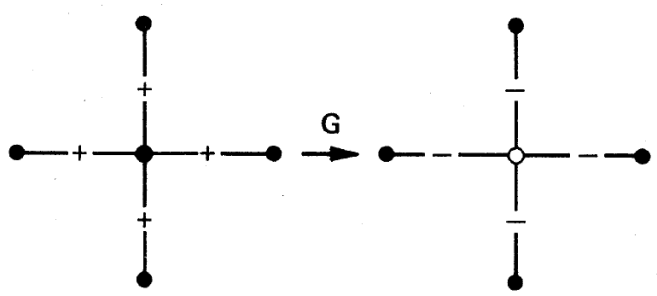

Fig. 2.9: Gauge transformation on the central site. Dark circles are spins pointing up and white circles are spins pointing down. All bonds stemming from the central site have been made negative; the gauge-modified configuration yields the same energy, with the central spin flipped (after Fradkin *et al.* [204]).

$Z[\{J_{ij}\}] = Z[\{T_i J_{ij} T_j\}]$. This invariance indicates that considering a new set of bonds does not alter the thermodynamic properties, hence Z is not a functional of the details of the distribution of the couplings $\{J_{ij}\}$ itself, but rather depends on the features of that configuration which are gauge invariant.

2.1.4.2 Gauge invariant frustration

H_{EA} is evidently preserved under the local gauge transformationas defined in equations (2.37) or (2.38). Under this procedure, only gauge invariant quantities conserve any meaning [204], since a gauge transformation can reverse signs at any site ensuring the vanishing of non-invariant averages.

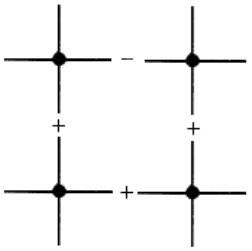

Fig. 2.10: Illustration of the concept of *frustration*, one of the key ingredients of a spin glass system. Dark circles represent spins pointing up. " + " denotes the ferromagnetic interaction, where parallel spins have the lowest energy, and " − " denotes the antiferromagnetic interaction, where the lowest energy is for anti-parallel spins. If there is an odd number of " − " interactions or bonds around the square, no spin configuration will simultaneously minimize each contribution to the energy. The configuration shown minimizes the energy of the upper and lower bonds, as well as the right hand bond, leaving the left hand bond in a high-energy state, the plaquette is frustrated, $\Phi = 1$ (after Fradkin *et al.* [204]).

Relevant disorder and the concept of frustration The necessity of probing the phase structure using exclusively gauge-invariant functions leads to a substantial analysis of disorder

in spin glasses. Namely, once the existence of a local symmetry is recognized [20, 204], it becomes apparent that two types of disorder have to be distinguished one from the other, that is, the so-called serious disorder, or relevant disorder, in contrast with the non-serious disorder, *i.e.*, the irrelevant one. Only serious disorder, which stems from frustration, is gauge-invariant, whereas trivial or irrelevant disorder can be eliminated by a transformation of the type (2.38).

Mattis model or trivial disorder Let us consider the spin glass model of Mattis [205] in which disorder is only deceptive. The model is of the form (2.35), but instead of equation (2.36) for the random exchange J_{ij}, one chooses the form $J_{ij} = J\tau_i\tau_j$, where J is a nonrandom exchange and $\tau_i = \pm 1$. Defining a new set of spins $\xi_i = \tau_i S_i$, one recovers an Ising ferromagnet, devoid of disorder [85]. Hence the randomness within this model is trivial since it can be eliminated, or gauged away, by a suitable redefinition of the spin variables. The Mattis model is thus frustration-free and can be seen as a gauge transformation of the pure Ising model.

Frustration function In order to filter out relevant from irrelevant disorder[19] Toulouse defined the frustration function [20]:

$$\Phi = \prod_{(C)} J_{ij} \tag{2.39}$$

defined on any closed contour (C) along connected bonds of the lattice. Φ is a geometrical property, independent of the "matter" field S_i [195], that provides a measure of the frustration within the contour. If $\Phi = +1$, it is possible to orient the spins along (C) without frustration; if $\Phi = -1$, it is not (see Fig. 2.10). If the lattice under consideration is a regular one, as it is the case for (2.35), then frustration of a plaquette (elementary square ${}^{l}_{i}\square^{k}_{j}$ whose corners are labeled by i, j, k, l) is the most fundamental notion since any larger loops can be expressed as a product of the plaquettes enclosed by the contour. The fundamental gauge-invariant frustration function is thus:

$$\Phi = J_{ij}J_{jk}J_{kl}J_{li} \tag{2.40}$$

From the topological standpoint, the plaquette variable Φ is reminiscent of the path dependent parallel transport of a tangent vector on a curved surface [20, 204] (see Fig. 2.11 for an

[19] Disorder and frustration often go together, but they refer to distinct concepts and neither implies the other. An example of frustration-free disorder has been given in the previous footnote while considering the Mattis model. The counterpart of frustration-free disorder is frustrated order. The most simple minded illustration of this concept is a triangle of Ising spins coupled with antiferromagnetic interactions. In such a case, one can not find a configuration where all interactions are satisfied. Such an ordered system is said to be geometrically frustrated.

illustration). It is the analog of the field strength or gauge curvature of conventional gauge theories[20, 204]. The misfit between the various lines of transport can thus interchangeably signal frustration, curvature or disclination (see Fig. 2.12). In this sense, frustrated plaquettes are curved whereas unfrustrated are flat. In this sense, all the plaquettes of the aforementioned Mattis model are flat, $\Phi = 1$.

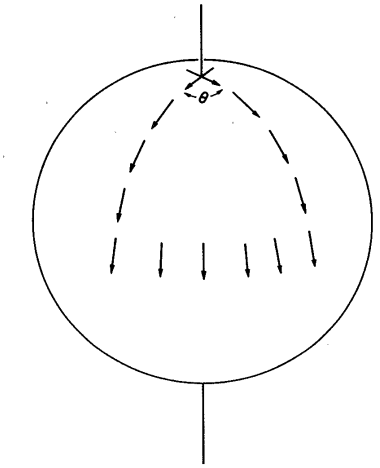

Fig. 2.11: Frustration on a sphere. The parallel transport of a vector on a sphere is defined by minimizing the energy locally as one moves around a path. When the path crosses itself forming a loop, there will in general be a change in the direction of the vector, and for small loops this change will be proportional to the area enclosed. The frustration represented by this change is described by the curvature tensor $\mathcal{R}$ of the sphere (after Sethna [203]).

As already pointed out, only gauge-invariant disorder (frustration) can change the nature of the phase transition, and thus the resort to gauge-invariant quantities is necessary to the probing of the transition. In order to isolate the effects of gauge-invariant disorder (*i.e.*, frustration), Fradkin *et al.* [204] have defined a gauge-invariant analog of the correlation function $\langle S_i S_j \rangle$ by inserting a string of J's between S_i and S_j. The gauge-invariant correlation function thus takes the form $\langle S_i \left(\prod J\right) S_j \rangle$, where $\prod J$ stands for the product of all the J variables along the links of an arbitrary path $\Gamma(i,j)$ connecting sites i and j. The difference between the correlation function evaluated along two different paths connecting the same end points i and j is given by $(-1)^{f_P}$, where f_P is the number of frustrated plaquettes enclosed by the loop defined by the two considered paths, explicitly showing that it is the frustration content, rather than the detailed distribution of the individual bonds, that characterizes the system.

We have so far investigated the gauge invariance of the Ising spin-glass model under (2.37). This treatment is not exclusive to Ising-like variables and can be extended to the XY model [204, 208], for which the degrees of freedom are fixed-length two dimensional vectors, subject to planar rotations. The introduction of disorder into the standard model can either be made via the randomness of the bonds or via random difference angles ψ_{ij},

such that in the latter case the interaction takes the form $J_0 \cos(\theta_i - \theta_j - \psi_{ij})$. Defining a link-gauge degree of freedom $U_{ij} = \exp(i\psi_{ij})$, the interaction can be rewritten as $J_0/2(S_i U_{ij}^\star S_j^\star + h.c)$, with $S_i \equiv \exp(i\theta_i)$, and remains invariant under the local gauge transformation $S_i \to V_i S_i$ and $U_{ij} \to V_i U_{ij} V_j^\star$, where $V_i = \exp(i\chi_i)$ (analog of equations (2.37) and (2.38)). Hence, to a local rotation of a spin by an angle χ_i is associated a rotation of the connecting link by the difference $\chi_i - \chi_j$. The frustration angle at plaquette $ijkl$ is now defined as $\exp(i2\pi\Phi_{ijkl}) = U_{ij}U_{jk}U_{kl}U_{li}$, where $2\pi\Phi_{ijkl} = \psi_{ij} + \psi_{jk} + \psi_{kl} + \psi_{li} \mathrm{mod}(2\pi)$. Thus only fractional values of Φ signal frustration, and in the continuum limit, the sum over the ψ_{ij} gives rise to the connection over a closed path, equivalent to the net change of curvature measured through the Berry phase [202].

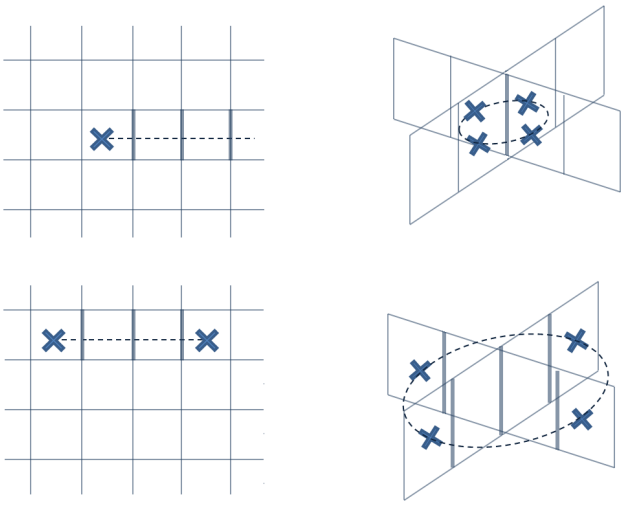

Fig. 2.12: *Left:* In the two-dimensional case, the elementary curved unit is one plaquette. It is thus possible to isolate a single frustrated plaquette at the expense of a dual string of flipped antiferromagnetic bonds starting from the frustration center to the boundary of the system. In the upper figure, the isolated frustrated plaquette is signaled by a cross, the antiferromagnetic bonds are shown in bold and the dual string crossing non-frustrated plaquettes is indicated by a dashed line. A ground state configuration is obtained by pairing the frustrated plaquettes, with minimal total length of the strings (going through adjacent non-frustrated plaquette centers), as shown is the lower figure. *Right:* In the three-dimensional case, a frustrated plaquette cannot be isolated. This follows from the conservation law of curvature, which is the strict analogue of the conservation of magnetic flux in electromagnetism [20]. The elementary unit is thus a *loop* of frustrated plaquettes, as shown in the upper figure. A ground state configuration involves loops of minimal area, enclosing non-frustrated plaquettes as shown in the lower figure. The spin direction across this area changes discontinuously, *i.e.*, one has disclinations. These disclinations induced by frustration have non-trivial topological properties and have been associated to the gauge fields in the continuous version of gauge theory for glasses as formulated by [21, 197, 198].

Frustration and ground-state degeneracy In order to appreciate the relevance of a gauge theoretical approach to spin glasses, it is worthwhile recalling that a defining characteristic of spin glasses is the existence, for a given realization of the couplings, of many configurations of spins which are locally stable minima of the energy. This large degeneracy

of the ground state introduces non-trivial multiplicity since the minima are not all related by standard global symmetry of the action. Now the cause behind this large degeneracy resides in the frustration, *i.e.*, in the existence of competing interactions (see Fig. 2.13 for an illustration). As a consequence of frustration, typically, there is no ideal low-lying ground state, and instead many metastable states of similar energies [190]. The notion of local invariance thus leads to that of gauge-invariant frustration, which in turn captures an essential feature of spin-glasses, that is the large degeneracy of their ground-state.

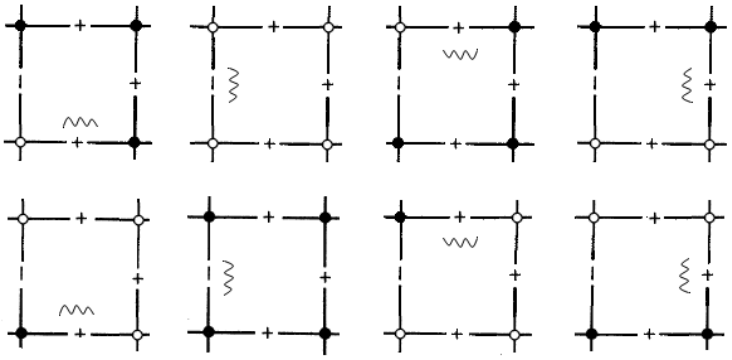

Fig. 2.13: Illustration of the degeneracy introduced by frustration. Dark circles are spins pointing up and white circles are spins pointing down. Represented is the 8-fold degenerate ground state of a frustrated plaquette composed of an odd (here one) number of antiferromagnetic bonds on its perimeter, i.e., $\Phi = -1$. Competing interactions render impossible the accommodation of all bonds. There exist a bond at which the lowest state is not achieved, such a bond is frustrated and indicated by the wavy line. This simple investigation shows that competing interactions raise the ground state energy and the ground state degeneracy.

On the connection between spin glasses and gauge field theories To conclude this section it remains to be pointed out that the local transformation as defined in equation (2.37) or equivalently in equation (2.38), is quite similar[20] to the local transformation under which the Lagrangian of electrodynamics is invariant (equations (2.7) and (2.12)), the bond interactions J_{ij} playing a role somewhat similar to that of the electromagnetic potential A_μ [20]. In the present case the lattice gauge group is the discrete Abelian group with two elements, Z_2, whereas in the former case of electrodynamics, the gauge group is the one dimensional Abelian continuous group $U(1)$. However, the analogy is not complete since in electrodynamics the gauge field A_μ is dynamical, whereas in the case of gauge glasses, the bond interactions J_{ij} are quenched [85, 199]. The analogy would thus be complete if the analogs of the vector potential, *i.e.*, the exchange variables J_{ij} were annealed variables. Nonetheless, as we shall now see, there have been attempts to reexpress the spin glass problem as a genuine gauge theory in which both spins and gauge variables are treated on the same footing. Toulouse *et al.* examined the connection between spin glasses and gauge field

[20]For an introductory review on the relation between gauge theories on the lattice and spin systems, one may refer to the monograph of Kogut [201]

theories [199]. They noticed that in the case of the annealed models of spin glasses, in which the S_i's and the J_{ij}'s are statistical variables to be averaged over at the same time, the thermal average of the frustration function Φ is nonzero $\langle\Phi\rangle_T \neq 0$, reflecting the low frustration content of the annealed system. Indeed, the non-vanishing of the frustration function in the annealed model stems from the fact that at low temperature, non-frustrated configurations of the J_{ij}'s are energetically favored and thus dominate the annealed free energy. In contrast, when considering the realistic $\pm J$ quenched models of spin glasses, before performing the average over distributions of the gauge degrees of freedom or bonds, one has to first perform the thermal average over the S_i's in a given distribution of the bonds. In this latter case of a quenched system with equal probabilities of positive and negative bonds, $[\Phi]_{av} = [J_{ij}J_{jk}J_{kl}J_{li}]_{av} = 0$, because the contour is equally likely to be frustrated ($\Phi < 0$) or non-frustrated ($\Phi > 0$). Toulouse and Vannimenus argued that an annealed description of the gauge-glass could in principle yield satisfactory results, provided that the error due to the annealed approximation, *i.e.*, basically the underestimate of frustration, is compensated by imposing a suitable constraint on the J_{ij}'s so as to restore an appropriate statistical account for frustration. The constraint naturally corresponds to the vanishing of the global frustration function:

$$\langle J_{ij}J_{jk}J_{kl}J_{li}\rangle_T = 0 \tag{2.41}$$

To ensure that equation (2.41) is satisfied, they defined the so-called "gauge annealing" scheme consisting in the introduction of a Lagrange multiplier β_P, the so-called plaquette temperature, for the frustration function into the Hamiltonian.

$$-\beta H_{GA} = \beta \sum_{(ij)} J_{ij}S_iS_j + \beta_P \sum_{\square} JJJJ \tag{2.42}$$

where the last term runs over plaquettes, and

$$\beta \frac{\partial F_{\mathrm{G}}}{\partial \beta_P} = \langle JJJJ\rangle_G = 0 \tag{2.43}$$

In this gauge annealing scheme, the phase transition lines are determined by the equation (2.42), and the frustration constraint (equation (2.43)), that can only be satisfied for negative β_P, defines a trajectory in the (β, β_P) plane. Thus, a spin glass transition would correspond to this trajectory crossing a phase transition line [85, 199]. Note that the equation (2.42) does describe a gauge theory since it is invariant under the gauge transformation (2.37). Monte-Carlo simulations aiming for the assessment of this approach [206, 207] revealed a discrepancy between what would be physically expected in quenched systems (e.g. a transition in $d = 3$) and the predictions of this annealed approximation for quenched systems (no intersection of the transition lines with the trajectory (2.43) was observed), thereby indicating the limited applicability of this latter approach in that it introduces correlations among the plaquettes

that are absent in the quenched system where the J_{ij}'s are independent random variables. However, as stated by Toulouse and Vannimenus [85, 199], this gauge annealing scheme can be further improved by the introduction of more constraints which would make the annealed system increasingly imitating the quenched one.

2.1.4.3 Continuum gauge glasses models

Gauge theories for spin glasses have been developed in two directions. Our discussion on frustration in spin-glass so far has been based on spin models on discrete lattices, let us now briefly consider the continuum counterpart.

Hertz suggested a description of a spin-glass based on the concept of frustration within a continuum Landau-Ginzburg model [197]. For a planar spin, the effective Hamiltonian has a form analogous to that of the Ginzburg-Landau functional for a superconductor in a magnetic field,

$$H_{\text{eff}} = \frac{1}{2}\int \mathrm{d}^d x \left[r_0 |\phi(x)|^2 + \frac{1}{4} u |\phi(x)|^4 + |\left(\nabla - i\mathbf{Q}(x)\right)\phi(x)|^2 \right] \tag{2.44}$$

except that the role of the vector potential is taken by a quenched random variable $\mathbf{Q}(x)$ which represents the wave vector of the lowest-energy spin-density wave, into which the spins condense below the Néel temperature. Thus $\mathbf{Q} = 0$ represents a ferromagnet and $\mathbf{Q} \neq 0$ an antiferromagnet. Since the model is based on the notion of randomly competing antiferromagnetic and ferromagnetic interactions, the probability distribution $P[\mathbf{Q}]$ of this random quenched variable is chosen not to depend directly on $\mathbf{Q}(x)$, in order not to privilege any value over any other. Rather, $P[\mathbf{Q}]$ is taken as a Gaussian distribution in the gauge invariant quantity :

$$F_{\mu\nu}(x) = \partial_\mu Q_\nu(x) - \partial_\nu Q_\mu(x) \tag{2.45}$$

involving the curl of $\mathbf{Q}(x)$.

$$P[\mathbf{Q}] \propto exp\left(-\frac{1}{2f}\int \mathrm{d}^d x \sum_{\mu\nu} F_{\mu\nu}^2(x) \right) \tag{2.46}$$

The parameter f corresponds to the mean-square vorticity in $\mathbf{Q}(x)$ and measures the degree of frustration in the model. In order to study the effects induced by the introduction of a small amount of frustration, Hertz performed renormalization near the $f = 0$ fixed point[21]. He found that the fixed point is unstable below $d < 4$, discarding the occurrence of conventional second order ferro or antiferromagnetic phase transitions and indicating that in the presence

[21] The situation where $f = 0$ refers to the unfrustrated Mattis model, in which the disorder is trivial or irrelevant.

of frustration, there is no uniquely favored spin configuration, but an infinite number of nearly equally favorable ones, i.e., frustration implies degeneracy. After having investigated the usual kind of order where the order parameter is characterized by the spin field, and proved its instability against the introduction of any frustration, Hertz considered a mean-field analysis of a transition to a state characterized by an Edwards-Anderson order parameter, $q_{EA} = \langle\langle S\rangle^2\rangle_c$ (where the inner brackets indicate a thermal average, and those followed by the subscript c indicate a configuration average). This second investigation yields the main qualitative features of mean-field theories for other models for spin glasses.

As already pointed out, frustration loops induce topological defects such as disclinations [20–22] (see Fig. 2.12). Leveraging on this genuine inhomogeneity in the spin orientation arising from frustration, Dzyaloshinskii and Volovik suggested that at a semi-macroscopic level, the gauge variables associated with the SO(n) group[22] and describing disclinations, should be introduced for a proper description of spin glass properties. Their theory consists in a reappraisal of concepts related to distortions in elasticity theory while formally it is based on Yang-Mills gauge theories[15].

There is a limited similarity between the work of Herzt [197] and Dzyaloshinskii and Volovik [21]. Hertz assumes that the field $\mathbf{Q}$ is induced by the frustration network which is produced by competing interactions and hence it is randomly quenched. He does not give a dynamical status to this field. Hence he averages the free energy expression with respect to the probability distribution $P[\mathbf{Q}]$. Dzyaloshinskii and Volovik on another hand argue that the field $\mathbf{Q}$ has two components, *i*) one random and static arising from the disclinations in the spin field produced by frustrations and *ii*) the other non-random, ascribed to thermal fluctuations, and thus of a dynamical nature. Hence a complete thermodynamical analysis of the gauge theory as introduced by Dzyaloshinskii and Volovik will involve the two following steps [193]. The gauge field is written as $\mathbf{Q}(\mathbf{r}) = \mathbf{q}(\mathbf{r}) + \eta(\mathbf{r})$, where the first part represents the random component and the second part the non-random component. The free energy also contains a term which is function of η only and representing the energetics of the thermally produced disclinations. The functional integral in the partition function involves integration over the $\mathbf{S}$ field as well as the $\eta(\mathbf{r})$ gauge field, resulting in a free energy depending on the random component $\mathbf{q}(\mathbf{r})$ only. The free energy is then averaged with the probability distribution for $\mathbf{q}$.

2.1.5 Gauge theory of defects

A second conceptual ground for a gauge model for relaxor ferroelectrics is provided by the modern trends in theoretical description of defects in condensed matter, which include geometrical and gauge theoretical methods (see, e.g., [17–19, 212, 217]). The theory of defects

[22] SO(n) is the continuous group associated with the rotation symmetry of the spins.

[210, 211] deals with bodies that are subjected to internal stresses even if there are no external forces acting on them. These stresses are caused by the presence of defects, which are alterations of the ideal and ordered structure of the medium that rearrange its structure to reach internal equilibrium.

2.1.5.1 Gauge theoretical approaches

The ordinary theory of elasticity requires that the displacement at any point of a body should be a single valued function of the coordinates of that point. This requirement ceases to be fulfilled when considering the theory of defects [17]. Indeed, dislocations and disclinations can be viewed as topological defects, in that their presence changes a simply connected region in a multiply connected one[23]. This implies that the components of displacement are not single-valued functions whenever a defect line or surface is crossed (see Fig. 2.14).

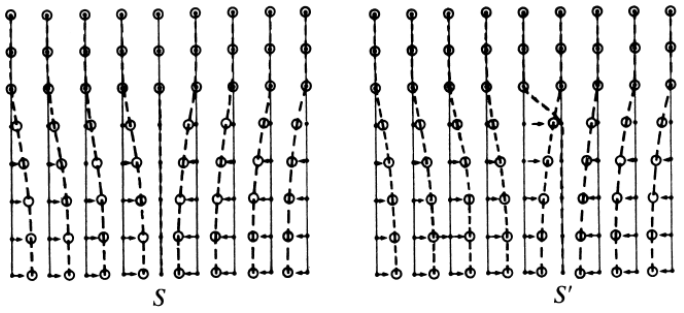

Fig. 2.14: Multivaluedness of displacement field: In the presence of a dislocation, the displacement field is intrinsically non-unique. The figure shows the ambiguity in the assignment of the displacement $u_i(\mathbf{x})$ to the nearest equilibrium position. When removing a layer of atoms, S, the result is a dislocation line along the boundary of the layer. Across the layer, the positions $u_i(\mathbf{x})$ jump by a lattice spacing. The same dislocation line could have been constructed by removing a different layer of atoms, S', just as long it has the same boundary line. Physically there is no difference. There is only a difference in the discriptions which amounts to a difference in the assignment of the equilibrium positions from where to count the displacement field $u_i(\mathbf{x})$ (After Kleinert [19]).

This is best illustrated by considering a doubly-connected body as exemplified by a torus (Fig. 2.15). This hollow ring has the property that a closed circuit in the medium cannot shrink to a point while always remaining inside of the medium. The body may be dislocated by performing cuts along the radial lines OAA′, OBB′, and removing the wedge AA′BB′ of angle ϕ. If the cut edges are now joined, the ring is in a state of self-strain. The coordinates of a point P in the strained ring may be expressed in polar coordinates r=OP, $\theta = \widehat{\mathrm{AOP}}$ (Fig. 2.15 *(b)*). The displacement u_θ of the point P is given by $u_\theta = r\theta\phi/2\pi$. For the point Q_1 the displacement is zero, whereas for the point Q_2 the displacement is $r\phi$. Thus for

[23]We say a domain D is simply connected if, whenever $C \subset D$ is a simple closed contour, every point in the interior of C lies in D. One can think of a simply-connected domain as one without holes. In contrast, domains with holes are said to be multiply-connected.

these two neighboring points lying on either side of the cut, the reference coordinates differ only infinitesimally, while their displacements differ significantly. The relative displacement $\delta u_i(Q) = u_i(Q_2) - u_i(Q_1)$ of neighboring points on either side of the cut is given by [211]:

$$\delta u_i(Q) = b_i + d_{ij} x_j(Q) \tag{2.47}$$

in which $d_{ji} = -d_{ij}$. This represents an arbitrary rigid-body displacement of a point with respect to a neighboring point. According to Eq.(2.47), the most general dislocation of a

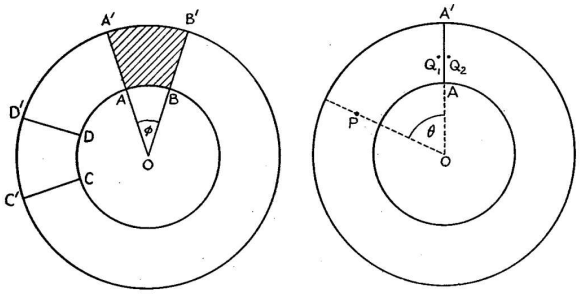

Fig. 2.15: *Left* Dislocation of a hollow ring. The ring is cut along the radial lines AA′ and BB′, the wedge AA′BB′ is removed, and AA′ is joined to BB′. The same dislocation could be made by cutting along CC′ and DD′. *Right* The dislocated ring. The neighbouring points Q_1 and Q_2 lie on opposite sides of the cut (after Nabarro [211])

doubly-connected body is thus described by three constants d_{ij} specifying the relative rotation of the two cut surfaces, and three constants b_i specifying their relative translation. These constants can be considered as the infinitesimal generators of the 3-parameter rotation group SO(3) and the infinitesimal generators of the 3-parameter translation group T(3), respectively. A semi-direct product of these two groups gives a 6-parameter group E(3)=SO(3)$\triangleright$ T(3) of all rigid body motions. Noticing that the incremental displacement δu_i can be obtained by allowing the group E(3) to act differently at different points, that is to act locally, or inhomogeneously, Kadic *et al.* developed the so-called gauge-theory for defects [17].

The gauge theory of defects essentially consists of the following ingredients [213] : *(i)* adopting an admissible Lagrangian which is invariant under a global symmetry group, that is, the Euclidean group in the elasticity E(3), *(ii)* making the group local, or inhomogeneous, spoils the invariance of the Lagrangian, *(iii)* restoring the lost invariance of the Lagrangian by means of minimal gauge coupling requires replacing the standard derivative by a covariant derivative and introducing compensating gauge fields, *(iv)* in this fashion a new Lagrangian is formed that also includes the compensating gauge fields together with a coupling constant. The new field equations are obtained as customary, via appeal to the Euler-Lagrange equations, and are supplemented by an appropriate choice of gauge to render a unique solution. For a simple illustrative example, one can refer to [218].

2.1.5.2 Geometrical approaches

Unlike Kadic and Osipov who consider the problem in the framework of the gauge theory of defects in an elastic continuum, the geometric approach [18, 19, 210] translates the theory of defects in solids to the language of three-dimensional gravity, involving nontrivial metric and torsion.

Topological defects, formed during phase transitions involving continuous symmetry breaking, can be conceptually generated by a "cut and glue" process, when layers or sections of matter are cut from a crystal with a subsequent smooth rejoining of the cutting surfaces[215]. This process, known as the Volterra process [214] (see Fig. 2.16), gives a unifying view of the topological line defects in crystals. Displacement of the surfaces of the cut with respect to each other and subsequent gluing will generate a line defect whose core coincides with the axis. A topological defect thus consists in a core region, characterized by the absence of order, and a smooth far field region.

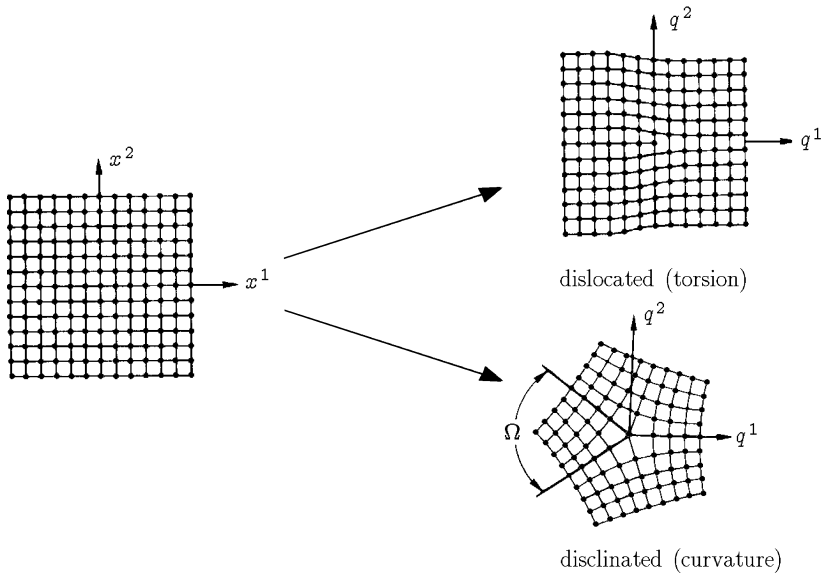

Fig. 2.16: Crystalline defects may be generated via so called Volterra process, when layers or sections of matter are cut from a crystal with a subsequent smooth rejoining of the cutting surfaces. A crystal can have two different types of topological defects, which are line-like defects in the 3-dimensional space. A first type of topological defects are translational defects called dislocations: a single-atom layer is removed from the crystal and the remaining atoms relax to equilibrium under the elastic forces. A second type of defects are of the rotation type and called disclinations. They arise by removing an entire wedge from the crystal and re-gluing the free surfaces. Geometrically, the former transformation introduces torsion, the latter curvature (After Kleinert [19]).

In the continuum approximation the core of such line defects is associated to a geometrical singularity, hence the formal analogy with gravity theory, in which singularities are sources of gravitational field, described by a deformation of the space-time from the flat Minkowsky geometry [18, 215]. A defect is thus treated as a source of a "gravitational" distortion field,

and the metric describing the medium surrounding the defect is then a solution to the three-dimensional Einstein-Cartan equation.

In this gravitational approach, crystals are considered as continuous elastic media endowed with a spin structure, and both dislocations (defects in elastic media) and disclinations (defects in the spin structure) are described within the framework of Riemann-Cartan geometry, the torsion and curvature tensors being identified with the surface density of dislocations and disclinations, respectively (Fig. 2.17).

Existence of defects	$R^{ij}_{\mu\nu}$	$T^{i}_{\mu\nu}$
Elastic deformations	0	0
Dislocations	0	$\neq 0$
Disclinations	$\neq 0$	0
Dislocations and disclinations	$\neq 0$	$\neq 0$

Fig. 2.17: Relation between physical and geometrical notions in the geometric theory of defects (after Katanaev [217]).

Whereas a smooth displacement vector field only indicates elastic deformations corresponding to diffeomorphisms of the Euclidean space[24] , discontinuities arising from cutting surfaces indicate the existence of defects in the elastic structure, and lead to the appearance of nontrivial geometry. Those discontinuities in the displacement vector field, or dislocations, correspond to a nonzero torsion tensor $T^{i}_{\mu\nu}$, equal to the surface density of the Burgers vector[25]. Setting the criterion for the presence of dislocations to nonzero torsion tensor allows accounting for punctual defects such as vacancies and impurities. In the first case a ball is cut from the Euclidean space and the boundary sphere is shrunk to a point (Fig. 2.18). In the case of impurity, a point of the Euclidean space is blown up to a sphere and the produced cavity is filled with the medium [217].

Disclinations on another hand, arise from discontinuities in the order parameter field (see Fig. 2.19), have already been accounted for within gauge approaches based on the rotational

[24]The elastic solid without defects is assumed to be a continuous, infinite medium, whose undeformed state is characterized by a flat Euclidean metric δ_{ij}. Ordinary elasticity theory [216] attaches a Cartesian reference x^i to the undistorted medium and describes its deformations locally by the displacement vector field $u^i(x)$, which is a smooth function. This way, after the deformation, the point x^i will have the coordinates $y^i = x^i + u^i(x)$ in the initial Cartesian frame, and from the mathematical standpoint this map $x^i \mapsto y^i$ by itself is the diffeomorphism of the Euclidean space R^3.

[25]Indeed, the lack of a preferred Cartesian coordinate frame stemming from the lack of symmetry associated to the presence of a defect implies an invariance of the Burgers vector, expressed as the integral of the displacement vector along a closed contour surrounding the dislocation axis, under arbitrary coordinate transformations. This invariance requires the consideration of the components of the displacement vector field with respect to the orthonormal basis in the tangent space. Resorting to Cartan formalism, the torsion tensor acquires the physical interpretation of the surface density of the Burgers vector $b^i = \iint dx^\mu \wedge dx^\nu \, T^i_{\mu\nu}$

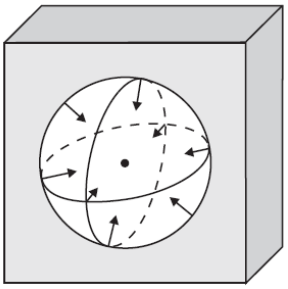

Fig. 2.18: Point defect: a vacancy appears when a ball is cut out from the medium, and the boundary sphere is shrunk to a point (after Katanaev [217]).

group SO(3) in spin glass models[21, 194, 197] (Section 2.1.4.3). Geometrically, the surface density of the Frank vector of a disclination is associated to the curvature tensor[26] $R^{ij}_{\mu\nu}$ [217].

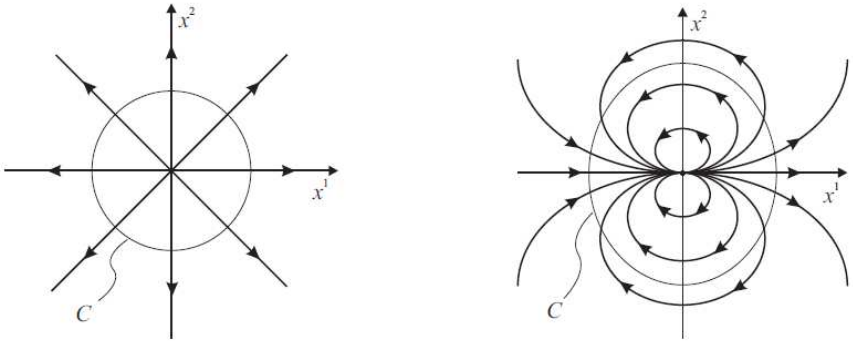

Fig. 2.19: Vector field distributions on the plane x^1,x^2 for linear disclinations parallel to the x^3 axis. The length of the Frank vector $|\Theta|$ is equal to the total angle of rotation (multiple of 2π) of the field as it goes around the disclination. In the left panel $|\Theta| = 2\pi$, whereas in the right panel $|\Theta| = 4\pi$ (after Katanaev [217]).

2.2 Methodology

2.2.1 Postulate of a gauge theoretical approach for relaxors

The phase structure of relaxor ferroelectrics is obviously not captured by the notion of local order parameter, such as the polarization, on account of the existence of at least two different phases in the paraelectric region. Whereas at short range, the local symmetry is polar, and the atomic shifts [7–9] from their ideal cubic symmetry positions are correlated, at long range, the global symmetry is cubic due to the statistical atomic disorder that results in a spatially variable polarization, yielding zero net global polarization. The relaxor behavior is thus contained within the paraelectric phase. Deviations from mean field expectations have

[26]Indeed, every linear disclination is characterized by the Frank vector $\Theta_i = \epsilon_{ijk}\Omega^{jk}$, where ϵ_{ijk} is the totally antisymmetric third-rank tensor and Ω^{jk} the integral of the spin structure or displacement field along closed contour surrounding the disclination axis. By identifying the rotation matrices field (associated to that of the spin structure) with a SO(3) connection, Katanaev gives the physical interpretation of the curvature tensor as the surface density of the Frank vector $\Omega^{ij} = \iint dx^\mu \wedge dx^\nu \, R^{ij}_{\mu\nu}$.

been associated with the onset of the relaxor behavior at T_d [82], and several propositions have been made in an attempt to define characteristic temperatures, invoking for instance random bonds or/and random fields models [64, 99, 122, 219, 220], or conceptually resorting to spatially modulated phases [62–65] or Griffiths phase [5, 153]. It was indeed very early realized that in relaxors, where intrinsic quenched randomness exists in form of defects, impurities or as a general structural property, the disorder stemming from spatial heterogeneities is substantial, in that it is an integral part of their characteristics. In certain circumstances, even a weak disorder can have a crucial effect on their critical behavior, by altering the stability of the low-temperature ordered phase, and inducing non-trivial properties governed by rare regions [2, 5, 166]. A local order parameter does not lead to any information, since by construction it averages over local fluctuations and overlooks the scale inhomogeneities. As well appreciated, both the physical dimension of a system and the symmetry of its degrees of freedom condition its propensity to undergo a phase transition. For example, continuous symmetries for two-dimensional theories with finite range interactions [184] and local symmetry based theories [14, 186] cannot exhibit spontaneous symmetry breaking [172, 183], yet it is possible to account for the different encountered phases at the expense of introducing nonlocal quantities. Whereas in the first case, the Kosterlitz-Thouless transition (KT) is captured by the correlation function whose dependence on distance changes from an exponential decay at high temperatures, to a power law decay below T_{KT} [184], in the case of gauge theories, it is the Wegner-Wilson loop that encodes the non-local features of the theory [14, 186]. Let us note that in both cases nontrivial topological properties are crucially involved[27] (binding-unbinding of vortex-antivortex pairs [184], 't Hooft-Polyakov monopole [173–177]). Revealing the relaxor behavior might thus necessitate the consideration of more complex symmetries, whose inability to be described by local order parameter would nevertheless capture the encountered phases.

Driven by these fundamental considerations, we argue that the disorder-induced nontrivial interplay between local and global scales in relaxors can be captured within the framework of the *local gauge symmetry*. Our proposition is further motivated by the large success of the concept of a gauge field in condensed matter physics, beyond its original formulation by Wegner as a probing tool of phase transitions without local order parameter [14], as a mean to account for glassy behavior and various kinds of topological defects.

We consequently propose a new scheme based upon the first-principles-derived effective Hamiltonian approach, local symmetry, and lattice gauge theory to describe and analyze relaxor behavior, emphasizing the role of disorder and the importance of local gauge invariance. This theoretical framework is then applied to a specific relaxor, namely, disordered $(Pb_{1-3/2x}La_x)(Zr_yTi_{1-y})O_3$ solid solutions.

[27] It was firstly observed by Anderson [13] that a second order phase transition is characterized by the breakdown of a generalized rigidity (i.e. the breakdown of the spatially uniform symmetry breaking), with a proliferation of defect structures, thus connecting critical behavior to geometrical properties of defects.

In this section, we will start by reviewing the theoretical background related to the microscopic modeling of ferroelectrics, namely, the first-principle based effective Hamiltonian construction. We will then present the gauge-modified effective Hamiltonian for relaxors.

2.2.2 Density functional theory

Ab initio methods (also referred to as first-principles methods) are used to predict the properties of materials by resolving quantum mechanics equations without any adjustable variables. Among *ab initio* methods, the density-functional theory (DFT) in its earliest formulation by Hohenberg, Khon and Sham [221, 222], consists in a reformulation of the many-body quantum problem in a problem solely depending on the electronic density. This reduction of the problem enables the access by calculations to the ground state of a system involving a large number of electrons. Thus DFT offers both conceptual simplicity and computational efficiency (see Appendix B). However, let us stress that first-principles methods are essentially restricted to the study of the zero-temperature electronic and structural properties.

2.2.3 Effective Hamiltonian for ferroelectrics

First-principles approaches, based upon a full solution for the quantum mechanical ground state of the electron system within the framework of density functional theory, have shown to yield highly accurate material-specific microscopic information, enabling the investigation of the origin of the behavior of a wide variety of system at the atomic-scale. These methods are free of empirically adjustable parameters, as they take as their only inputs the atomic numbers of the constituent atoms, thereby overcoming the oversimplifications related to inherent limitations of phenomenological models that are usually constrained by the availability of experimental data. However, first-principles methods are essentially restricted to the study of the zero-temperature electronic and structural properties, while phase transitions for instance require finite-temperature treatment. Despite this temperature limitation, first-principles methods constitute a foundation to a computational scheme combining the advantages of density functional theory predictions together with temperature dependent expansion within the so-called first-principles effective Hamiltonian approach.

In order to overcome the lack of temperature dependency in DFT predictions, a first-principles effective Hamiltonian approach had been proposed by K. Rabe and J.D. Joannopoulos in order to study the displacive phase transition of GeTe [225, 226]. Their approach consisted in *(i)* identifying the relevant degrees of freedom for describing the transition though the local mode approximation of Lines [36] that incorporates lattice instabilities, and *(ii)* performing a low-order expansion of the energy in terms of these degrees of freedom, with coefficients directly determined from total energy DFT calculations

within a well-established procedure [230]. This model was then successfully generalized to ferroelectric perovskite oxides by W. Zhong, K. Rabe and D. Vanderbilt [12, 227, 228]. In what follows, we briefly summarize the effective Hamiltonian approach as it was developed for ferroelectric bulk simple perovskites.

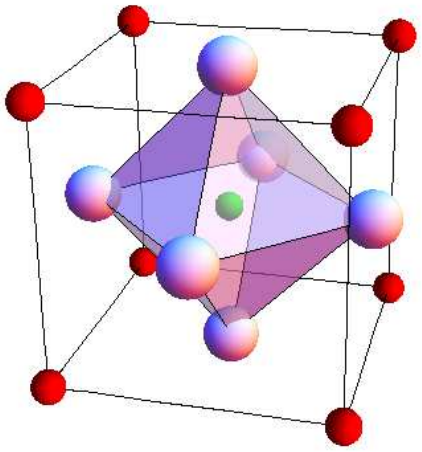

Fig. 2.20: Perovskite cubic structure ABO_3, where A and B atoms are respectively located at the corners and in the center of the cube. The octahedra connect O atoms.

2.2.3.1 General framework

Perovskite structure oxides (Fig.2.20) exhibit a wide range of low temperature structural distortions associated with lattice instabilities of the prototype cubic structure. This class of materials includes a large number of ferroelectrics, characterized by uniform polar distortions and associated lattice relaxation.

Both experiments and first-principles calculations suggest that ferroelectricity involves only small atomic displacements and strain deformations from the equilibrium cubic structure. The first fundamental approximation is thus to represent the energy surface, *i.e.* the total potential energy, by a Taylor expansion around the high-symmetry cubic perovskite structure, including fourth-order anharmonic terms, required to stabilize the low-symmetry ferroelectric phase.

The second approximation follows the soft-mode theory [59] and thereby allow the identification of the relevant degrees of freedom as the unstable phonons of the high-symmetry reference structure, which freeze in to produce the low temperature distorted structure. This approximation simplify the expansion by reducing the number of degrees of freedom per cell from 15 (3 acoustic and 12 optical normal-mode coordinates per k points) to 6, that is the lowest transverse-optical TO modes (*soft-modes*) and the long-wavelength acoustic phonons (*strain variables* η). Since the contribution to the partition function decreases exponentially with increasing energy, these low-energy phonon excitations enable the obtainment of

a simple effective Hamiltonian yielding accurate partition function for studying equilibrium properties at low temperatures.

The effective Hamiltonian therefore acts in the restricted subspace defined by the branches containing the unstable phonons, and consists in a low-order Taylor expansion of the bulk energy around the cubic phase[28] in terms of these relevant degrees of freedom, expansion which coefficients are determined from first-principles calculations. The lowest transverse optical phonon, or *soft-mode*, denoted $\mathbf{u}$, characterizes the collective displacements inside a given primitive cell and can be written as:

$$u_\alpha^j = \sum_\tau \xi_\alpha^\tau(j,\alpha) v_\alpha^\tau \tag{2.48}$$

where ξ_α^τ is the eigenvector of the soft mode phonon and v_α^τ are components of the displacement vector. α goes over x, y, z respectively, τ runs over the different atoms in the unit cell and j is the cell index.

2.2.3.2 Construction of the effective Hamiltonian

With these two fundamental approximations, the effective Hamiltonian consists of five parts[12, 227, 228]: a local mode self energy, a long-range dipole-dipole interaction, a short-range interaction between soft modes, an elastic energy, and an interaction between the local mode and the local strain:

$$E^{\text{tot}} = E^{\text{self}}(\{\mathbf{u}\}) + E^{\text{dip}}(\{\mathbf{u}\}) + E^{\text{short}}(\{\mathbf{u}\}) + E^{\text{elas}}(\{\eta_l\}) + E^{\text{int}}(\{\mathbf{u}\},\{\eta_l\}) \tag{2.49}$$

where $\mathbf{u}$ is the soft mode local amplitude and η_l is the six-component local strain tensor in Voigt notation ($\eta_1 = e_{11}$,$\eta_4 = 2e_{23}$).

Local mode self energy The first term corresponds to the local mode self energy:

$$E^{\text{self}}(\{\mathbf{u}\}) = \sum_i E(\mathbf{u}_i) \tag{2.50}$$

where $E(\mathbf{u}_i)$ is the energy of an isolated local mode at cell $\mathbf{R}_i$ with amplitude $\mathbf{u}_i$, relative to that of the perfect cubic structure. Since ferroelectrcity is intrinsically an anharmonic phenomenon, the expansion contains harmonic and anharmonic contributions up to the fourth order at least:

$$E(\mathbf{u}_i) = \kappa_2 u_i^2 + \alpha u_i^4 + \gamma(u_{ix}^2 u_{iy}^2 + u_{iy}^2 u_{iz}^2 + u_{iz}^2 u_{ix}^2) \tag{2.51}$$

[28] only even-order terms are allowed by the cubic symmetry

where $\mathbf{u}_i$ are local soft-mode vectors in each 5-atom cell i (directly proportional to the local electric dipole moment centered in cell i), $u_i = |\mathbf{u}_i|$ and κ_2, α, and γ are expansion parameters obtained by fitting first-principles results.

Dipole-dipole interaction The second term represents long-range interactions between local modes. The dipole moment associated with the local mode in cell i is $\mathbf{d}_i = Z^*|\mathbf{u}_i|$, where Z^* is the Born effective charge for the soft mode. Z^* is calculated from the eigenvector of the soft-mode [231]:

$$Z^* = \xi_A Z_A^* + \xi_B Z_B^* + \xi_{O\parallel} Z_{O\parallel}^* + 2\xi_{O\perp} Z_{O\perp}^* \tag{2.52}$$

The dipole-dipole energy is written as:

$$E^{\text{dip}}(\{\mathbf{u}\}) = \frac{Z^{*2}}{\epsilon_\infty} \sum_{i<j} \frac{\mathbf{u}_i\mathbf{u}_j - 3(\hat{\mathbf{R}}_{ij}.\mathbf{u}_i)(\hat{\mathbf{R}}_{ij}.\mathbf{u}_j)}{R_{ij}^3} \tag{2.53}$$

where ϵ_∞ is the optical dielectric constant, $R_{ij} = |\mathbf{R}_{ij}|$, $\mathbf{R}_{ij} = \mathbf{R}_i - \mathbf{R}_j$ and $\hat{\mathbf{R}}_{ij} = \mathbf{R}_{ij}/R_{ij}$. In practice, for three-dimensional systems with periodic boundary conditions, an Ewald construction is used to evaluate E^{dip}. It can then be written as:

$$E^{\text{dip}} = \sum_{ij,\alpha\beta} Q_{ij,\alpha\beta} u_{i,\alpha} u_{j,\beta} \tag{2.54}$$

with Q being a matrix:

$$Q_{ij,\alpha\beta} = \frac{2Z^{*2}}{\epsilon_\infty} \left[\frac{\pi}{\Omega_c} \sum_{\mathbf{G}\neq 0} \frac{1}{|\mathbf{G}|^2} \exp\left(-\frac{|\mathbf{G}|^2}{4\lambda^2}\right) \cos(\mathbf{G}.\mathbf{R}_{ij}) G_\alpha G_\beta - \frac{\lambda^3}{3\sqrt{\pi}} \delta_{\alpha\beta}\delta_{ij} \right] \tag{2.55}$$

where $\mathbf{G}$ are the reciprocal lattice vectors, $\mathbf{R}_{ij}$ are the lattice vectors joining sites i and j, Ω_c is the volume of the unit cell and λ denotes the decay of the Gaussian function, or Ewald parameter. Another approximation increasing the computational efficiency is performed by fixing $\mathbf{G}$ and $\mathbf{R}_i$, the atomic position vectors, that is by neglecting the strain dependency of $\mathbf{R}_{ij}$. Thus Q is treated as a constant. α and β denote Cartesian components, i and j run over the cells. and z respectively, i and j run over the cells.

Short-range interaction For the short-range interaction between neighboring local modes, quadratic interactions up to third nearest neighbors with the most general form allowed by the space group symmetry are considered. This contribution yields

$$E^{\text{short}}(\{\mathbf{u}\}) = \frac{1}{2} \sum_{i\neq j} \sum_{\alpha\beta} J_{ij,\alpha\beta} u_{i\alpha} u_{j\beta} \tag{2.56}$$

where $J_{ij,\alpha\beta}$ is the coupling matrix which can be simplified by symmetry consideration. It is a function of R_{ij} and decays quickly with increasing $|R_{ij}|$. For a cubic lattice, there are only seven interaction parameters $j_1, \cdots, j_7$ determined from first-principles calculations and schematically depicted in Fig. 2.21. The couplings matrices for 1^{st}, 2^{nd} and 3^{rd} nearest neighbors (NN) are given by:

$$1^{\text{st}}\text{ NN}: \quad J_{ij,\alpha\beta} = (j_1 + (j_2 - j_1)|\hat{R}_{ij,\alpha}|)\delta_{\alpha\beta} \tag{2.57}$$

$$2^{\text{nd}}\text{ NN}: \quad J_{ij,\alpha\beta} = (j_4 + \sqrt{2}(j_3 - j_4)|\hat{R}_{ij,\alpha}|)\delta_{\alpha\beta} + 2j_5\hat{R}_{ij,\alpha}\hat{R}_{ij,\beta}(1 - \delta_{\alpha\beta}) \tag{2.58}$$

$$3^{\text{rd}}\text{ NN}: \quad J_{ij,\alpha\beta} = j_6\delta_{\alpha\beta} + 3j_7\hat{R}_{ij,\alpha}\hat{R}_{ij,\beta}(1 - \delta_{\alpha\beta}) \tag{2.59}$$

where $\hat{R}_{ij,\alpha}$ is the α component of $\mathbf{R}_{ij}/R_{ij}$.

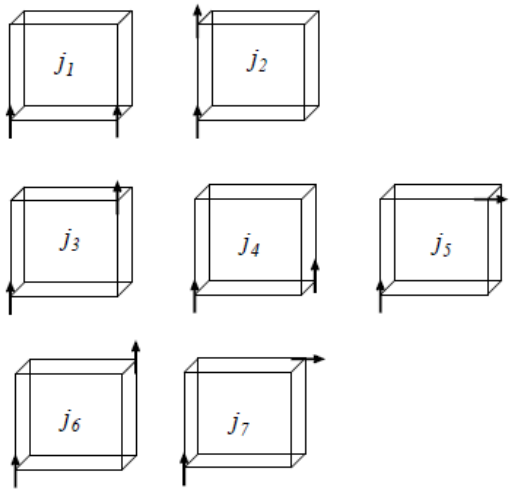

Fig. 2.21: Independent intersite interactions corresponding to the parameters j_1, j_2 (first neighbor), j_3, j_4, j_5 (second neighbor), and j_6, j_7 (third neighbor). (After Zhong *et al.* [226]).

Elastic energy The fourth term in the energy sum is the elastic energy which accounts for both the homogeneous η_H and inhomogeneous η_I strains:

$$E^{\text{elas}}(\{\eta\}) = E_I^{\text{elas}}(\{\eta_I\}) + E_H^{\text{elas}}(\{\eta_H\}) \tag{2.60}$$

Using the Voigt convention, $\eta_1 = \eta_{xx}$, $\eta_2 = \eta_{yy}$, $\eta_3 = \eta_{zz}$, $\eta_4 = \eta_{xz}$, $\eta_5 = \eta_{yz}$ and $\eta_6 = \eta_{xy}$, the homogeneous strain can be written as:

$$\begin{aligned} E_H^{\text{elas}}(\{\eta_H\}) &= \frac{N}{2} B_{11}(\eta_{H,1}^2 + \eta_{H,2}^2 + \eta_{H,3}^2) \\ &+ N\, B_{12}(\eta_{H,1}\eta_{H,2} + \eta_{H,2}\eta_{H,3} + \eta_{H,3}\eta_{H,1}) \\ &+ \frac{N}{2} B_{44}(\eta_{H,4}^2 + \eta_{H,5}^2 + \eta_{H,6}^2) \end{aligned} \tag{2.61}$$

where B_{11}, B_{12} and B_{44} are elastic constants determined from first-principles calculations, and N the number of primitive cells composing the supercell. The inhomogeneous term is better expressed in terms of dimensionless local displacements $\mathbf{v}(\mathbf{R}_i)$. Translation and rotation invariances require the expansion of the energy in terms of differences between the $\mathbf{v}(\mathbf{R}_i)$:

$$\begin{aligned} E_I^{\text{elas}} &= \sum_i \{\gamma_{11}[v_x(\mathbf{R}_i) - v_x(\mathbf{R}_i \pm \mathbf{x})]^2 \\ &+ \gamma_{12}[v_x(\mathbf{R}_i) - v_x(\mathbf{R}_i \pm \mathbf{x})][v_y(\mathbf{R}_i) - v_y(\mathbf{R}_i \pm \mathbf{y})] \\ &+ \gamma_{44}[v_x(\mathbf{R}_i) - v_x(\mathbf{R}_i \pm \mathbf{y}) + v_y(\mathbf{R}_i) \\ &- v_y(\mathbf{R}_i \pm \mathbf{x})]^2 + \text{ cyclic permutations}\} \end{aligned} \tag{2.62}$$

corresponding to bond stretching, bond correlation and bond bending, respectively, with $\mathbf{x} = a\hat{x}$, $\mathbf{y} = a\hat{y}$ and $\mathbf{z} = a\hat{z}$. The γ coefficients are related to the elastic constants by $\gamma_{11} = B_{11}/4$, $\gamma_{12} = B_{12}/8$ and $\gamma_{44} = B_{44}/8$.

Elastic-mode interaction The last term in the energy form is the contribution stemming from on-site elastic strains and local modes interaction[29]:

$$E^{\text{int}}(\{\mathbf{u}\}, \{\eta_l\}) = \frac{1}{2} \sum_i \sum_{l\alpha\beta} B_{l\alpha\beta}\ \eta_l(\mathbf{R}_i)\, u_\alpha(\mathbf{R}_i)\, u_\beta(\mathbf{R}_i) \tag{2.63}$$

Cubic symmetry considerations yield three independent coupling constants $B_{l\alpha\beta}$:

$$\begin{aligned} B_{1xx} &= B_{2yy} = B_{3zz} \\ B_{1yy} &= B_{1zz} = B_{2xx} = B_{2zz} = B_{3xx} = B_{3yy} \\ B_{4yz} &= B_{4zy} = B_{5xz} = B_{5zx} = B_{6xy} = B_{6yx} \end{aligned} \tag{2.64}$$

2.2.3.3 Generalization of H_{eff} to mixed compounds

The effective Hamiltonian approach is not restricted to pure ABO_3 compounds and can be generalized to solid solutions, such as $PbZr_{1-x}Ti_xO_3$ (PZT) [233, 234] or to the relaxor

[29] This term is particularly important in ferroelectrics and, for instance, at the origin of the piezoelectric response.

$PbSc_{1-x}Nb_xO_3$ (PSN) [47, 232, 235].

For such $A(B'B'')O_3$ compounds, the generalization consists in *(i)* considering an averaged Hamiltonian within the virtual crystal approximation [236, 237] accounting for the energy of a hypothetical $Pb\langle B\rangle O_3$ system in which $\langle B\rangle$ is a virtual atom averaging between B′ and B″ and *(ii)* including first-order correction terms that take into account the real nature of atom on the B-site, i.e., B′ or B″. The total energy is thus written as a sum of two energies and has the form

$$E(\{\mathbf{u}_i\},\{\mathbf{v}_i\},\eta_H,\{\sigma_i\}) = E_{\text{ave}}(\{\mathbf{u}_i\},\{\mathbf{v}_i\},\eta_H) + E_{\text{loc}}(\{\mathbf{u}_i\},\{\mathbf{v}_i\},\{\sigma_i\}) \tag{2.65}$$

where $\mathbf{u}_i$ is the local soft mode in cell i, $\{\mathbf{v}_i\}$ are the dimensionless local displacements which are related to the inhomogeneous strain variables inside each cell, η_H is the homogeneous strain tensor, and $\{\sigma_i\}$ is the set of variables characterizing the atomic configuration of the alloy ($\sigma_i = 1$ for B′ and -1 for B″).

The average term E_{ave} depends only on the soft mode and strain variables, and has the same analytical expression as Eq.(2.49). It thus consists of five parts: a local-mode self-energy, a long-range dipole-dipole interaction, a short-range interaction between soft modes, an elastic energy, and an interaction between the local modes and local strain. E_{ave} is fitted as previously described for simple compounds only from DFT calculations performed on a uniform virtual system $Pb\langle B\rangle O_3$ that compositionally averages the potentials of the pure parent compounds

$$V_{\text{VCA}} = (1-x)\,V_{PbB'O_3} + x\,V_{PbB''O_3} \tag{2.66}$$

The local corrections term E_{loc} involves the $\{\sigma_i\}$ parameters and includes *(i)* on-site effect of alloying on the self-energy up to the fourth order in the local-mode vector $\mathbf{u}_i$, and *(ii)* intersite contributions linear in $\mathbf{u}_i$ and in $\mathbf{v}_i$:

$$\begin{aligned} E_{\text{loc}}(\{\mathbf{u}_i\},\{\mathbf{v}_i\},\{\sigma_i\}) &= \sum_i \left[\Delta\alpha(\sigma_i)u_i^4 + \Delta\gamma(\sigma_i)(u_{ix}^2u_{iy}^2 + u_{iy}^2u_{iz}^2 + u_{iz}^2u_{ix}^2)\right] \\ &+ \sum_{ij}\left[Q_{ji}(\sigma_j)\mathbf{e}_{ji}.u_i + R_{ji}(\sigma_j)\mathbf{f}_{ji}.\mathbf{v}_i\right] \end{aligned} \tag{2.67}$$

where $\mathbf{e}_{ji}$ and $\mathbf{f}_{ji}$ are unit vectors joining site j to the center of $\mathbf{u}_i$ and $\mathbf{v}_i$. The parameters $\Delta\alpha(\sigma_i)$, $\Delta\gamma(\sigma_i)$, $Q_{ji}(\sigma_j)$ and $R_{ji}(\sigma_j)$ are derived by performing first-principles calculations on small supercells in which a true atom is surrounded by virtual atoms.

2.2.3.4 Physical properties

Once the effective Hamiltonian is fully determined, it can be subjected to classical Monte Carlo [12, 227, 238, 240] or molecular dynamics [241] simulations in order to access finite-temperature properties of the considered materials[30].

Such calculations are usually performed with periodic boundary conditions and typically require $12\times12\times12$ supercell. As an output, one can access the mean values $\langle\mathbf{u}\rangle$ and $\langle\eta\rangle$ in terms of temperature, external pressure and electric field. The macroscopic polarization is also accessible since it is directly proportional to the amplitude of the local mode $\mathrm{P_i} = (1/\Omega_c)\mathrm{Z^\star u_i}$ where $Z^\star$ is the Born effective charge of the mode and Ω_c is the unit cell volume. In addition to the phase transition sequences and transitions temperatures, simulations also give direct access to the temperature dependence of various functional properties such as dielectric and piezoelectric responses (through the correlation function approach [245]).

Among the achievements enabled by the first-principles-based effective Hamiltonian approach has been the quantitative assessment of the ferroelectric instability. Following the initial idea of Cochran [59], the ferroelectric instability of ABO_3 compounds can be regarded as a collective phenomenon arising from the competition between short-range covalent repulsions which favor the cubic phase, and long-range Coulomb interactions which favor the ferroelectric state. Beyond the qualitative picture, first-principles effective Hamiltonian simulations allowed to reinvestigate this model and to enhance the microscopical understanding of the interplay between electronic and dynamical properties in generating the ferroelectric instability.

ABO_3 perovskite structures can be subject to competing structural instabilities. The two most common instabilities result from the softening of either a polar zone-center phonon mode, leading to a FE phase, or the softening of a non-polar zone-boundary mode involving rotations of oxygen octahedra, leading to an antiferrodistortive (AFD) phase. When different kinds of instabilities are present and compete with each other, the effective Hamiltonian model can be extended in order to include properly all the relevant ionic degrees of freedom, such as antiferrodistortive degrees of freedom [238, 239]. Polar and non-polar instabilities compete in a delicate way and tend to suppress one another, yielding rich phase diagrams showing a large variety of different structures (see for example $PbZr_{1-x}T_xO_3$ phase diagram near its morphotropic phase boundary in Fig. 2.22 [233, 244]).

First-principles-based approach within the effective Hamiltonian framework have also been used to address the relaxor behavior. Let us report the comparative study of $PbSc_{1/2}Nb_{1/2}O_3$, a ferroelectric with relaxor-like characteristics, and $PbZr_{60}Ti_{40}O_3$,a normal ferroelectric, by means of the generalized effective Hamiltonian for mixed compounds [48]. The main con-

[30] Quantum Monte Carlo simulations have also been reported [242, 243], allowing to assess the effects of quantum fluctuations on structural phase transitions

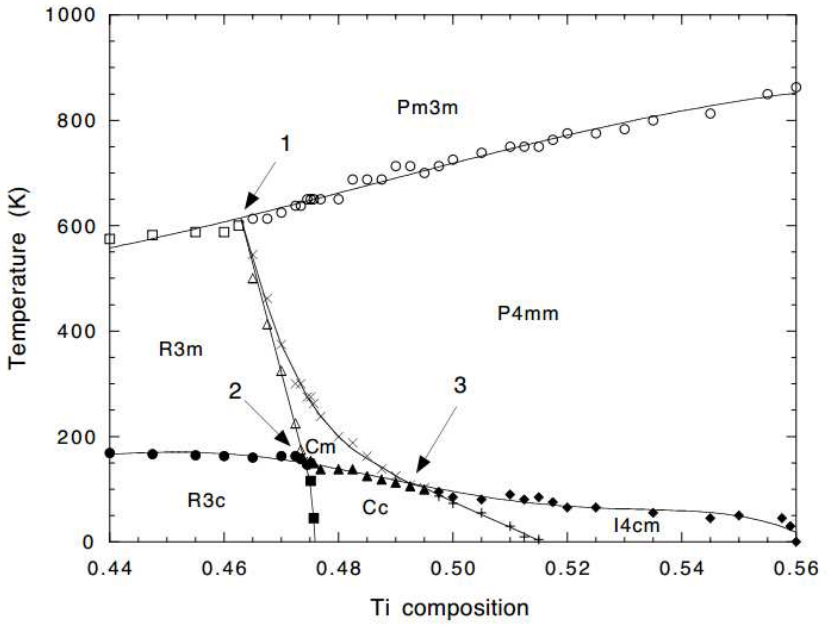

Fig. 2.22: Phase diagram of $PbZr_{1-x}T_xO_3$ near the MPB, as predicted by a first-principles-derived scheme that incorporates ferroelectric and antiferrodistortive degrees of freedom. In addition to recovering five of the well-known expected phases (namely, the paraelectric $Pm\bar{3}m$, FE rhombohedral $R3m$, FE tetragonal $P4mm$, FE monoclinic Cm, and the rhombohedral $R3c$ phases), accounting for both FE and AFD motions leads to the prediction of a sixth phase, a monoclinic Cc ground state at intermediate Ti compositions, thereby resolving controversies about its nature. Moreover, a seventh phase $I4cm$ emerges as a discovery for the largest displayed Ti compositions. (After Kornev *et al.* [244]).

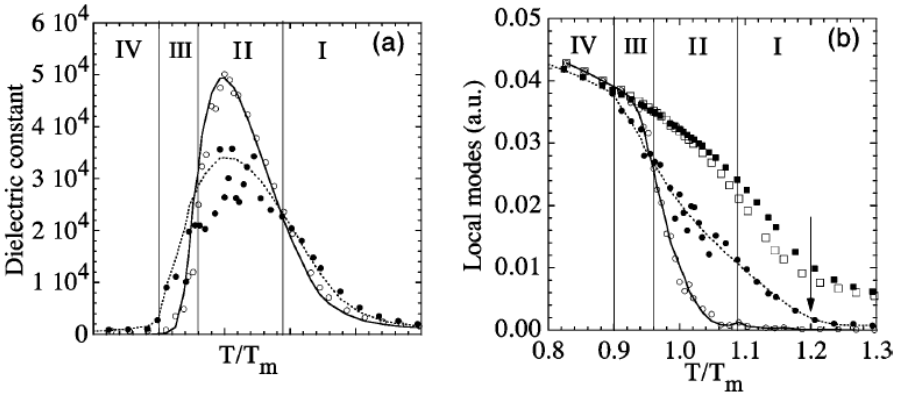

Fig. 2.23: Properties of PZT (open dots), and PSN (filled dots), as a function of T/T_m. Panel (a) shows one third of the trace of the dielectric susceptibility tensor directly obtained from MC simulations. Dots in panel (b) show the supercell averaged mean component of the local modes. The arrow in panel (b) emphasizes the highest temperature at which the polarization begins to develop in PSN (After Iniguez *et al.* [48]).

clusions of this study are the following: unlike in PZT, it was found that PSN exhibits a broad dielectric response and a high-temperature polarization tail (Fig. 2.23). The results show that the static simulations of PSN reproduce the broad dielectric peak measured in

relaxors, which implies that the relaxor behavior is not a purely dynamic effect, as it exhibits a static component. Moreover, oscillations across T_m in the case of PSN (Fig. 2.23) are put in relation with complicated multiminima free energy landscape. Such features are attributed to the breaking of the macroscopic symmetry at the nanoscale due to the large internal electric fields associated with the heterovalent PSN alloy. It was concluded that the broad peak has also a static component, i.e., it is not only due to dynamical effects. The picture of a macroscopic sample as a collection of noninteracting nanometric regions, each associated with its own locally large anisotropic internal field, was found to be sufficient to yield typical static relaxor features.

A recent study [169] aiming at gaining microscopic insight into the properties of $Ba(Zr_{50}, Ti_{50})O_3$ relaxor ferroelectric, showed that, in this particular system, turning off random fields and random strains does not significantly affect the results. On the other hand, the computations revealed that it is the difference in polarizability between Ti and Zr ions that leads to the relaxor behavior in BZT. It was found that the average magnitude of the local modes centered on Zr are much smaller than those centered on Ti, and while the temperature behavior of the former shows a continuous shrinking of the magnitude with decreasing temperature, that of Ti on the opposite reveals an enlargement of the magnitude. Moreover, it was shown that large chemically ordered regions were not necessary to reproduce the relaxor behavior.

2.2.4 Gauge modified effective Hamiltonian for relaxors

We now provide the methodology pertaining to the gauge-implementation in the effective Hamiltonian so as to recover the relaxor behavior. The gauge-modified effective Hamiltonian is then applied to a specific relaxor, namely, disordered $(Pb_{1-3/2x}La_x)(Zr_yTi_{1-y})O_3$ solid solutions, extensively studied for their promising characteristics for various applications [155].

These compounds have substitutional disorder on both the A and B sites of the perovskite structure. The B-site disorder (the replacement of Zr^{4+} with Ti^{4+}) alone leads to the well known ferroelectric PZT [233, 244], whereas the additional A-site disorder (the additional La^{3+} substitution for Pb^{2+}) can induce the relaxor behavior within a certain concentration range of lanthanum [166, 246]. Substitution of La^{3+} for Pb^{2+} and accompanying A- and B-vacancies, i.e., $2La^{3+} \rightarrow 1V_{Pb}$ and $4La^{3+} \rightarrow 1V_{Zr/Ti}$, can substantially affect the involved energetics by disrupting the balance between competing short and long ranged interactions [247–249].

As already pointed out (chapter 1), in complex structures such as relaxor ferroelectrics, the condition of balance between competing ordering and disordering interactions has to be assessed on a local scale rather than on a global one, since the only consideration of the global scale may conceal the underlying local effects [6]. Indeed, relaxor ferroelectrics

exhibit significant structural distortions occurring at the local scale that are not reflected in the average global structure which remains cubic [7–11]. While the average structure determined by crystallography presents a global view of the structure (point or space groups), the relevance of the local, short-range point of view to the properties of relaxors has a direct implication for the method of theoretical analysis.

We thus adopt the local point of view since our approach essentially consists in accounting for *continuous local symmetry*, and stands on a generalization of the first-principles-derived effective Hamiltonian of Ref.[12], so as to incorporate gauge fields, in addition to ferroelectric and elastic degrees of freedom. Constructed in a manifestly gauge-invariant manner, this new theoretical framework encompasses the local signature of relaxors and aims at getting deeper insight into underlying mechanisms. In the following, we will explicit the two main steps involved in the construction of this model.

2.2.4.1 Gauge-invariant short-range interaction

A crucial feature in our construction thus revolves around the observation that *short-range* interactions and *local* structure play the major role in driving relaxor behavior [7–11]. We are then motivated to restrict the gauge-implementation to the short-range interaction (Eq.(2.56)) in the effective Hamiltonian.

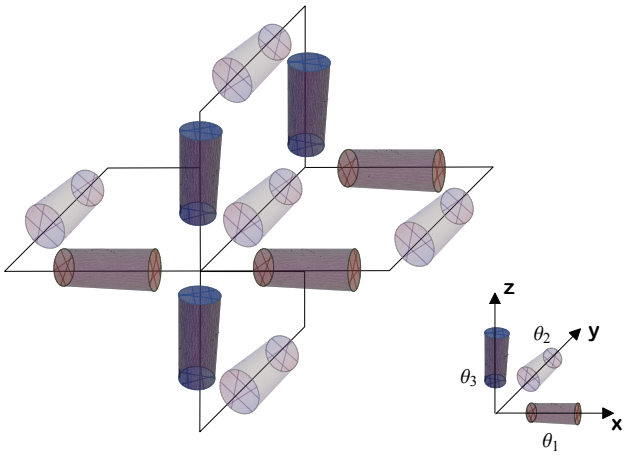

Fig. 2.24: Schematic illustration of the global directional SO(2) symmetry of the first nearest neighbors short-range interaction. Local modes vectors attached to the vertices are omitted. Cylinders, each of which axes coincide with either the x, y or z direction, represent rotations by angles θ_1, θ_2 and θ_3 respectively (three different colors). These rotation angles affect all points in the lattice equivalently, *i.e.*, they are independent of the lattice point i. E^{short} is thus invariant under global directional SO(2) rotations acting in the internal space of the dipole moments $\mathbf{u}_i$ in the plane perpendicular to the linking direction $\hat{\mathbf{R}}_{ij}$.

The short-range interaction among first nearest neighbors features directional anisotropy (Eq.(2.57)) with respect to which it is readily seen that E^{short} displays a global directional SO(2) symmetry. This is schematically depicted in Fig. 2.24, where depending on the direction ($\hat{\mathbf{R}}_{ij}$ along x, y or z) linking two first nearest neighbors local modes, cylindrical SO(2) rotation operations (by angles θ_1, θ_2 and θ_3, respectively) such that the axes around which the rotation is performed coincides with the linking direction $\hat{\mathbf{R}}_{ij}$, leave E^{short} invariant. In this case the invariance is global, *i.e.*, the rotation angles θ_1, θ_2 and θ_3 exhibit no spatial dependence.

The postulate we make resides in the extension of this global symmetry to the *local* scale, thus allowing independent transformations of individual $\mathbf{u}_i$ while the remaining system stays unaffected. In such a construction, the angles θ_1, θ_2 and θ_3 now acquire a spatial dependence on the lattice points i, *i.e.*, $\theta_1(i)$, $\theta_2(i)$ and $\theta_3(i)$ (Fig.2.25). This requires the introduction of compensating gauge fields, needed to ensure the postulated invariance under the action of the local directional SO(2) group G. The gauge degrees of freedom are then position-dependent rotational matrices U_{ij} taking values in the gauge group G and assigned to every link between neighboring sites i and j. They satisfy the condition $U_{ij} = U_{ji}^{-1}$and act as parallel transporters between adjacent sites. Simultaneous transformations operating on local modes $u_i \mapsto g_i u_i$ and links $U_{ij} \mapsto g_i U_{ij} g_j^{-1}$ with $g_i \in G$ leave the product $u_i U_{ij} u_j$ unaltered (Eq.(2.28)).

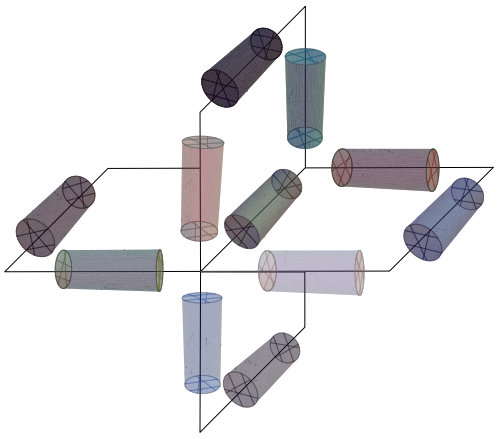

Fig. 2.25: Schematic illustration of the local directional SO(2) symmetry of the first nearest neighbors short-range interaction. Local modes vectors attached to the vertices are omitted. From each lattice site i stem three cylinders, each of which axes coincide with either the x, y or z direction. These cylinders represent space-dependent rotations (as many colors as there are rotations) by angles $\theta_1(i)$, $\theta_2(i)$ and $\theta_3(i)$ respectively, and are associated with the compensating gauge fields that have been introduced so as to guarantee the invariance of E^{short} under local directional SO(2) rotations acting in the internal space of the dipole moments $\mathbf{u}_i$ in the plane perpendicular to the linking direction $\hat{\mathbf{R}}_{ij}$.

The presence of the additional local gauge symmetry thus implies the form of the coupling between local modes and gauge fields, the gauge-invariant form of the short-range interaction yields:

$$E_{\mathrm{FE-G}}(\{\mathbf{u}_i\},\{U_{ij}\}) = \frac{1}{2}\sum_{\substack{i\neq j\\ \alpha,\beta}} J_{ij,\alpha\beta}u_{i\alpha}U_{ij,\alpha\beta}u_{j\beta}, \tag{2.68}$$

with

$$U_{ij} = \exp\left(-i\theta_k(i)T^k\delta_{|\hat{\mathbf{R}}_{ij}|,k}\right) \in G \tag{2.69}$$

Here T^k are the three SO(3) generators. U_{ij} are elements of the local directional SO(2) group and can be expressed as 3×3 matrices, *i.e.*, U_{ij} are embedded in SO(3). The parameters $\boldsymbol{\theta}(i) = (\theta_1(i),\theta_2(i),\theta_3(i))$ are specific to each lattice points i with $\theta_k(i) \in [-\pi,\pi)$. The requirement of local gauge invariance for E^{short} has thus resulted in the introduction of a rotation U_{ij} with each bond ij[31]. The effect of the gauged interaction is to favor, energetically, a certain relative orientation for each pair of interacting local modes, rather than merely ferroelectric alignment.

The energy of the gauge degrees of freedom can be written as a sum over elementary squares (plaquettes, Eq.(2.29), Fig. 2.7) of links in the lattice [14, 186]:

$$E_{\mathrm{G}}(\{\mathbf{U}_{ij}\}) = k\sum_{\square} E_{\square} = k\sum_{\square}\left(1-\frac{1}{3}\mathrm{Tr}[\mathbf{U}_{\square}]\right), \tag{2.70}$$

where $\mathbf{U}_{\square} = U_{ij}U_{jk}U_{kl}U_{li} \in \mathrm{SO}(3)$ is the product of transporters around a plaquette, and k is the coupling parameter, which governs the strength of the gauge field self-interaction. We note that since U_{ij} matrices need to be chosen with respect to the directional anisotropy (*i.e.*, the axis of rotations $\hat{\mathbf{R}}_{ij}$ are different for these matrices) the product belongs to SO(3). The gauge-field energy then is a scalar obtained by taking the trace of the product.

The extension of the global directional SO(2) symmetry as featured by the short-range interaction among first nearest neighbors to the local scale consequently leads to a gauge-modified effective Hamiltonian $\tilde{E}_{tot}$ that can be formally cast into the form:

$$\tilde{E}_{tot} = E_{\mathrm{FE}}(\{\mathbf{u}_i\},\{\eta\}) + E_{\mathrm{G}}(\{U_{ij}\}) + E_{\mathrm{FE-G}}(\{\mathbf{u}_i\},\{U_{ij}\}) \tag{2.71}$$

[31] The effective Hamiltonian respects the cubic symmetry. However some terms in it such as E^{short}, possess a higher symmetry. If all the terms entering in the Hamiltonian were to be made gauge invariant, then the corresponding gauge group would have been $m\bar{3}m \triangleright \mathrm{T}(3)$ where T(3) is the 3-parameter translation group, with at least two different gauge fields [17]. In such a case the resulting gauge group would have been discrete. This approach is used, for example, to treat disclinations and dislocations in continuum approximation [17] (section 2.1.5). The restriction of the gauge-implementation to E^{short} is an approximation motivated by the observation that short-range interaction plays a major role in driving relaxor behavior. Unlike the Heisenberg Hamiltonian, the short-range interaction E^{short} in perovskites features directional anisotropy, with respect to which there is a global and continuous intrinsic symmetry. This is the reason why rendering it local involves the introduction of matrices (the gauge field) from SO(2) rather than from SO(3).

with E_{FE} being the energy of the parent PZT system provided in Eq.(2.65)[233, 234], where $\{\mathbf{u}_i\}$ are the local modes, directly proportional to the electrical dipole moments and $\{\eta\}$ are the homogeneous and inhomogeneous strain tensors. E_{G} and $E_{\mathrm{FE-G}}$ on the other hand are the additional terms gathering gauge degrees of freedom $\{U_{ij}\}$, and their couplings with ferroelectricity. The first-principles obtained coefficients involved in this effective Hamiltonian are listed in Table 2.26. We note that additional parameters are introduced by the gauge-implementation, namely, the self-coupling parameter of the gauge field, k, and the angles parameters $\boldsymbol{\theta}(i) = (\theta_1(i), \theta_2(i), \theta_3(i))$ of the rotational matrices U_{ij}, they will be addressed in the following section.

Lattice constant (P= −4.68 GPa)	$a = 7.56$
Born effective charge	$Z^\star = 7.342$
Optical dielectric constant	$\epsilon_\infty = 7.15$
Soft mode on-site energy	$\kappa_2 = 0.0138 \quad \alpha = \gamma = 0$
Soft mode 1st NN interaction	$j_1 = -0.00577 \quad j_2 = 0.014245$
Soft mode 2nd NN interaction	$j_3 = 0.0014016 \quad j_4 = -0.00094$ $j_5 = 0.00141$
Soft mode 3rd NN interaction	$j_6 = 0.000062 \quad j_7 = 0.000031$
Elastic constants	$B_{11} = 5.22 \quad B_{12} = 1.67$ $B_{44} = 1.215$
Elastic - Soft mode interaction	$B_{1xx} = -0.374 \quad B_{1yy} = -0.1545$ $B_{4yz} = -0.068$
On-site alloying (Zr) $\sigma_i = 1$ (40% Ti)	$\Delta\alpha = 0.016 \quad \Delta\gamma = -0.022$
On-site alloying (Ti) $\sigma_i = -1$ (40% Ti)	$\Delta\alpha = 0.01 \quad \Delta\gamma = 0.003$
Alloy - Soft mode 1st NN coupling	$Q_{i1}/2 = 0.0008001$
Alloy - Soft mode 2nd NN coupling	$Q_{i2}/(2\sqrt{2}) = -0.0001007$
Alloy - Soft mode 3rd NN coupling	$Q_{i3}/(2\sqrt{3}) = -0.0000512$
Alloy - Strain coupling	$R_{i1}/\sqrt{3} = -0.0071997$

Fig. 2.26: First-principles derived coefficients in the case of PZT with 60% of Zr and 40% of Ti [233, 244].

2.2.4.2 Quenched and dynamic contributions to disorder

It is widely believed that both *dynamic and quenched* defects associated with compositional inhomogeneities play a major role in the behavior of relaxors. In this second step, we are therefore led to study an intermediate situation where there is inherent quenched as well as dynamic disorder. On another hand, local symmetry has proven to be reliable in describing defects (section 2.1.5) and in probing disorder-induced frustration (section 2.1.4). Specifically, gauge approaches have been resorted to in order to account for the twofold nature of disorder, *i.e.*, for its randomly quenched component and its thermally fluctuating dynamical one (section 2.1.4.3). We here leverage on this ability of gauge approaches to handle such

features. Within our model, disorder and frustration are provided by a random gauge-field type of interaction.

Expressly, quenched disorder is introduced via fixing links on the lattice and can be thought of as arising due to an explicit breaking of the local symmetry. To mimic random La^{3+}-disorder, we thus fix the rotation angles of adjacent links U_{ij} defining the edges of cubes enclosing randomly selected A-sites (upper panel of Fig. 2.27 and Fig. 2.28). These quenched links[32]

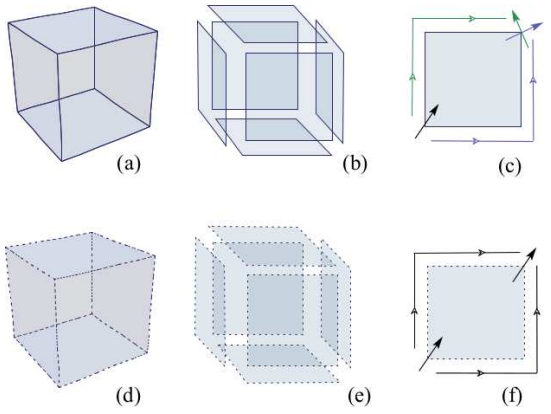

Fig. 2.27: Schematic view of two unit cells (cubes) centered around La^{3+} (a) and Pb^{2+} (d). Solid lines indicate quenched links, whereas dotted lines signal relaxing ones. The boundaries of each cube consists of six (b) curved (frustrated) or (e) flat (unfrustrated) plaquettes. Panels (c) and (f) show the parallel transport of a vector around a curved and flat plaquette, respectively.

are drawn independently and uniformly from G, so as to introduce genuine frustration[33]. An elementary plaquette $\mathbf{U}_{\square}$ in Eq. (2.70) determines the frustration-induced *local curvature*[34] of the gauge fields, *i.e.*, it measures the difference in orientation of a vector being transported along the two paths on a plaquette, as depicted in Fig. 2.27(c,f). Each elementary quenched cube (La^{3+}-containing) consisting of six randomly frustrated plaquettes (Fig. 2.27(b,c)) thus introduces non-trivial constraints on the gauge field[35] which force the system to locally deviate from energetically optimizing configurations. There is here a mechanism analogous to that in spin glasses which produces complicated behavior leading to ground state degeneracy.

[32] By fixing the links around La^{3+} ions we also assume that the dynamics of the corresponding quenched defects is much slower then the dynamics of the local modes.

[33] By frustration of a plaquette, we mean that the angles associated to the four links making up the plaquette cannot simultaneously minimize all the bond energies for the neighboring local modes in $E_{\mathrm{FE-G}}$ (Eq.(2.68)).

[34] Indeed, in the continuum limit $a \to 0$, the link variable $U_{i,\mu}$, assigned to the link stemming from the lattice site i to its nearest neighbor $i + a\hat{\mu}$ in direction μ, can be viewed as $\exp[a\mathcal{A}_{\mu}(i)]$ and the plaquette variable, $U_{\square}$ as $\exp[a^2\mathcal{F}_{\mu\nu}(i) + \mathcal{O}(a^3)]$, where $\mathcal{F}_{\mu\nu}$ is the curvature tensor. The link product is then nothing but a parallel transporter around a closed loop which determines curvature. In this sense, the $1 - \frac{1}{3}\mathrm{Tr}[U_{\square}]$ term appearing in the Wilson action of Eq.(2.70) can be seen as a measure of deviation from flatness. Indeed, in the case of trivial identity link matrices, the traced plaquette variable amounts to three, yielding vanishing energy term.

[35] As a matter of fact, each set of links assigned to the edges of a quenched cube is in violation of the Bianchi identity [23].

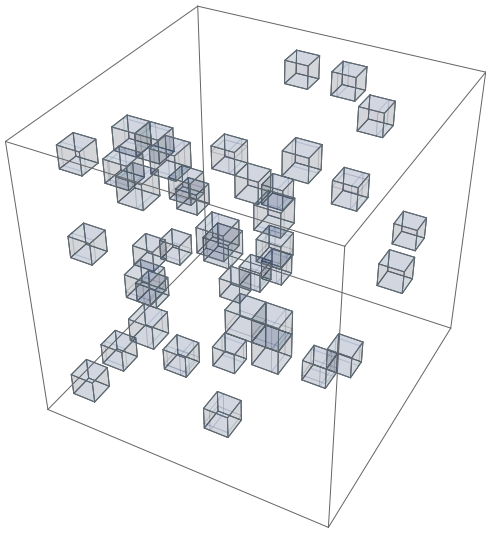

Fig. 2.28: Schematic view of the random La^{3+}-disorder in the supercell. La^{3+}-containing unit cells are the elementary blue cubes whose edges are associated to quenched links.

Other links (defining the edges of Pb^{2+}-containing unit cells, lower panel of Fig. 2.27) are initially set to identity and treated as *fluctuating* quantities, *i.e.*, on the same footing as local modes and the strain[36].

We now address that additional parameters introduced by the gauge-implementation, namely, the self-coupling parameter of the gauge field, k, and the angles $\boldsymbol{\theta}(i) = (\theta_1(i), \theta_2(i), \theta_3(i))$ of the rotational matrices U_{ij}. Since disorder originates from the randomly quenched gauge field which are coupled through the k parameter, the gauge term E_{G} can be seen as the energy of disorder, while the term $E_{\mathrm{FE-G}}$ represents the short-range interaction between local dipole moments in the presence of disorder. Relaxor behavior is thought to precisely arise from the synergy of competing yet balanced interactions[6]. Asymptotically, a very weak disorder will leave the system unaffected and the order intact, while a very strong one will preclude any form of ordering. The two parameters of the model, namely the coupling parameter k and the angular interval, effectively control the degree of frustration and the strength of quenched disorder in the system.

Insight into the evolution of disorder is gained by considering Eq. (2.70) as a function of βk while disregarding all other terms in the effective Hamiltonian, *i.e.*, by pure-gauge considerations. In this case, the probability of a gauge configuration is proportional to $\exp(-\beta E_G)$. Figure 2.29 shows the plaquette energy $E_{\square}$ as a function of βk. Let us mention that in a pure gauge theory, the k parameter entering in Eq. (2.70) can be seen as an inverse temperature with the plaquette energy playing the role of internal energy of the system in analogy with statistical mechanics [16]. A regime of weak coupling (small k) corresponds to high

[36]Let us note again that this approach can be put in conceptual relation with that of the gauge glass model of Dzyaloshinskii and Volovik [21], who endowed the gauge field with both static and dynamic contributions, the former being associated to the quenched defects while the latter is ascribed to thermal fluctuations, and thus to thermally produced defects.

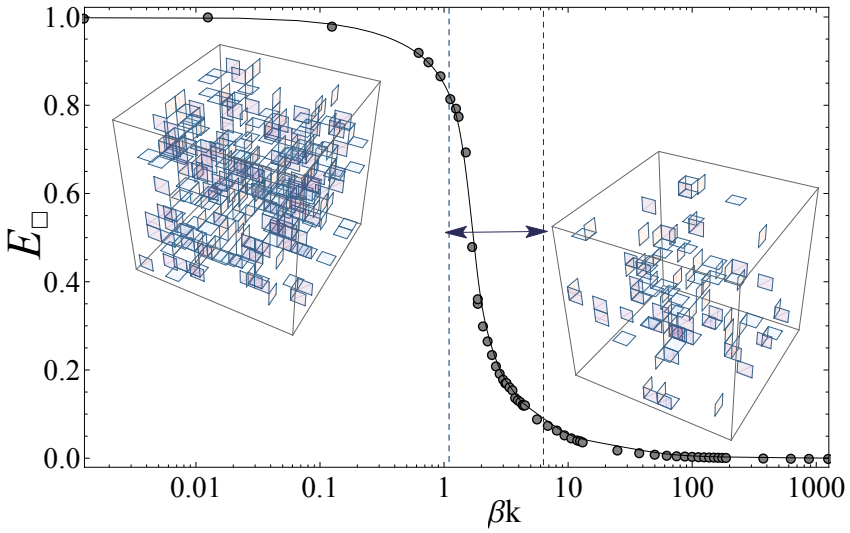

Fig. 2.29: The plaquette energy $E_\square$ as a function of βk, with k the gauge coupling parameter and β the inverse temperature, on a 12^3 cubic lattice with cold start configuration (*i.e.* all links are initially set to unit matrices). The temperature is kept fixed at high values in the course of this simulation. Right and left insets show snapshots of plaquettes $\mathbf{U}_\square$ that deviate from unity for high and low values of βk, respectively.

temperature, whereas strong coupling becomes equivalent to low temperature. However, the analogy is only formal and the true physical temperature of the pure-gauge field is zero. On the other hand, since our interest is to study thermally activated configurations, we need to introduce the temperature, and this is achieved by considering βk at high temperatures, T$\sim$ 2000 K. Although no phase transition is expected for this pure-gauge case of Eq. (2.70) in three dimensions, there is a pronounced crossover region in the plaquette energy, as marked by dashed lines and indicated by an arrow in Fig. 2.29. The density of frustrated plaquettes undergoes a rapid change as we proceed through the crossover region marked by dashed lines. This crossover is thought to be reminiscent of phase transitions occurring in higher dimensions [16, 250]. Clearly, in the asymptotic $k \to \infty$ limit, a starting configuration is frozen-in, effectively breaking the gauge symmetry and suppressing fluctuations of the link angles $\theta_k(i)$. This limit thus corresponds to vanishing gauge-disorder.We numerically found that the interplay between ferroelectricity and gauge fields is most pronounced when the angular interval for quenched links[37] is $[-\pi/2, \pi/2]$ and k is in the crossover region. Technically, since the energy of a gauge configuration is given by Eq. (2.70), and the probability with which the thermal fluctuations can generate that configuration is proportional to $\exp(-\beta E_G)$, with β being the inverse temperature, k was chosen such that the product βk is within the crossover

[37]Three extreme cases for the choice of quenched $\{U_{ij}\}$ can be pointed out. Indeed, (1) by setting the links to unity, one recovers the usual ferroelectric model, (2) for $G = Z_2$ the model can be seen as the one of ferroelectrics with local frustration arising from competing ferroelectric and antiferroelectric interactions, and (3) we expect that our model with *fully quenched* random link variables and the corresponding angles, uniformly distributed between $-\pi$ and π, is similar to the gauge glass model [200, 251].

region (see Fig. 2.29) at high temperatures, we found $k = 0.05$. This value is obtained by taking $k\beta = 6.35\times$ T/(3.18×10^5) where T=2500 K corresponds to the non-rescaled fixed temperature.

As for the distribution of the random gauge rotations associated with the remaining fluctuating links, those angles to be independent and identically distributed with the Haar measure (see footnote 16). This describes the case in which all twists are equally possible.

Let us stress that knowing the exact relation between La^{3+} induced vacancies at A/B-sites and gauge fields would allow us to calculate the value of k in Eq. (2.70) from first-principles. Instead, we mimic the presence of defects in the way it is done in the gauge theory of defects (*i.e.*, by introducing frustration in the gauge field) and check the entire range for the parameter. We then numerically found the range of values (the crossover region in Fig.2.29) which leads to relaxor behavior. Calculating the parameter from first-principles and thus describing the exact relation between La^{3+} and gauge fields is a challenge and beyond the scope of this work. Let us also mention that pure-gauge investigations has hinted a value for the k parameter that is not as fortuitous as it might seem. Indeed, the range of k which yields competing and balanced interactions is very narrow, and any precise determination of k would merely result in relatively small corrections.

We would like to stress that the purpose of this work is not to prove a relation between defects and gauge theories, but rather to answer the question of whether the postulate of a local symmetry on the leading short-range interaction term in a system where disorder-induced frustration is provided by a random gauge-field type of interaction, enables to retrieve the relaxor behavior. Behind this postulate lies the strong belief that such a model would meet the physics of relaxor ferroelectrics on length scales in which frustration effects dominate.

2.2.4.3 Monte-Carlo simulations

In order to access finite-temperature properties, we use Monte-Carlo simulations, which main features we here review [253].

Meaningful quantities of a physical system in thermal equilibrium usually involve thermal expectation value of some observable $A(\mathbf{X})$ which depends on the systems configuration:

$$\langle A \rangle = \frac{1}{Z} \int_\Omega d^k X \, A(\mathbf{X}) \exp\left[-\beta E(\mathbf{X})\right] \tag{2.72}$$

where Z is the partition function

$$Z = \int_\Omega d^k X \exp\left[-\beta H(\mathbf{X})\right] \tag{2.73}$$

Ω denoting the (k-dimensional) volume of phase space $\{\mathbf{X}\}$ over which is integrated, $E(\mathbf{X})$ being the Hamiltonian, and $\beta = 1/k_B T$, where k_B is the Boltzmann factor. In the present case, the partition function is expressed in terms of the dynamical variables $\mathbf{u}$, η, and U and takes the following form:

$$Z = \int d\mathbf{u}\, d\eta\, dU \exp\left[-\beta \tilde{E}_{tot}(\mathbf{u}, \eta, U)\right] \tag{2.74}$$

where $d\mathbf{u}$ and $d\eta$ denote the integration over ferroelectric and elastic degrees of freedom respectively, and dU is the integration measure (gauge invariant Haar measure, see footnote 16) over individual link variables taking values in a Lie group. $\tilde{E}_{tot}$ refers to the gauge-modified effective Hamiltonian given by Eq.(2.71).

This expression is analytically intractable, except for very small lattices[38]. The probability distribution $p(\mathbf{X}) = \frac{1}{Z}\exp\left[-\beta E(\mathbf{X})\right]$ has a very sharp peak in phase space where all extensive variables $A(\mathbf{X})$ are close to their average values $\langle A\rangle$. Hence, when summing over the configurations it is more important to consider the configurations with larger weight than those with smaller weight, i.e., the configurations $\mathbf{X}_n$ in the vicinity of the peak of this probability distribution. This goal is achieved by the so-called *importance sampling* Monte Carlo method, whose central idea is to approximate the very large sum by a comparatively small subset of configurations $\{\mathbf{X}_n\}$ of finite number N, sampled according to the weight factor $\propto \exp\left[-\beta E(\mathbf{X}_n)\right]$. The average of an observable $A(\mathbf{X})$ can then be approximated by the mean value taken by the observable over the N configurations in this sequence:

$$\langle A\rangle = \lim_{N\to\infty} \frac{1}{N} \sum_{n=1}^{N} A(\mathbf{X}_n) \tag{2.75}$$

The statistical error of the result will be proportional to $1/\sqrt{N}$, and the exact value will be reached in the limit $N \to \infty$.

Starting from some initial configuration $\mathbf{X}_1$, one constructs a stochastic sequence of configurations that eventually follows the equilibrium distribution $p(\mathbf{X})$. This is done with the so-called *Markov chain* or *Markov process*

$$\mathbf{X}_1 \to \mathbf{X}_2 \to \mathbf{X}_3 \to \cdots \tag{2.76}$$

In this Markov chain configurations $\mathbf{X}_n$ are generated subsequently[39], with the property that the next state depend on the present state, and does not depend on any other past state. The change of a field configuration to a new one is called an update, or a Monte-Carlo step. The

[38] The number of configurations available for a system grows exponentially with its size (This is in relation with the fact that the entropy is an extensive quantity, proportional to the logarithm of the number of configuration).

[39] The index n is often referred to as computer time, not to be mistaken with the Euclidean time of a 4D spacetime [189].

Markov chain is constructed such that it visits configurations with larger probability more often (see Fig. 2.30). The convergence of this Markov process towards thermal equilibrium is ensured by imposing the condition of detailed balance, which requires that the probability to reach a given state is the same as that to leave a given state

$$W(\mathbf{X} \to \mathbf{X}')p(\mathbf{X}') = W(\mathbf{X} \to \mathbf{X}')p(\mathbf{X}) \tag{2.77}$$

where $W(\mathbf{X} \to \mathbf{X}')$ is the transition probability to change from state $\mathbf{X}$ to state $\mathbf{X}'$, and $p(\mathbf{X})$ is the weight of state $\mathbf{X}$.

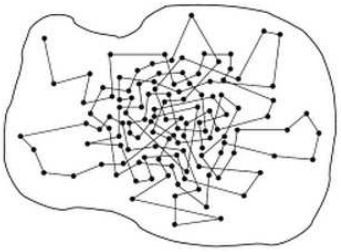

Fig. 2.30: Schematic sketch of a Markov chain in the space of all configurations. The boundary delimits the space of all configurations. The dots represent configurations visited by a Markov chain and are connected with straight lines to indicate that they are visited subsequently. The Markov chain starts in the upper left corner and then evolves towards the center, where the density of dots is larger. This corresponds to a region where the Boltzmann factor $\exp[-\beta H(\mathbf{X})]$ is large, and thus with large probability (After C. Gattringer *et al.* [189]).

The transition probability $W(\mathbf{X} \to \mathbf{X}')$ still needs to be specified. The widely used Metropolis algorithm accomplishes both tasks of importance sampling and detailed balance. It proposes a change in the system state $\mathbf{X} \to \mathbf{X}'$ and evaluates the energy change $\Delta E = E_{\mathbf{X}'} - E_{\mathbf{X}}$. If $\Delta E < 0$ the proposed change is accepted, otherwise it is only accepted with a probability $\exp(-\beta \Delta E)$, i.e.

$$W(\mathbf{X} \to \mathbf{X}') = \begin{cases} 1 & \text{if} \quad \Delta E < 0 \\ \exp(-\beta \Delta E) & \text{if} \quad \Delta E > 0 \end{cases} \tag{2.78}$$

In this latter case, a pseudo-random number r, selected in the interval between 0 and 1 with uniform probability distribution, is generated and if $r \leqslant \exp(-\beta \Delta E)$ the change is accepted, otherwise, it is rejected. Let us sum up the steps involved in the Metropolis algorithm:

start Generate an arbitrary initial configuration for all the dynamical variables at all sites. In the present case, the initial state for the matter field ($\mathbf{u}$,η) is taken to be zero at high temperature, while that of the dynamical gauge field U is taken to be identity (cold start).

update & **accept/reject** Proceeding site by site through the lattice, propose a random change to each of the dynamical variables and apply for each of the variables the acceptance/rejection procedure. The local mode is updated according to $\mathbf{u}_i \to \mathbf{u}_i' =$

$\mathbf{u}_i + \mathrm{d}\mathbf{u}_i$. The three components of $\mathrm{d}\mathbf{u}_i$ are updated at once, the energy difference between $\mathbf{u'}_i$ and $\mathbf{u}_i$ is then computed and submitted to the accept/reject test. The inhomogeneous strain is updated in terms of the local displacement vector $\mathbf{v}_i \rightarrow \mathbf{v}'_i = \mathbf{v}_i + \mathrm{d}\mathbf{v}_i$, in same fashion as for the local mode. For each of the three links stemming for the considered lattice site and pointing in the $\hat{\mathbf{x}}$, $\hat{\mathbf{y}}$ and $\hat{\mathbf{z}}$ directions, the involved angle is updated from the angular interval $[-\pi, \pi]$, and the energy difference between the old and new configurations is computed and evaluated according to the accept/reject test.

sweep Once all the dynamical variables have been updated and all the sites have been considered, a final update of the homogeneous strain (the six components of the tensor at once) is performed, which completes one sweep of the lattice.

Let us note that the acceptance ratio, defined within one sweep for each of the dynamical variables as the number of accepted updates over the number of sites, allows to adjust the range of the updates in a next sweep so as to efficiently probe the phase space. Expectation values are approximated by average values of observables taken over 50000 sweeps after 50000 initial configurations have been discarded to allow for the onset of statistical equilibrium. We use $12 \times 12 \times 12$ supercells with periodic boundary conditions. This procedure effectively eliminates boundary effects. However, finite size effects are to be expected since the system is still characterized by a finite lattice size, as it yields an upper bound for the maximum value of correlation length. The resulting properties of the system differ from those of the corresponding infinite lattice. In general all singularities that can occur only in the thermodynamic limit will be rounded, in particular this means that response functions expected to diverge at the critical point, like the dielectric susceptibility or the specific heat, will instead reach finite values. Moreover functions which should be vanishing above T_C will generally exhibit a finite tail, as the polarization for instance. And finally, discontinuous jumps occurring across first-order transitions will instead appear continuous with large slopes over narrow regions.

Chapter 3

Numerical results

We investigate the influence of lanthanum-mimicking quenched spatial disorder on gauge-modified lead zirconate titanate effective Hamiltonian. Disorder is achieved by the quenching of gauge variables along edges of randomly chosen unit cells, whose percentage can be seen as that of the lanthanum substitution for lead, x, effectively yielding PLZT systems. In this chapter we report the results obtained for $PL_xZ_{60}T_{40}$[1] compositions, with $0\% \leq x \leq 20\%$, whose parent compound, $PZ_{60}T_{40}$, is a prototypical soft-mode ferroelectric with a rhombohedral FE phase. $PL_xZ_{60}T_{40}$ systems exhibit relaxor behavior arising from compositionally induced disorder for $x \geq 5\%$, and upon cooling in the absence of an electric field, a spontaneous relaxor-to-ferroelectric transition occurs [155].

3.1 Macroscopic observables

In order to probe the characteristics of $PL_xZ_{60}T_{40}$ systems, the expectation value of observables (Eq.2.72) is estimated within the Monte Carlo simulations as a simple arithmetic mean over the Markov chain, or number of sweeps (Eq.2.75). The commonly used order parameter for dipolar systems is polarization. To compute this quantity, one takes the sum of all the local modes vectors in the lattice, divided by the number of lattice sites and averaged over the sweeps

$$\langle \mathbf{u} \rangle = \frac{1}{N} \langle \sum_{i=1}^{N} \mathbf{u}_i \rangle \tag{3.1}$$

where i runs over the lattice sites and where N is their total number ($N = 12^3$). The statistical average over sweeps is denoted by $\langle\,\rangle$. Since $\mathbf{u}_i$ is directly proportional to the local electric dipole moment, $\langle \mathbf{u} \rangle$ is proportional to the polarization.

[1] Throughout this chapter, we will be using the following $PL_xZ_{60}T_{40}$ notation for lanthanum modified lead zirconate titanate for convenience.

3.1.1 Polarization and specific heat

Figures 3.1 to 3.5 depict the temperature evolutions of the specific heat C and the norm of the statistical average of the local modes, $|\langle \mathbf{u} \rangle|$, for $PZ_{60}T_{40}$ and $PL_xZ_{60}T_{40}$, with $x = 5, 10, 15$ and 20%. The specific heat is estimated from energy fluctuations

$$C = \frac{1}{k_B T^2}(\langle E^2 \rangle - \langle E \rangle^2) \tag{3.2}$$

where $\langle E \rangle$ corresponds to the average over Monte Carlo sweeps of the internal energy E and $\langle E^2 \rangle$ to that of its square, and where k_B is the Boltzmann constant. The peak in the specific heat reflects the onset of a long-range collective behavior and is thus used for the determination of T_C. The norm of the statistical average of the local modes, $|\langle \mathbf{u} \rangle|$, directly proportional to the norm of the polarization, corresponds to

$$|\langle \mathbf{u} \rangle| = (\langle u_x \rangle^2 + \langle u_y \rangle^2 + \langle u_z \rangle^2)^{1/2} \tag{3.3}$$

where $(\langle u_x \rangle, \langle u_y \rangle, \langle u_z \rangle)$ are the Cartesian components of $\langle \mathbf{u} \rangle$, and where $\langle\, \rangle$ denotes the average over sweeps performed on the average over the supercell of the local modes. Regarding the temperature scale, since the effective Hamiltonian does not include antiferrodistortive (AFD) motions (associated with the oxygen octahedra rotation [244]), the transition temperatures are shifted upwards with respect to the true ones [155]. In order to provide a better comparison of our simulation results to experiment, we have linearly rescaled the temperature (as in Ref [233]), so that the theoretical Curie temperature in disordered $PZ_{60}T_{40}$ (960 K) coincides with the experimental value of 652 K [155]. From figures 3.1 to 3.5, one sees that T_C (the temperature at which the specific heat peaks) coincides with the inflection point of $|\langle \mathbf{u} \rangle|$. Moreover, with increasing lanthanum content, the specific heat C broadens while $|\langle \mathbf{u} \rangle|$ exhibits a quasi-linear behavior.

Figure 3.6 is recapitulative of the temperature behavior of $|\langle \mathbf{u} \rangle|$ with increasing lanthanum content. Error bars clearly indicate that whereas the subsisting tail practically reduces to zero within the error bars above T_C for $PZ_{60}T_{40}$, thus indicating its finite-size effects origin, it retains a substantial non-vanishing value for $PL_xZ_{60}T_{40}$ systems with $x = 5\%, 10\%, 15\%$ and 20%, that can be ascribed to the nucleation of local order (this is further evidenced by the temperature evolution of the correlation length shown in Fig. 3.17.). T_C lowers monotonically with the substitution of La, which is in remarkable agreement with the available experimental data [155]. The account for lanthanum by means of the randomly quenched gauge variables thus reproduces both the linear Curie point lowering and the drop in magnitude of the polarization (proportional to $|\langle \mathbf{u} \rangle|$) for increasing lanthanum concentrations.

Figure 3.7 depicts the integral curves for $PZ_{60}T_{40}$ and $PL_xZ_{60}T_{40}$ with $x = 5\%, 10\%, 15\%$ and 20% associated to the corresponding local modes vector fields within a given (x, y) plane

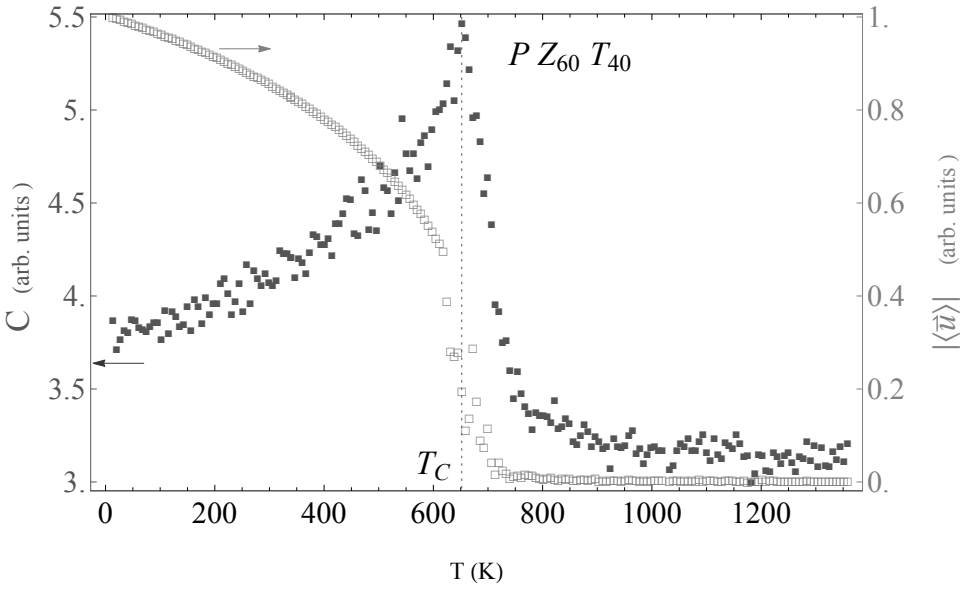

Fig. 3.1: Temperature evolutions of the specific heat (filled symbols) and the scaled polarization (open symbols) in $PZ_{60}T_{40}$ system. Dotted vertical line corresponds to T_C.

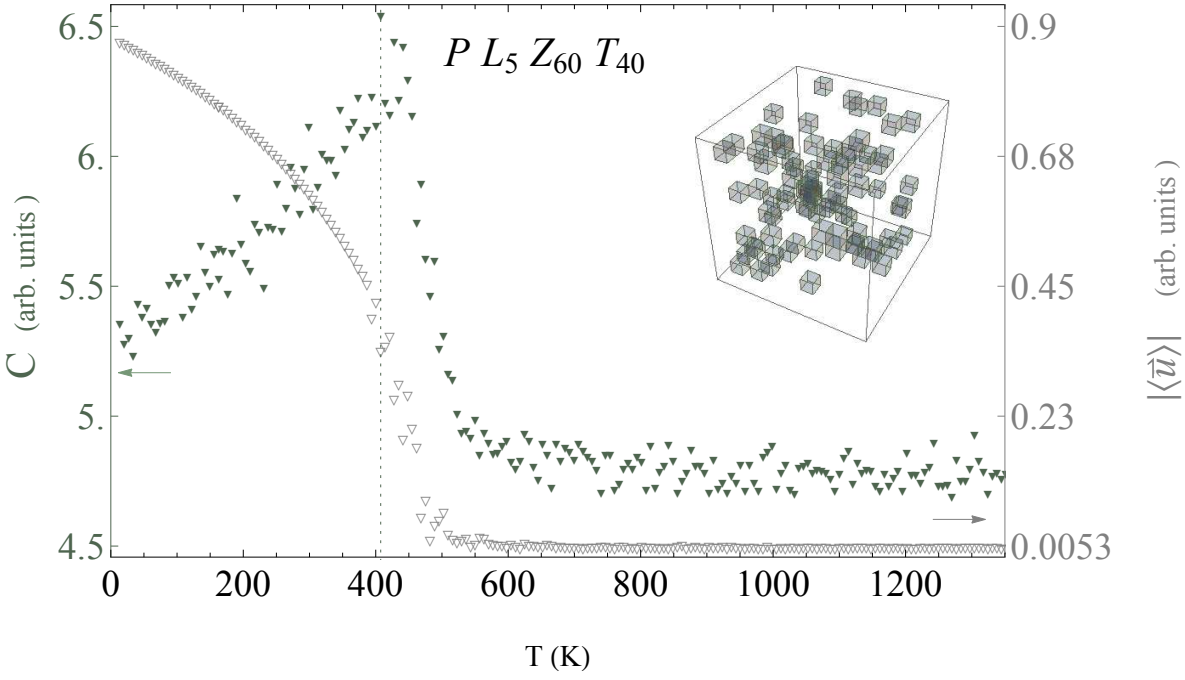

Fig. 3.2: Temperature evolutions of the specific heat (filled symbols) and the scaled polarization (open symbols) in $PL_5Z_{60}T_{40}$ system. The inset shows the distribution of the quenched (lanthanum containing) unit cells inside the supercell. Dotted vertical line corresponds to T_C.

of the supercell at $T = 34$ K.

Integral curves are a very simple way of conveying the structure of vector fields. By following the vector field path, they convey this information in an intuitive manner with enhanced visibility.

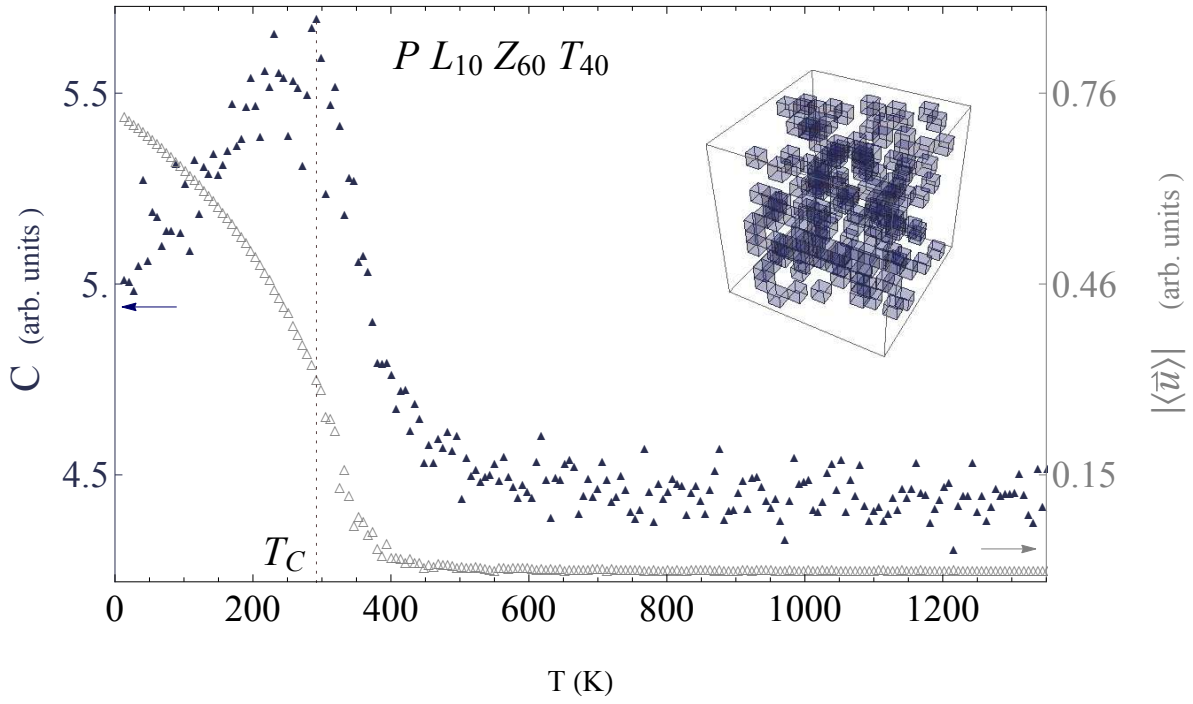

Fig. 3.3: Temperature evolutions of the specific heat (filled symbols) and the scaled polarization (open symbols) in $PL_{10}Z_{60}T_{40}$ system. The inset shows the distribution of the quenched (lanthanum containing) unit cells inside the supercell. Dotted vertical line corresponds to T_C.

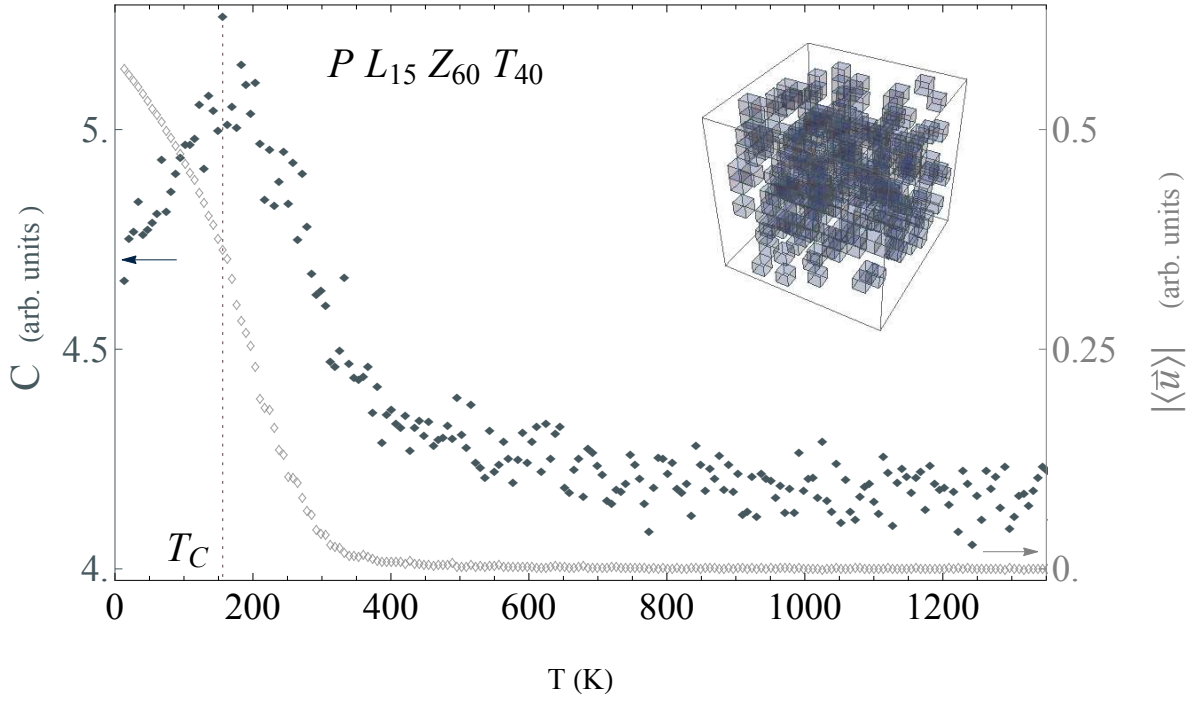

Fig. 3.4: Temperature evolutions of the specific heat (filled symbols) and the scaled polarization (open symbols) in $PL_{15}Z_{60}T_{40}$ system. The inset shows the distribution of the quenched (lanthanum containing) unit cells inside the supercell. Dotted vertical line corresponds to T_C.

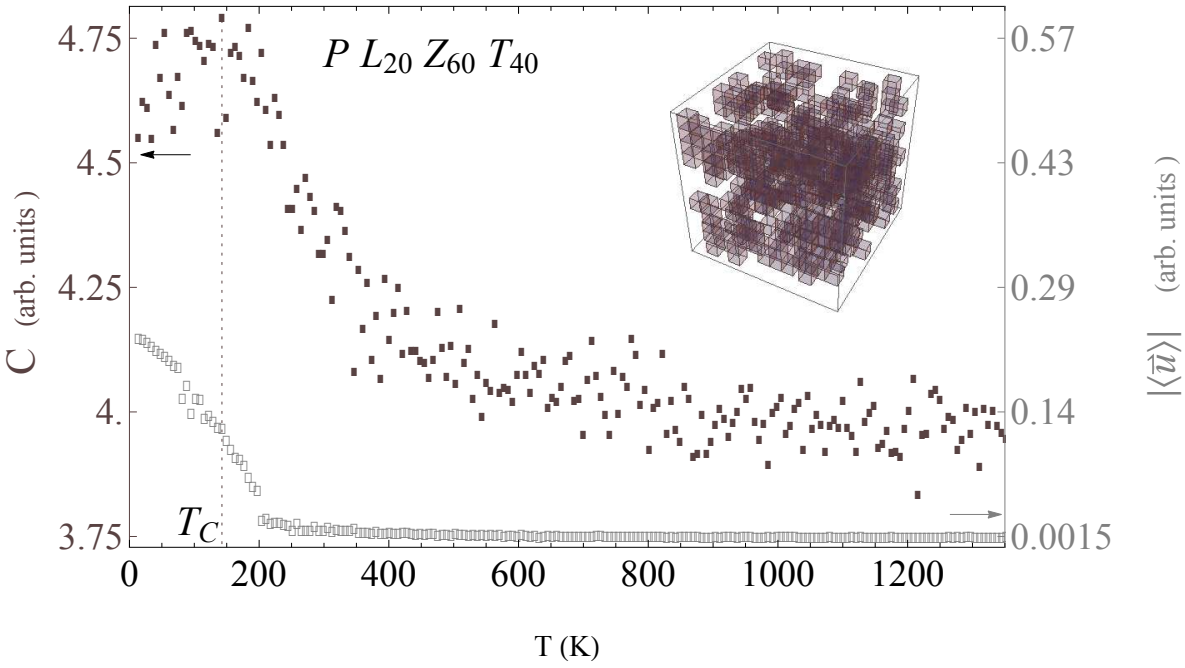

Fig. 3.5: Temperature evolutions of the specific heat (filled symbols) and the scaled polarization (open symbols) in $PL_{20}Z_{60}T_{40}$ system. The inset shows the distribution of the quenched (lanthanum containing) unit cells inside the supercell. Dotted vertical line corresponds to T_C.

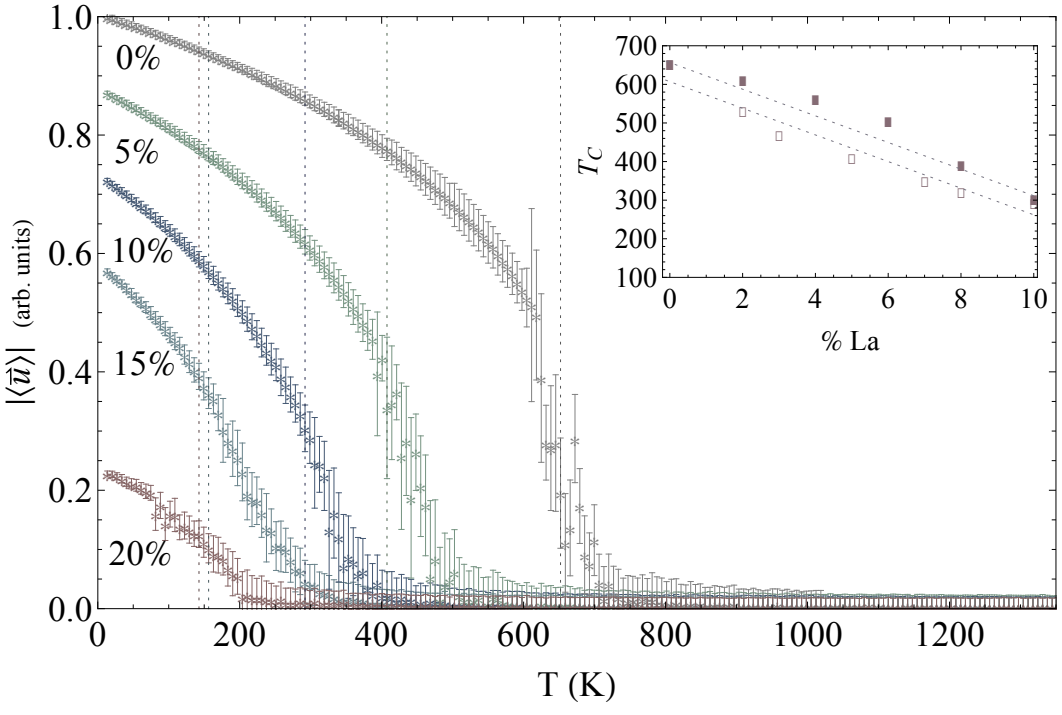

Fig. 3.6: Temperature evolution of $|\langle \mathbf{u} \rangle|$ for $PZ_{60}T_{40}$ and $PL_xZ_{60}T_{40}$ with $x = 5\%, 10\%, 15\%$ and 20%. The inset shows the variation of the transition temperature T_C with different concentration of lanthanum. Filled symbols refer to the experimental results of Ref. [155], whereas empty symbols correspond to the results of our simulations, dashed lines are guide to the eye.

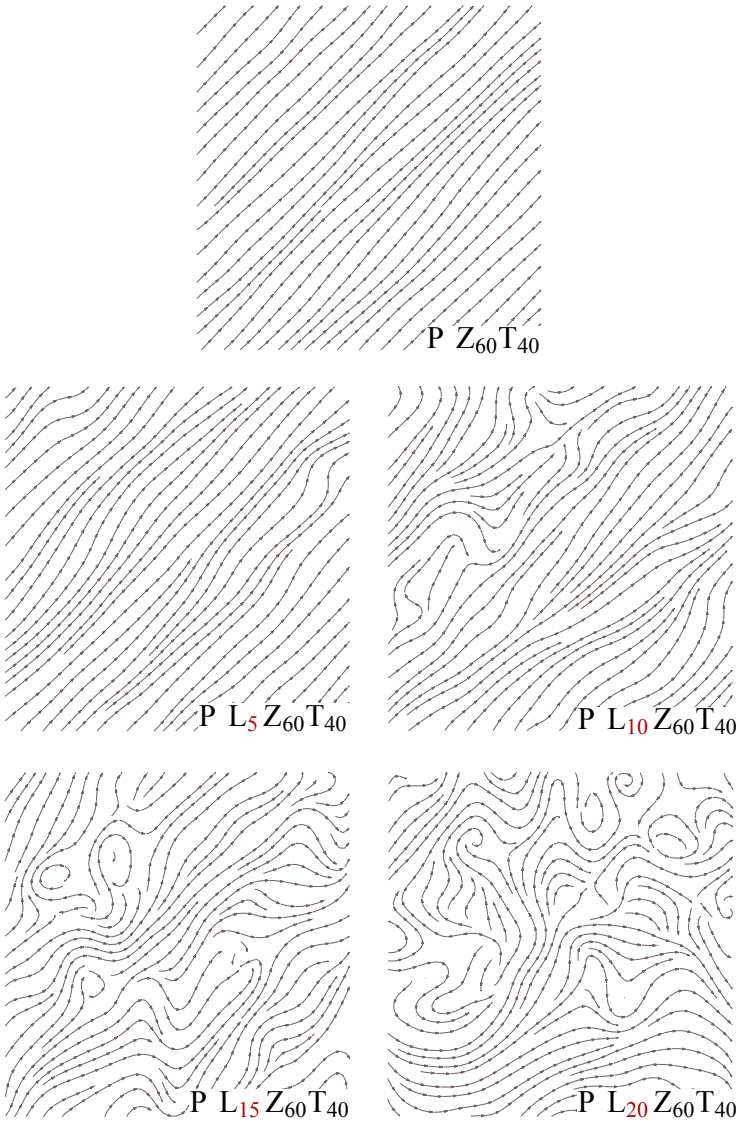

Fig. 3.7: Integral curves of the local modes ($\propto$ the dipole moments) within a given (x, y) plane of the supercell at $T = 34$ K for $PZ_{60}T_{40}$, $PL_5Z_{60}T_{40}$, $PL_{10}Z_{60}T_{40}$, $PL_{15}Z_{60}T_{40}$ and $PL_{20}Z_{60}T_{40}$ systems. The integral curves are obtained from the local Cartesian components $(\langle u_x \rangle, \langle u_y \rangle)$ averaged over sweeps.

Let us briefly recall that integral curves require solving differential equations determined by vector fields [255]. Let U be a domain of the Euclidean space, and let $\mathbf{v}$ be a vector field in U. The differential equation determined by $\mathbf{v}$ corresponds to :

$$\dot{x} = \mathbf{v}(x), \quad x \in U \tag{3.4}$$

while its solution involves a differential mapping $\gamma : I \to U$ of the interval $I = \{t \in \mathcal{R}, a < t < b\}$ of the real t-axis into U, such that

$$\frac{d}{dt}\bigg|_{t=\tau} \gamma(t) = \mathbf{v}(\gamma(\tau)), \quad \forall\, \tau \in I \tag{3.5}$$

In other words, the tangent vector to γ at each point is equal to the value of $\mathbf{v}$ at that point. If the value of a solution $\gamma : I \to U$ at the point t_0, $a < t_0 < b$ equals x_0 , then γ is said to satisfy the initial condition

$$\gamma(t_0) = x_0, \quad t_0 \in \mathcal{R}, \quad x_0 \in U. \tag{3.6}$$

Comparing these integral curves reveals that *turning on* the gauge degrees of freedom has drastic effects on the behavior of the system even in the ferroelectric phase. $PZ_{60}T_{40}$ shows the uniform configuration that is reached by the pure system, whereas a remarkably high deviation from perfect ordering exists in $PL_xZ_{60}T_{40}$ systems over a wide temperature range, even far below the transition point. These non-perfectly ordered regions can be seen as *non-ordered nanodomains* in the ordered matrix, which are formed as a consequence of gauge fields and their fluctuations. Interestingly, the microdomain distribution due to quenched random-fields and their spatial fluctuations appears to have a rather similar structure [152]. It is then possible that the gauge-induced local ferroelectric disorder gives rise to similar macroscopic characteristics as the disorder in random fields. This point will further be addressed in section 3.1.6.

3.1.2 Effects of quenched disorder on the dipoles pattern

A spontaneous question regarding the account of quenched disorder by means of the quenching of the links concerns the influence of the latter on the local modes. We investigate this matter by first subdividing the local modes population according to whether they are attached to quenched links defining quenched cubes QC (left panel of Fig. 3.8), or to relaxing links attached to non-quenched cubes $nonQC$ (right panel of Fig. 3.8).

We then define the mean angular deviation between the direction of the local modes $\mathbf{u}_i$ and that of the ground-state spontaneous polarization $\mathbf{P}_s$ in the following way

$$\frac{1}{8N_{QC}} \sum_{j=1}^{N_{QC}} \sum_{i \in QC_j}^{8} \text{Arccos}\left[\mathbf{u}_i.\mathbf{P}_s\right] \tag{3.7}$$

and

$$\frac{1}{8N_{nonQC}} \sum_{j=1}^{N_{nonQC}} \sum_{i \in nonQC_j}^{8} \text{Arccos}\left[\mathbf{u}_i.\mathbf{P}_s\right] \tag{3.8}$$

for local modes attached to the nodes of quenched cubes (Eq.3.7), and to those attached to the nodes of non-quenched cubes (Eq.3.8), respectively. N_{QC} refers the total number of quenched cubes and N_{nonQC} to that of non-quenched cubes. Fig. 3.9 enables the following observations.

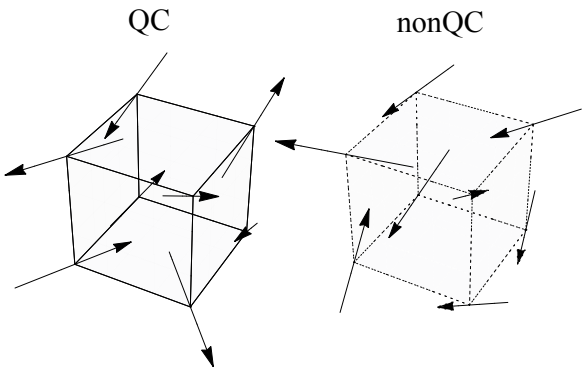

Fig. 3.8: Schematic view of two unit cubes. Left cube has edges corresponding to quenched links (solid lines) and will be referred to as quenched cube (lanthanum containing) QC. Right cube has edges associated with relaxing link variables (dotted lines) and will be reffered to as non-quenched cube (lead containing) $nonQC$. Each of QC and $nonQC$ have relaxing local modes attached to their nodes.

For the pure system PZT devoid of disorder, and thus of quenched cubes, the mean angular deviation from the ground state direction tends to zero with decreasing temperature, thereby signaling that local modes achieve perfect low temperature ordering. For each of the PLZT systems on another hand, depending on whether local modes are attached to QC or to $nonQC$, their deviation from the ground state direction is more or less pronounced at low temperatures. Increasing the amount of quenched disorder enhances theses deviations. The underlying quenched gauge disorder thus affects the local modes by hindering their ordering process below T_C (signaled by vertical dotted lines). The extension of its effect beyond the local modes directly attached to QC, is due to the correlations developed by the gauge field and to those developed by the local modes (section 3.1.4). As it will be later shown, it is also a signature of quenched-disorder-induced non-vanishing density of topological defects associated to the local modes (section 3.4).

The disordering effect of the partially quenched gauge field on the dipoles pattern is further illustrated in Fig. 3.10. Both the integral curves associated to the local modes at $T = 34$ K, and the location of quenched cubes are shown within a given (x, y) plane of the supercell. One observes that the propensity to achieving order is more pronounced in regions devoid of quenched disorder.

3.1.3 Dielectric response and departure from Curie-Weiss behavior

We now turn to the study of the dielectric susceptibility. The dimensionless dielectric susceptibility $\chi_{\alpha\beta}$ is defined by [256]:

$$\chi_{\alpha\beta} = \frac{1}{V\varepsilon_0}\left(\frac{\partial u_\alpha}{\partial E_\beta}\right)_T = \frac{(NZ^*)^2}{V\varepsilon_0 k_B T}\left[\langle u_\alpha u_\beta\rangle - \langle u_\alpha\rangle\langle u_\beta\rangle\right] \tag{3.9}$$

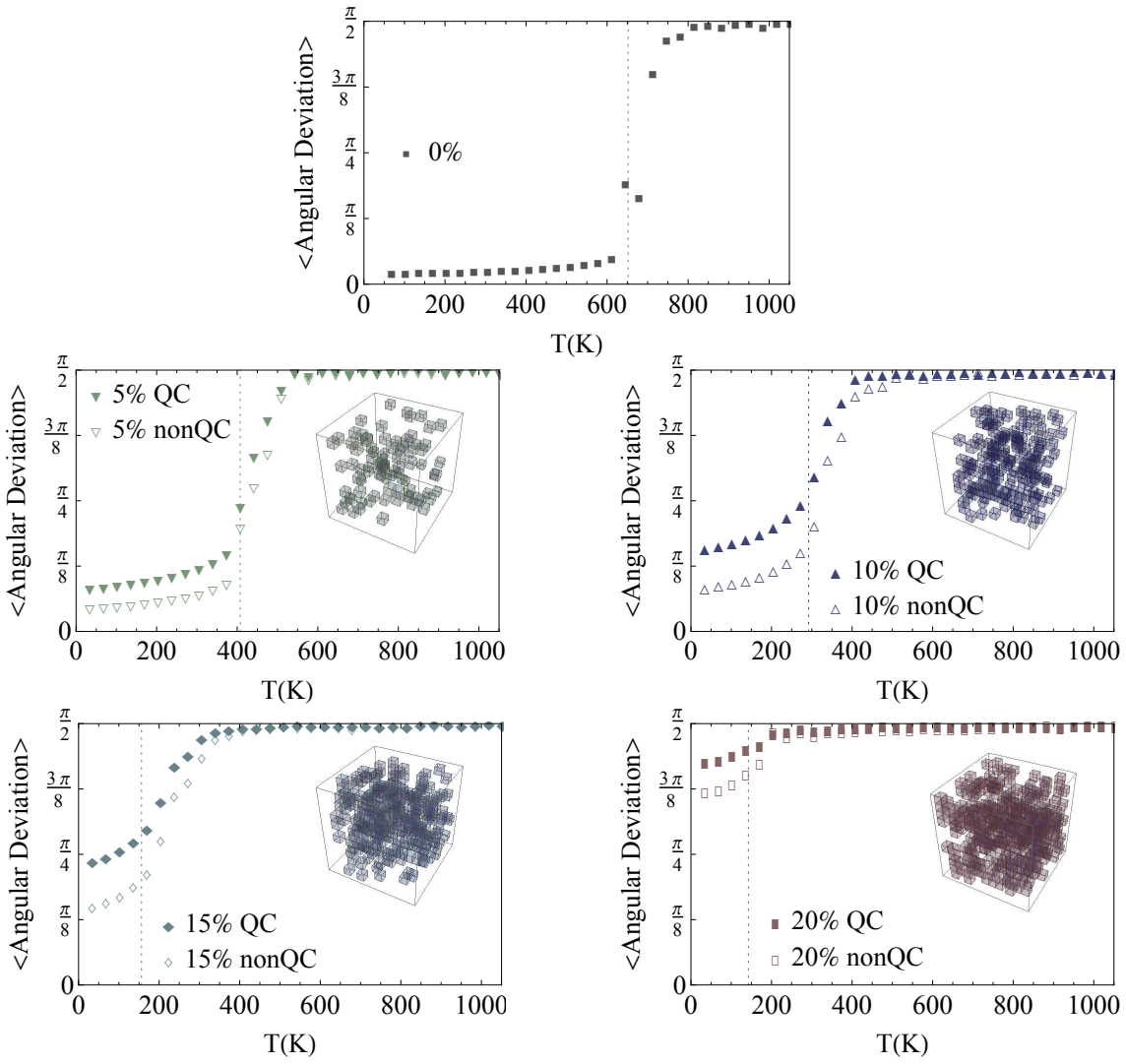

Fig. 3.9: Temperature evolution of the mean angular deviation between the local modes u_i and the ground-state spontaneous polarization $\mathbf{P}_s$ for PZT, PL_5ZT, $PL_{10}ZT$, $PL_{15}ZT$ and $PL_{20}ZT$ systems. Open symbols denote the deviation as experienced by local modes attached to non-quenched cubes *nonQC*, whereas filled symbols denote the deviation of the local modes when attached to quench cubes *QC*. Dotted vertical lines correspond to T_C. Insets show the distribution of the quenched cubes (lanthanum containing unit cells) inside the supercell.

where u_α is the α component of the supercell average of the local modes and where $\langle u_\alpha u_\beta \rangle$ refers to the statistical average of the product between α and β components of the supercell average of local modes vectors. N is the number of sites in the supercell, V its volume and ε_0 the permittivity of vacuum. Figures 3.11 to 3.15 show the gradual effect of Lanthanum disorder on the reduced temperature evolution of the inverse susceptibility $3/(\chi_{11}+\chi_{22}+\chi_{33})$. In the case of $PZ_{60}T_{40}$ system, the reduced temperature corresponds to T/T_C (where T_C is the temperature at which the specific heat peaks), whereas in the cases of $PL_xZ_{60}T_{40}$ systems, it corresponds to T/T_m (where T_m is the temperature at which the dielectric susceptibility peaks). For each of the considered systems, we show both the specific heat and the inverse susceptibility to demonstrate the disorder-induced shift between T_C and T_m.

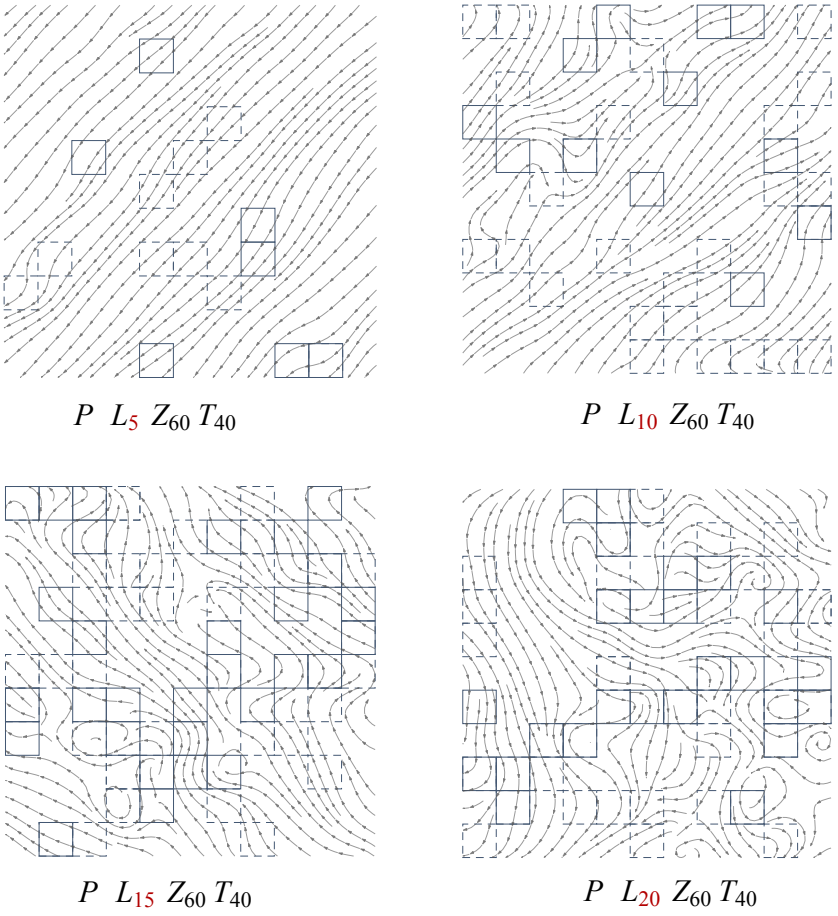

Fig. 3.10: Integral curves of the local modes ($\propto$ the dipole moments) within a given (x, y) plane of the supercell at $T = 34$ K for $PL_5Z_{60}T_{40}$, $PL_{10}Z_{60}T_{40}$, $PL_{15}Z_{60}T_{40}$ and $PL_{20}Z_{60}T_{40}$ systems. The integral curves are obtained from the local Cartesian components $(\langle u_x \rangle, \langle u_y \rangle)$ averaged over sweeps. Straight lined squares refer to in plane quenched cubes and dotted ones stand for those contained in the upper and lower parallel planes.

In the case of $PZ_{60}T_{40}$ system (Fig. 3.11), T_C and T_m nearly coincide. Moreover, the inverse dielectric susceptibility at $T > T_C$ can be well approximated to a Curie-Weiss form $\chi^{-1} = \mathrm{C}\,(\mathrm{T}/\Theta - 1)^{\gamma}$, with $\gamma \simeq 1$ and $\Theta \simeq \mathrm{T_C}$, indicative of a typical ferroelectric behavior.

We then investigate the origin of the rounding of the inverse susceptibility near T_C in $PZ_{60}T_{40}$ by increasing the simulation box size L (Fig. 3.12). We approximate the behavior of χ^{-1} to a Curie-Weiss form $\chi^{-1} = C(T - T_0)$, and collect the parameters of the fits (Curie temperature T_0, Curie constant C) above and below the transition [256]. The values of the Curie constants above and below the transition are predicted from mean field arguments [257] to satisfy $C_{below} = -2C_{above}$ for second-order transitions, whereas for first-order transitions, the values of C_{below} and $2C_{above}$ are not related in a simple way, generally yielding a $|C_{below}|/-2C_{above}$

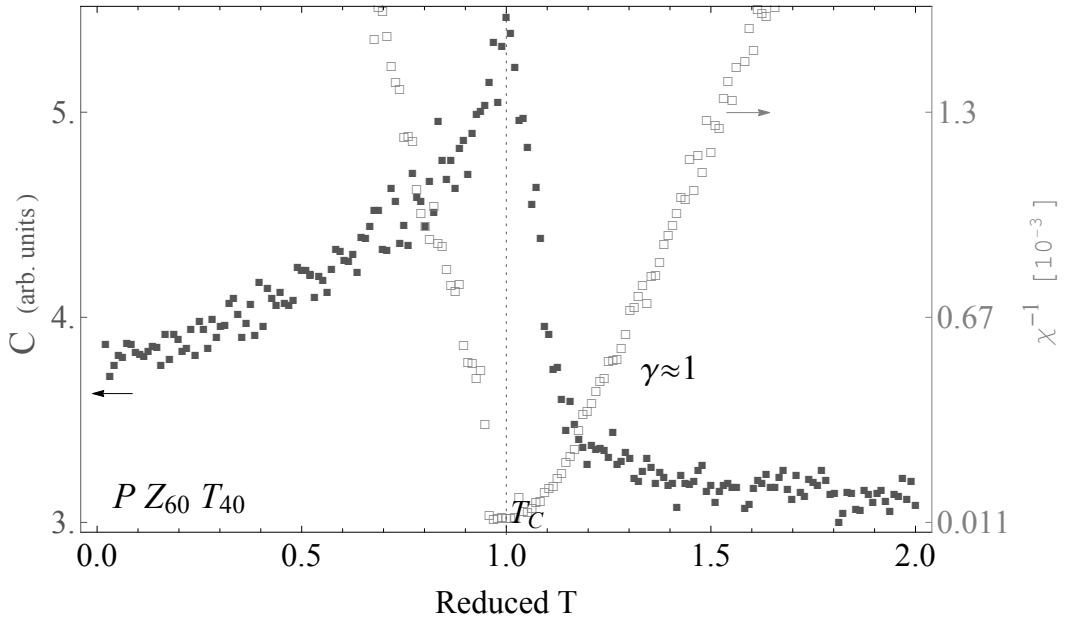

Fig. 3.11: Temperature evolution of the inverse dielectric susceptibility and the specific heat for $PZ_{60}T_{40}$. $T_C = 652$ K corresponds to the maximum of the specific heat and the reduced temperature refers to T/T_C. The inverse dielectric susceptibility at $T > T_C$ can be well approximated to a Curie-Weiss form $\chi^{-1} = C\,(T/\Theta - 1)^{\gamma}$ with $\gamma \simeq 1$ and $\Theta \simeq T_C$.

ratio larger than one [256]. Results indicate that the extracted Curie temperature T_0 are close but not identical to T_C, moreover, the $|C_{below}|/-2C_{above}$ ratio is close to (and slightly smaller than) 1. In view of this results and of the absence of a jump in the polarization (Fig. 3.1), we conclude that the rounding can be ascribed to finite-size effects, and that the ferroelectric transition is close to a second order one.

Figures 3.13 to 3.15 show the temperature evolution of the inverse dielectric susceptibility and the specific heat for $PL_xZ_{60}T_{40}$ systems, with $x = 5, 10$ and 15% of lanthanum. Inverse dielectric susceptibilities at $T \gg T_C$ can be well approximated to a Curie-Weiss form $\chi^{-1} = C\,(T/\Theta - 1)^{\gamma}$ with $\gamma \simeq 1$ and $\Theta > T_C$, indicating a departure from the typical ferroelectric behavior. Below T_d, the data is better fitted with the modified Curie-Weiss law

$$\chi^{-1} - \chi^{-1}_{max} = C'\,(T/T_m - 1)^{\gamma} \tag{3.10}$$

with $\gamma \simeq 1.45, 1.69, 1.91$, for $x = 5, 10$ and 15% respectively. The fits were performed on $\mathrm{Ln}(\chi^{-1} - \chi^{-1}_{max})$ versus $\mathrm{Ln}\,(T/T_m - 1)$, from which the parameter γ corresponding to the slope and indicative of the diffuseness of the transition was extracted.

The significant broadening of the minima of the inverse dielectric susceptibility with increasing La^{3+} content as well as the monotonically increasing deviation from the normal Curie-Weiss behavior quantified by a value of $\gamma > 1$ below T_d, differing from that associated with the mean-field approach, are indicative of diffuseness in the phase transition, in agreement with Ref. [258]. Static simulations of $PL_xZ_{60}T_{40}$ thus reproduce the broad dielectric

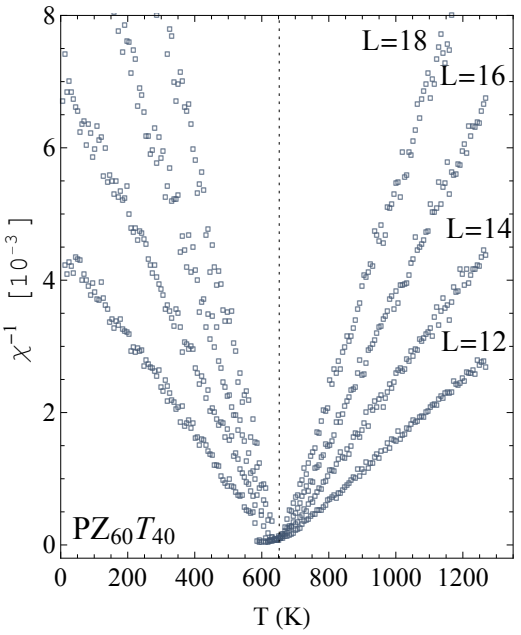

L	$\frac{\lvert C_{below}\rvert}{-2\,C_{above}}$	$T_{0_{above}}$(K)	$T_{0_{below}}$(K)
12	0.79	657	631
14	0.78	657	638
16	0.77	658	639
18	0.76	657	644

$$\chi^{-1}=\mathrm{C}\,(\mathrm{T}-T_0)$$

Fig. 3.12: Inverse susceptibility of $PZ_{60}T_{40}$ with varying box size $L = 12, 14, 16, 18$. Table indicates the parameters of the fitted values of the inverse susceptibility to the Curie-Weiss law $\chi^{-1} = C(T - T_0)$.

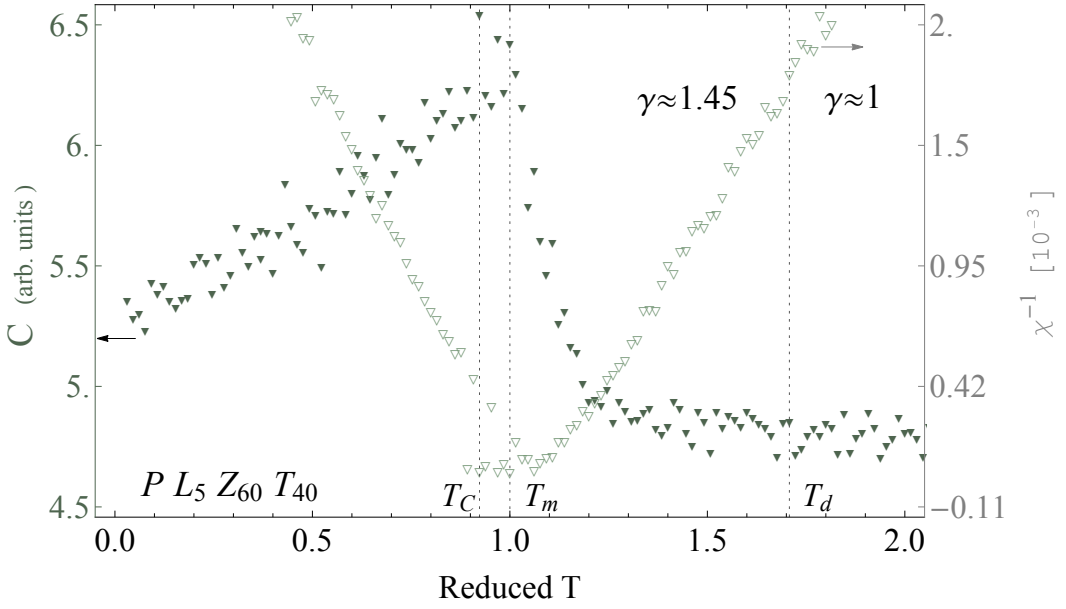

Fig. 3.13: Temperature evolution of the inverse dielectric susceptibility and the specific heat for $PL_5Z_{60}T_{40}$. $T_C \simeq 408$ K corresponding to the maximum of the specific heat and $T_m \simeq 442$ K corresponding to that of the dielectric susceptibility, are indicated by vertical dashed lines. The reduced temperature refers to T/T_m. The onset of deviation from the Curie-Weiss law at $T_d \simeq 754$ K is indicated by a vertical dashed line.

peak measured in relaxors in low frequency experiments, which implies the existence of a static component in the smeared peak [169].

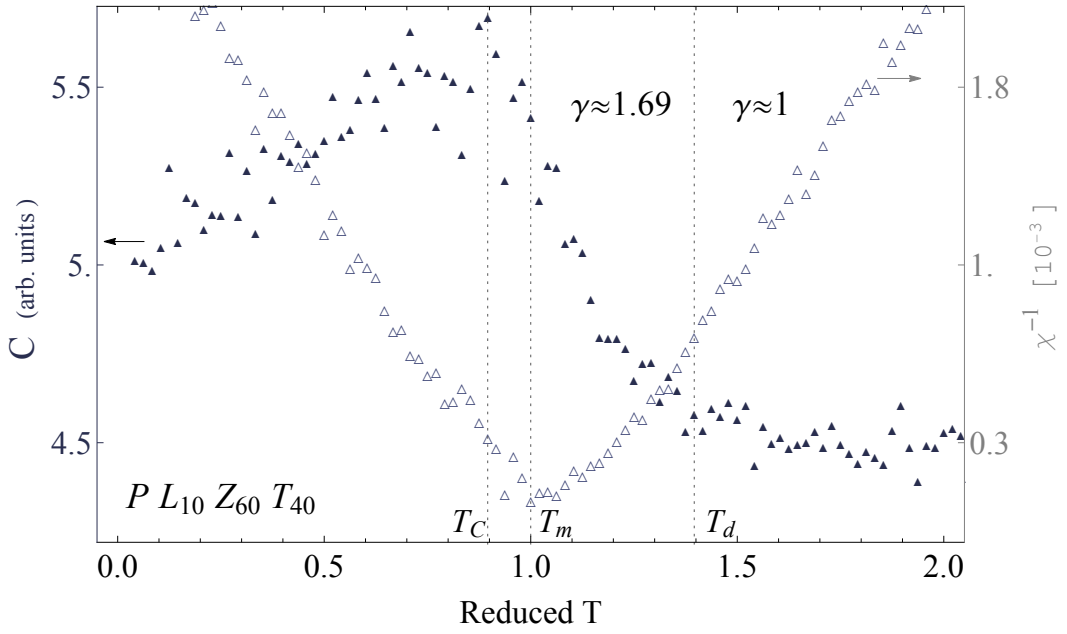

Fig. 3.14: Temperature evolution of the inverse dielectric susceptibility and the specific heat for $PL_{10}Z_{60}T_{40}$. $T_C \simeq 292$ K corresponding to the maximum of the specific heat and $T_m \simeq 326$ K corresponding to that of the dielectric susceptibility, are indicated by vertical dashed lines. The reduced temperature refers to T/T_m. The onset of deviation from the Curie-Weiss law at $T_d \simeq 455$ K is indicated by a vertical dashed line.

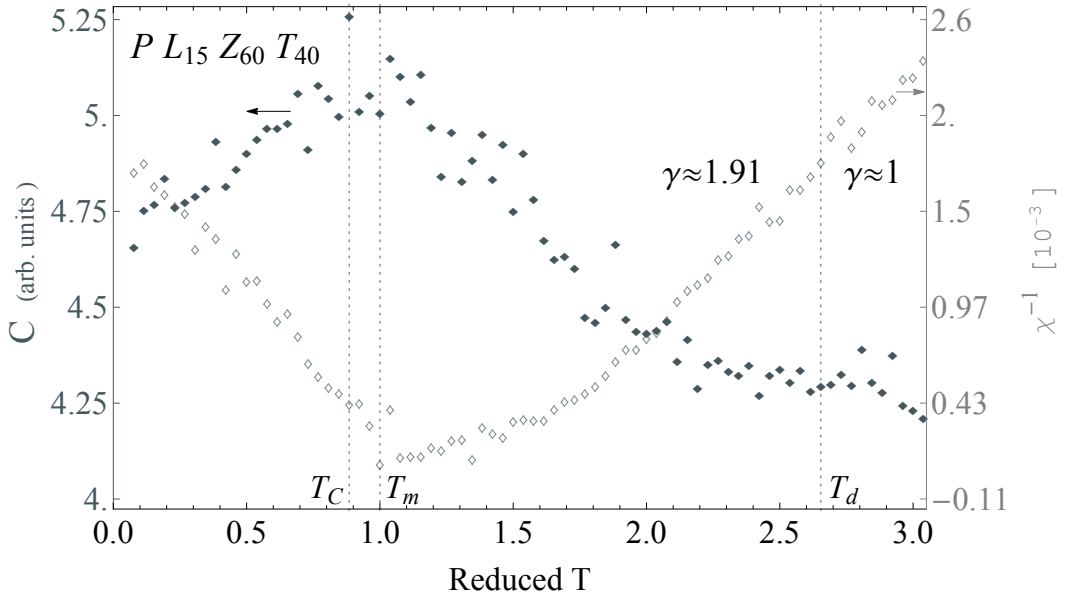

Fig. 3.15: Temperature evolution of the inverse dielectric susceptibility and the specific heat for $PL_{15}Z_{60}T_{40}$. $T_C \simeq 156$ K corresponding to the maximum of the specific heat and $T_m \simeq 176$ K corresponding to that of the dielectric susceptibility, are indicated by vertical dashed lines. The reduced temperature refers to T/T_m. The onset of deviation from the Curie-Weiss law at $T_d \simeq 469$ K is indicated by a vertical dashed line.

3.1.4 Correlation length

We now analyze the temperature evolution of the correlation length, which corresponds to the length scale over which the fluctuations of the microscopic degrees of freedom are significantly correlated with each other [259].

Figures 3.16 and 3.17 display the correlation length's evolution with temperature of the gauge field, $\xi_{g.f.}$, and the local modes, $\xi_{l.m.}$, respectively. In the case of the gauge field, $\xi_{g.f.}$ is extracted from the asymptotical decay of the spatial plaquette-plaquette correlation function

$$C(d) = \langle \mathrm{Tr}U_{\square}\mathrm{Tr}U_{\square'}\rangle - \langle \mathrm{Tr}U_{\square}\rangle^2 \tag{3.11}$$

where $U_{\square}$ and $U_{\square'}$ stand for two plaquette variables facing each other and separated by d lattice links [260]. In practice $\xi_{g.f.}$ is averaged over the three spatial directions $\hat{x}$, $\hat{y}$ and $\hat{z}$:

$$\xi_{g.f.} = \frac{1}{3}(\xi^{\hat{x}}_{g.f.} + \xi^{\hat{y}}_{g.f.} + \xi^{\hat{z}}_{g.f.}) \tag{3.12}$$

where for example $\xi^{\hat{x}}_{g.f.}$ corresponds to the correlation length extracted from the correlation function computed for plaquettes facing each other and lying in the (y, z) planes. Let us note that the obtaining of values for $\xi_{g.f.}$ lower than 1 is due to the considered continuum approximation.

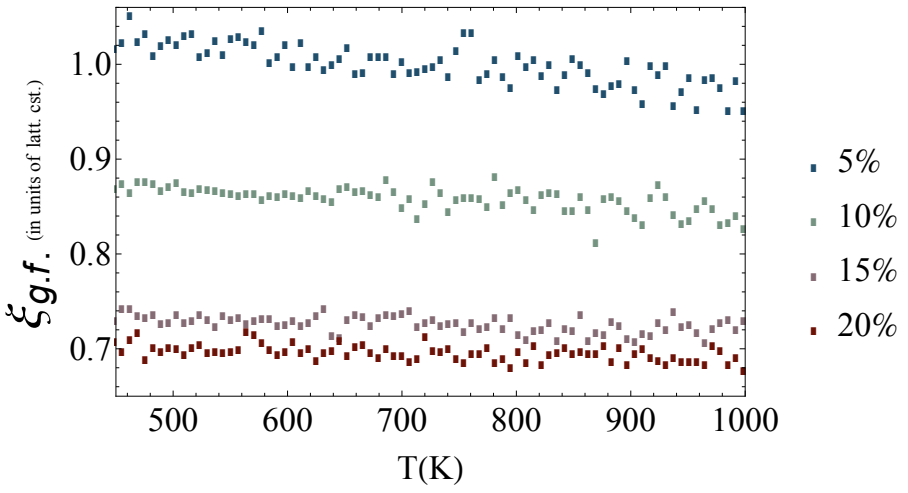

Fig. 3.16: Temperature evolution of the correlation length of the gauge field $\xi_{g.f.}$ for $PL_5Z_{60}T_{40}$, $PL_{10}Z_{60}T_{40}$, $PL_{15}Z_{60}T_{40}$ and $PL_{20}Z_{60}T_{40}$ systems.

Results indicate a short-range correlated gauge field, with a global drop of the correlation length with increasing % La content. One also observes a quasi linear decrease of $\xi_{g.f.}$ with temperature, with a slope tending to zero as the disorder content is increased (Fig. 3.16). Thus the underlying gauge field is not sensitive to structural phase transitions, and does

not display one of its own. Increasing the amount of quenched cubes (*i.e.* the lanthanum content) reduces both the correlation length and its range of temperature variation.

The ordering process of the local modes (the matter field), and the eventual crossover from local, short-ranged correlations to long-ranged ones, can be assessed by the two-points correlation function defined by

$$G(\mathbf{r}_i - \mathbf{r}_j) = G(r_{ij}) = \langle \mathbf{u}_i . \mathbf{u}_j \rangle - \langle \mathbf{u}_i \rangle \langle \mathbf{u}_j \rangle \tag{3.13}$$

with $\mathbf{r}_i = (x_i, y_i, z_i)$ the coordinate of the lattice site i, $r_{ij} = |\mathbf{r}_{ij}|$ the distance between local modes on sites i and j, and where the first equality reflects the translational invariance due to periodic boundary conditions. The range in which the direction of one local mode influences other local modes is given by the correlation length $\xi_{l.m.}$, extracted from the asymptotic behavior of the correlation function at large separations between the local observables:

$$G(r_{ij}) \propto \exp(-r_{ij}/\xi_{l.m.}) \tag{3.14}$$

Since a direct estimation of the correlation length from the correlation function is inefficiently costly, one can alternatively resort to the computation of the second-momentum correlation length [261], defined by:

$$\xi_{l.m.} = \left[\frac{\mu_2}{z\mu_0} \right]^{1/2} \tag{3.15}$$

where

$$\mu_2 = \sum_{i,j=1}^{N} r_{ij}^2 G(r_{ij}) \tag{3.16}$$

is the second moment of the correlation function and μ_0 its zero-th moment

$$\mu_0 = \sum_{i,j=1}^{N} G(r_{ij}). \tag{3.17}$$

z is the number of nearest neighbors, which for a hypercubic lattice equals $2d$, with d the space dimension. For a cubic lattice of size $V = L^3$, the coordination number thus equals 6. In practice, the moments of the correlation function μ_0 and μ_2 are computed in the reciprocal space. Using the decomposition of the correlation function into Fourier modes

$$G(\mathbf{r}_i - \mathbf{r}_j) = \frac{1}{V} \sum_{n_1,n_2,n_3=0}^{L-1} \hat{G}(\mathbf{k}) e^{i\mathbf{k}.(\mathbf{r}_i - \mathbf{r}_j)} \tag{3.18}$$

with $\mathbf{k} = \frac{2\pi}{L}(n_1, n_2, n_3)$, the integration of the correlation function over the lattices sites

yields $\mu_0 = \hat{G}(0) = V(\langle \mathbf{u}^2 \rangle - \langle \mathbf{u} \rangle^2)$. Numerically, $\xi_{l.m.}$ is averaged over the three spatial directions $\hat{x}$, $\hat{y}$ and $\hat{z}$:

$$\xi_{l.m.} = \frac{1}{3}(\xi_{l.m.}^{\hat{x}} + \xi_{l.m.}^{\hat{y}} + \xi_{l.m.}^{\hat{z}}). \tag{3.19}$$

To compute each of those three terms $\xi_{l.m.}^{\hat{x}}$, $\xi_{l.m.}^{\hat{x}}$ and $\xi_{l.m.}^{\hat{x}}$, the Fourier transform of μ_2 is taken at minimal non zero momentum, respectively, $\mathbf{k}_m^{\hat{x}} = (2\pi/L, 0, 0)$, $\mathbf{k}_m^{\hat{y}} = (0, 2\pi/L, 0)$ and $\mathbf{k}_m^{\hat{z}} = (0, 0, 2\pi/L)$. For example, in the case of $\xi_{l.m.}^{\hat{x}}$, equation 3.15 yields

$$\xi_{l.m.}^{\hat{x}} = \frac{1}{|\mathbf{k}_m^{\hat{x}}|} \left[\frac{\hat{G}(0)}{\hat{G}(\mathbf{k}_m^{\hat{x}})} - 1 \right]^{1/2} \tag{3.20}$$

Since simulations were performed on finite L^3 (with $L = 12$) systems with periodic boundary conditions, the maximum value of the correlation length is limited to $\approx L/2$, and thus the resultant properties differ from those of the corresponding infinite lattices. Although finite size effects smooth the thermodynamic behavior of finite systems whether they pass through a first order phase transition or through a second order one, it is possible to assess their strength by examining the maximal value of $\xi_{l.m.}$. Whereas in the pure PZT system, $\xi_{l.m.}$ is found to peak at a value $\approx L/2$, thus indicating a finite or bounded signature of divergence, thereby signaling a second order phase transition together with strong finite size effects, in the case of PLZT systems, $\xi_{l.m.}$ remains lower than $L/2$, thus signaling smaller finite size effects together with a probable first-order like thermodynamic behavior (Fig. 3.17). This latter observation is somewhat in contradiction with the continuous behavior of of the polarization (Fig. 3.2,3.3 and 3.4), suggesting that disorder gradually turns the transition into a crossover. We note that with increasing lanthanum content, the maximal value of $\xi_{l.m.}$ decreases, thus supporting the idea of a hindered long-range order owing to disorder introduction and thereby explaining the decrease in magnitude of the polarization.

Whether quenched disorder affects the critical behavior of an ideal system or not has been a matter of many experimental and theoretical investigations. Under certain circumstances, quenched disorder can lead to the destruction of any critical point. In this case, due to the presence of defects, different parts of the system independently undergo the phase transition at different temperatures, resulting in a global phase transition smeared by disorder. At such a smeared phase transition, a unique critical temperature for the entire system does not exist, as a consequence of which a rounding of the singularities in the thermodynamic quantities is obtained [262, 263]. The origins of the disorder-induced smearing of the phase transition and of Griffiths phenomena [153] are very similar, both are caused by rare large spatial regions which are locally in the ordered phase. The difference lies in the dynamics of the rare regions.

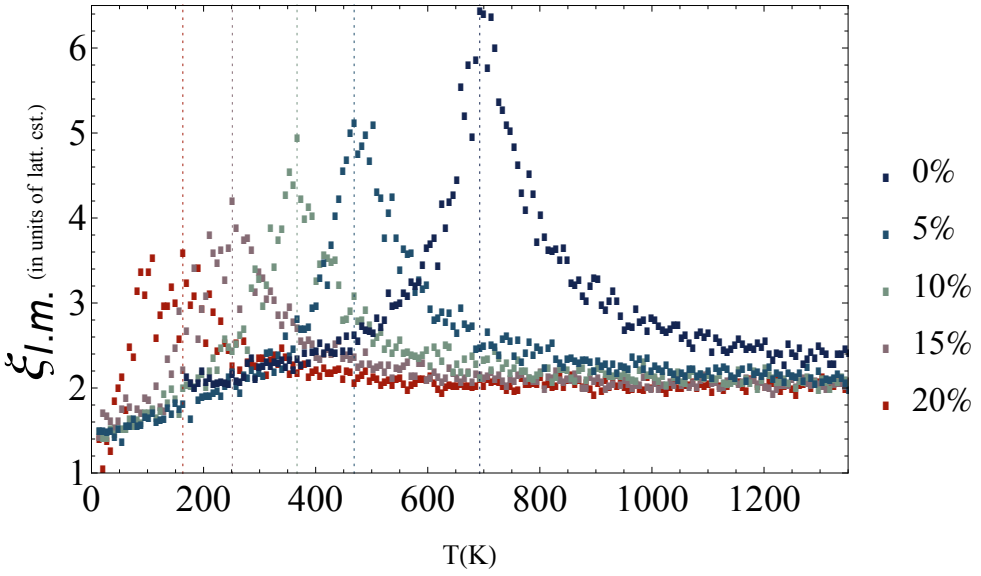

Fig. 3.17: Temperature evolution of the correlation length of the the local modes $\xi_{l.m.}$ for $PZ_{60}T_{40}$, $PL_5Z_{60}T_{40}$, $PL_{10}Z_{60}T_{40}$, $PL_{15}Z_{60}T_{40}$ and $PL_{20}Z_{60}T_{40}$ systems. Dotted vertical lines refer to the temperatures at which the correlation lengths peak.

Disorder in general decreases the critical temperature T_C from its clean (pure counterpart) value T_C^0. In the Griffiths phase corresponding to the temperature interval $T_C < T < T_C^0$, the system does not exhibit global order, however, in the limit of an infinitely large system, the probability of finding an arbitrarily large region devoid of disorder, although exponentially small, is nevertheless non-zero [153, 262]. Such rare regions can consequently develop local order, with a true phase transition independently from the bulk. Griffiths has shown that these rare regions result in a singular free energy in the interval $T_C < T < T_C^0$. They are endowed with slow dynamics owing to the requirement of a coherent change of the order parameter over a large volume. Consequently, the long-time dynamics is dominated by these rare regions [264]. In contrast, disorder-induced smearing occurs if the rare regions actually develop true static order [262].

However, generically, the effect of disorder on a phase transition is encoded by its spatial correlation. Subsequently it is possible that a phase transition retains its sharpness even in presence of quenched disorder, provided that this latter is only short-range correlated. This is assessed by the Harris criterion [265], which provides a condition enabling the discrimination between relevant and irrelevant disorder for the critical behavior of the pure system. Specifically, it states that any d-dimensional pure system undergoing a second order phase transition with a correlation length exponent $\nu > 2/d$ is stable against weak disorder.

In order to gain some insight about the relative effects of quenched disorder on the sharpness of the phase transition, we investigated the correlation length exponent of the $PZ_{60}T_{40}$ system. We should keep in mind that although $PZ_{60}T_{40}$ stands as the pure counterpart of $PLZ_{60}T_{40}$ systems, replacing Zr with Ti already introduces disorder, so that $PZ_{60}T_{40}$ is already disordered though exhibiting a sharp ferroelectric transition.In a study pertaining to

the critical behavior in ferroelectrics from first principles, a finite-size scaling analysis was conducted on bulk $PZ_{50}T_{50}$, whose critical behavior revealed to be (1) strongly deviating from that given by the mean-field model ($\nu(PZ_{50}T_{50})$ was reported to be different from 0.5, $\nu(PZ_{50}T_{50}) = 0.6723$), and (2) instead consistent with that associated with the 3D random Ising model universality class (RIM). Independently, it was shown that the critical behavior ($\nu(\text{RIM}) = 0.6832$) of such random systems appears to be approximately independent of the impurity concentration, thereby supporting the existence of random Ising universality class which differs from the one of pure Ising systems [267].

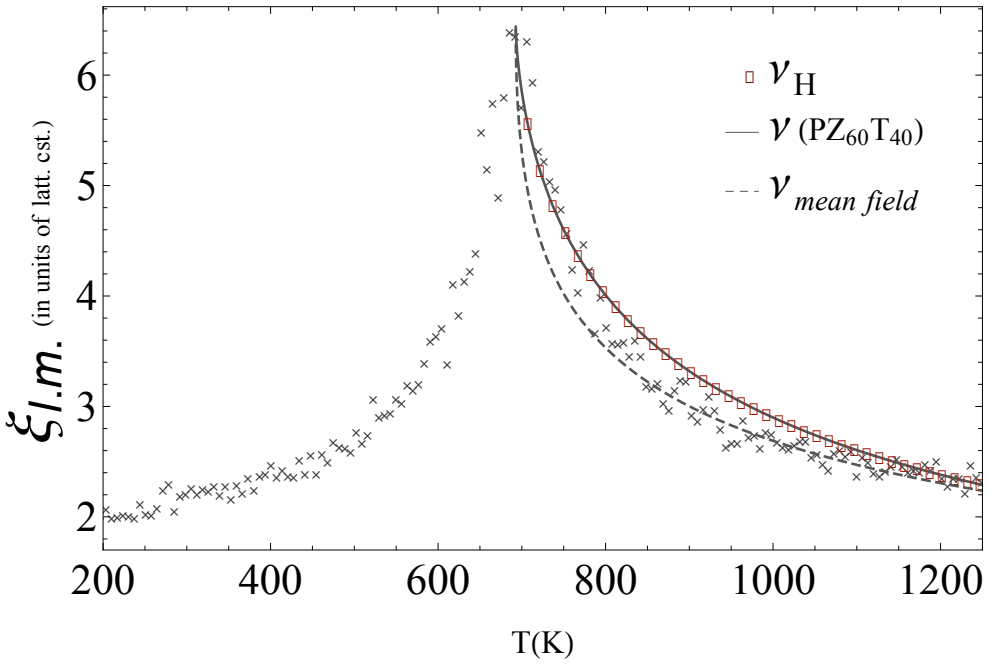

Fig. 3.18: Temperature evolution of the correlention length of $PZ_{60}T_{40}$ (cross symbols). Solid line corresponds to the result of the fit yielding $\nu(PZ_{60}T_{40})= 0.664$ and red squares correspond to the Harris threshold critical exponent $\nu(H)= 0.667$. Dashed line corresponds to the mean field expectations $\nu(\text{mean field}) = 0.5$.

Leveraging on both these observations, we started by linearly fitting $\text{Ln}\left(\xi^{-1} - \xi_m^{-1}\right)$ versus $\text{Ln}\left(T/T_\xi - 1\right)$, with T_ξ denoting the temperature at which the correlation function peaks and ξ_m its maximal magnitude. We obtained a critical exponent $\nu(PZ_{60}T_{40})= 0.664$. This result, although obtained for a 12^3 lattice, is quite close to (and slightly smaller than) the critical exponent $\nu(PZ_{50}T_{50}) = 0.672$ reported by finite-size scaling analysis [266]. This likeness between $\nu(PZ_{50}T_{50})$ and $\nu(PZ_{60}T_{40})$ is rather in agreement with the thesis of a RIM critical behavior, approximately independent of the impurity concentration [267] (*i.e.* of the Zr/Ti ratio). The obtained fit is shown by the solid line in Fig. 3.18. Also shown on this figure is the curve associated with the Harris threshold critical exponent (red squares), denoted by $\nu(H)$ and equal to 2/d, *i.e.*, $\nu(H)= 0.667$. Parenthetically, we note that while the temperature interval in close vicinity of the peak is characterized by $\nu(PZ_{60}T_{40})$, the high temperature region exhibits a deviation from this value, becoming closer to the mean field expectation

value $\nu(\text{mean field}) = 0.5$ (dashed line). Since $\nu(\text{H})$ and $\nu(PZ_{60}T_{40})$ nearly coincide, $PZ_{60}T_{40}$ seems to be on the verge of stability against weak disorder. This observation can explain why a somewhat sharp ferroelectric phase transition is retained in the weakly disordered $PL_5Z_{60}T_{40}$, while its dielectric susceptibility already shows a weak departure from the Curie-Weiss behavior (Fig. 3.13). The question is then how much disorder can the system tolerate before the transition becomes smeared. Strengthening the disorder by a further increase of the lanthanum content seems to gradually smear out the phase transition, progressively changing into a crossover and ultimately destroying it, thus indicating the development of a spatially inhomogeneous (attested by the drop in magnitude of the global polarization) quasi-static (attested by the drop in magnitude of the dielectric response) local order.

On another hand, fitting the correlation length in the vicinity of the peak for $PL_{10}Z_{60}T_{40}$ yielded $\nu(PL_{10}Z_{60}T_{40}) = 0.612$. This result is only a rough estimate of the critical exponent since more careful analysis should involve finite-size scaling procedure. Combining it with $\gamma(PL_{10}Z_{60}T_{40}) = 1.69$ (section 3.1.3) according to the scaling relation $2 - \eta = \gamma/\nu$ implies the anomalous dimension (Fisher critical exponent of the correlation function) $\eta(PL_{10}Z_{60}T_{40}) = -0.762$. It is in rather good qualitative agreement with the available experimental data ($\eta(PL_9Z_{65}T_{35}) = -0.865$, as extracted from Kallaev *et al.*'s critical exponents α and γ for PLZT 9/65/35 [28]). Most importantly, it is negative. According to Fisher [24–26], a negative η as the one also yielded by Kleemann *et al.*'s [27] critical exponents β and γ for strontium barium niobate (SBN61) is unphysical. Interestingly, in gauge theories the proof of a non-negative η is not applicable due to the non-gauge invariant form of the correlation function [29–31]. This is in remarkable contrast to the canonical models of relaxors and also suggests that SBN61 may be described within our gauge model with a suitable gauge symmetry.

3.1.5 Phase Sequence

We now discuss the structural phase sequence displayed by $PL_xZ_{60}T_{40}$ with increasing lanthanum content $x = 0, 5, 10, 15, 20\%$ (Fig. 3.19 to 3.23). For each of the systems, we analyze the temperature evolution of the Cartesian components $\langle u_x \rangle$, $\langle u_y \rangle$ and $\langle u_z \rangle$ of $\langle \mathbf{u} \rangle$, where $\langle\,\rangle$ denotes the average over sweeps performed on the average over the supercell of the local modes. We also report the temperature evolution of the lattice parameters $\langle |a_1| \rangle$, $\langle |a_2| \rangle$ and $\langle |a_3| \rangle$, and that of the lattice angles α, β and γ.

Fig. 3.19 indicates a transition from a high temperature cubic phase to a low temperature rhombohedral ferroelectric phase, in agreement with experimental observations for $PZ_{60}T_{40}$ [246]. Left insets of figures 3.20, 3.21, 3.22 and 3.23 show that two of the Cartesian components are zero within the error bars near T_C, thus indicating that $PL_xZ_{60}T_{40}$ systems

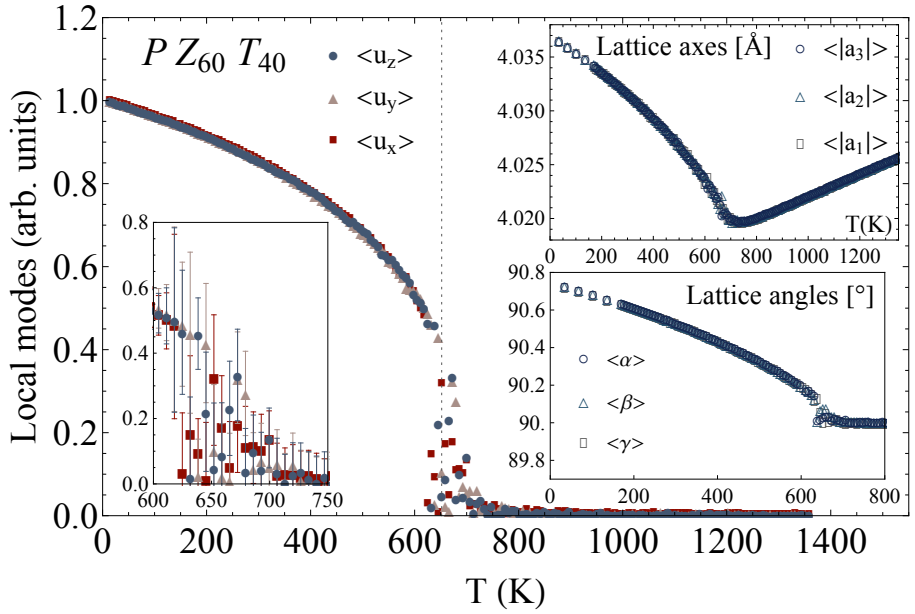

Fig. 3.19: Cartesian components ($\langle u_x \rangle$, $\langle u_y \rangle$ and $\langle u_z \rangle$) of $\langle \mathbf{u} \rangle$ in $PZ_{60}T_{40}$ as a function of rescaled temperature [155]. T_C corresponds to the maximum of the specific heat and is signaled by a vertical dotted line. Left side inset shows that all the Cartesian components are zero within the error bars in the close vicinity of T_C. Right side insets correspond to the temperature evolution of the lattice axes and the lattice angles.

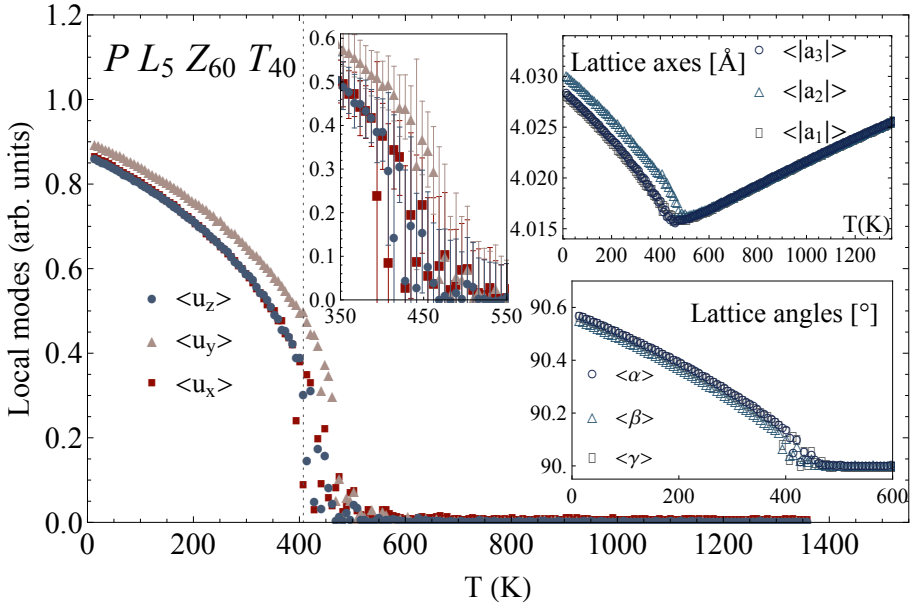

Fig. 3.20: Cartesian components ($\langle u_x \rangle$, $\langle u_y \rangle$ and $\langle u_z \rangle$) of $\langle \mathbf{u} \rangle$ in $PL_5Z_{60}T_{40}$ as a function of rescaled temperature [155]. T_C corresponds to the maximum of the specific heat and is signaled by a vertical dotted line. Left side inset shows that two of the Cartesian components are zero within the error bars near T_C. Right side insets correspond to the temperature evolution of the lattice axes and the lattice angles, and indicate a transition from a high temperature cubic phase to a low temperature monoclinic (M_A) ferroelectric phase.

with $x = 5, 10, 15$ and 20% are tetragonal in the close vicinity of the transition (as exemplified in Fig. 3.24 for $PL_5Z_{60}T_{40}$ at $T = 461$K), in agreement with Ref. [270].

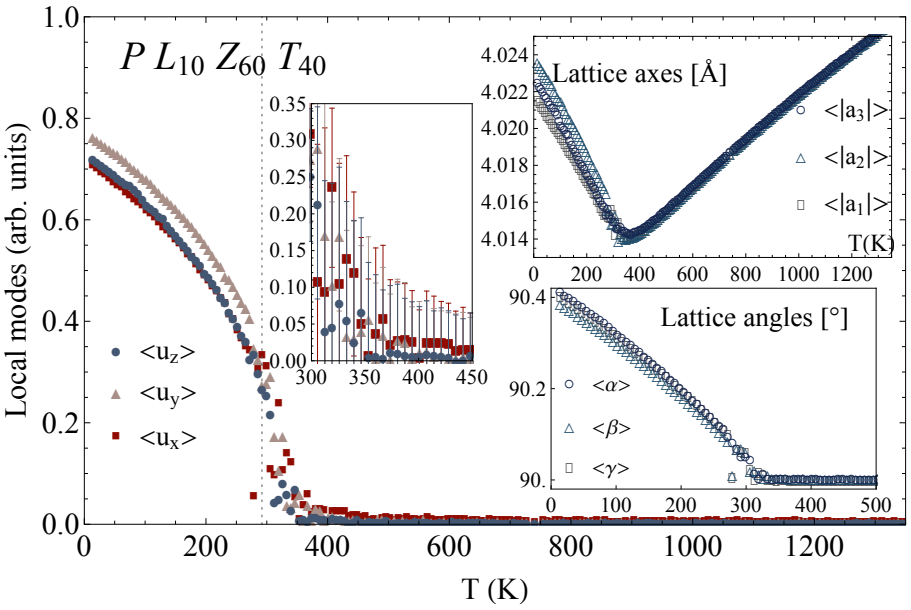

Fig. 3.21: Cartesian components ($\langle u_x\rangle$, $\langle u_y\rangle$ and $\langle u_z\rangle$) of $\langle \mathbf{u}\rangle$ in $PL_{10}Z_{60}T_{40}$ as a function of rescaled temperature [155]. T_C corresponds to the maximum of the specific heat and is signaled by a vertical dotted line. Left side inset shows that two of the Cartesian components are zero within the error bars near T_C. Right side insets correspond to the temperature evolution of the lattice axes and the lattice angles, and indicate a transition from a high temperature cubic phase to a low temperature monoclinic (M_A) (close to triclinic) ferroelectric phase.

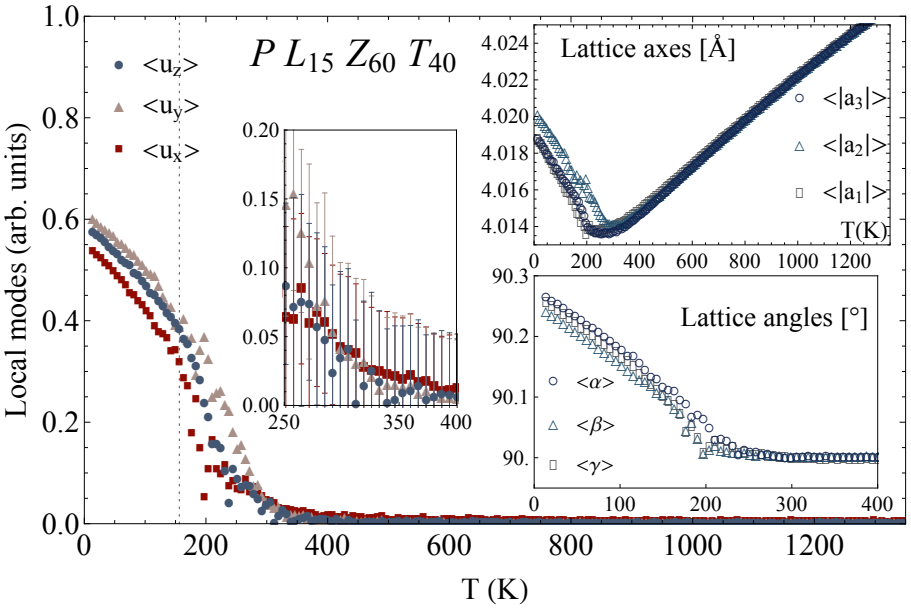

Fig. 3.22: Cartesian components ($\langle u_x\rangle$, $\langle u_y\rangle$ and $\langle u_z\rangle$) of $\langle \mathbf{u}\rangle$ in $PL_{15}Z_{60}T_{40}$ as a function of rescaled temperature [155]. T_C corresponds to the maximum of the specific heat and is signaled by a vertical dotted line. Left side inset shows that two of the Cartesian components are zero within the error bars near T_C. Right side insets correspond to the temperature evolution of the lattice axes and the lattice angles, and indicate a transition from a high temperature cubic phase to a low temperature monoclinic (M_B) (close to triclinic) ferroelectric phase.

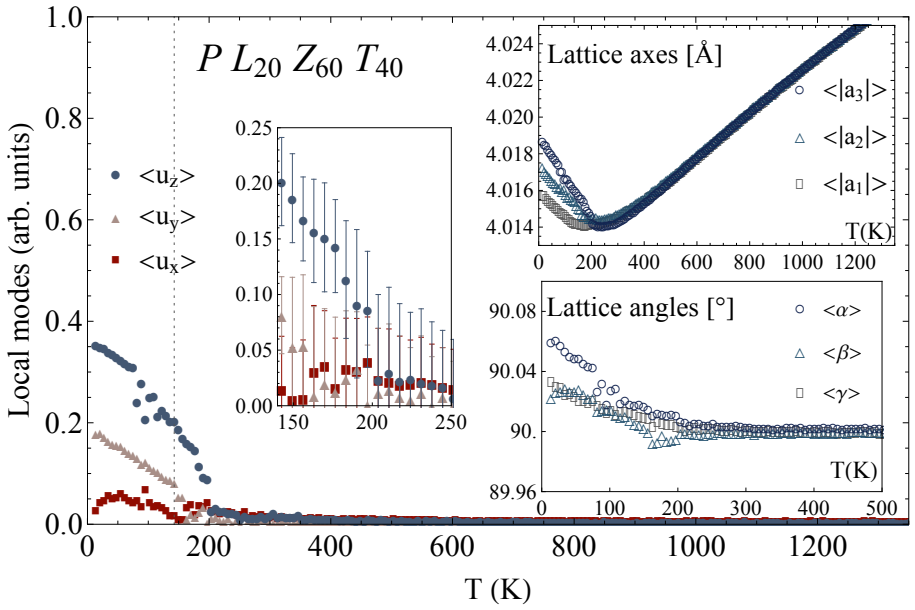

Fig. 3.23: Cartesian components ($\langle u_x \rangle$, $\langle u_y \rangle$ and $\langle u_z \rangle$) of $\langle \mathbf{u} \rangle$ in $PL_{20}Z_{60}T_{40}$ as a function of rescaled temperature [155]. T_C corresponds to the maximum of the specific heat and is signaled by a vertical dotted line. Left side inset shows that two of the Cartesian components are zero within the error bars near T_C. Right side insets correspond to the temperature evolution of the lattice axes and the lattice angles, and indicate a transition from a high temperature cubic phase to a low temperature triclinic phase.

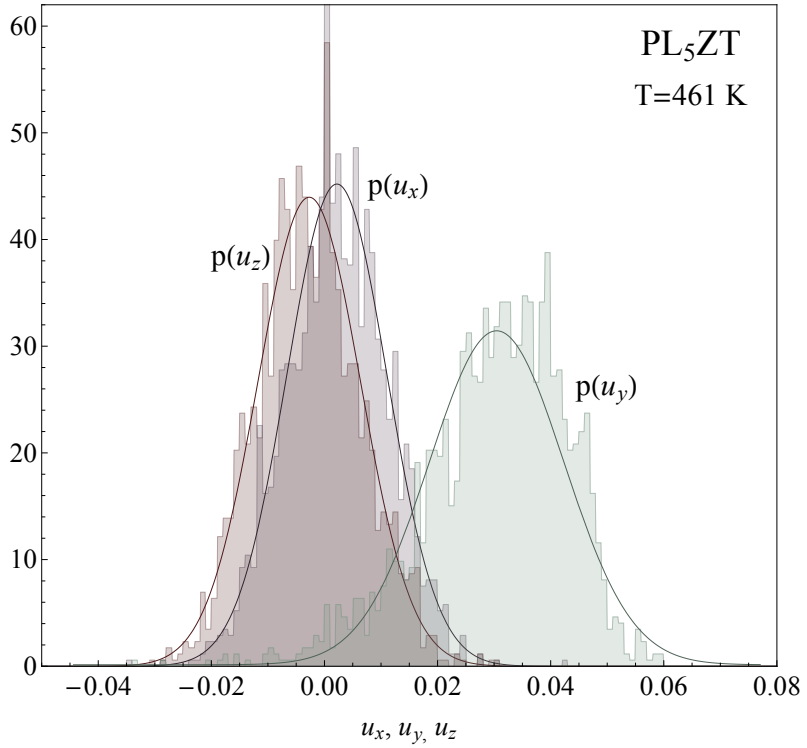

Fig. 3.24: Probability histograms for the averaged over sweeps unit cell local mode components of $PL_5Z_{60}T_{40}$ in the tetragonal phase (T= 461K) in the close vicinity of the transition.

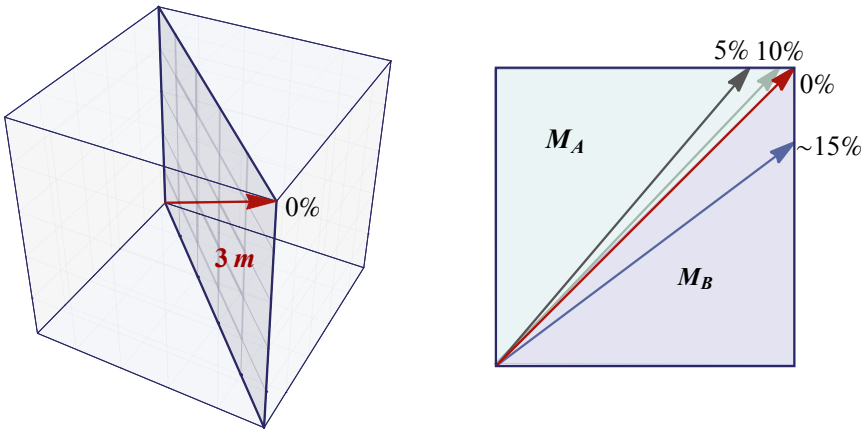

Fig. 3.25: Schematic representation of the influence of the lanthanum substitution on the low temperature structural properties of $PL_xZ_{60}T_{40}$ for increasing lanthanum content $x = 0, 5, 10, 15\%$.

Moreover, results indicate transitions from a high temperature cubic phase to a low temperature phase deviating from the rhombohedral one for $PL_xZ_{60}T_{40}$ systems (Fig. 3.25). Whereas for 0% the ground state is rhombohedral (left panel of Fig. 3.25), with increasing lanthanum content, the low-temperature phase is in fact monoclinic for $x < 15\%$ (M_A for 5% and 10%, M_B for 15%) and triclinic for $x > 15\%$ rather than rhombohedral (right panel of Fig. 3.25). Moreover, the unit cell is becoming increasingly metrically cubic in the ground states, with the maximal angles being approximately 90.75° for 0%, 90.58° for 5%, 90.41° for 10%, 90.25° for 15% and 90.06° for 20% at low temperatures.

3.1.6 Glassy-like signature and effects of local electric fields

Burns and Dacol have attributed the drop in the temperature dependence of the refractive index in $PL_8Z_{65}T_{35}$ occurring at a temperature T_d, much higher than T_C, to the onset of regions of non-reversible local polarization P_d [82]. They argued that the ferroelectric transition occurs first in lanthanum deficient regions, and as the temperature is lowered, P_d and the standard remanent reversible polarization acquire the same magnitude. This view has motivated glassy-like interpretations of the relaxor behavior within a general picture according to which, for $T_C < T < T_d$ and at short range, the local symmetry is polar and the atomic displacements from their cubic symmetry positions are correlated. The local regions are dispersed in the disordered host matrix. At long range, the atoms are statistically disordered and uncorrelated, so that the local polarizations are randomly oriented leading to a zero net polarization.

In order to enquire whether $PL_xZ_{60}T_{40}$ systems exhibit such features, namely if some local order can be retrieved within our simulations, we have investigated the temperature dependence of the Edwards-Anderson parameter [81], q_{EA}, that we calculated as in Ref. [169],

according to

$$q_{\mathrm{EA}} = \left\langle \langle \mathbf{u}_i \rangle_t^2 \right\rangle_i \tag{3.21}$$

where the inner averaging is performed on the t Monte Carlo sweeps while the outer one is made over the i lattice sites. Fig. 3.26 depicts the temperature evolution of both the squared polarization $\langle \mathbf{u} \rangle^2$ and the Edwards-Anderson parameter q_{EA} for PZT, PL_5ZT, $PL_{10}ZT$, $PL_{15}ZT$ and $PL_{20}ZT$ systems. The choice of contrasting q_{EA} and the squared polarization is motivated by the need to compare the local order, encoded by the quadratic in polarization q_{EA} parameter, to the global one. Moreover, we have rescaled the magnitude of both $\langle \mathbf{u} \rangle^2$ and q_{EA} for all compositions with the maximal magnitude of $\langle \mathbf{u} \rangle^2$ displayed by the pure $PZ_{60}T_{40}$ system.

In contrast with PZT and PL_5ZT (threshold composition) systems, for which q_{EA} and $\langle \mathbf{u} \rangle^2$ coincide, the cases of PL_xZT systems with $x > 5\%$ reveal that the q_{EA} parameters are higher than $\langle \mathbf{u} \rangle^2$ and retain a non-vanishing tail above T_C, thus signaling the onset of local order. This trend is enhanced with increasing lanthanum content, the subsisting tail extends to higher temperatures while the inflection point shifts to lower temperatures. Moreover, q_{EA} for $x > 5\%$ bears strong similarity with that experimentally measured and theoretically predicted within the spherical random-bond random-field model for PMN relaxor [268]. One also observes that the glass transition is not sharp, *i.e.*, it is not possible to define a temperature above which $q_{\mathrm{EA}} = 0$ and below which $q_{\mathrm{EA}} \neq 0$. Within the SRBRF model that accounts for the effects of both random fields and bonds, therefore displaying a conceptual link and a continuous interpolation between the two main interpretations of the nature of the diffuse phase transition in relaxors, *i.e.*, between a ferroelectric state broken up into nanodomains due to the presence of random fields, and a glassy state, Blinc *et al.* have attributed the lack of sharp glass transition in relaxors to the presence of random fields [99].

We are thus led to the examination of the local fields and their properties. The analysis can take two possible paths. Whereas the first relies on the electrical nature of the fields, the second is an attempt of redefinition of the gauge-modified effective Hamiltonian with the intention of paralleling random-field Ising model.

In the first case, the local electric fields are extracted from the long-range dipole-dipole interactions between local modes

$$E^{\mathrm{dip}} = \sum_{ij,\alpha\beta} Q_{ij,\alpha\beta} u_{i,\alpha} u_{j,\beta} \tag{3.22}$$

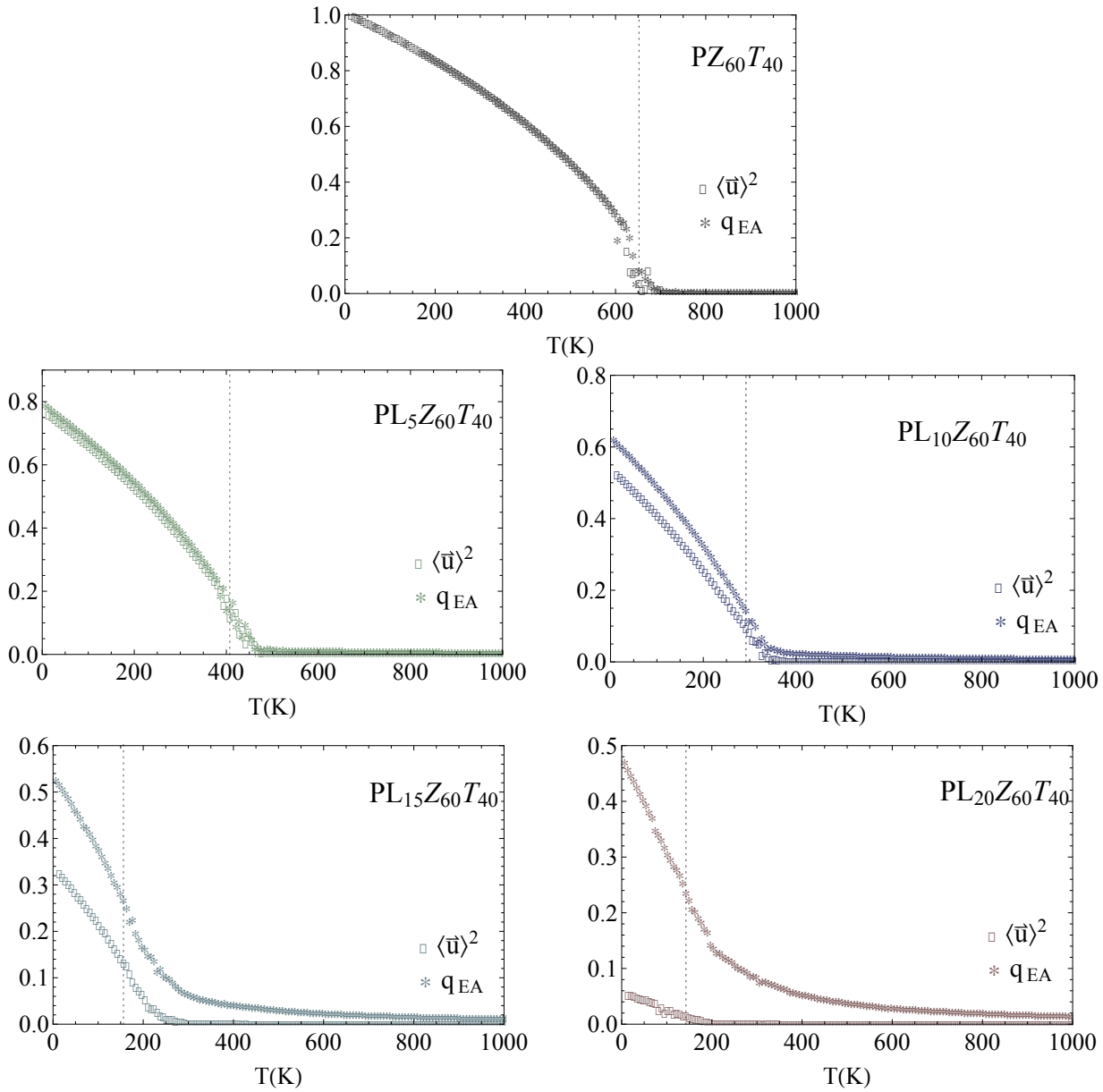

Fig. 3.26: Temperature evolutions of the Edwards-Anderson parameter q_{EA} and squared polarization $\langle \mathbf{u} \rangle^2$, for PZT, PL_5ZT, $PL_{10}ZT$, $PL_{15}ZT$ and $PL_{20}ZT$ systems. Dotted vertical lines correspond to T_C (*i.e.*, the temperature at which the specific heat peaks).

with Q being a matrix treated as a constant. The components of the local electric field on site i takes the following form

$$E_{i,\alpha} = \sum_{j,\beta} Q_{ij,\alpha\beta} u_{j,\beta} \tag{3.23}$$

and thus E_i is stemming from the contribution of all the local modes on a given site.

Fig. 3.27 shows the temperature evolution of the mean angular deviation between the local modes $\mathbf{u}_i$ and the local electric fields $\mathbf{E}_i$. The mean angular deviation is defined by

$$\frac{1}{N}\sum_i \text{Arccos}\left[\mathbf{u}_i.\mathbf{E}_i\right] \tag{3.24}$$

with N the number of sites, and corresponds to the supercell average of the angle between $\mathbf{u}_i$ and $\mathbf{E}_i$. Whereas in the pure system PZT, u_i and E_i tend towards collinearity at low temperatures, in PLZT systems, a more pronounced deviation from collinearity sets in at low temperatures with increasing lanthanum disorder. This is further illustrated by the inset of Fig. 3.27 that displays superposed low temperature snapshots of both the local electric fields and the local modes. One can see that the propensity to achieving collinearity is more pronounced in the ordered regions rather than in the disordered ones. Since the local electric fields are computed from the local modes, they cannot be put in one to one correspondence with quenched random fields. However, because of the quenched nature of the introduced disorder, local modes (directly coupled to the link variables) and local fields (emanating from the local modes and thus indirectly coupled to the link variables) freeze at low temperatures in configurations reflecting the disorder content.

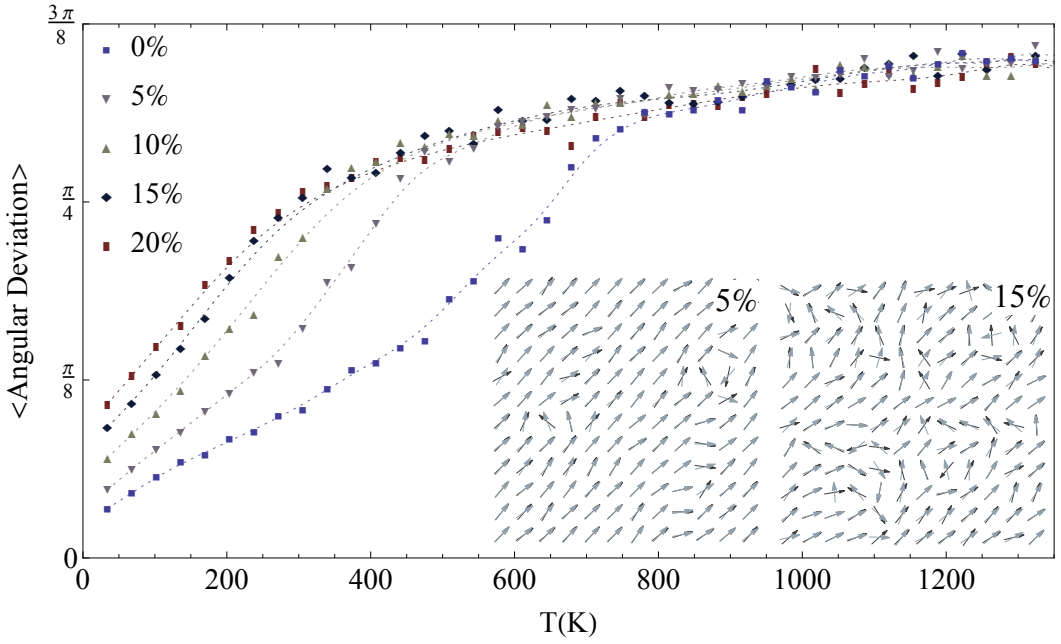

Fig. 3.27: Temperature evolution of the mean angular deviation between the local modes u_i and the local electric fields E_i, for PZT, PL_5ZT, $PL_{10}ZT$, $PL_{15}ZT$ and $PL_{20}ZT$ systems.Insets show snapshots of the local modes (in blue) and fields (in light purple) configurations for PL_5ZT and $PL_{15}ZT$ at $T = 34$ K in (x, y) plane.

After having considered orientational effects, we now discuss the magnitude of the local electric fields. Fig. 3.28 collects the temperature evolution of the mean magnitude of the local electric fields (upper panel) and of their standard deviation (lower panel) for $PZ_{60}T_{40}$ and $PL_xZ_{60}T_{40}$ with $x = 5\%, 10\%, 15\%$ and 20%. We note that $\langle|\mathbf{E}|\rangle$ globally decreases with

increasing *La* content. Moreover, whereas in the case of $PZ_{60}T_{40}$ the mean magnitude $\langle|\mathbf{E}|\rangle$ exhibits a minimum at T_C, in the case of $PL_xZ_{60}T_{40}$, the minimum is shifted towards $T > T_C$, thus indicating the relatively empowered role of the local fields above T_C in $PL_xZ_{60}T_{40}$ systems. The standard deviation indicates that whereas the distribution of the local fields' magnitude tends to sharpen around the mean value in the case of $PZ_{60}T_{40}$, a broader distribution is displayed by the $PL_xZ_{60}T_{40}$ systems, thus appending the orientational disorder with inhomogeneity in magnitude.

We now turn to the second case, where we abandon the idea of the electrical nature of the fields, instead relying on their formal definition, that is, a vector field linearly coupled to the order parameter (local modes) field such as in the $\sum_i h_i S_i$ term appearing in the random-field Ising model Hamiltonian:

$$H = -J \sum_{\langle ij \rangle} S_i S_j - \sum_i h_i S_i \tag{3.25}$$

In order to get more insight into the underlying mechanism and draw parallels with our approach, we write the gauge-modified short-range interaction term in the following form

$$\begin{aligned} E_{\mathrm{FE-G}} &= \frac{1}{2} \sum_{\substack{i \neq j \\ \alpha,\beta}} J_{ij,\alpha\beta} u_{i\alpha} U_{ij,\alpha\beta} u_{j\beta} \\ &= \frac{1}{2} \sum_{\substack{i \neq j \\ \alpha,\beta}} J_{ij,\alpha\beta} u_{i\alpha} u_{j\beta} + \frac{1}{2} \sum_{j,\beta} \underbrace{\left\{ \sum_{i,\alpha} J_{ij,\alpha\beta} u_{i\alpha} \{ \sum_{k=1}^{\infty} \frac{1}{k!} A_{ij,\alpha\beta}^k \} \right\}}_{E_{j\beta}^{\mathrm{RF}}} u_{j\beta} \end{aligned} \tag{3.26}$$

where we have used the exponential representation of the link matrices and performed its Taylor series expansion in powers of A_{ij}

$$U_{ij,\alpha\beta} = e^{A_{ij,\alpha\beta}} = \mathbb{1} + \sum_{k=1}^{\infty} \frac{1}{k!} A_{ij,\alpha\beta}^k \tag{3.27}$$

where depending on the linking direction between coupled nearest neighbors, $A_{ij,\alpha\beta}$ takes one of the following forms

$$A_{\hat{x}} = \begin{pmatrix} 0 & 0 & 0 \\ 0 & 0 & -\theta \\ 0 & \theta & 0 \end{pmatrix} \quad A_{\hat{y}} = \begin{pmatrix} 0 & 0 & \phi \\ 0 & 0 & 0 \\ -\phi & 0 & 0 \end{pmatrix} \quad A_{\hat{z}} = \begin{pmatrix} 0 & -\delta & 0 \\ \delta & 0 & 0 \\ 0 & 0 & 0 \end{pmatrix} \tag{3.28}$$

The latter matrices are the three generators of SO(3) group, multiplied by the corresponding rotation angles. $E_{i\alpha}^{\mathrm{RF}}$ is constructed according to:

$$E_{i\alpha}^{\mathrm{RF}} \propto \sum_{\beta} \sum_{j \in \mathrm{NN}} u_{j\beta} (U_{ij\alpha\beta} - \delta_{\alpha\beta}) \tag{3.29}$$

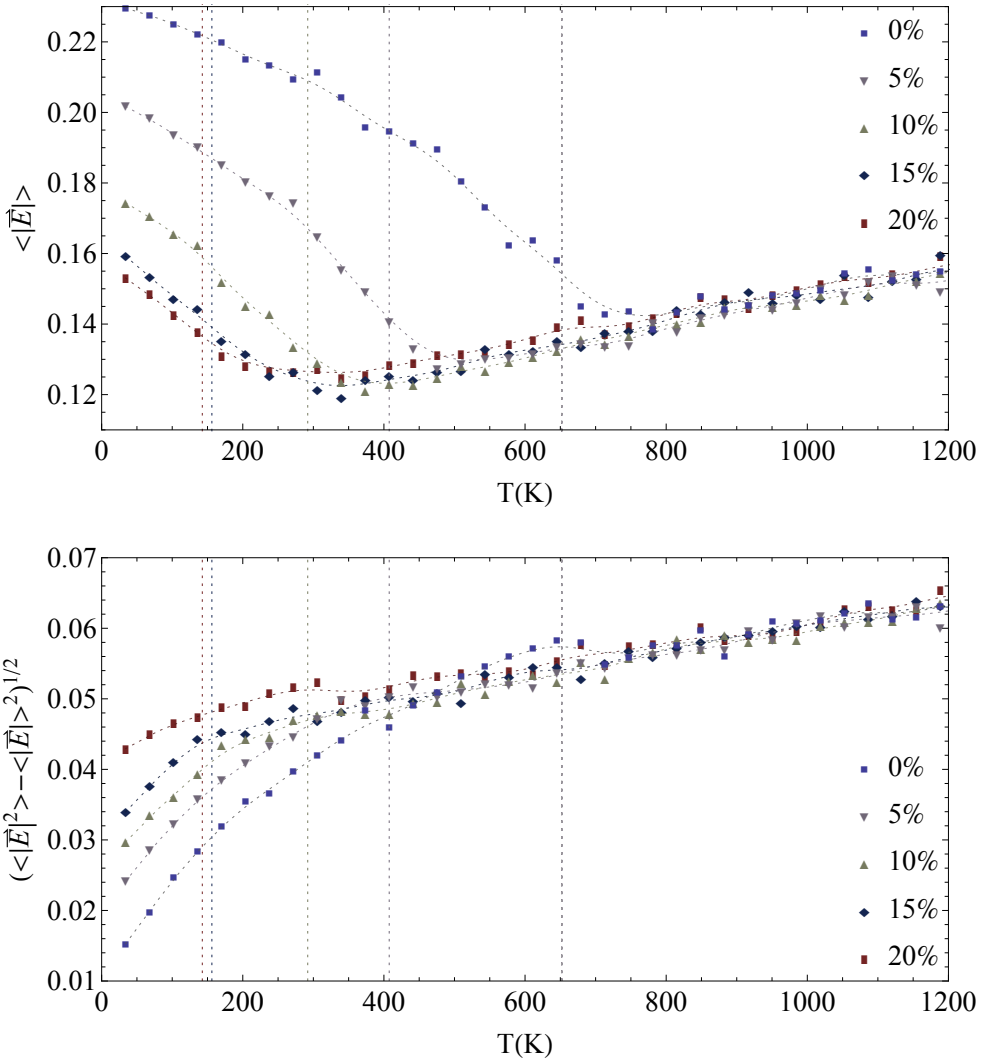

Fig. 3.28: Temperature evolution of the mean magnitude of the local electric fields (upper panel) and of their standard deviation (lower panel) for $PZ_{60}T_{40}$ and $PL_xZ_{60}T_{40}$ with $x = 5\%, 10\%, 15\%$ and 20%. Dotted vertical lines refer to T_C, obtained from the maximum of the specific heat.

Let us stress that, despite the formal analogy, since the gauge field is only partially quenched, the constructed $E_{i\alpha}^{\rm RF}$ fields are not quenched random fields per se. Indeed, they involve local modes which are variables quantities, and angles θ, ϕ and δ, which are quenched only when associated to the links defining the edges of quenched (lanthanum containing) unit cells. However, since the links are self-coupled and short-range correlated, $E_{i\alpha}^{\rm RF}$ has the fingerprint of quenched local disorder. Fig. 3.29 shows the temperature evolution of the mean angular

deviation between the local modes $\mathbf{u}_i$ and the local fields $\mathbf{E}_i^{\mathrm{RF}}$. The mean angular deviation is defined by Eq.3.24. As in the first case, one observes that the deviation from collinearity at low temperatures increases with increasing quenched local disorder. However, in the present second case, the deviation is much stronger than the one obtained in the first case. This can be ascribed to both the derivation of $\mathbf{E}_i^{\mathrm{RF}}$ in a manner directly involving link matrices which encode disorder, and the short-range nature of the coupling to local modes.

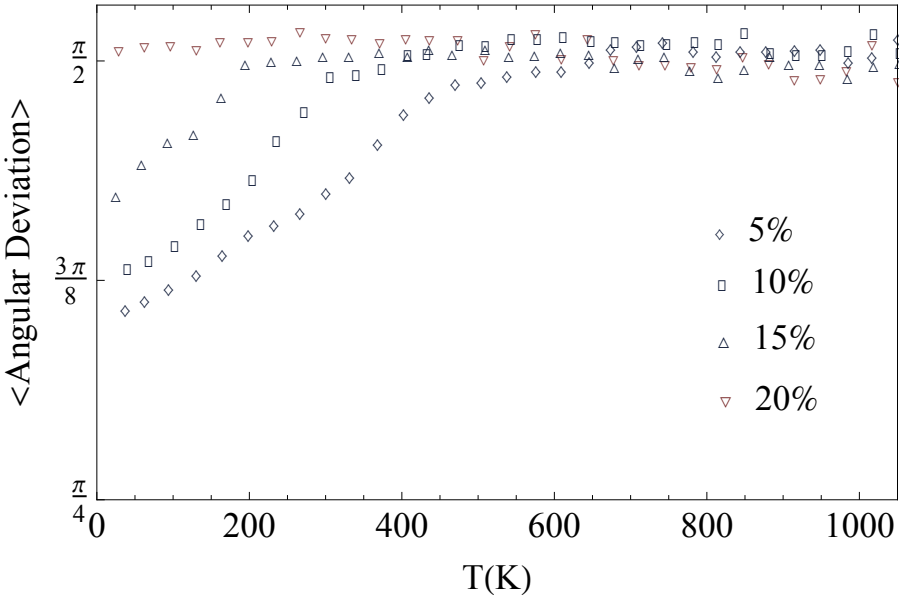

Fig. 3.29: Temperature evolution of the mean angular deviation between the local modes u_i and the local fields E_i^{RF}, for $PL_{10}ZT$, $PL_{15}ZT$ and $PL_{20}ZT$ systems.

This is further confirmed by Fig. 3.30 which depicts the integral curves associated with the local modes vector field (LM) together with the vectors representing $\mathbf{E}_i^{\mathrm{RF}}$ (LF) for $PL_{10}ZT$ at T= 34K and at T= 1358K, within a (x, y) plane. At high temperatures the two vector fields exhibit uncorrelated disorder. At low temperatures on another hand, while both LM and LF have gained in order, the one featured by the LF is much weaker thereby attesting its quenched component. Moreover, one observes that the derived LF tend to bend the integral curves of the LM, as shown in the encircled regions. Thus these non-genuine self-consistently-derived local fields nonetheless act as disordering entities.

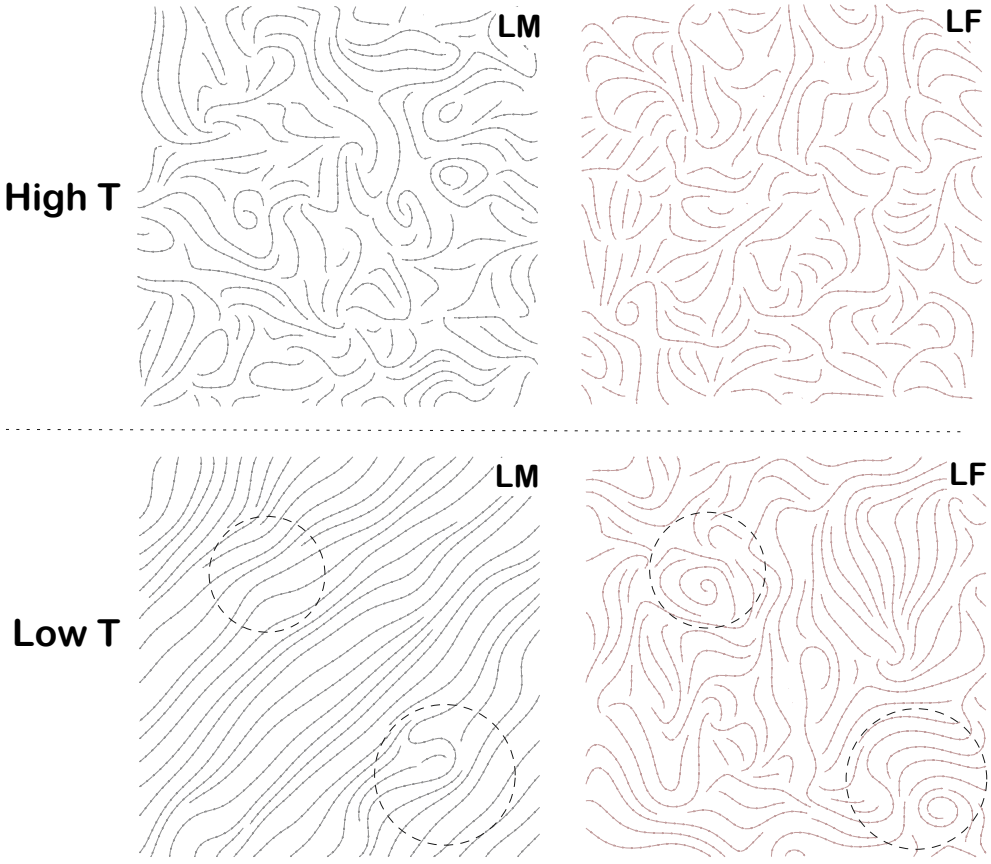

Fig. 3.30: Integral curves within a (x, y) plane associated with the local modes (LM) and with the derived $E_{i\alpha}^{\mathrm{RF}}$ local field (LF) for $PL_{10}ZT$. The upper and lower panels show the configurations for T= 34K and T= 1358K, respectively. At low temperatures, encircled regions illustrate the bending effect of the LF on the LM.

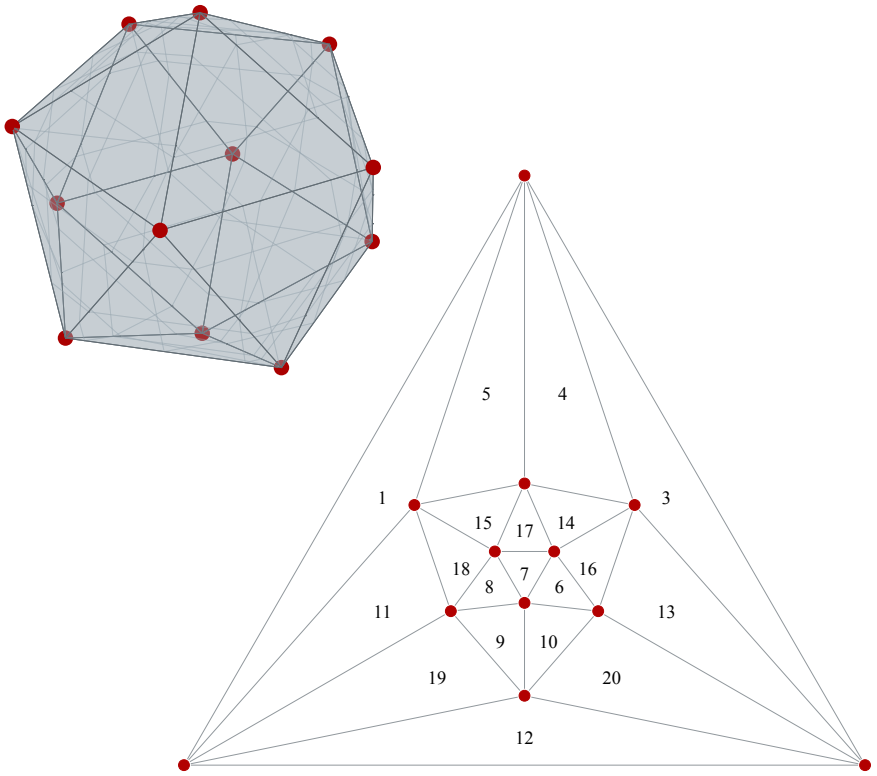

Fig. 3.31: Icosahedron and its associated planar graph representation. The icosahedron is a regular polygon of twelve nodes and twenty triangular faces. Its spherical projection defines a regular tiling of the circumscribing sphere, therefore splitting the maximal solid angle into twenty equal parts. The numbers appearing in the planar graph representation of the icosehdraon correspond to a labeling of the faces.

3.2 Clustering of the local modes

We now turn to the investigation of local order, its morphology and its temperature evolution. To achieve this purpose, we adopt a two-step procedure, consisting in the spatial clustering of orientational subsets of local modes.

The first step amounts to an orientational partitioning of the local modes population in orientational subsets. To achieve this partitioning, one needs to define a uniform tiling of the sphere according to which the local modes will be segregated. A triangulation of the sphere based on the spherical projection of a regular polygon fulfills such a need. Indeed, it is circumscribed by a sphere, and the spherical projection of its faces splits the maximal solid angle into equal parts. Here we choose a twenty-fold tiling, thereby involving the icosahedron figure (Figures 3.31 and 3.32).

This icosahedron-based spherical triangulation enables the division of the local modes population into twenty subsets corresponding to the spherical projection of the twenty faces. In order to evaluate whether or not local modes belonging to the same orientational subset

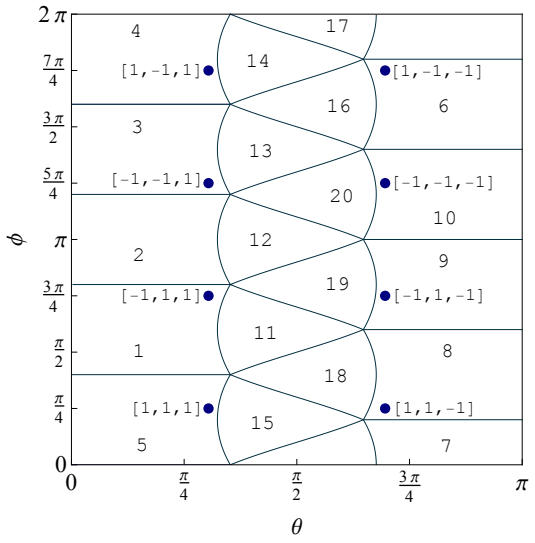

Fig. 3.32: Theta-Phi diagram of the considered regular triangulation. Each region of the diagram represents the theta-phi extension of the solid angle associated to the face. The blue dots correspond to the eight equivalent rhombohedral ground-state directions. In the chosen labeling, one can see that the $[1, 1, 1]$ direction for example is assigned to the fifth face.

exhibit spatial clustering in the lattice, we then implement the Hoshen-Kopelman clustering algorithm [283], for each of the obtained population per icosahedron face. This constitutes the second step of the procedure, which enables us to systematically extract for each of the faces, the evolution with temperature of the number of clusters (N_{Cl}), their average volume (V_{Cl}^{av}) and their total volume (V_{Cl}^{tot}), this latter referring to the total population of a face. The results are provided by figures 3.33 to 3.37 and discussed therein.

In order to illustrate the previous discussion (figures 3.33 to 3.37), we have extracted the biggest clusters for $PZ_{60}T_{40}$ system, just above T_C, and for $PL_5Z_{60}T_{40}$, $PL_{10}Z_{60}T_{40}$, $PL_{15}Z_{60}T_{40}$ and $PL_{20}Z_{60}T_{40}$ systems, for temperatures just above their T_m. One clearly sees that local order has developed around T_m (section 3.1.6). Moreover, this local order is comprised within clusters exhibiting rugged boundaries, as attested by their fractal dimension that we computed using the *box counting* method [277, 278] (Eq.3.33). We found that the fractal dimension all the more deviates from the physical dimension with increasing quenched disorder.

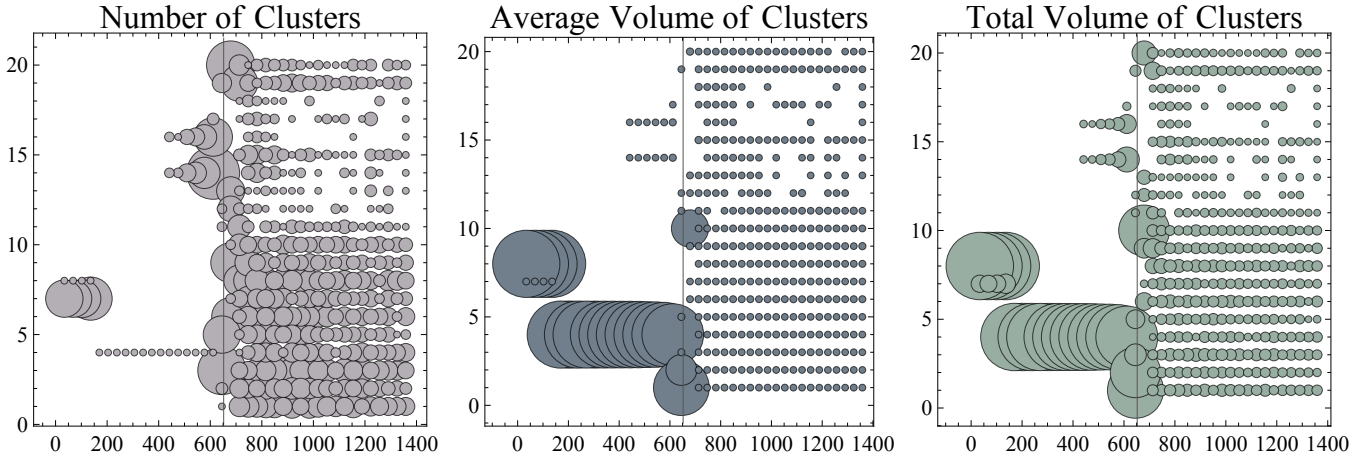

Fig. 3.33: $PZ_{60}T_{40}$: Temperature evolution of the number of clusters (N_{Cl}), their average volume (V_{Cl}^{av}) and their total volume (V_{Cl}^{tot}) per face. The y axis refers to the face label, the x axis denotes temperature. Let's first put our attention on the high-temperature region. *(i)* High temperatures are characterized by small values of N_{Cl}, V_{Cl}^{av} and V_{Cl}^{tot} for all faces. Thus spatial correlations are very weak, and all directions are equivalent. This is merely indicative of full disorder. *(ii)* While approaching T_C (indicated by a vertical line) from above, one observes signatures of critical fluctuations, such as emergence of preferred orientations (some directions are no longer represented while large spatial clusters corresponding to certain equivalent rhombohedral orientations appear) and scale invariance (indicated by the fact that differently populated directions acquire equal number of clusters). *(iii)* Below T_C, up to $\sim$ 440K, one observes the condensation of only several clusters oriented in $[1,-1,1]$ and $[1,-1,-1]$ directions (faces 4, 14 and 16). Whereas the single cluster corresponding to $[1,-1,1]$ (major phase) direction stands out in terms of large volume, the clusters with $[1,-1,-1]$ (minor phase) orientation are numerous and, in contrast, relatively much smaller in volume. This latter observation shows that below T_C the percolation of $[1,-1,1]$ clusters has been achieved, however the volume corresponding to the major phase is not simply connected. This situation is not persistent since a further decrease of the temperature drives this minor phase to gradually shrink, ultimately disappearing at 440K. *(iv)* At temperatures below $\sim$ 440K the ground state is achieved. It is important to mention that what could appear as a switching of direction is, in fact, only an artifact of Metropolis Monte-Carlo method.

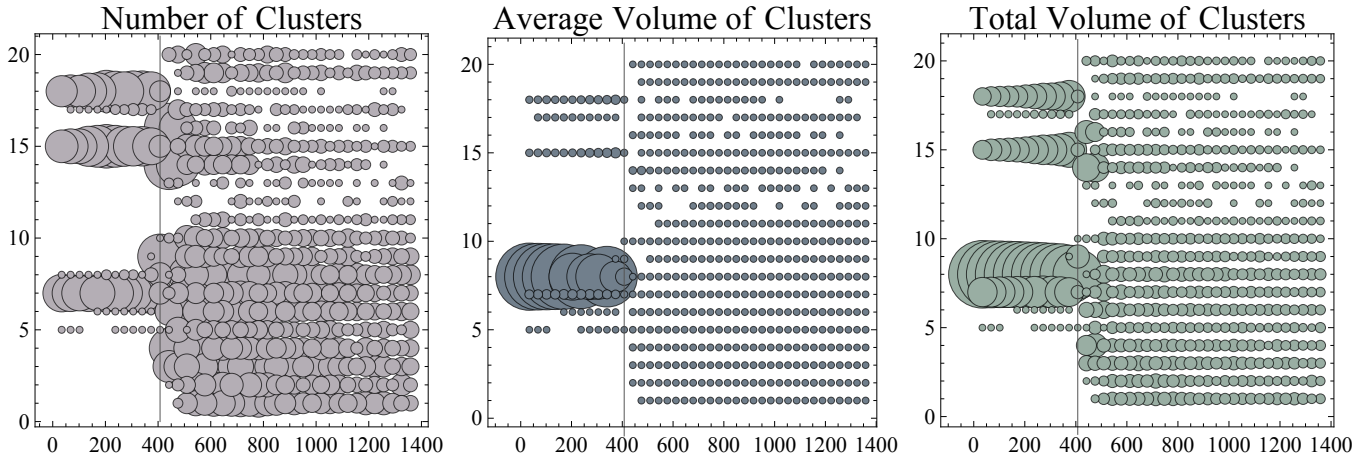

Fig. 3.34: $PL_5Z_{60}T_{40}$: Temperature evolution of the number of clusters (N_{Cl}), their average volume (V_{Cl}^{av}) and their total volume (V_{Cl}^{tot}) per face. The y axis refers to the face label, the x axis denotes temperature. *(i)* Qualitatively, the high temperature region features the same full-disorder characteristics as those featured by the pure system $PZ_{60}T_{40}$. *(ii)* However, on approaching T_C from above, a slight difference emerges in comparison with $PZ_{60}T_{40}$. The proloferation of clusters is enhanced, as attested by the increase of both the N_{Cl} and V_{Cl}^{tot}, while V_{Cl}^{av} stays the same for the two systems. This indicates the emergence of a somewhat shy, short-range correlated order above T_C *(iii)* Just below T_C, the main difference between $PL_5Z_{60}T_{40}$ and $PZ_{60}T_{40}$ concerns the dispersion of the major phase around its rhombohedral direction. Indeed, while the ground state corresponds to $[1, 1, -1]$ direction (contained in face 8), V_{Cl}^{av} of faces 7, 15 and 18 stays comparable to that of face 8 on a wide temperature range, thereby indicating a dispersion around the ground state direction. *(iv)* At low temperatures, the aforementioned dispersion subsists, explaining the drop in magnitude of $PL_5Z_{60}T_{40}$ relatively to $PZ_{60}T_{40}$.

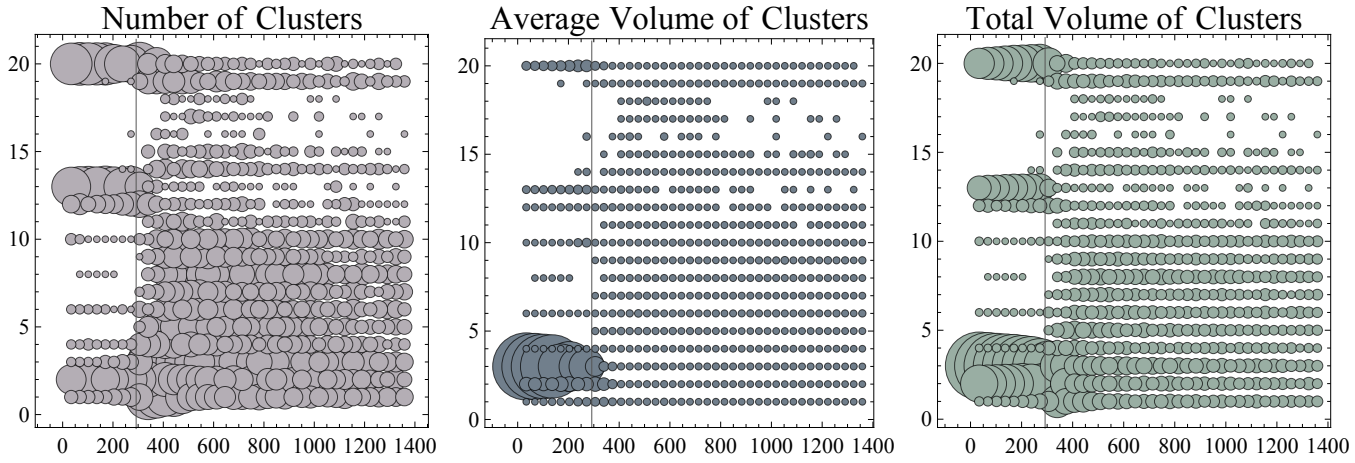

Fig. 3.35: $PL_{10}Z_{60}T_{40}$: Temperature evolution of the number of clusters (N_{Cl}), their average volume (V_{Cl}^{av}) and their total volume (V_{Cl}^{tot}) per face. The y axis refers to the face label, the x axis denotes temperature. *(i)* The high temperature range exhibits full-disorder characteristics. *(ii)* Above T_C and up to ∼500 K, one observes that for faces labeled by 1, 2 and 3, both N_{Cl} and V_{Cl}^{tot} gradually increase, while V_{Cl}^{av} stays the same. This trend seems of the same nature as that described for $PL_5Z_{60}T_{40}$, yet monotonical and more pronounced. *(iii)* Below T_C, faces 1, 13 and 20 experience a weak depopulation of their clusters, as attested by the decay of V_{Cl}^{tot}. This trend is similar to that described for $PL_5Z_{60}T_{40}$, but weaker. *(iv)* The ground state is thus populated by clusters belonging to faces dispersed around two rhombohedral directions (a main one, $[-1,-1,1]$ associated with face 3, and $[-1,1,1]$ associated with face 1), making the average symmetry monoclinic (section 3.1.5).

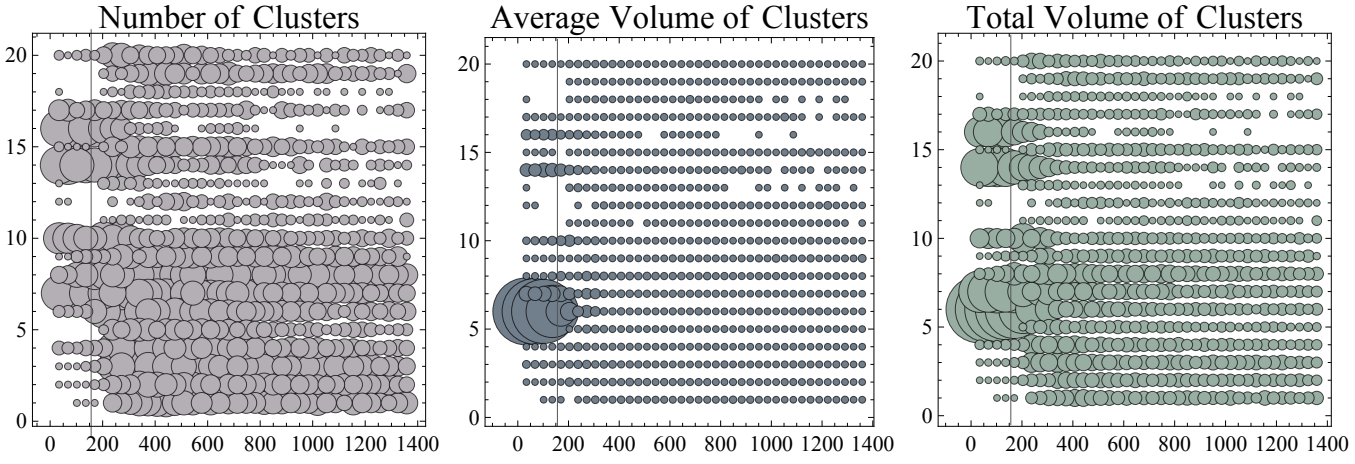

Fig. 3.36: $PL_{15}Z_{60}T_{40}$: Temperature evolution of the number of clusters (N_{Cl}), their average volume (V_{Cl}^{av}) and their total volume (V_{Cl}^{tot}) per face. The y axis refers to the face label, the x axis denotes temperature. *(i)* The high temperature range exhibits full-disorder characteristics. *(ii)* Above T_C, faces 6, 14 and 16 exhibit a monotonical increase of V_{Cl}^{tot} and of V_{Cl}^{av}. The fact that V_{Cl}^{av} also increases in the case of $PL_{15}Z_{60}T_{40}$ is an indication of a more developed local order. *(iii)* Below T_C, large volumes of differently ordered regions make the ground state direction mixed between different directions, mainly composed of the directions $[1,-1,-1]$ (faces 6, 7, 14 and 16) and $-[1,-1,-1]$ (faces 10, 20), making the average symmetry monoclinc on the verge of being triclinic (section 3.1.5).

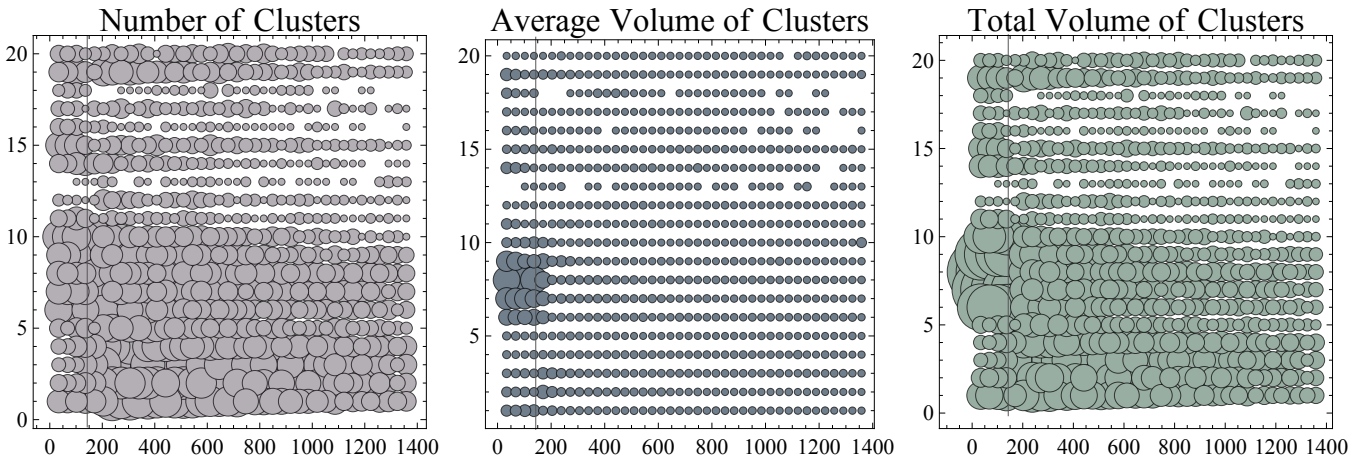

Fig. 3.37: $PL_{20}Z_{60}T_{40}$: Temperature evolution of the number of clusters (N_{Cl}), their average volume (V_{Cl}^{av}) and their total volume (V_{Cl}^{tot}) per face. The y axis refers to the face label, the x axis denotes temperature. *(i)* In this case, disorder extends over a wide temperature range. *(ii)* The ground state is strongly mixed, resulting in a triclinic average symmetry (section 3.1.5).

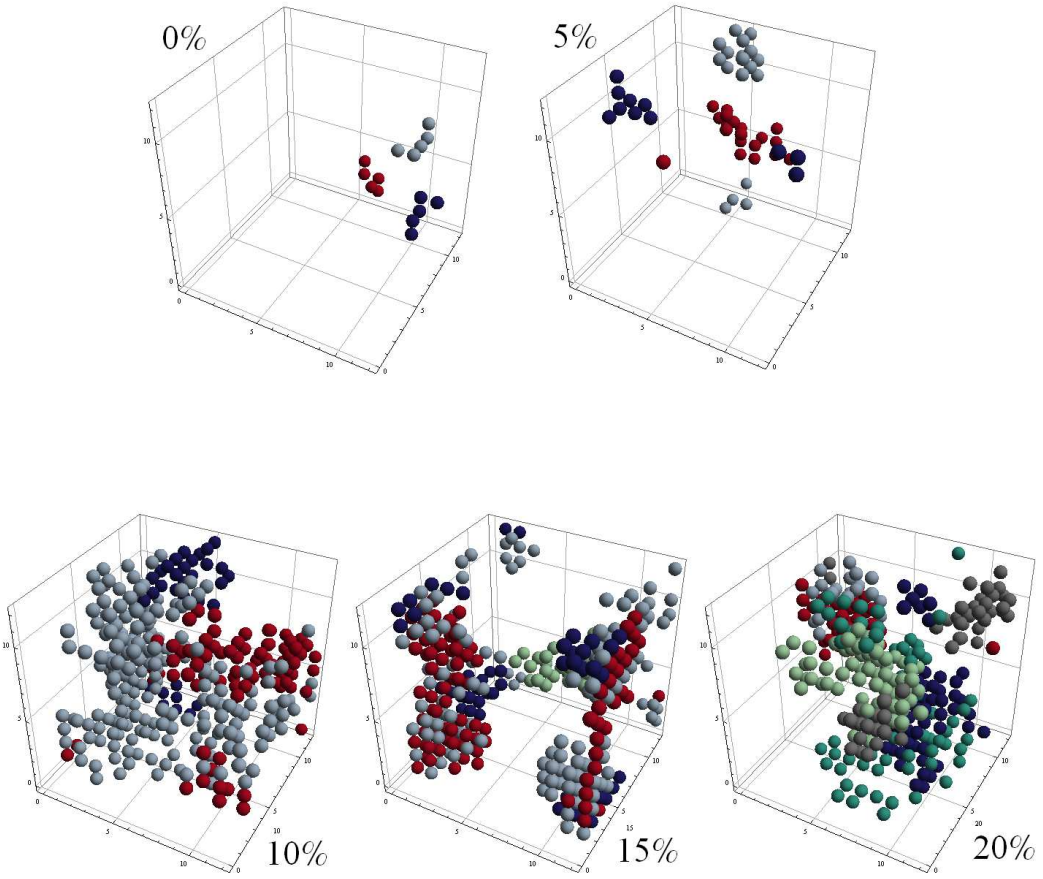

Fig. 3.38: Biggest clusters of local modes for $PZ_{60}T_{40}$ system, just above T_C, and for $PL_5Z_{60}T_{40}$, $PL_{10}Z_{60}T_{40}$, $PL_{15}Z_{60}T_{40}$ and $PL_{20}Z_{60}T_{40}$ systems, for temperatures just above their T_m.

3.3 Under Pressure

The application of hydrostatic pressure on a system with fixed composition has been advocated as a suitable probe of the interatomic interactions and thusly of the mechanisms underlying the relaxor behavior. Indeed, pressure has been shown to be a "clean" relaxor-inducing variable. In contrast to the usual approach relying on the change of compositions in order to drive the onset of the relaxor behavior, pressure on the other hand, without altering the disorder content, rather enhances its effects by disrupting the balance between long and short range interactions, favoring the latter and weakening the former [104]. In $PL_xZ_{60}T_{40}$ systems, relaxor behavior becomes discernible above x>%5 [155, 269]. We thus investigate the influence of pressure on the properties of $PL_5Z_{60}T_{40}$ system. For this composition of disorder, the system is on the verge of the relaxor behavior [269] and hence constitutes a good candidate to test whether our model reproduces the expected ferroelectric-to-relaxor crossover.

3.3.1 Strengthened disorder

Fig. 3.39 provides the effect of various pressures on the evolution with temperature of the norm of the statistical average of the local modes, $|\langle \mathbf{u} \rangle|$ (Eq.3.3), directly proportional to polarization. The effect of pressure is investigated in the range $0 \leq P \leq 100$ kbar. Increasing pressure destabilizes the ferroelectric phase. It depresses T_C and lowers the magnitude of the polarization at low temperatures, ultimately preventing the onset of a ferroelectric phase for high enough pressure (∼100 kbar).

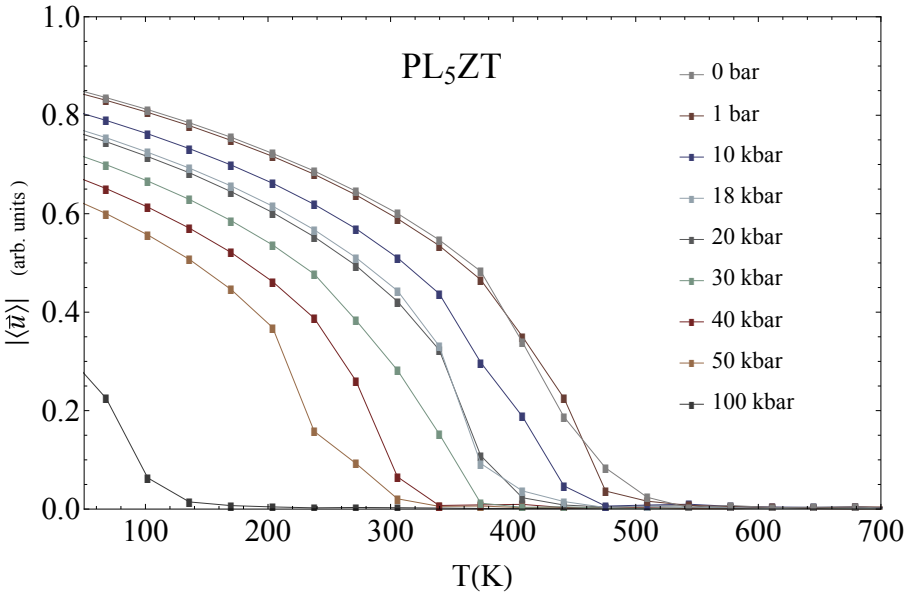

Fig. 3.39: Influence of pressure on the temperature evolution of $|\langle \mathbf{u} \rangle|$ in $PL_5Z_{60}T_{40}$ systems. Plot of the polarization as a function of T for various pressures in the range $0 \leq P \leq 100$ kbar.

Fig. 3.40 corroborates this observation by providing a microscopic insight of the effect of an increasing pressure on the integral curves associated to the dipole moments field in a (x, y) plane of $PL_5Z_{60}T_{40}$ system. For the same disorder realization (*i.e.*, the same spatial distribution of quenched disorder), the increasing pressure reveals its substantial disordering effect in that it engenders gradual deviation from the low pressure quasi-ordered configuration.

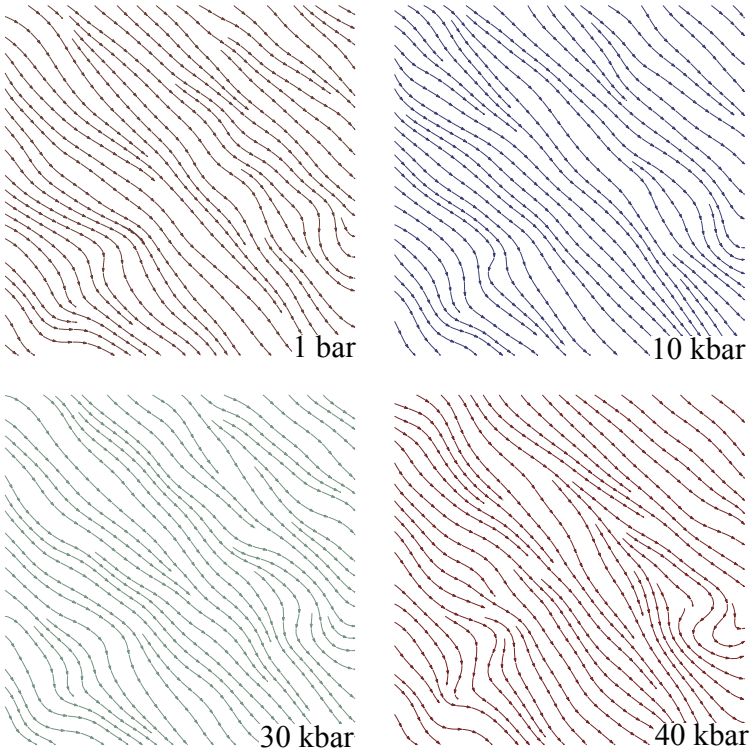

Fig. 3.40: Integral curves of the local dipole moments within a given (x, y) plane for $PL_5Z_{60}T_{40}$ at $T = 34K$ under 1 bar, 10 kbar, 30 kbar and 40 kbar for the same realization of random disorder.

3.3.2 Temperature-Pressure phase diagram

The results displayed in Fig. 3.41 show the influence of pressure on the specific heat and on the inverse susceptibility. The temperature at which the specific heat peaks is used for the determination of T_C while that at which the dielectric response peaks corresponds to T_m. Both T_C and T_m feature a shift towards lower temperatures with increasing pressure, in a manner somewhat analogous to the effect of an increasing disorder content. These characteristic temperatures are collected in Fig. 3.42, which provides the Temperature-Pressure phase diagram of $PL_5Z_{60}T_{40}$. We find that the shifts of T_C and T_m with pressure are characterized by similar slopes, namely, $dT_C/dP = -4.85$ K/kbar and $dT_m/dP = -4.66$ K/kbar. These results are fully consistent with those experimentally found by Samara [104] who reports $dT_{C,m}/dP = -5$ K/kbar for $PL_6Z_{65}T_{35}$. However, we find no evidence of a relaxor/ferroelectric phase boundary terminating in a critical point [104]. Let us note that in contrast

with Ref. [148], our results are in both qualitative and quantitative agreement with those reported by Samara [104], specifically the pressure range that we investigate is identical to the experimental one.

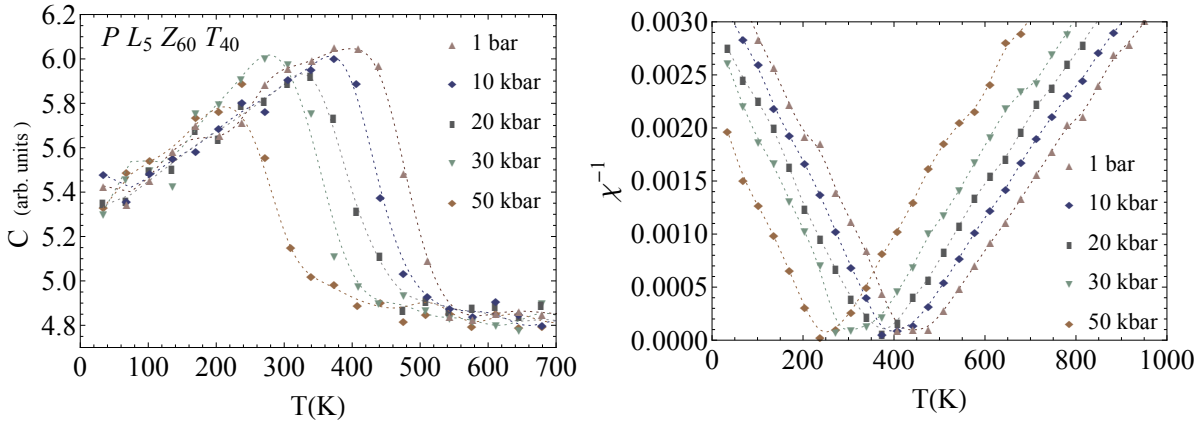

Fig. 3.41: Evolution with temperature of the specific heat (left) and the inverse dielectric response (right) for $PL_5Z_{60}T_{40}$ under 1 bar, 10 kbar, 20 kbar, 30 kbar and 50 kbar. The temperature at which the specific heat peaks is used for the determination of T_C while that at which the dielectric response peaks corresponds to T_m.

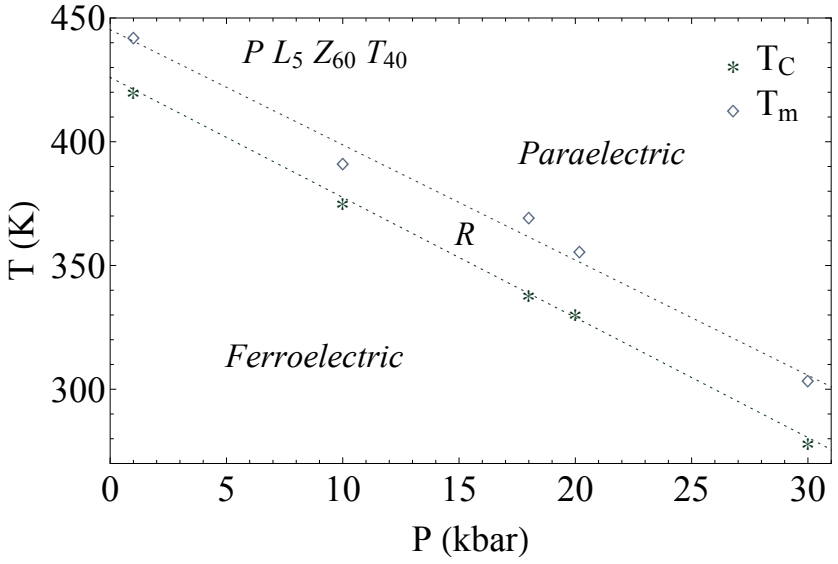

Fig. 3.42: Temperature-Pressure phase diagram for $PL_5Z_{60}T_{40}$. Dotted lines delimit the relaxor region and their slopes are exctracted from linear fits of the T_C and T_m data, $dT_C/dP = -4.85$ K/kbar and $dT_m/dP = -4.66$ K/kbar respectively.

3.3.3 Pressure-induced diffuseness

The decrease of both T_C and T_m with increasing pressure points to a manifest similarity between pressure and quenched disorder content. The analogy is further supported by the rounding of the inverse susceptibility as pressure is increased. Fig. 3.43 shows plots of $\mathrm{Ln}(\chi^{-1} - \chi_m^{-1})$ versus $\mathrm{Ln}\,(T/T_m - 1)$ in the paraelectric regions for $PL_5Z_{60}T_{40}$ under 1 bar

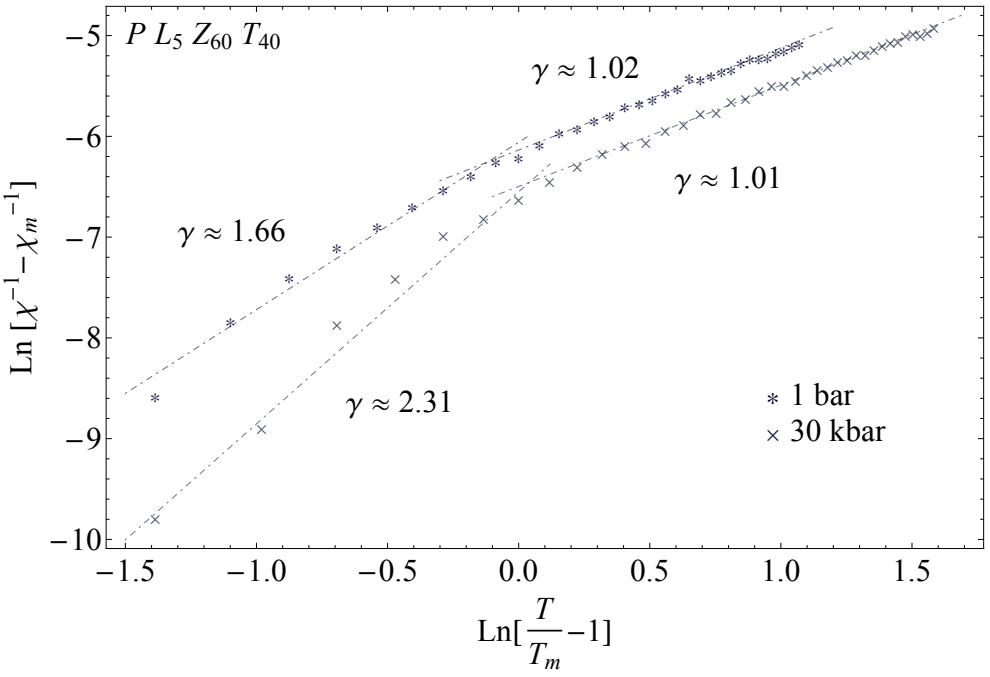

Fig. 3.43: Plots of $\mathrm{Ln}(\chi^{-1} - \chi_m^{-1})$ versus $\mathrm{Ln}\,(T/T_m - 1)$ in the paraelectric regions for $PL_5Z_{60}T_{40}$ under 1 bar and 30 kbar. Linearly fitting the data yields $\gamma \simeq 1$ in both cases for high enough temperatures. As the temperature is lowered slopes increase, $\gamma \simeq 1.66$ and $\gamma \simeq 2.31$ for 1 bar and 30 kbar respectively.

and 30 kbar, from which γ (Eq.3.10) are extracted. As temperature is lowered, a departure from the Curie-Weiss behavior occurs, all the more pronounced with increasing pressure. Extracted slopes yield $\gamma \simeq 1.66$ and $\gamma \simeq 2.31$ for 1 bar and 30 kbar respectively, thus signaling a pressure-induced diffuseness.

3.3.4 Correlation length reduction

As already discussed (section 1.4.1), the analogy between the pressure induced ferroelectric to relaxor crossover, and the compositionally mediated one is not fortuitous, and has been ascribed to the decrease of the correlation length $\xi_{l.m.}$ in both cases [104]. Increasing the La content increases the degree of disorder, and effectively reduces $\xi_{l.m.}$ (Fig. 3.17). Above a certain amount of quenched disorder, $\xi_{l.m.}$ is sufficiently short, ordered regions do not percolate and relaxor behavior sets in for T $<$T$_m$. The effect of pressure is also to reduce $\xi_{l.m.}$, as a consequence of the pressure dependence of the soft-mode frequency which controls the polarizability of the system [104]. This interpretation is recovered within our model, as shown in Fig. 3.44 whose left panel provides the dependence of the correlation length of the local modes $\xi_{l.m.}$ on pressure. The right panel also indicates a reduction of the correlation length associated to the gauge field $\xi_{g.f.}$ when subjected to pressure, similarly to its reduction with increasing quenched disorder (Fig. 3.16).

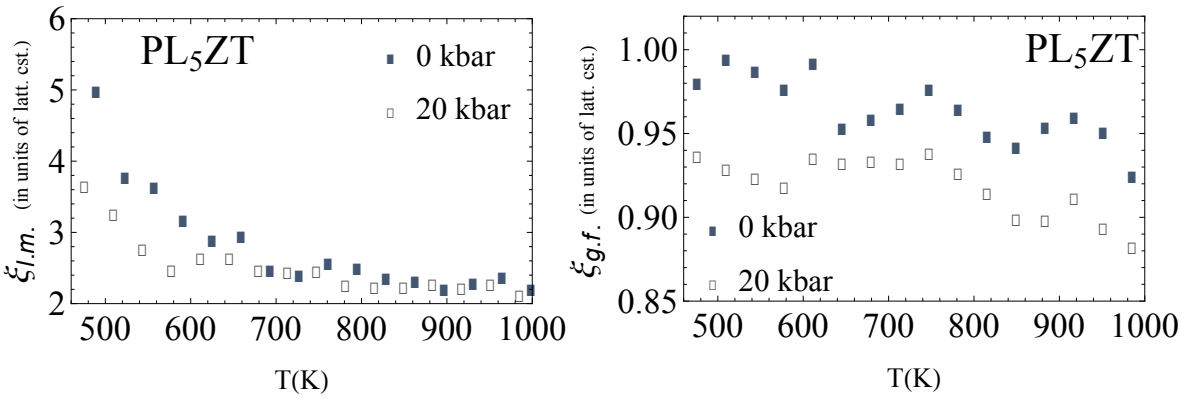

Fig. 3.44: Variation of the correlation length for local modes $\xi_{l.m.}$ (left panel) and gauge field $\xi_{g.f.}$ (right panel) fluctuations for $PL_5Z_{60}T_{40}$ showing the influence of pressure. (Both $\xi_{l.m.}$ and $\xi_{g.f.}$ are computed according to the method provided in section 3.1.4).

We end this section by reporting the pressure dependence of the density of pairs of topological defects n_p (Fig. 3.45). The obtention of topological defects will be later exposed in section 3.4.1. Topological defects are associated to strong orientational fluctuations of the order parameter field and hence act as order-destabilizing agents. The main observation obtained from Fig. 3.45 relates to the shift of the inflection point to lower temperatures with increasing pressure, thereby supporting and elucidating both the lowering of T_C and the magnitude reduction of the polarization, as experienced by $PL_5Z_{60}T_{40}$ when subjected to an increasing pressure (Fig. 3.39).

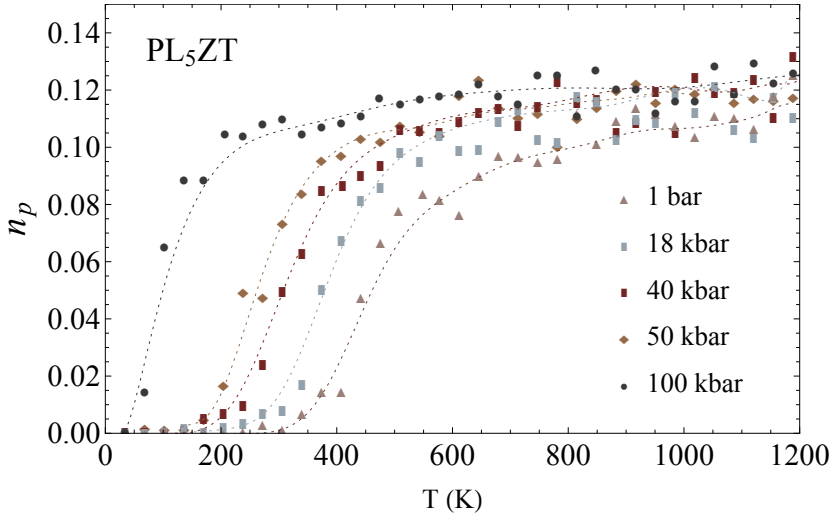

Fig. 3.45: Temperature evolution of the density of pairs of hedgehogs n_p for PL_5ZT under increasing pressure.

3.4 Topological defects

In this section, we enquire whether topological defects play a role in the relaxor behavior. Topologically stable defects are localized excitations that overcome the finite creation energy associated with them by carrying large configurational entropy. They are known to induce phase transitions in two-dimensional systems [182], including the superfluid transition in thin ^{4}He films, the superconducting transition in thin metallic films and the melting transition in two dimensions. They appear as points, lines, surfaces, etc., depending on the models and dimensionality. Several canonical examples illustrate the role of topological excitations in bringing about phase transitions. Among them is the Berezinsky-Kosterlitz-Thouless in the two-dimensional XY model [184]. The role of topological defects has also been investigated in the three-dimensional Heisenberg transition [276].

Intuitively, since quasi-ordered clusters (section 3.2) exhibit fractal geometry associated with the strong irregularities of their boundaries, we are led to expect that topological defects should occur at the contact points between rugged interfaces of differently ordered clusters (Fig. 3.46). By resorting to such a description, we are somehow adopting the dual view to that attributing the polarization response to interphase boundaries vibration [79].

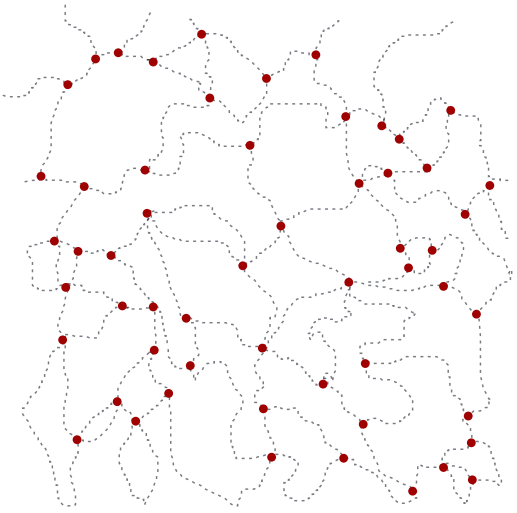

Fig. 3.46: Schematic view of the ordered clusters pattern within a plane. Jaggerred perimeters cross at contact points, depicted by red points and representing hedgehogs.

3.4.1 Finding hedgehogs

These contact points merely correspond to singularities in the order parameter field. They are topological defects, or hedgehogs, generated by strong directional fluctuations and thus positioned at the junctions of differently ordered regions, at isolated points, where the order changes discontinuously and is thus ill-defined. At low enough temperatures, they can be seen as reminiscent of the disordered symmetric phase trapped within the lower symmetry

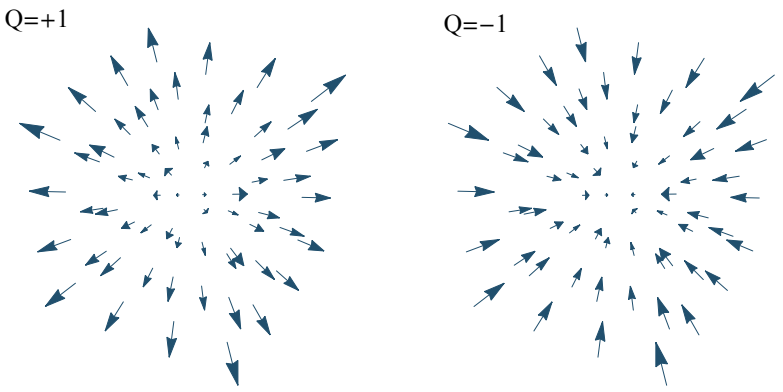

Fig. 3.47: Schematic view of dipoles configurations showing ideal hedgehogs of charges $Q = +1$ (source-like) and $Q = -1$ (sink-like).

phase. Topological defects carry an integer topological charge referred to as the winding number, which indicates how many times one meets all possible orientations of the vector field while moving along an oriented closed surface enclosing the defect core [271]. Adopting this topological approach, we thus exchange order for disorder as a probe of the relaxor behavior. We believe that by doing so, at least part of the current complexity is reducible while the gained information is not.

In order to assign a topological charge within each of the unit cells composing the supercell, we follow Ref. [272–274] and first introduce an auxiliary variable, the gauge potential $\mathcal{A}_{ij}$ between any pair of neighboring sites with normalized local modes $\mathbf{u}_i$, $\mathbf{u}_j$. This is defined by introducing an arbitrary reference unit vector $\mathbf{u}_\star$ and forming the spherical triangle $(\mathbf{u}_\star, \mathbf{u}_i, \mathbf{u}_j)$. The edges of the spherical triangle are segments of great circles, and if the solid angle subtended by this spherical triangle is denoted by $\Omega\,[\mathbf{u}_\star, \mathbf{u}_i, \mathbf{u}_j]$, then the explicit expression for half its area, $\mathcal{A}_{ij}$ is

$$e^{i\mathcal{A}_{ij}} = e^{(i/2)\Omega[\mathbf{u}_\star,\mathbf{u}_i,\mathbf{u}_j]} = \frac{1 + \mathbf{u}_\star.\mathbf{u}_i + \mathbf{u}_\star.\mathbf{u}_j + \mathbf{u}_i.\mathbf{u}_j + i\mathbf{u}_\star.(\mathbf{u}_i \times \mathbf{u}_j)}{\sqrt{2(1 + \mathbf{u}_\star.\mathbf{u}_i)(1 + \mathbf{u}_\star.\mathbf{u}_j)(1 + \mathbf{u}_i.\mathbf{u}_j)}} \tag{3.30}$$

In practice $\mathbf{u}_\star = (0, 0, 1)$, but a different choice of the reference vector $\mathbf{u}'_\star$ merely amounts to a gauge transformation of $\mathcal{A}$: $\mathcal{A}_{ij} \to \mathcal{A}_{ij} + \chi_i - \chi_j$, where $\chi_i = (1/2)\Omega\,[\mathbf{u}_\star, \mathbf{u}'_\star, \mathbf{u}_j]$. Thus gauge invariant quantities are independent of the choice of the reference vector. A flux $F_\square \in (-\pi, \pi]$ is then defined on every face bounded by the sites (i, j, k, l, i):

$$e^{iF_\square} = e^{i(\mathcal{A}_{ij}+\mathcal{A}_{jk}+\mathcal{A}_{kl}+\mathcal{A}_{li})} \tag{3.31}$$

$F_\square$ is gauge invariant and hence independent of the choice of the reference unit vector $\mathbf{u}_\star$. The hedgehog topological charge Q enclosed by the unit cube corresponds to the flux out of

its volume:

$$\sum_{\square=1}^{6} = 2\pi Q \tag{3.32}$$

and is guaranteed to be an integer from the previous definitions. Moreover, this definition of Q ensures that the net topological charge (the supercell sum of topological charges associated to units cells) is always equal to zero in the considered system with periodic boundary conditions.

3.4.2 Dipoles pattern and hedgehogs network

Following this prescription, we determined the topological charge associated with each unit cube of the lattice for different local modes configurations. Generally, we found that the magnitude of the non-zero charges is almost always equal to unity, only a few topological defects with $Q = \pm 2$ (mostly appearing at high temperatures), and none with $|Q| > 2$ were found. Fig. 3.48 shows integral curves associated with the local modes within a (x, y) plane for PL_5ZT, $PL_{10}ZT$, $PL_{15}ZT$ and $PL_{20}ZT$ systems at $T \geqslant T_m$, together with the topological defects computed from the considered local modes configurations and projected onto the (x, y) plane. One observes that while quasi-ordered regions are indeed devoid from topological defects, the latter coincide with the vector field singularities, at the junction between different quasi-ordered regions.

3.4.3 Density of hedgehogs

Fig. 3.49 shows the temperature evolution of the density of pairs of hedgehogs $\langle n_p \rangle$ (averaged over MC sweeps) for PZT, PL_5ZT, $PL_{10}ZT$, $PL_{15}ZT$ and $PL_{20}ZT$. The density of pairs corresponds to the ratio of half of topologically defective cells to the total number of cells 12^3. The first observation relates to the non-vanishing values of $\langle n_p \rangle$ for $x = 10\%, 15\%$ and 10% at low temperatures. The horizontal dashed line indicates the site percolation threshold p_c for pairs for Rubik neighborhood, i.e. for a regular lattice with NN+2NN+3NN neighborhood [275]. The rapid increase of $\langle n_p \rangle$ near T_C is clearly seen in the right figure, which shows the temperature dependence of the derivative $\mathrm{d}\langle n_p \rangle / \mathrm{d}T$ of the density of pairs. As the lanthanum content is increased, the $\mathrm{d}\langle n_p \rangle / \mathrm{d}T$ peak becomes broader. Dotted vertical lines in both left and right figures correspond to the temperature at which the derivative peaks, and are found to be in close vicinity of T_C. The remarkable intersection of the p_c line with $\langle n_p \rangle$ at the temperature at which $\mathrm{d}\langle n_p \rangle / \mathrm{d}T$ peaks enables the following interpretation. The percolation threshold p_c denotes the critical probability above which a cluster spanning through the whole system appears. Thus in the temperature region above p_c, the development of long-range order is hindered by percolating clusters of topological defects. On the other

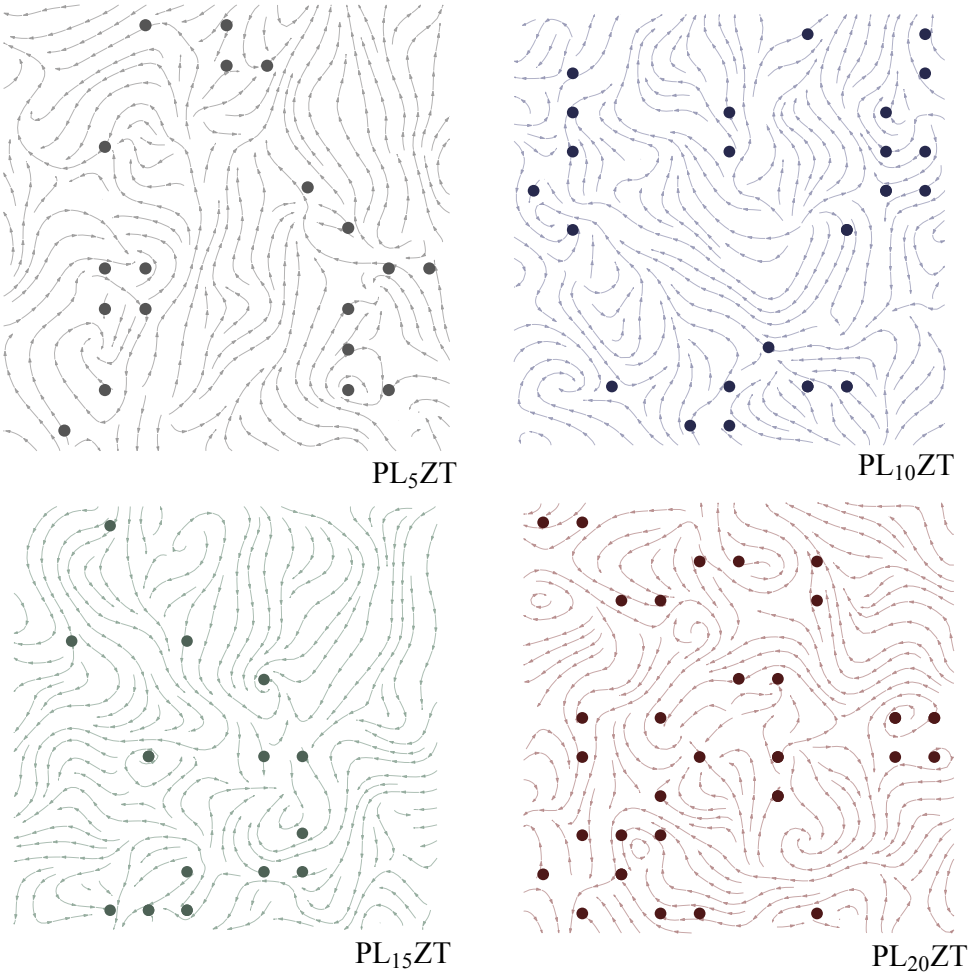

Fig. 3.48: Integral curves associated to the local modes vector fields within a (x, y) plane and projection onto the plane of topological defects (represented by points) for PL_5ZT, $PL_{10}ZT$, $PL_{15}ZT$ and $PL_{20}ZT$. Results correspond to $T \geqslant T_m$, specifically, $T = 441$K, $T = 340$K, $T = 203$K and $T = 170$K for 5%, 10%, 15% and 20%, respectively.

hand, in the temperature region below p_c, the density of pairs of hedgehogs is such that long-range ferroelectric order is possible. The case of $PL_{20}ZT$ is of special interest. The significant value of $\langle n_p \rangle$ as $T \to 0$, and its non-intersection with the p_c line totally precludes the onset of a long-ranged ferroelectric order. Percolation is a purely geometric process which, when applied to the topological defects population, enables a qualitative understanding of the destabilizing effect of quenched disorder.

At low temperature the defect pair density is expected to be proportional to $\exp(-E_a/T)$, where E_a is the minimum energy required to create a pair of oppositely charged defects [276]. Plotting $\mathrm{Ln}(\langle n_p \rangle)$ versus T^{-1} (Fig. 3.50), and fitting it linearly reproduces the expected form. The activation energy is found to exponentially decrease with increasing disorder, in agreement with the observed increasing defects proliferation with increasing disorder (Fig. 3.49).

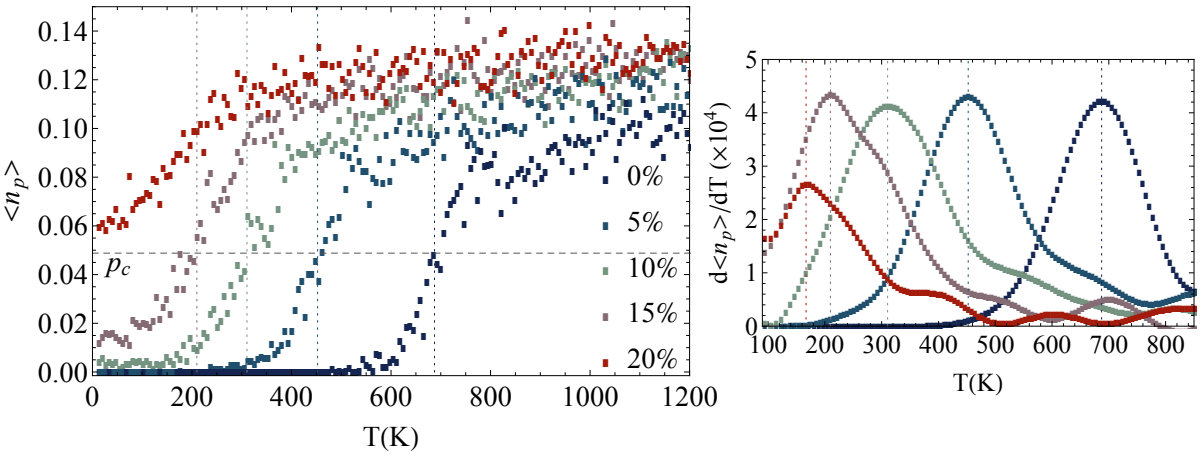

Fig. 3.49: Temperature evolution of the density of pairs of hedgehogs $\langle n_p \rangle$ (averaged over MC sweeps) for PZT, PL_5ZT, $PL_{10}ZT$, $PL_{15}ZT$ and $PL_{20}ZT$ (left figure). The horizontal dashed line indicates the site percolation threshold p_c for pairs for Rubik neighborhood. Right figure shows the temperature dependence of the derivative $\mathrm{d}\langle n_p \rangle / \mathrm{d}T$ of the density of pairs. Dotted vertical lines in both left and right figures correspond to the temperature at which the derivative peaks.

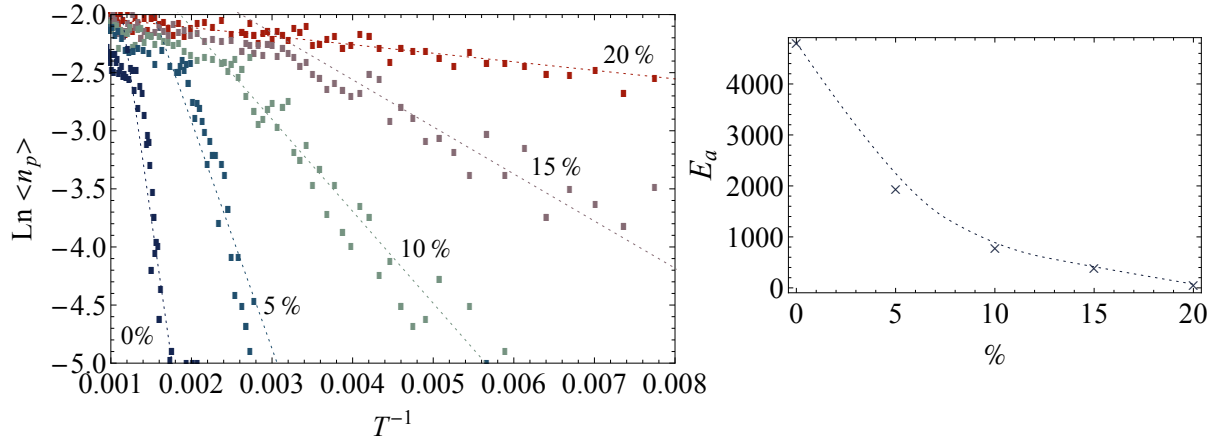

Fig. 3.50: Plot of the logarithm of the defect pair density versus the inverse temperature for $PZ_{60}T_{40}$, $PL_5Z_{60}T_{40}$, $PL_{10}Z_{60}T_{40}$, $PL_{15}Z_{60}T_{40}$ and $PL_{20}Z_{60}T_{40}$. Dotted lines are linear fits to the data for $T < T_C$. The right figure collects the extracted slopes of the fit, yielding the evolution of the activation energy (arb. units) with the percentage of quenched disorder.

3.4.4 Mobility of hedgehogs ···

We now investigate the role of topological defects in the relaxor behavior. We are specifically interested in inquiring whether the relaxor behavior is defect driven or not. Fig. 3.51 indicates that the structure of the hedgehogs network is "loose" and that the location of defects varies in the course of calculations. Hedgehogs, or else singular contact points among differently quasi-ordered regions (Figures 3.46 and 3.48), are hence spatially fluctuating entities. Their mobility, indicative of a dynamical nature, dually reflects the fluctuations of boundaries between differently quasi-ordered regions. This observation can be put in correspondence

with the breathing model proposed by Glazounov and Tagantsev [79], within which the polarization response of relaxors is ascribed to the vibration of interphase boundaries, rather than to the reorientation of dipole moments.

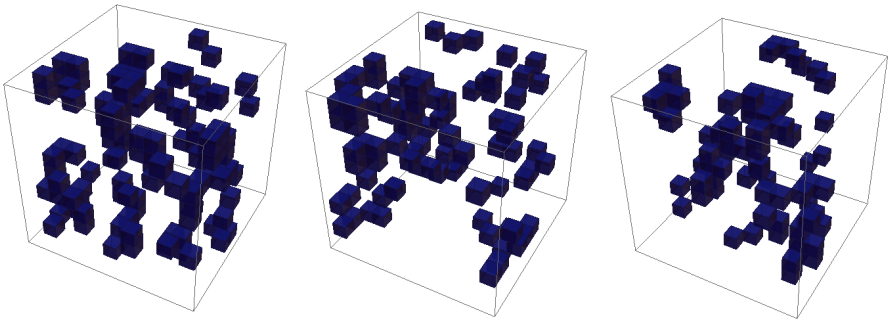

Fig. 3.51: Supercell snapshots of $PL_5Z_{60}T_{40}$, as obtained for three consecutive MC sweeps at $T = 407K$. Dark blue cubes are associated to the topologically defective unit cells whose variable location in the supercell over the sweeps is indicative of a dynamical nature.

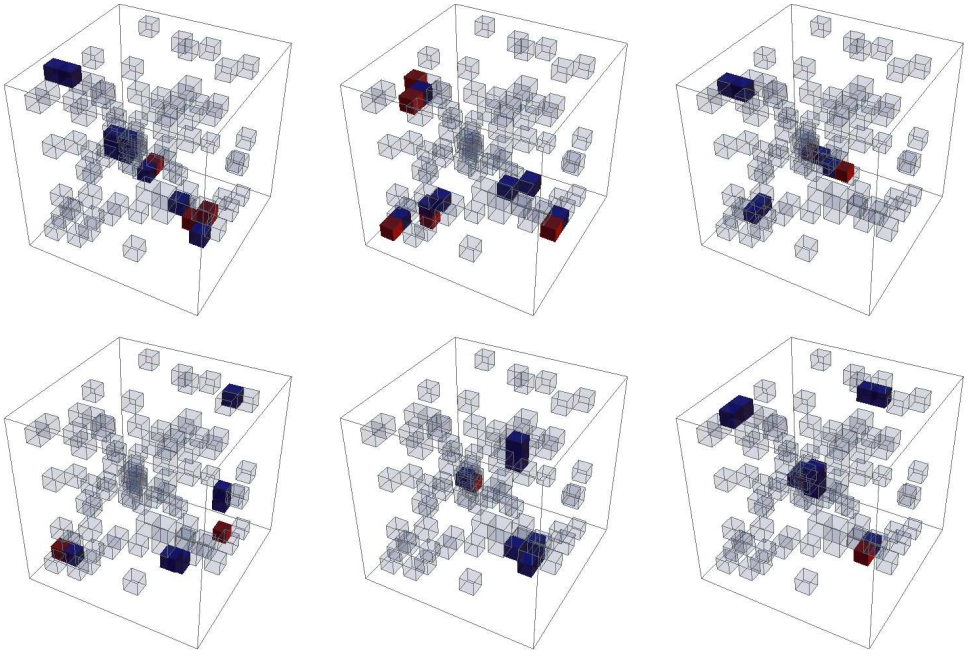

Fig. 3.52: Supercell snapshots of $PL_5Z_{60}T_{40}$, as obtained for six consecutive MC sweeps at $T = 271K$. Pale cubes are associated to the quenched (*i.e.* lanthanum containing) unit cells and thus display a fixed spatial distribution in the supercell over the sweeps. Red cubes correspond to quenched unit cells which are also topologically defective while dark blue cubes are associated to topologically defective unit cells whose location is different from that of the quenched unit cells. Topological defects are hence hopping dynamical entities, whose location in the supercell is not necessarily in correspondence with that of the quenched cells.

As to the influence of quenched disorder on singularities in the dipole moments field, Fig. 3.52 indicates that the spatial distribution of singularities does not necessarily coincide with that

of the quenched cubes. Fig. 3.53 provides the evolution with temperature of the fraction of quenched cubes QC carrying a non-zero topological charge $N_{QC_{Q\neq 0}}$, for PL_5ZT, $PL_{10}ZT$, $PL_{15}ZT$ and $PL_{20}ZT$. At high temperature the spatial overlap between these two entities is significant, nearly 30% of the quenched cubes are found to carry a non-zero topological charge for all the four systems, *i.e.*, regardless of the amount of QC. This observation can be attributed to the occurrence of strong thermal fluctuations, which effectively uncouple the dipole moments from the gauge field. At lower temperatures however, the overlap-ratio $N_{QC_{Q\neq 0}}/N_{QC}$ more or less decreases dependently on the amount of quenched disorder. This is closely related to the exponential decay of the activation energy of topological defects with increasing lanthanum content (Fig. 3.50). Indeed, the number of topological defects induced by quenched disorder scales exponentially with respect to the latter at low temperatures, thereby enhancing the probability for a quenched cube to carry a non-zero topological charge.

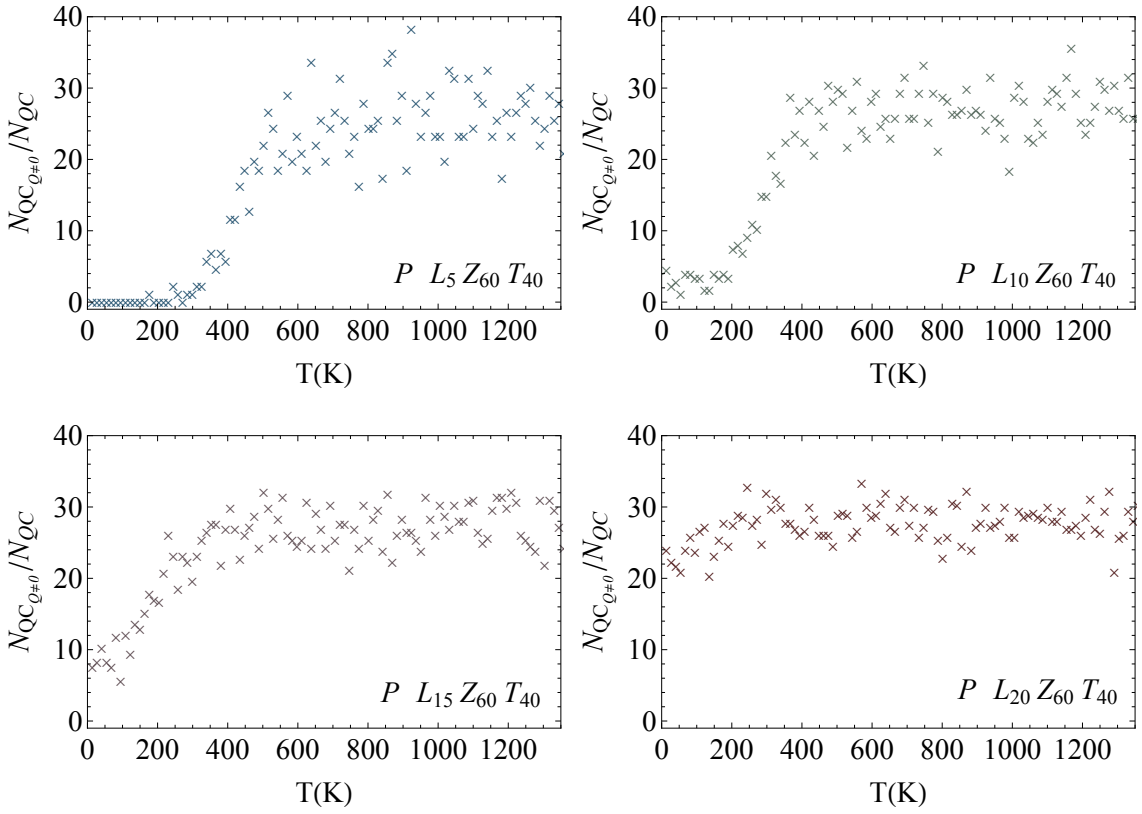

Fig. 3.53: Evolution with temperature of the fraction $N_{QC_{Q\neq 0}}/N_{QC}$ of quenched cubes QC carrying a non-zero topological charge $Q \neq 0$, for PL_5ZT, $PL_{10}ZT$, $PL_{15}ZT$ and $PL_{20}ZT$.

3.4.5 ··· in a free background

As the temperature is lowered, the mobility of hedgehogs is associated to a decrease of their density. Hedgehogs hence evolve in a smooth background, whose volume can be obtained from the ratio of topologically free cells (*i.e.* those cells with zero topological charge $Q = 0$) to the total number of cells 12^3. This background is denominated by free volume, and since it is defined as the complementary to the density of topological defects, it is merely indicative of the maximal potentially ordered volume. The left panel of Fig. 3.54 provides the temperature evolution of the free volume $d_{f.v}$ for different PL_xZT systems. Since $d_{f.v}$ increases with decreasing temperature, this suggests an annihilation mechanism among oppositely charged topologically defective cells. Moreover, a study of the fractal dimension d_H was carried out on the basis of the *box counting* method [277, 278], that defines the Haussdorff dimension as a limit

$$d_H = \lim_{\varepsilon \to \infty} \frac{\mathrm{Ln} N_\varepsilon}{\mathrm{Ln}(1/\varepsilon)} \tag{3.33}$$

where N_ε is the number of boxes needed to cover the free volume and ε is the side length of the box. For "loose" structures, the fractal dimension is different from the topological dimension of the physical space in that it measures the deviation from compactness [279]. The right panel of Fig. 3.54 shows the temperature evolution of the fractal dimension d_H of the free volume $d_{f.v}$. While at high temperatures d_H is quasi independent of the lanthanum content with a value revolving around ∼2.6, quenched disorder content discriminates between different low temperature values. For the pure PZT system, the fractal dimension of the free volume reaches the physical dimension 3. Increasing lanthanum content on the other hand depresses d_H, it is only of ∼2.82 for $PL_{20}ZT$. These observations clearly indicate that the extent and compactness of the maximal ordered region is hindered by low temperature persisting topological defects. Moreover, these findings contradict models within which PNRs are described as compact [99] spherical entities [146]. Let us however stress that in our model, polar regions are free to appear rather than constrained to exist.

3.4.6 From an hydrodynamic approach ···

According to Fig. 3.52, the sinks ($Q < 0$) and sources ($Q > 0$) in the dipoles field are not stationary. They not only constantly dissolve and emerge, but generically propagate through the system and interact with one another. Defects of opposite topological charge can readily annihilate one another, reminiscent of the dynamics in nematic liquid crystals [280]. The lessening of hedgehogs (Fig. 3.49) and their mobility within a smooth and expanding free volume most likely emanates from an annihilation mechanism. To evaluate the temperature dependence of the characteristic relaxation times, we resorted to a simple hydrodynamic description, according to which defects diffuse freely and annihilate instantaneously upon

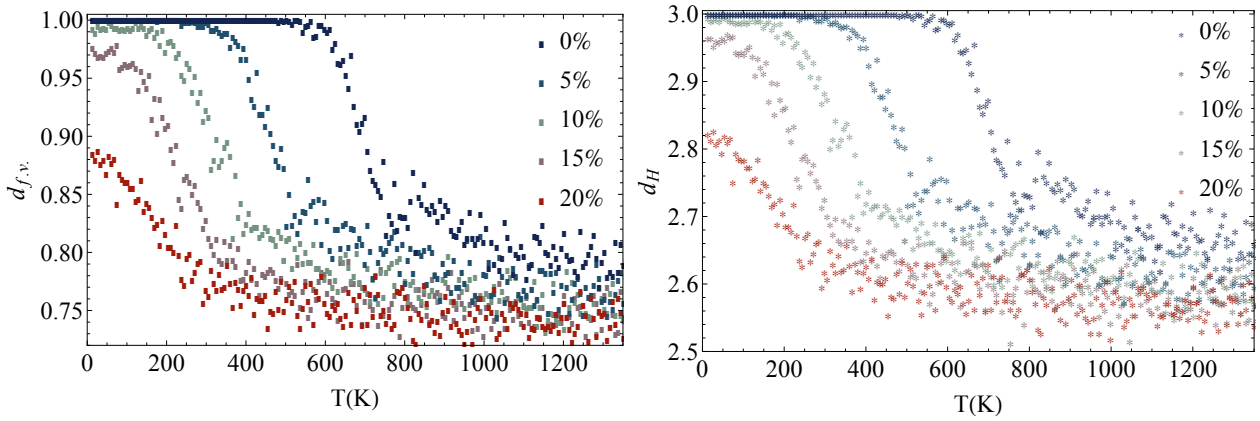

Fig. 3.54: Temperature evolution of the free volume $d_{f.v}$ (left figure) and of its fractal dimension (right figure) for the pure system PZT and different PL_xZT systems.

contact [281]. The hedgehog density decays with time according to the rate equation

$$\frac{d\langle n\rangle}{dt} = -2K\langle n\rangle^2 \tag{3.34}$$

where K is the reaction rate that describes the propensity of two diffusing defects to interact,

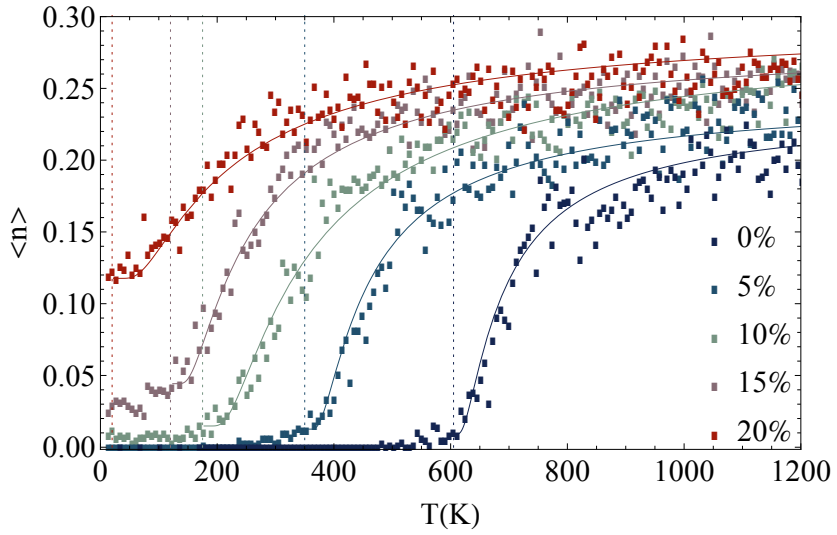

Fig. 3.55: Evolution with temperature of the density of topological defects $\langle n\rangle$. Solid lines correspond to the $\langle n\rangle = a + \langle n_0\rangle \exp[-b/(T - T_0)]$ fits, where T_0 are signaled by dotted vertical lines .

and where the prefactor 2 accounts for the annihilation of two defects upon contact. The solution of this governing equation yields

$$\langle n\rangle(t) \sim t^{-1}, \qquad d > 2 \tag{3.35}$$

where d is the spatial dimension. Thus the density of hedgehogs decreases as t^{-1}.

3.4.7 ··· to Vogel-Fulcher's kinetics law

Consequently, fitting the density of hedgehogs $\langle n \rangle$ with

$$\langle n \rangle = a + \langle n_0 \rangle \exp[-b/(T - T_0)] \tag{3.36}$$

valid for T>T_0 where T_0<T_C (Fig. 3.55) and using the relation of Eq.3.35 leads to the following relation between the relaxation time τ and T

$$\tau = \tau_0 \exp[U/k(T - T_0)] \tag{3.37}$$

which is nothing but the characteristic Vogel-Fulcher (VF) relaxation kinetics law [41, 42]. Thus, within our model, the VF law can be immediately derived from a microscopical annihilation mechanism among defects of opposite topological charge which are associated to strong directional fluctuations in the dipole moments field.

3.4.8 Polarization and deformation

We now investigate whether the topologically charged cells corresponding to singularities of the dipole moments vector field exhibit elastic deformations. Extracting the unit cell volume v/v_0 from the inhomogeneous symmetric strain tensor η (expressed in Voigt notation 11≡1, 22≡2, 33≡3, 23≡4, 13≡5, 12≡6) according to

$$\frac{v}{v_0} = \begin{vmatrix} 1+\eta_1 & \eta_6/2 & \eta_5/2 \\ \eta_6/2 & 1+\eta_2 & \eta_4/2 \\ \eta_5/2 & \eta_4/2 & 1+\eta_3 \end{vmatrix} \tag{3.38}$$

where v_0 is the reference volume of the cubic unit cell, we compared the average volume of topologically charged (with Q=1 and Q=-1) unit cells to the average volume of the zero-charged unit cells (Q=0).

The results, shown in Fig. 3.56, indicate a systematic deviation of the average volume of topologically charged cell from that associated to topological defect-free cells. Interestingly, local structural distortions [82] are reflected in quasielastic diffuse scattering DS appearing below T_d in the vicinity of the Bragg reflections [282]. Consequently, the local volume fluctuations subtended by topological defects which are computed from the local modes, can be put in qualitative correspondence with the mixing of polarization and elastic deformation from which diffuse scattering is thought to originate.

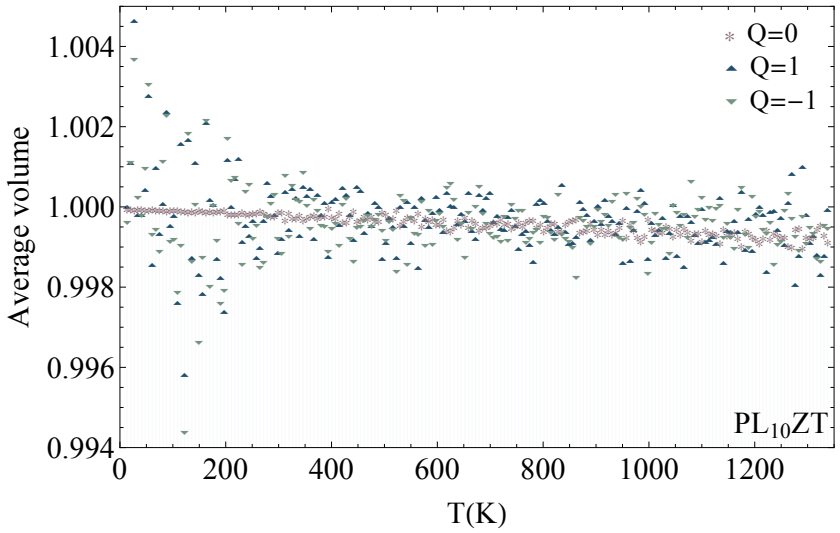

Fig. 3.56: Evolution with temperature of the average volume of zero-charged unit cells (Q=0) and of topologically defective cells (with Q=1 and Q=-1) for $PL_{10}ZT$.

3.4.9 Binding-unbinding mechanism

An important question pertaining to the role of topological defects is whether the observed proliferation of defects as T increases is accompanied by unbinding of defect pairs. Since topological charges are additive [271], a hedgehog/anti-hedgehog bound state between opposite charges yields a vanishing far field distortion. Indeed, the flux out of any surface enclosing their core amounts to zero. An unbound state on the other hand can strongly distort the vector field within a correlation length which depends on the interaction among hedgehogs and its screening. It is thus important to develop criteria by which one may determine whether a given system is in a bound or unbound hedgehog state. We investigate this question according to the following procedure.

The hedgehog content of each unit cell is determined by means of the aforementioned method (Eq.3.32). For each field realization, we thus dispose of the associated hedgehog network of the supercell. Applying the Hoshen-Kopelman clustering algorithm [283], we conduct a comparative study between two different clustering decompositions. In the first case, the cluster decomposition of the hedgehog population is performed without charge differentiation, meaning that two adjacent oppositely charged unit cells were considered to belong to the same cluster. In the second case, each hedgehog subpopulation is clustered on its own, meaning that only identically charged adjacent unit cells are agglomerated.

Figures 3.57 and 3.58 provide the outcome of this comparative study for $PZ_{60}T_{40}$ and $PL_5Z_{60}T_{40}$ on one hand, and $PL_{10}Z_{60}T_{40}$, $PL_{15}Z_{60}T_{40}$ and $PL_{20}Z_{60}T_{40}$ on the other hand, and show the temperature evolution of the number of clusters and their average volume. Left and right panels of Fig. 3.57 and Fig. 3.58 indicate that the clustering decomposition

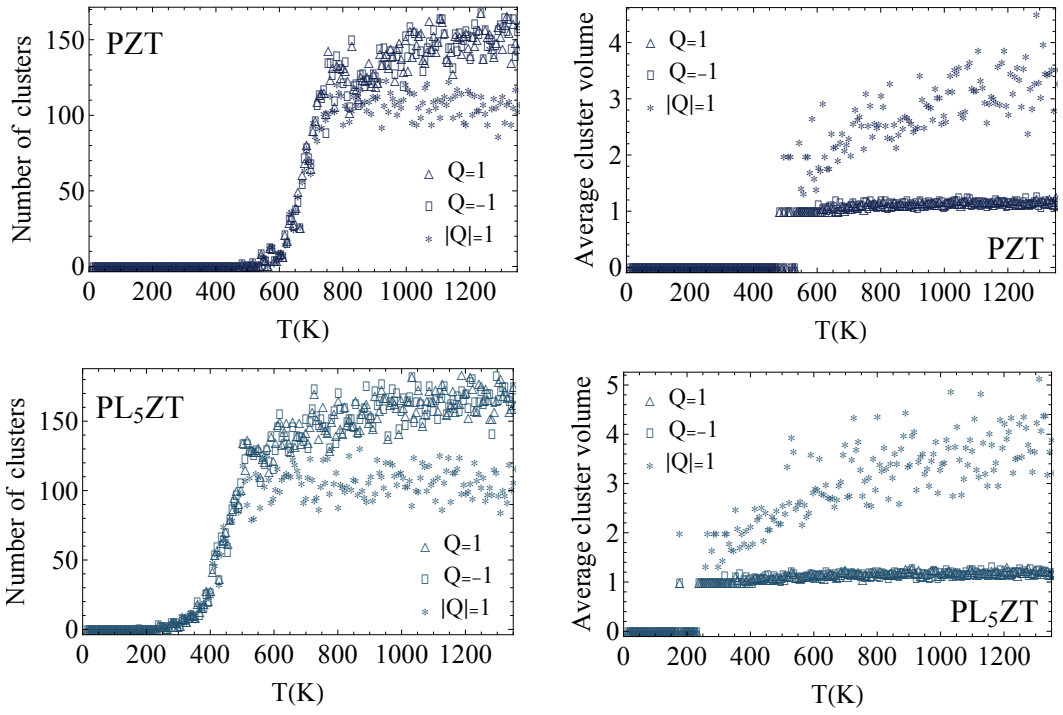

Fig. 3.57: Temperature evolution of the number of clusters (left panels) and their average volume (right panels) for $PZ_{60}T_{40}$ and $PL_5Z_{60}T_{40}$ systems. Curves associated to $|Q| = 1$ correspond to the clustering procedure performed on the hedgehogs population regardless of the sign of the charge they carry, while curves associated to $Q = 1$ and $Q = -1$ correspond to the charge-specific clustering carried out on each of the subpopualtions of hedgehogs independently, *i.e.*, on that of the positively charged hedgehogs and on that of the antihedgehogs, respectively.

performed on the hedgehogs regardless of their charge ($|Q| = 1$) yields lower number of clusters with higher average volume, thereby suggesting that hedgehogs preferably cluster within mixed charge sets comprising hedgehogs and anti-hedgehogs, rather than in identical charge sets solely comprising either hedgehogs ($Q = 1$) or anti-hedgehogs ($Q = -1$). The vanishing values of the average volume of clusters in $PZ_{60}T_{40}$ and $PL_5Z_{60}T_{40}$ at low temperatures only reflects that hedgehogs are suppressed below a certain temperature in these systems (right panels of Fig. 3.57).

In the cases of $PL_{10}Z_{60}T_{40}$, $PL_{15}Z_{60}T_{40}$ and $PL_{20}Z_{60}T_{40}$, an additional feature emerges from the temperature evolution of the average cluster volume. While the charge-specific clustering (either Q=1 or Q=-1) yields a quasi-constant average cluster volume, the charge-independent ($|Q| = 1$) average cluster volume first decreases before increasing with increasing temperature (right panels of Fig. 3.58). Supplementing this observation with the fact that in the temperature range where the average volume decreases, the number of clusters is quasi-constant for either Q=1 or Q=-1 while it is found to be increasing for $|Q| = 1$, strongly

suggests a gradual binding-unbinding occurrence.

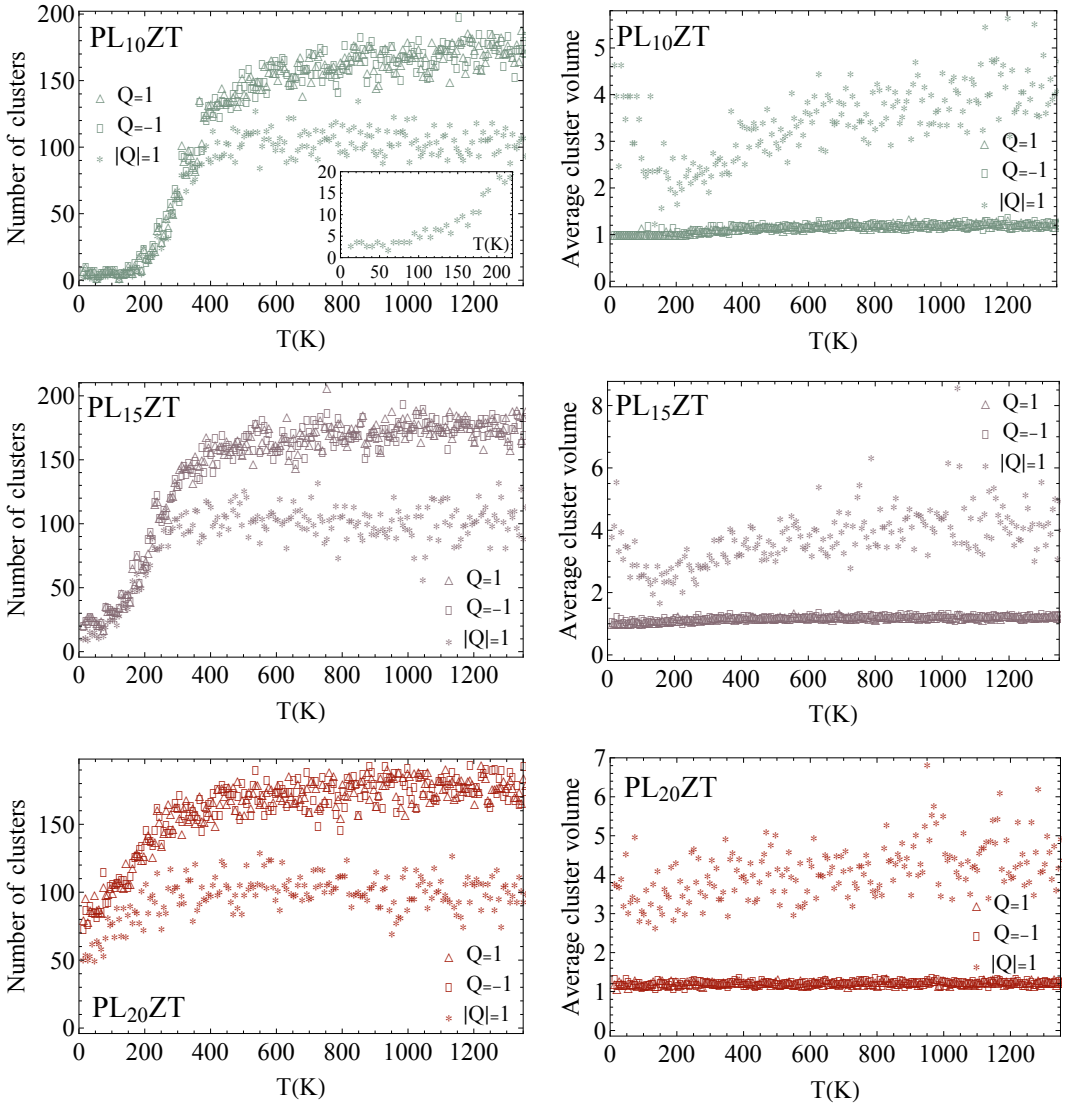

Fig. 3.58: Temperature evolution of the number of clusters (left panels) and their average volume (right panels) for $PL_{10}Z_{60}T_{40}$, $PL_{15}Z_{60}T_{40}$ and $PL_{20}Z_{60}T_{40}$ systems. Curves associated to $|Q| = 1$ correspond to the clustering procedure performed on the hedgehogs population regardless of the sign of the charge they carry, while curves associated to $Q = 1$ and $Q = -1$ correspond to the charge-specific clustering carried out on each of the subpopualtions of hedgehogs independently, *i.e.*, on that of the positively charged hedgehogs and on that of the antihedgehogs, respectively. The inset of the figure depicting the number of clusters for $PL_{10}Z_{60}T_{40}$ shows that clusters corresponding to $\{|Q| = 1\}$-clustering procedure increase in number in the $0 < T < 200$ K temperature range.

Thus, the ferroelectric phase in PL_xZT systems with x>5% seems to be driven by an alternative mechanism to that driving ferroelectricity in the pure PZT system or in the very weakly disordered PL_5ZT one. Indeed, for $PL_{10}Z_{60}T_{40}$, $PL_{15}Z_{60}T_{40}$ and $PL_{20}Z_{60}T_{40}$, the decrease of the average volume of $\{|Q| = 1\}$-obtained clusters as the temperature is raised,

occurs in a temperature range lower than T_C, where the non-vanishing and mixed hedgehogs population gradually unbinds with increasing temperature. This dissociation of pairs of oppositely charged topological defects induces empowered distortions in the dipole moments field, progressively destroying the ground-state order. Consequently, the ferroelectric phase in these systems is concomitant with a bound state of oppositely charged topological defects in hedgehog/anti-hedgehog pairs, *i.e.*, with a topological configuration that minimizes the distortion of the order parameter field. As the temperature is increased beyond the temperature range in which the average volume of $\{|Q| = 1\}$-obtained clusters features a decrease, the average volume increases due to the increase of the density of topological defects.

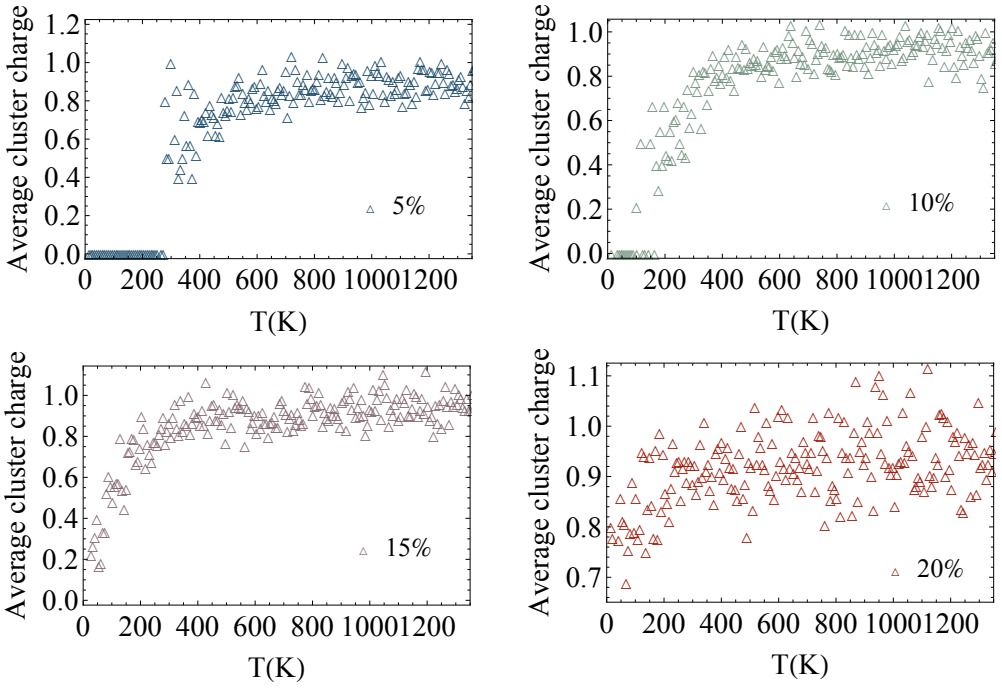

Fig. 3.59: Temperature evolution of the average charge of $\{|Q| = 1\}$-obtained clusters for $PL_5Z_{60}T_{40}$, $PL_{10}Z_{60}T_{40}$, $PL_{15}Z_{60}T_{40}$ and $PL_{20}Z_{60}T_{40}$ systems.

The gradual pairs dissociation is further corroborated by Fig. 3.59, which provides the temperature evolution of the average charge of $\{|Q| = 1\}$-obtained clusters. For each temperature, the average charge of clusters is quantified according to

$$\frac{1}{N_{cl}} \sum_{cl_i} \left| \sum_{h \in cl_i} Q_h \right| \tag{3.39}$$

with N_{cl} the total number of clusters, cl_i the i^{th}-cluster, and where h runs over the unit cells belonging to cl_i, and carrying a charge Q_h. The charge of a cluster i consisting solely of hedgehog/antihedgehog pairs, $\sum_{h \in cl_i} Q_h$, is zero. Deviations from zero thus signal unbound isolated topological charges whose absolute value contributes to the average charge of clusters.

As the temperature is increased, one observes that the average charge of clusters increases, thus confirming the unbinding mechanism of pairs (Fig. 3.60).

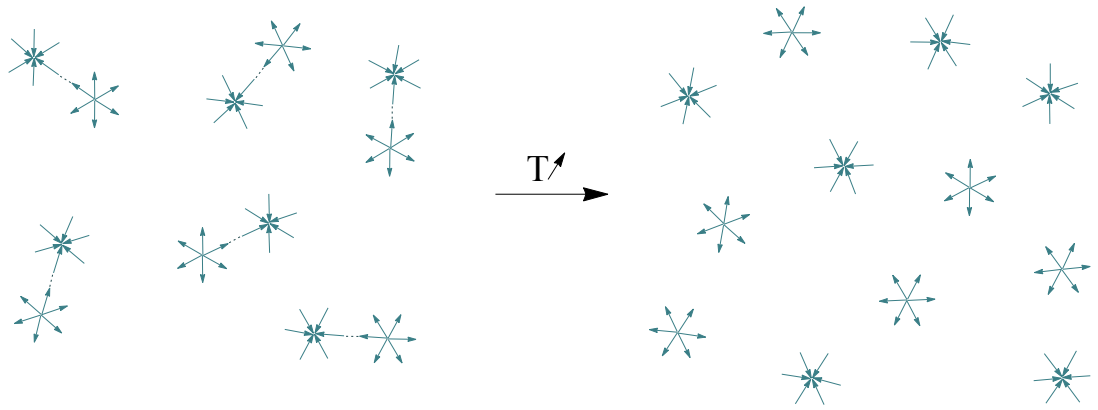

Fig. 3.60: Two-dimensional schematic representation of the unbinding mechanism of hedgehog/antihedgehog pairs with increasing temperature. While at low temperatures, pairs of oppositely charged defects are bound yielding a phase akin to a gas of (hedgehog/antihedgehog) dipoles, the higher temperature phase constitutes a plasma of unbound hedgehogs.

3.4.10 The underlying gauge

We wish to conclude this section by stressing that topological defects are controlled by the gauge. More specifically, for a certain fixed amount of quenched disorder, the temperature evolution of the number of disorder-induced topological defects is dictated by the gauge self-coupling parameter k. As k is decreased, deviations of the link variables from identity becomes less energetically unfavorable, consequently affecting the order parameter field via the gauge-modified short-range interaction term. The more k is reduced, the more the disorder is empowered, ultimately preventing the onset of an ordered state by an induced proliferation of topological defects. This is illustrated in Fig. 3.61 which shows the temperature evolution of the density of pairs of hedgehogs n_p in $PL_{15}ZT$ for k=0.01 and k=0.05. In contrast to the case k=0.05 where n_p drops around T_C thus signaling the existence of an interplay between local modes variable and gauge variables, the case k=0.01 is typical of a situation where the disorder-mediating gauge has taken over ferroelectricity. Symmetrically, a further increase of k (>0.05) depresses the strength of disorder, leading to a defect suppression [276]. Integral curves are also shown in the lower panel of Fig. 3.61. For a same quenched disorder realization (whose spatial distribution is indicated by squares), decreasing k yields a lattice of hedgehogs, somewhat similar to Abrikosov's vortex lattice [284].

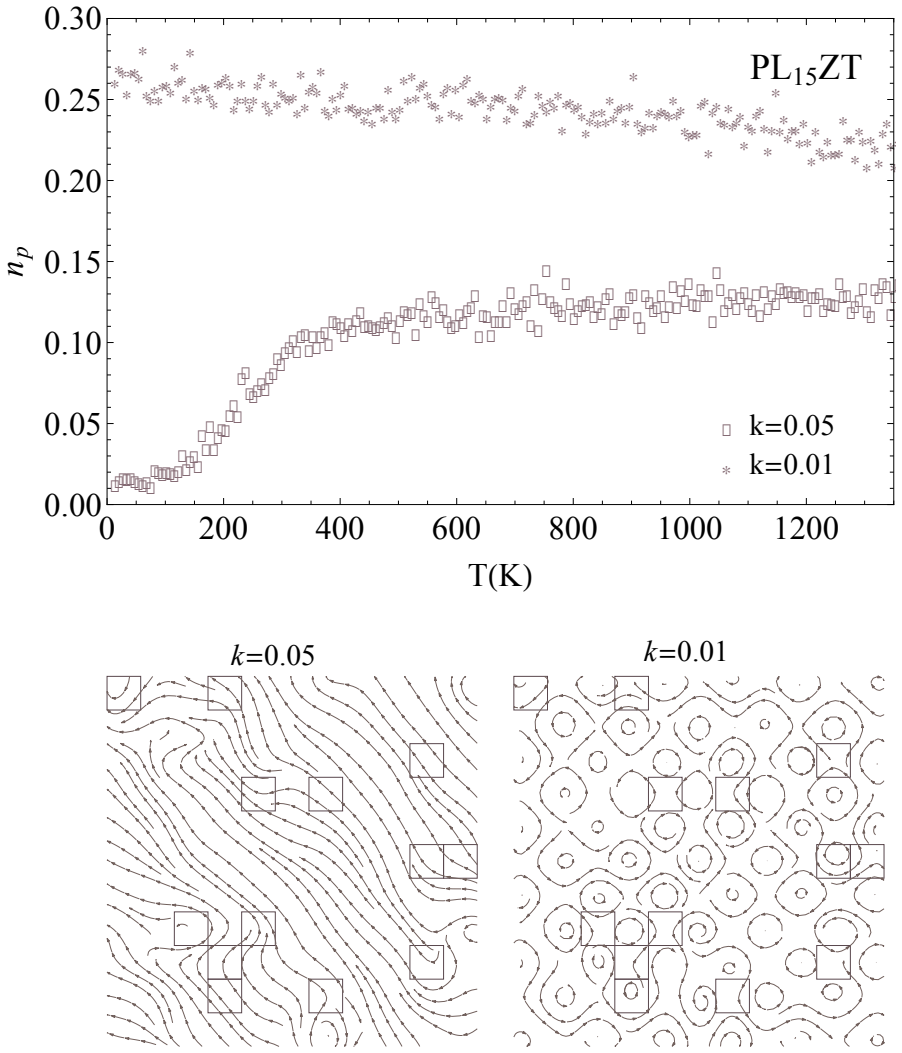

Fig. 3.61: Temperature evolution of the density of pairs of hedgehogs n_p in $PL_{15}ZT$ for k=0.01 and k=0.05. Lower panels depict the integral curves of the order parameter field within a (x, y) plane for T=17 K. Squares indicate the spatial distribution of the quenched cells.

Conclusion

To summarize, we have formulated the disorder-induced discrepancy between local and global scales in terms of local symmetry. This formulation has led to the introduction of a gauge field endowed with both a quenched component and a fluctuating one. Whereas the former encodes disorder as it subjects the field of dipole moments to frustration, the latter gives dipoles leeway to achieving order. As a result, a non-trivial interplay subtended by local symmetry constraints arises between competing ordering and disordering interactions.

The use of this approach and its combination with the first-principles based effective Hamiltonian enables to reproduce many generic features of PLZT such as the characteristic temperatures and their dependence on the La content and the effect of pressure in reducing the correlation length and driving the relaxor behavior. Within our model, local order is free to appear rather than constrained to exist, and is found to spontaneously emerge from the gauge field relaxation in the shape of polar regions. In this sense, the recovered departure from the Curie-Weiss behavior can be ascribed to local symmetry constraints to which the system is subjected. Moreover, the gauged disorder impacts the field of dipole moments by inducing stable topological defects, whose non-vanishing density at low temperatures weakens the ordered state. Our calculations additionally indicate that the dynamical behavior in relaxor ferroelectrics seems to be related to that of the topological defects. This question needs to be further addressed.

Note that we focused on the static aspects, since obtaining low-frequency dynamical quantities from first-principles-based effective Hamiltonian is not currently feasible. A further development could thus relate to the time implementation on the lattice, *i.e.*, in a 4-dimensional Euclidean spacetime that would account for the dynamics of both the gauge and the matter (dipole moments and strain) fields.

Another development pertains to elucidating the exact algebraic structure of the local symmetry. Indeed, due to the underlying perovskite structure and associated directional anisotropy, the local symmetry does not constitute a full rotational group but rather hints a groupoid type of structure.

Appendix A

Parallel transport

In order to formulate a gauge theory on a lattice, it is instructive to recall the geometrical role of the potentials $A_\mu(x)$ in the continuum theory. Since two internal space vector residing at two different space-time locations can not be compared in their natural bases, one needs a definition of what would physically equivalent internal space vectors mean at different space-time points. This is achieved by the parallel transport or connection; the potentials $A_\mu(x)$ specify the rotation of the frame in some intrinsic internal symmetry space upon transport between neighboring space-time points x and $x + dx$ [15, 16].

The general form of a local symmetry transformation for an arbitrary (non-Abelian) group can be expressed as:

$$U\psi = e^{-iq\sum_k \theta^k(x)T_k}\psi \tag{A.1}$$

The local character of the transformation is indicated by the parameters $\theta^k(x)$ which are continuous functions of x. The general transformation given by Eq.A.1 is to be identified with the usual form of an ordinary spatial rotation where the position dependent parameter $\theta^k(x)$ designates rotation angles. The T_k are the generators of the internal symmetry group and satisfy the usual commutation relations:

$$[T_i, T_j] = T_iT_j - T_jT_i = ic_{ijk}T_k \tag{A.2}$$

where c_{ijk} are the structure constants of the group (of vanishing values in the case of Abelian groups).

To see how the transformation given by Eq.A.1 defines a connection, let us now consider a test particle described by a wavefunction $\psi(x)$ and moving between two points x and $x+\mathrm{d}x$ in spacetime through an external potential field. As shown in Fig.A.1, the initial $\theta^k(x)$ internal direction at point x continuously changes until reaching the point $x + \mathrm{d}x$ where it acquires

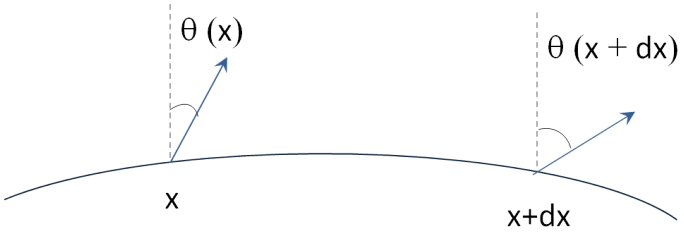

Fig. A.1: Rotation of the internal space direction of a moving test particle. The internal angles change from $\theta(x)$ to $\theta(x + \mathrm{d}x)$ as the test charge moves from x to $x + \mathrm{d}x$ (after Moriyasu, [15]).

a new internal direction $\theta^k(x + \mathrm{d}x)$. For an infinitesimal distance $\mathrm{d}x$, this change can be described by the effect of the transformation given by Eq.A.1 action on $\psi(x)$ which produces a rotation of the internal direction equal to the difference $\mathrm{d}\theta^k = \theta^k(x + \mathrm{d}x) - \theta^k(x)$.

In order to interpret the effect of the external potential field (the gauge field) on the particle as a precession of the internal basis, we explicitly decompose the particle's wavefunction $\psi(x)$ into external and internal parts:

$$\psi(x) = \sum_{\alpha} \psi_{\alpha}(x) u_{\alpha} \tag{A.3}$$

where the $\{u_\alpha\}$ denote the set of basis vectors in the internal space, and the $\{\psi_\alpha(x)\}$ are the components of $\psi(x)$ in the basis $\{u_\alpha\}$. Under an internal symmetry transformation, the components transform as usually:

$$\psi_{\beta} = U_{\beta\alpha}\psi_{\alpha} \tag{A.4}$$

where $U_{\beta\alpha}$ is some matrix representation of the symmetry group. When the particle moves from x to $x + dx$ through the external potential field, $\psi(x)$ changes by an amount $\mathrm{d}\psi$ given by:

$$\mathrm{d}\psi = \psi(x + dx) - \psi(x) \tag{A.5}$$

The expansion of $\mathrm{d}\psi$ to the first order in $\mathrm{d}x$ yields:

$$\mathrm{d}\psi = \sum_{\alpha} \left[(\partial_{\mu}\psi_{\alpha})\, \mathrm{d}x^{\mu} u_{\alpha} + \psi_{\alpha} \mathrm{d}u_{\alpha} \right] \tag{A.6}$$

The second term in Eq.(A.6) contains the change $\mathrm{d}u_\alpha$ in the internal space basis. It is given by the connection and describes the effect of the external potential field on the internal space direction of the particle. In order to access $\mathrm{d}u_\alpha$, we consider the infinitesimal internal rotation $U(\mathrm{d}x)$,

$$U(\mathrm{d}x) = e^{-iq\sum_k \mathrm{d}\theta^k(x) T_k} \qquad (\text{with} \quad \mathrm{d}\theta^k = \left(\partial_{\mu}\theta^k\right) \mathrm{d}x^{\mu}) \tag{A.7}$$

which rotates the internal basis u by an amount $\mathrm{d}u$,

$$U(\mathrm{d}x)u = u + \mathrm{d}u\,. \tag{A.8}$$

The generators T_k act as matrix operators on the column basis vectors u_α, yielding:

$$U(\mathrm{d}x)u_\alpha = e^{-iq\sum_k \left(\partial_\mu \theta^k\right)\mathrm{d}x^\mu (T_k)_{\alpha\beta}} u_\beta \tag{A.9}$$

Expanding $U(\mathrm{d}x)$ to the first order in $\mathrm{d}x$, we obtain:

$$u_\alpha + \mathrm{d}u_\alpha = \left[\delta_{\alpha\beta} - iq \sum_k \left(\partial_\mu \theta^k\right) \mathrm{d}x^\mu \left(T_k\right)_{\alpha\beta}\right] u_\beta \tag{A.10}$$

from which we infer the infinitesimal change in the internal basis,

$$\mathrm{d}u_\alpha = -iq \sum_k \left(\partial_\mu \theta^k\right) \mathrm{d}x^\mu \left(T_k\right)_{\alpha\beta} u_\beta\,. \tag{A.11}$$

The change $\mathrm{d}u_\alpha$ gives the sought connection. We therefore introduce the connection operator:

$$\left(A_\mu\right)_{\alpha\beta} = \sum_k \left(\partial_\mu \theta^k\right) \left(T_k\right)_{\alpha\beta}\,. \tag{A.12}$$

The total change $\mathrm{d}\psi$ can thus be finally written as follows:

$$\mathrm{d}\psi = \sum_{\alpha\beta} \left[\left(\partial_\mu \psi_\alpha\right) \delta_{\alpha\beta} - iq \left(A_\mu\right)_{\alpha\beta} \psi_\alpha\right] \mathrm{d}x^\mu u_\beta \tag{A.13}$$

where $\delta_{\alpha\beta}$ enables the factoring of the basis vector u_β. The change $\mathrm{d}\psi$ can be expressed in terms of its own external and internal parts, yielding:

$$\mathrm{d}\psi = \sum_\beta \left(\mathrm{d}\psi\right)_\beta u_\beta \equiv \sum_\beta \left(D_\mu \psi_\beta\right) \mathrm{d}x^\mu u_\beta \tag{A.14}$$

where the operator D_μ is a generalized form of derivative, referred to as the gauge covariant derivative, already mentioned in a previous section, and describing the changes in both the external and internal parts of $\psi(x)$. From Eq.(A.13), we can explicitly write:

$$D_\mu \psi_\beta = \sum_\alpha \left[\delta_{\alpha\beta}\partial_\mu - iq \left(A_\mu\right)_{\beta\alpha}\right] \psi_\alpha \tag{A.15}$$

Coming back to the case of the electromagnetic gauge group U(1), the internal space being one-dimensional, Eq.(A.15) reduces to:

$$D_\mu \psi = \left(\partial_\mu - iqA_\mu\right) \psi \tag{A.16}$$

From this geometrical derivation [15] of the covariant derivative, one concludes that the

vector potential is both an external field and an internal space operator, since it acts as a connection in the internal symmetry space.

Appendix B

Density functional theory

When considering a system consisting of N electrons and M nuclei, a first simplification naturally arises from the large mass difference between electrons and nuclei, enabling the decoupling of their dynamics and degrees of freedom, within the so-called Born-Oppenheimer approximation. This leads to a first reduction of the many-body problem to the study of interacting electrons in a frozen-in configuration of the nuclei whose positions, $\mathbf{r}_\alpha$, are regarded as parameters. Within this first approximation, the ground state of N electrons is determined by solving the following Hamiltonian of a stationary many-body system:

$$\hat{H}_v \quad = \hat{T} + \hat{U} + \hat{V}_{\text{ext}} \tag{B.1}$$

The constituent terms are explicitly given as

$$\hat{T} = -\frac{1}{2}\sum_i \nabla_i^2 \tag{B.2}$$

$$\hat{U} = \sum_i u(\mathbf{r}_i) = \sum_i \sum_{i>j} \frac{1}{|\mathbf{r}_i - \mathbf{r}_j|} \tag{B.3}$$

$$\hat{V}_{\text{ext}} = \sum_i v(\mathbf{r}_i) = \sum_i \sum_\alpha \frac{-Z_\alpha}{|\mathbf{r}_i - \mathbf{r}_\alpha|} \tag{B.4}$$

where latin subindices refer to the electrons whereas Greek subindices refer to the nuclei and where the operators denote the kinetic energy of the electrons, the two-particle Coulomb interaction and the external potential arising from the nuclei, respectively. For all N-electrons systems, $\hat{T}$ and $\hat{U}$ are the same, they are said to be universal, or system-independent, so that the specificity of the system is encapsulated in the external potential v_{ext}. The Hamiltonian $\hat{H}_v$ is thereby denoted with a subindex v indicating that the operator can be regarded as

a functional of the external potential. This is in particular the case for the ground state wavefunction $|\psi_0[v]\rangle$ and the ground state energy $E_0[v]$, which are related by the Schrodinger equation

$$(\hat{T} + \hat{U} + \hat{V}_{\text{ext}}) \, |\psi_0[v]\rangle = E_0[v] \, |\psi_0[v]\rangle \tag{B.5}$$

The ground state $|\psi_0[v]\rangle$ gives rise to a ground state electronic density $n(\mathbf{r})$

$$n(\mathbf{r}) = \langle\psi_0| \, \hat{n} \, |\psi_0\rangle = \langle\psi_0| \sum_{i=1}^{N} \delta(\mathbf{r} - \mathbf{r}_i) \, |\psi_0\rangle = N \int \prod_{i=2}^{N} \mathrm{d}\mathbf{r}_i |\psi_0(\mathbf{r}, \mathbf{r}_2, \cdots, \mathbf{r}_N)|^2 \tag{B.6}$$

Hohenberg-Kohn theorems

The first Hohenberg-Kohn theorem demonstrates that the density may be used in place of the potential as the fundamental function uniquely characterizing the system, rather than the many electron wavefunction. It may be stated as: *the ground-state density $n(\mathbf{r})$ uniquely specifies the potential, to within a constant, and hence the ground state wavefunction, to within a phase factor.* This means that the external potential is a well defined functional $v[n]$ of the density. In the original Hohenberg-Kohn paper [221], this theorem is proven by *reductio ad absurdum* for densities with non-degenerate ground states. Assume that there exist two different external potentials V_{ext} and V'_{ext} which both give the same electron density $n(\mathbf{r})$. Then the corresponding Hamiltonians H and H' have the same ground state density but different ground state wavefunctions $|\psi_0\rangle$ and $|\psi'_0\rangle$ respectively. Using the variational principle, and taking $|\psi'_0\rangle$ as a trial function for H yield the strict inequality

$$\begin{aligned} E_0 < \langle\psi'_0| \, H \, |\psi'_0\rangle = & \quad \langle\psi'_0| \, H' \, |\psi'_0\rangle + \langle\psi'_0| \, (H - H') \, |\psi'_0\rangle \\ = & \quad E'_0 + \int \mathrm{d}\mathbf{r} \, n(\mathbf{r}) [V_{\text{ext}}(\mathbf{r}) - V'_{\text{ext}}(\mathbf{r})] \end{aligned} \tag{B.7}$$

Whereas taking $|\psi_0\rangle$ as a trial function for H' gives

$$\begin{aligned} E'_0 < \langle\psi_0| \, H' \, |\psi_0\rangle = & \quad \langle\psi_0| \, H \, |\psi_0\rangle + \langle\psi_0| \, (H' - H) \, |\psi_0\rangle \\ = & \quad E_0 - \int \mathrm{d}\mathbf{r} \, n(\mathbf{r}) [V_{\text{ext}}(\mathbf{r}) - V'_{\text{ext}}(\mathbf{r})] \end{aligned} \tag{B.8}$$

Adding these two equations results in the contradiction

$$E_0 + E'_0 < E_0 + E'_0 \tag{B.9}$$

from which it is concluded that different ground states must yield different densities. The first Hohenberg-Kohn theorem[1] thus indicates that there is a unique invertible mapping between the external potential v and the ground state density $n(\mathbf{r})$. This implies that the total energy is a functional of the density, $E = E[n]$. The universal Hohenberg-Kohn functional $F_{\mathrm{HK}}[n]$ given by

$$F_{\mathrm{HK}}[n] = \langle \psi[n] | \, \hat{T} + \hat{U} \, | \psi[n] \rangle \tag{B.10}$$

defines the energy functional $E[n]$ as

$$E[n] = \int n(\mathbf{r}) v(\mathbf{r}) \mathrm{d}\mathbf{r} + F_{\mathrm{HK}}[n] \tag{B.11}$$

The second Hohemberg-Kohn theorem [221] generalises the *variational principle* from wave functions to electron densities in that it states that the functional for the ground state energy is minimized by the ground state electron density. If n_0 is the ground state density corresponding to an external potential v_0 and $\tilde{n}$ an arbitrary other ground state density satisfying $\tilde{n}(\mathbf{r}) \geqslant 0$ and $\int \tilde{n}(\mathbf{r}) \mathrm{d}\mathbf{r} = N$ then

$$\begin{aligned} E_{v_0}[n_0] &\leqslant E_{v_0}[\tilde{n}] \\ \langle \psi[n_0] | \, \hat{T} + \hat{U} + \hat{V}_0 \, | \psi[n_0] \rangle &\leqslant \langle \psi[\tilde{n}] | \, \hat{T} + \hat{U} + \hat{V}_0 \, | \psi[\tilde{n}] \rangle \end{aligned} \tag{B.12}$$

This second Hohenberg-Kohn theorem thus states that $E[n]$ has an extremum in correspondence to the ground state electron density. It demonstrated the *existence* of such a functional but did not provide any explicit instructions as how to build or find this functional.

The Kohn-Sham ansatz

The central assertion of Kohn and Sham's reformulation of DFT [222] stands in the mapping of the intractable system of interacting electrons in a external potential v_{ext} onto a fictitious system of independent electrons, chosen to have the same density as the physical system and evolving in a effective potential v_s. In this approach, the exact kinetic energy functional can be written as

$$T[n] = T_s[n] + T_c[n] \tag{B.13}$$

[1] Lieb [223] was the first to point out the connection between density-functional theory and Legendre transforms. In this approach, potential and density are conjugate variables, and the first Hohenberg-Kohn theorem simply trades one set of variational parameters for another via a Legendre transform: writing the ground state energy as a functional of the external potential $E_0[v]$ and taking its functional derivative yield the following expression for the density $n(\mathbf{r}) = \delta E[v]/\delta v(\mathbf{r})$. The one-to-one correspondence between v and n is thus due to the fact that the Legendre transform $F_{\mathrm{HK}}[n(\mathbf{r})] = E_0[v(\mathbf{r})] - \int n(\mathbf{r}) v(\mathbf{r}) \mathrm{d}\mathbf{r}$ of the ground state energy $E_0[v]$ is the $F_{\mathrm{HK}}[n]$ functional.

where $T_s[n]$ is the kinetic energy of the auxilliary non interacting N-electron system, and where $T_c[n]$ is the remainder. The subscripts s and c stand for single-particle and correlation, respectively. Similarly, the exact Coulomb functional $U[n]$ is written as $U[n] = E_H[n]+\Delta U[n]$ where the Hartree term $E_H[n]$ describes the electron-electron repulsion and where $\Delta U[n]$ is a contribution that accounts for the quantum nature of the interacting electrons. The exact energy functional is then rewritten as:

$$E[n] = T_s[n] + \int n(\mathbf{r}) v_{\text{ext}}(\mathbf{r})\, \mathrm{d}\mathbf{r} + E_H[n] + E_{\text{xc}}[n] \tag{B.14}$$

where the exchange-correlation function $E_{\text{xc}}[n]$ corresponds by definition to

$$E_{\text{xc}}[n] = (T[n] - T_s[n]) + (U[n] - E_H[n]) \tag{B.15}$$

and should account for the exchange effects (Pauli repulsion), the correction that compensates the self-interaction term in $E_H[n]$ and the correlations effects. The variational equation its Euler-Lagrange form for the exact functional is thus:

$$\frac{\delta E[n]}{\delta n(\mathbf{r})} = \frac{\delta T_s[n]}{\delta n(\mathbf{r})} + v_{\text{ext}}(\mathbf{r}) + \int \frac{n(\mathbf{r})}{|\mathbf{r}-\mathbf{r}'|}\, \mathrm{d}\mathbf{r} + \frac{\delta E_{\text{xc}}[n]}{\delta n(\mathbf{r})} = \mu \tag{B.16}$$

where μ is a Lagrange multiplier constraining the number of electrons to N. Kohn and Sham introduced an auxiliary non interacting system S of N particles with the property that it yields the same ground state density as the real interacting system in a given external potential $v_{\text{ext}}(\mathbf{r})$. This correspondence implies that the non interacting electrons must be subjected to another external potential $v_{\text{s}}(\mathbf{r})$, which must compensate the contributions arising from the electron-electron interactions. For the virtual system S, the variational equation writes:

$$\frac{\delta E[n]}{\delta n(\mathbf{r})} = \frac{\delta T_s[n]}{\delta n(\mathbf{r})} + v_s(\mathbf{r}) = \mu \tag{B.17}$$

Equations (*B*.16) and (*B*.17) coincide whenever:

$$v_s(\mathbf{r}) = v_{\text{ext}}(\mathbf{r}) + \int \frac{n(\mathbf{r})}{|\mathbf{r}-\mathbf{r}'|}\, \mathrm{d}\mathbf{r} + v_{\text{xc}}[n](\mathbf{r}) \qquad v_{\text{xc}}(\mathbf{r}) = \frac{\delta E_{\text{xc}}[n]}{\delta n(\mathbf{r})} \tag{B.18}$$

Consequently, one can calculate the density of the interacting (many-body) system in potential $v_{\text{ext}}(\mathbf{r})$, described by a many-body Schrodinger equation of the form given by Eq.*B*.5, by solving the equations of a noninteracting (single-body) system in potential $v_s(\mathbf{r})$. In particular, the Schrodinger equation of the auxiliary system

$$\left\{ -\frac{1}{2}\nabla^2 + v_s(\mathbf{r}) \right\} \phi_i(\mathbf{r}) = \epsilon_i \phi_i(\mathbf{r}) \tag{B.19}$$

yields orbitals that reproduce the density $n(\mathbf{r})$ of the original system:

$$n(\mathbf{r}) = \sum_{i}^{N} f_i |\phi_i(\mathbf{r})|^2 \tag{B.20}$$

where f_i is the occupation of the ith orbital.

Given a practical approximation for $E_{\text{xc}}[n]$, one obtains $v_{\text{xc}}(\mathbf{r})$, and can thus find $v_s(\mathbf{r})$ from $n(\mathbf{r})$ for a given $v_{\text{ext}}(\mathbf{r})$. The set of coupled non linear equations (*B*.18), (*B*.19) and (*B*.20) are the Khon-Sham equations, and should hold simultaneously. In particular, the density must be self-consistent. The computational procedure usually starts with an initial guess for the input density $n(\mathbf{r})$, leading to a potential $v_s(\mathbf{r})$ which in turn gives rise to a set of orbitals ϕ_i from which a new density is constructed. This procedure is reiterated until reaching a convergence criteria (equality of the input and output densities to required precision) within this self-consistency cycle. Again, this scheme only holds for an explicit form of $E_{\text{xc}}[n]$ that is *a priori* unknown but can be efficiently approximated.

The local density approximation

As stated previously, the quality of the results using DFT depends on the ability of the universal exchange-correlation functional $E_{\text{xc}}[n]$ to model the many-body electronic interactions. The first, and most widely used approach is the Local Density Approximation (LDA) [222], which treats the inhomogeneous system locally as an homogeneous electron gas. It assumes *(i)* that the exchange-correlation energy per particle at point $\mathbf{r}$, $\epsilon_{\text{xc}}(\mathbf{r})$, only depends on the density at this point, and *(ii)* that it is equal to the exchange-correlation energy per particle of a homogeneous electron gas of density $n(\mathbf{r})$ in a neutralizing background.

$$E_{\text{xc}}^{\text{LDA}}[n] = \int n(\mathbf{r})\, \epsilon_{\text{xc}}^{\text{LDA}}(\mathbf{r})\, \mathrm{d}\mathbf{r} \qquad\qquad \epsilon_{\text{xc}}^{\text{LDA}}(\mathbf{r}) = \epsilon_{\text{xc}}^{\text{hom}}[n(\mathbf{r})] \tag{B.21}$$

The quantity $\epsilon_{\text{xc}}^{\text{hom}}[n(\mathbf{r})]$ can be further split into exchange and correlation contributions:

$$\epsilon_{\text{xc}}^{\text{hom}}[n(\mathbf{r})] = \epsilon_{\text{x}}^{\text{hom}}[n(\mathbf{r})] + \epsilon_{\text{c}}^{\text{hom}}[n(\mathbf{r})] \tag{B.22}$$

The exchange part describes the energy lowering due to antisymmetrization (Pauli repulsion) and can be evaluated analytically by the method of Bloch and Dirac, and scales as

$$\epsilon_{\text{x}}^{\text{hom}}[n(\mathbf{r})] = -\frac{3}{4\pi}\left(\frac{3}{\pi}\, n(\mathbf{r})\right)^{1/3} \tag{B.23}$$

For the correlation part, that describes the propensity for two electrons of unequal spin to choose different orbitals and to mutually avoid along their motion in space, one may rely on accurate values obtained by Ceperley-Alder [224] from Monte-Carlo simulations of the

energy of the homogeneous electron gas. By its very construction, the LDA is expected to be a good approximation for spatially slowly varying densities. Although this condition is hardly ever met for real electronic systems, LDA has proved to be remarkably accurate for a wide variety of systems[2] providing access to the ground state energy and thereby to structural and dynamical properties of solids such as equilibrium structures, elastic, dielectric and vibrational properties. Atomic positions and lattice constants reproduce the experiment within 1% whereas phonon frequencies are usually obtained within 5%. Although an accuracy of 1% on the lattice constant might be considered as successful for a method without any adjustable parameter, it can constitute a limitation in some cases. In perovskite oxides for example, the ferroelectric instability is very sensitive to pressure, and thus to the lattice constant. In this context, in order to avoid this problem, it appeared convenient in some circumstances to fix the lattice parameters to their experimental values, or to apply a negative pressure [227] in the calculation that compensates for the typical LDA underestimate of the lattice constant.

[2]This is due in part to the fact that the LDA fulfills the sum rule on the exchange-correlation hole, $\int \mathrm{d}\mathbf{r}' n_{\mathrm{xc}}(\mathbf{r}, \mathbf{r}') = -1$, $\forall \mathbf{r}$, which must be obeyed by the real functional, and which describes how an electron at $\mathbf{r}$ completely depletes the total density of the other electron at $\mathbf{r}'$. This gives rise to error compensation when computing the exchange-correlation energy (typically, the LDA overestimates E_{x} and underestimates E_{c})

Bibliography

[1] L.E. Cross, Ferroelectrics 76 (1987) 241, 151 (1994) 305

[2] A. Bokov and Z. Ye, J. Mater. Sci. 41 (2006) 31

[3] K. Hirota, S. Wakimoto, D.E. Cox, J. Phys. Soc. Jpn.75 (2006) 111006

[4] G.A. Samara, Solid State Physics vol 56 (2001) 239

[5] W. Kleemann, J. Mater. Sci. 41 (2006) 129

[6] T. Egami, S.J.L. Billinge, Underneath the Bragg peaks: structural analysis of complex materials (Pergamon Materials Series, Cambridge, 2003)

[7] N. Mathan, E. Husson, G. Calvarin , J.R. Gavarri , A.W. Hewat, A. Morell 1991 J. Phys.: Condens. Matter 3 (1991) 8159-71

[8] P. Bonneau, P. Gamier, E. Husson, A. Morell, Mat. Res. Bull. XXIV, (1989) 201

[9] H.D. Rosenfeld, T. Egami, Ferroelectrics 158 (1994) 351

[10] I. Grinberg, H. Takenaka, Y.-H. Shin, A.M. Rappe, J. Adv. Dielect. 02 (2012) 1241009

[11] T. Egami, Ferroelectrics 267 (2002) 101

[12] W. Zhong, D. Vanderbilt, K. M. Rabe, Phys. Rev. Lett. 73 (1994) 1861

[13] P.W. Anderson, Basic notions in condensed matter (Addison-Wesley, California, 1984)

[14] F.J. Wegner, J. Math. Phys. 12 (1971) 2259

[15] K. Moriyasu, An elementary primer for Gauge Theory (World Scientific, Singapore, 1983)

[16] M. Creutz, L. Jacobs, C. Rebbi, Physical Reports 95, 4 (1983) 201

[17] A. Kadic, D.G.B. Edelen, A Gauge Theory of Dislocations and Disclinations (Springer, Berlin, 1983)

[18] M.O. Katanaev, I.V. Volovich, Annals of Physics 216 (1992) 1

[19] H. Kleinert, Gauge fields in condensed matter, vol. 1 and 2 (World Scientific, Singapore, 1989)

[20] G. Toulouse, Communications on Physics 2 (1977) 115

[21] I.E. Dzyaloshinskii, G.E. Volovik, Le journal de Physique 39 (1978) 693

[22] I.E. Dzyaloshinskii, Modern Trends in the Theory of Condensed Matter, Eds. A. Pekalski and J. Przystawa, Vol. 115, Lecture Notes in Physics (Spinger-Verlag) 204

[23] S. Hands, Nuclear Physics B 305 (1988) 597

[24] M. E. Fisher, Physica 28 (1962) 172

[25] M. E. Fisher, Journal of Mathematical Physics 5 (1964) 944

[26] M. E. Fisher, Reports on Progress in Physics 30 (1967) 615

[27] W. Kleemann, J.Dec, P. Lehnen, R. Blinc, B.Zalar, R. Pankrath, Europhys. Lett. 57 (2002) 14

[28] S.N. Kallaev, Z.M. Omarov, R.G. Mitarov, A.R. Bilalov, K. Bormanis, S.A. Sadykov, Journal of Experimental and Theoretical Physics 111 (2010) 421

[29] F. S. Nogueira, Phys. Rev. B 62 (2000) 14559

[30] H. Kleinert and F. S. Nogueira, Nuclear Physics B 651 (2003) 361

[31] H. Kleinert and A. M. J. Schakel, Phys. Rev. Lett. 90 (2003) 097001

[32] A.S. Bhalla, R. Guo, R. Roy, Mater. Res. Innovations 4 (2000) 3-29

[33] K. Uchino, Ferroelectric Devices. New York: Decker (2000)

[34] A. Gruverman, A. Kholkin, Rep. Prog. Phys., 69 (2006) 2443-2474

[35] A.K. Tagantsev, L.E. Cross, J. Fousek, *Domains in Ferroic Crystals and Thin Films*, New York, Springer (2010).

[36] M.E. Lines and A.M. Glass, *Principles and Applications of Ferroelectrics and Related Materials*, Clarendon press, Oxford (2001).

[37] A. Akbarzadeh, PhD Thesis, *Simulating Quantum Effects in Ferroelectrics from First-Principles* (2005)

[38] S. Arrhenius, Z. Phys. Chem. 4 (1889) 226

[39] H. Eyring, Chem. Rev. 17 (1935) 65

[40] H. Eyring, J. Chem. Phys. 3 (1935) 107

[41] H. Vogel, Phys. Z. 22 (1921) 645

[42] G.S. Fulcher, J. Am. Ceram. Soc. 8 (1925) 339

[43] G. Tammann, W. Hesse, Z. Anorg. Allg. Chem. 156 (1926) 245

[44] L.L. Boyer, R.E. Cohen, H. Krakauer, W.A. Smith, Ferroelec. 111 (1990) 1

[45] R.E. Cohen, Journal of Physics and Chemistry of Solids 61 (2000) 139

[46] R. E. Cohen and H. Krakauer, Phys. Rev. B 42 (1990) 6416 ; Ferroelectrics 136 (1992) 65

[47] R. Hemphill, L. Bellaiche, A. Garcia, D. Vanderbilt, Appl. Phys. Lett. 77 (2000) 3642

[48] J. Iniguez, L. Bellaiche, Phys. Rev. B 73 (2006) 144109

[49] P. Ghosez, J. Junquera, Ed. by M. Rieth and W. Schommers, American Scientific Publisher 2006 (Stevenson Ranch, CA, USA)

[50] P. Chandra, P.B. Littlewood, in K. Rabe, Ch. H. Ahn and J-M. Triscone eds., The Physics of Ferroelectrics: A Modern Perspective (SpringerVerlag, Berlin, 2007)

[51] A.P. Levanyuk, Sov. Phys. JETP 36 (1959) 571

[52] V.L. Ginzburg, Fiz. tverd. Tela 2 (1960) 2031 ; English translation in Sov. Phys.-Solid State 2 (1960) 1824

[53] V.L. Ginzburg, ZhETF 15 (1945) 739

[54] V.L. Ginzburg, ZhETF 19 (1945) 36

[55] V.L. Ginzburg, Usp. Fiz. Nauk 38 (1949) 490

[56] A. F. Devonshire, Phil. Mag. 40 (1949) 1040

[57] A. F. Devonshire, Phil. Mag. 42 (1951) 1065

[58] W. Cochran, Phys. Rev. Lett. 3 (1959) 412

[59] W. Cochran, Adv. Phys. 9 (1960) 387, 20 (1961) 401

[60] V. Bobnar, C. Filipic, A. Levstik, Z. Kutnjak, J. Appl. Phys. 107 (2010) 84104

[61] J. Hlinka, J. Adv. Diel. 2 (2012) 1241006

[62] G.A. Smolensky, V.A. Isupov, Sov. J. Techn. Phys. 24 (1954) 1380

[63] G.A. Smolenskii, V.A. Isupov, A.I. Agranovskaya, S.N. Popov, Sov. Phys. Solid State 2 (1961) 2584

[64] G.A. Smolenski, J. Phys. Soc. Jpn. 28 (1970) 26

[65] V.V. Kirillov, V.A. Isupov, Ferroelectrics 5 (1973) 3

[66] S. Nambu, K. Sugimoto, Ferroelectrics 198 (1997) 11

[67] A.A. Bokov, Z.-G. Ye, Solid State Communications 116 (2000) 105-108

[68] H.T. Martirena, J.C. Burfoot, Ferroelectrics 7 (1974) 151

[69] R. Clarke, J.C. Burfoot, Ferroelectrics 8 (1974) 505

[70] K. Uchino, S. Nomura, Ferroelectrics Lett. 44 (1982) 55, K. Uchino, S. Nomura, L.E. Cross, S.J. Jang, R.E. Newnham, J. Appl. Phys. 51 (1980) 1142

[71] V.A. Isupov, Sov. Phys. Solid State 28 (1986) 1253.

[72] D. Viehland, S.J. Jang, L.E. Cross, M. Wuttig, Phys. Rev. B 46 (1992) 8013

[73] D. Viehland, M. Wuttig, L.E. Cross, Ferroelectrics 120 (1991) 71

[74] X. Dai, Z. Xu, D. Viehland, Phil. Mag. B 70 (1994) 33

[75] PH. Sciau, G. Calvarin, J. Ravez, Sol. Stat. Commun. 113 (2000) 77

[76] A. Simon, J. Ravez, M. Maglione, J. Phys.: Condens. Matter 16 (2004) 963

[77] N. Yasuda, H. Ohwa, S. Asano, Jpn. J. Appl. Phys. Pt. 1 35 (1996) 5099

[78] L. Neel, C. R. Acad Sci 228 (1949) 664

[79] A.E. Glazounov, A.K. Tagantsev, Ferroelectrics 221 (1999) 57

[80] V.A. Isupov, Phys. Solid State 45 (2003) 1107

[81] S.F. Edwards, P.W. Anderson, J. Phys. F 5 (1975) 1965

[82] G. Burns, F.H. Dacol, Sol. Stat. Commun. 48 (1983) 853, Phys. Rev B 28 (1983) 2527

[83] F. Chu, N. Setter, A.K. Tagantsev, J. Appl. Phys. 74 (1993) 5129

[84] J. Zhao, A.E. Glazounov, Q.M. Zhang, B. Toby, Appl. Phys. Lett 72 (1998) 1048

[85] K. Binder, A.P. Young, Rev. Mod. Phys. 58 (1986) 801

[86] K.H. Fisher, Phys. Status Solidi B 116 (1983) 357

[87] G. Jonker, Mater. Res. Bull. 18 (1983) 301

[88] H. Nishimori, Statistical Physiscs of Spin Glasses and Information Processing An Introduction, Clarendon Press, Oxford, 2001

[89] D. Sherrington, S. Kirpatrick, Phys. Rev. Lett. 35 (1975) 1972

[90] D. Sherrington, cond-mat/9906289

[91] V. Bobnar, Z. Kutnjak, R. Pirc, R. Blinc, A. Levstik, Phys. Rev. Lett. 84 (2000) 5892

[92] E. Courtens, Ferroelectrics 72 (1987) 229

[93] G.A. Samara, Ferroelectrics 117 (1991) 347

[94] Z.-Y. Cheng, L.-Y.Zhang, Xi Yao, J. Appl. Phys. 79 (1996) 8615

[95] S.B. Vakhrushev, B.E. Kvyatkovsky, A.A. Naberezhnov, N.M. Okuneva, B.P. Toperverg, Ferroelectrics 90 (1989) 173

[96] G. Xu, G. Shirane, J.R.D. Copley, P.M. Gehring, Phys. Rev. B 69 (2004) 64112

[97] R. Pirc, R. Blinc, Phys. Rev. B 76 (2007) 20101

[98] R. Pirc, R. Blinc, Phys. Rev. B 60 (1999) 13470

[99] R. Blinc, J. Dolinsek, A. Gregorovic, B. Zalar, C. Filipic, Z. Kutnjak, A. Levstik, R. Pirc, Phys. Rev. Lett, 83 (1999) 424

[100] J. Hemberger, H. Ries, A. Loidl, Phys. Rev. Lett, 76 (1996) 2330

[101] A. Levstik, Z. Kutnjak, C. Filipic, R. Pirc, Phys. Rev. B 57 (1998) 11 204

[102] Z. Kutnjak, C. Filipic, R. Pirc, A. Levstik, r. Farhi, M. El Marssi, Phys. Rev. B 59 (1999) 294

[103] R. Blinc, V. Bobnar, R. Pirc, Phys. Rev. B 64 (2001) 132103

[104] G. Samara, Phys. Rev. Lett. 77 (1996) 314 , J. App. Phys. 84 (1998) 2538

[105] G. Samara, L.A. Boatner, Phys. Rev. B 61 (2000) 3889

[106] A.G. Beattie, G.A. Samara, J. App. Phys. 42 (1971) 2376

[107] A.E. Glazounov, A.K. Tagantsev, Appl. Phys. Lett. 73 (1998) 856

[108] D. Viehland, S.J. Jang, L.E. Cross, M. Wuttig, J. App. Phys. 68 (1990) 2916

[109] A.K. Tagantsev, Phys. Rev. Lett. 72 (1994) 1100

[110] B.E. Vugmeister, Phys. Rev. B 73 (2006) 174117

[111] B.E. Vugmeister, H. Rabitz, Phys. Rev. B 57 (1998) 7587

[112] B.E. Vugmeister, H. Rabitz, Phys. Rev. B 61 (2000) 14448

[113] V.M. Ishchuk, Ferroelectrics 555 (2001) 73

[114] J. Bricmont, A. Kupiainen, Comm. Math. Phys. 116 no. 4 (1988) 539

[115] M. Aizenman, J. Wehr, Comm. Math. Phys. 130 no. 3 (1990) 489

[116] Y. Imry and S. Ma, Phys. Rev. Lett. 39 (1975) 1399

[117] B.I. Halperin, C.M. Varma, Phys. Rev. B 14 (1976) 4030

[118] G. Parisi, N. Sourlas, Phys. Rev. Lett. 43 (1979) 744

[119] R. Peierls, Proc. Camb. Phil. Soc. 32 (1936) 477

[120] D. Fisher, G. M. Grinsrein, A. Khurana, Physics Today (1988) 56

[121] B. Fischer, M.W. Klein, Phys. Rev. Lett. 37 (1976) 756

[122] V. Westphal, W. Kleemann, M. D. Glinchuk, Phys. Rev. Lett. 68 (1992) 847

[123] W. Kleemann, R. Lindner, Ferroelectrics 199 (1997) 1

[124] E. Courtens, J. Phys. (Paris) Lett. 43 (1982) L199

[125] C.A.M. Mulder, A.J. van Duyneveldt, J.A. Mydosh, Phys. Rev. 8 23 (1981) 1384

[126] S. Nagata, P.H. Keesom, H.R. Harrison, Phys. Rev. 8 19 (1979) 1633

[127] D. Viehland, M. Wuttig, L. E. Cross, Ferroelectricss 120 (1991)

[128] P. Juhas, I. Grinberg, A.M. Rappe, W. Dmowski, T. Egami, P.K. Davies, Phys. Rev. B 69 (2004) 214101

[129] I. Grinberg, A.M. Rappe, Phys. Rev. B 70 (2004) 220101

[130] I. Grinberg, M.R. Suchomel, P.K. Davies, A.M. Rappe, J. App. Phys. 98 (2005) 94111

[131] Y.-H. Shin, V.R. Cooper, I. Grinberg, A.M. Rappe, Phys. Rev. B 71 (2005) 54104

[132] I. Grinberg, P. Juhas, P.K. Davies, A.M. Rappe, Phys. Rev. Lett. 99 (2007) 267603

[133] I. Grinberg, Y.-H. Shin, A.M. Rappe, Phys. Rev. Lett. 103 (2009) 197601

[134] I. Grinberg, H. Takenaka, Y.-H. Shin, A.M. Rappe, J. Adv. Dielect. 2 (2012) 1241009

[135] J. Hlinka, J. Adv. Dielect. 2 (2012) 1241006

[136] I. Grinberg, V.R. Cooper, A.M. Rappe, Nature (London) 419 (2002) 909

[137] R.E. Cohen, Nature (London) 358 (1992) 136

[138] N. Setter, L.E. Cross, J. Appl. Phys. 51 (1980) 4356

[139] P. Juhas, P.K. Davies, M.A. Akbas, J. Am. Ceram. Soc. 87 (2004) 2086

[140] B.P. Burton, E. Cockayne, Phys. Rev. B 60 (1999) R12542

[141] R. Fish, Phys. Rev. B 67 (2003) 94110

[142] F. Chu, N. Setter, A. K. Tagantsev, J. Appl. Phys. 74 (1993) 5129

[143] H. Quian, L.A. Bursill, Int. J. Mod. Phys. B 10 (1996) 2027

[144] E. Cockayne, B.P. Burton, Phys. Rev. B 69 (2004) 144116

[145] I.-K. Jeong, T. W. Darling, J. K. Lee, Th. Proffen, R. H. Heffner, J. S. Park, K. S. Hong, W. Dmowski, T. Egami, Phys. Rev. Lett. 94 (2005) 147602

[146] B.P. Burton, E. Cockayne, U.V. Waghmare, Phys. Rev. B 72 (2005) 64113

[147] B.P. Burton, E. Cockayne, S. Tinte, U.V. Waghmare, Phase Transit. 79 (2006) 91

[148] S. Tinte, B.P. Burton, E. Cockayne, U.V. Waghmare, Phys. Rev. Lett. 97 (2006) 137601

[149] K. M. Rabe, U.V. Waghmare, Phys. Rev. B 52 (1995) 13236

[150] U.V. Waghmare, K. M. Rabe, Phys. Rev. B 55 (1997) 6161

[151] U.V. Waghmare, E. Cockayne, B. P. Burton, Ferroelectrics 291 (2003) 187

[152] W. Kleemann, J. Adv. Diel. 2 (2012) 1241001

[153] R.B. Griffiths, Phys. Rev. Lett. 23 (1969) 17-19

[154] G. Samara, E. L. Venturini, Phase Transit. 79 (2006) 21

[155] G.H. Haertling, C.E. Land, J. Am. Ceram. Soc. 54 (1971) 303, G.H. Haertling, Ferroelectrics 75 (1987) 25

[156] X. Dai, A. DiGiovanni, D. Viehland. J. Appl. Phys. 74 (1993) 3399

[157] A. Krumins, T. Shiosaki, S. Koizumi, Jap. J. Appl. Phys. 33 (1994) 4940

[158] D. Viehland, S.J. Jang, L.E. Cross, M. Wuttig, J. App. Phys. 69 (1991) 6595

[159] H. Weyl, Gravitation and electricity, Sitz. Preuss. Akad. Wiss. Berlin (Math. Phys.) (1918) 465

[160] F. London, Quantenmechanische Deutung der Theorie von Weyl. Z. Phys. 42 (1927) 375

[161] H. Weyl, Elektron und Gravitation. I. Z. Phys. 56 (1929) 330

[162] J.D. Jackson, L.B. Okun, Rev. Mod. Phys. 73 (2001) 663-680

[163] L. O'Raifeartaigh, N. Straumann, Rev. Mod. Phys. 72 (2000) 1

[164] N. Straumann, Acta Phys.Polon. B37 (2006) 575-594

[165] G.A. Smolenskii, A.I. Agranovskaya, Sov. Phys. Solid State 1, 10 (1960) 1429-1437

[166] G.A. Samara, Solid State Physics 56 (2001) 239

[167] V. V. Bhat, A. M. Umarji, V. B. Shenoy, and U. V. Waghmare, Phys. Rev. B 72 (2005) 14104

[168] S. Tinte, B. P. Burton, E. Cockayne, and U. V. Waghmare, Phys. Rev. Lett. 97 (2006) 137601

[169] A. R. Akbarzadeh, S. Prosandeev, E. J. Walter, A. Al-Barakaty, and L. Bellaiche, Phys. Rev. Lett. 108 (2012) 257601

[170] G. A. Samara, J. Phys.: Condens. Matter 15 (2003) R367

[171] D.J. Gross, Chinese Journal of Physics 30 (1992) 955

[172] S. Elitzur, Phys. Rev. D 12 (1975) 3978

[173] A.M. Polyakov, Zh. Eksp. Teor. Fiz. Pis'ma. Red. 20 (1974) 430 [JETP Lett. 20 (1974) 194]

[174] G. 'tHooft, Nuclear Physics B 79 (1974) 276

[175] P. Woit, Phys. Rev. Lett. 51 (1983) 638

[176] J. Polonyi, Phys. Rev. D 29 (1984) 716

[177] A. Rajantie, Physica B 255 (1998) 108-115

[178] G.D. Moore, *Informal Lectures on Lattice Gauge Theory*, 2003

[179] Y. Makeenko, *Methods of contemporary gauge theory* (2002) Cambridge University Press

[180] J. Polonyi, *Basic equations of general relativity*, 2012

[181] J. Schwinger, Phys. Rev. 82 (1951) 664

[182] D.R. Nelson, Phase transitions and critical phenomena, Academic, New-York, 1983, Vol.7

[183] N.D. Mermin, H. Wagner, Phys, Rev. Lett. 17 (1966) 113

[184] J.M. Kosterlitz, D.J. Thouless, J. Phys. C 6 (1973) 1181

[185] V.V. Kornyak, *Lecture Notes in Computer Science*, V. 5743, pp. 180-194 (2009) Springer

[186] K. Wilson, Phys. Rev. D 10 (1974) 2445 ; Phys. Reports 23 (1975) 331

[187] R.B. Pearson, Physica 106A (1981) 159-174

[188] H.J. Rothe, *Lattice Gauge Theories. An Introduction* (1997) World Scientific, Singapore

[189] C. Gattringer, C.B. Lang, *Quantum chromodynamics on the lattice* (2010), Springer

[190] G. Toulouse, Tr. J. of Physics 23 (1999) 29

[191] C.L. Henley, Annals of Physics 156 (1984) 358

[192] D. Chowdhury, *Spin glasses and other frustrated systems* (1986) World Scientific

[193] P. Shukla, *Physics of disordered solids* (1982) Mittal Publications

[194] N. Rivier, D.M. Duffy, J. Physique 43 (1982), 239

[195] N. Rivier, Revista Brasileira de Fisica 15 (1985) 311

[196] D.L. Stein, C.M. Newman, *Spin Glasses and Complexity (Primers in Complex Systems)* (2013) Princeton University Press

[197] J.A. Hertz, Phys. Rev. B 18 (1978) 4875

[198] M. Vasin, J. Stat. Mech. (2011) P05009

[199] G. Toulouse, J. Vannimenus, Physics Reports (Review section of Physics Letters) 67 (1980), 47

[200] P. Goldbart, O. Martin, E. Fradkin, Phys. Rev. B 34 (1986) 301

[201] J.B. Kogut, Reviews of Modern Physics 51 (1979) 659

[202] M.V. Berry, Proc. R. Soc. London A392 (1984) 45

[203] J.P. Sethna, Phys. Rev. B 31 (1985) 6278

[204] E. Fradkin, B.A. Huberman, S. Shenker, Phys. Rev. B 18 (1978) 4789

[205] D.C. Mattis, Phys. Lett. A 56 (1976) 421

[206] G. Bhanot, M. Creutz, , Phys. Rev. B 22 (1980) 3370

[207] G. Aeppli, G. Bhanot, J. Phys. C 14 (1981) L593

[208] K.H. Fischer, J.A. Hertz, Spin Glasses (1991) Cambridge University Press

[209] W.F. Harris, *Disclinations*, Scientific American 237 (1997) 130

[210] E. Kroner, *Continuum theory of defects* in Les Houches 1980, Session XXXV: Physics of Defects, ed R. Balian; Int. J. Solids Struc. 29 (1992) 1849-1857; Int. J. Solids Struc., 38 (2001) 1115-1134

[211] F.R.N. Nabarro, Theory of crystal dislocations (Oxford University Press, Oxford, 1967)

[212] V.I. Osipov, Phys. Lett. A 175 (1993) 65

[213] P. Sharma, S. Ganti, Proc. R. Soc. A 461 (2005) 1081-1095

[214] M. Kleman, *Points, Lignes, Parois: dans les fluides anisotropes et les solides cristallins* (Edition de Physique, France 1977).

[215] A. de Padua, F. Parisio-Filho, F. Moraes, Phys. Lett. A 238 (1998) 153-158

[216] L. Landau, E. Lifchitz, Theory of Elasticty, (Pergamon Press, England, 1970)

[217] M.O. Katanaev, Phys.-Usp. 48 (2005) 675

[218] M.C. Valsakumar, D. Sahoo, Gauge theory of defects in elastic continua I-II, Proceedings of Science, PoS(SMPRI2005)005,006

[219] M.D. Glinchuk, R.Farhi, J. Phys.: Condens. Matter 8 (1996) 6985

[220] A. A. Bokov, Phys. Solid State 36 (1994) 19; Ferroelectrics 190 (1997) 197

[221] P. Hohenberg, W. Kohn, Phys. Rev. 136 (1964) B864

[222] W. Kohn and L. J. Sham, Phys. Rev. 140 (1965) A1133

[223] E.H. Lieb, Int. J. Quantum Chem. 24 (1983) 243

[224] D.M. Ceperley, B.J. Alder, Phys. Rev. Lett. 45 (1980) 566

[225] K.M. Rabe, J.D. Joannopoulos, Phys. Rev. Lett. 59 (1987) 570

[226] K.M. Rabe, J.D. Joannopoulos, Phys. Rev. B 36 (1987) 6631

[227] W. Zhong, D. Vanderbilt, K. M. Rabe, Phys. Rev. B 52 (1995) 6301

[228] U. V. Waghmare, K. M. Rabe, Phys. Rev. B 55 (1987) 6161

[229] M.E. Lines, Phys. Rev. 177 (1969) 797

[230] M.T. Yin, Marvin L. Cohen, Phys. Rev. B 26 (1982) 5668

[231] W. Zhong, R.D. King-Smith, D. Vanderbilt, Phys. Rev. Lett. 72 (1994) 3618

[232] A. M. George, J. Iniguez, L. Bellaiche, Nature (London) 413 (2001) 54

[233] L. Bellaiche, A. Garcia, D. Vanderbilt, Phys. Rev. Lett. 84 (2000) 5427

[234] A. M. George, J. Iniguez, L. Bellaiche, Phys. Rev. Lett. 91 (2003) 45504

[235] J. Iniguez, L. Bellaiche, Phys. Rev. Lett. 87 (2001) 95503

[236] L. Bellaiche, D. Vanderbilt, Phys. Rev. B 61 (2000) 7877

[237] N. Ramer, A. M. Rappe, Phys. Rev. B 62 (2000) R743

[238] W. Zhong, D. Vanderbilt, Phys. Rev. Lett. 74 (1995) 2587

[239] D. Vanderbilt, W. Zhong, Ferroelectrics 206 (1998) 181

[240] U. V. Waghmare, K. M. Rabe, Phys. Rev. B 55 (1997) 6161

[241] H. Krakauer, R. Yu, C.-Z. Wang, K. M. Rabe, U. V. Waghmare, J. Phys.: Condens. Matter 11 (1999) 3779

[242] W. Zhong and D. Vanderbilt, Phys. Rev. B 53 (1996) 5047

[243] A. R. Akbarzadeh, L. Bellaiche, K. Leung, J. Iniguez, D. Vanderbilt, Phys. Rev. B 70 (2004) 54103

[244] I. A. Kornev, L. Bellaiche, P.-E. Janolin, B. Dkhil, E. Suard, Phys. Rev. Lett. 97 (2006) 157601

[245] A. Garcia, D. Vanderbilt, Appl. Phys. Lett. 72 (1998) 2981

[246] D. Viehland, X.H. Dai, J.F. Li, Z.Xu, J. Appl. Phys. 84 (1998) 458

[247] L. Bellaiche, J. Iniguez, E. Cockayne, B.P. Burton, Phys. Rev. B 75 (2007) 14111

[248] D.-Y. Kim, J.-J. Choi, H.-E. Kim, Appl. Phys. Lett. 81 (2002) 706

[249] O. Garcia-Zaldivar, A. Pelaiz-Barranco, J.D.S. Guerra, M.E. Mendoza, F. Calderon-Pinar, D.A. Hall, Physica B 406 (2011) 1622

[250] M. Baig, Phys. Rev. Lett. 54 (1985) 167

[251] T. Olson, A. Young, Phys. Rev. B 61 (2000) 12467

[252] D.R. Stump, Phys. Rev. D 38 (1988) 1198

[253] D.P. Landau, K. Binder, *A guide to Monte Carlo Simulations in Statistical Physics* (2005) Cambridge University Press

[254] B.E. Vugmesiter, M.D. Glinchuk, Rev. Mod. Phys. 62 (1990) 993

[255] V.I. Arnold, Ordinary Differential Equations, MIT Press (1973)

[256] A. Garcia, D. Vanderbilt, cond-mat/9802208 (1998)

[257] L. Landau, E.M. Lifshitz, Electrodynamics of Continuous Media (Pergamon, Oxford, 1960)

[258] A. Shukla, V. Agrawal, I. Das, J. Singh, and S. Srivastava, B. Mater. Sci. 34 (2011) 133

[259] D.M. Ceperley, Rev. Mod. Phys. 67 (1995) 279

[260] G. Bhanot, C. Rebbi, Nuclear Physics B 180 (1981) 469

[261] W. Janke, K. Nather, Phys. Rev. B 48 (1993) 4719

[262] T. Vojta, R. Sknepnek, phys. stat. sol. (b) 241, 2118 (2004), cond-mat/0405070

[263] G. Grinstein, Fundamental Problems in Statistical Mechanics VI, ed E.G.D. Cohen (Elsevier, New York, 1985) p.147

[264] S. Huether, R. Kinney, T. Vojta, Phys. Rev. B 74 (2006) 094425

[265] A.B. Harris, J. Phys. C 7 (1974) 1671

[266] E. Almahmoud, I. Kornev, L. Bellaiche, Phys. Rev. Lett. 102 (2009) 105701

[267] M. Hasenbusch, F. P. Toldin, A. Pelissetto, E. Vicari, J. Stat. Mech. (2007) P02016

[268] R. Blinc, A. Gregorovic, B. Zalar, R. Pirc, V.V. Laguta, M.D. Glinchuk, Phys. Rev. B 63 (2000) 024104

[269] G. Samara, L. Hansen, Mat. Res. Soc. Symp. Proc. 499 (1998) 461

[270] O.P. Thakur, C. Prakash, Integrated Ferroelectrics 122 (2010) 100

[271] N.D. Mermin, Reviews of Modern Physics, Vol. 51, 3 (1979) 591

[272] O.I. Motrunich, A. Vishwanath, Phys. Rev. B 70 (2004) 075104

[273] S. Sachdev, K. Park, Ann. Phys. (N.Y.) 298 (2002) 58

[274] B. Berg, M. Luscher, Nucl. Phys. B 190 (1981) 412

[275] L. Kurzawski, K. Malarz, Reports on mathematical physics 70 (2012) 163

[276] M. Lau, C. Dasgupta, Phys. Rev. B 39 (1989) 7212

[277] S. Buczkowskia, P. Hildgenb, L. Cartiliera, Physica A 252, 1-2 (1998) 23

[278] B.B. Mandelbrot, *The Fractal Geometry of Nature* (1982) Freeman, San Fransisco

[279] A.I. Olemskoi, A. Ya. Flat, Phys. Usp. 36, 12 (1993) 1087

[280] G. Toth G, C. Denniston, J.M. Yeomans, Phys Rev Lett 88, 10 (2002) 105504

[281] P.L. Krapivsky, S. Redner, E. Ben-Naim, *A Kinetic View of Statistical Physics*, Cambridge University Press, 2010

[282] R. G. Burkovsky, A. V. Filimonov, A. I. Rudskoy, K. Hirota, M. Matsuura, S. B. Vakhrushev, Phys. Rev. B 85 (2012) 094108

[283] J. Hoshen, R. Kopelman, Phys. Rev. B 14 (1976) 3438

[284] A.A. Abrikosov, Journal of Physics and Chemistry of Solids, 2(3) (1957) 199